

AFIT/DS/ENY/97-4

**Thickness Effects on a Cracked Aluminum
Plate with Composite Patch Repair**

DISSERTATION

**Joel J. Schubbe B.S., M.S.
Captain, USAF**

AFIT/DS/ENY/97-4

DTIC QUALITY INSPECTED 2

Approved for public release; distribution unlimited

19970805 026

Disclaimer

The views expressed in this dissertation are those of the author and do not reflect the official policy or position of the Department of Defense or the U. S. Government.

AFIT/DS/ENY/97-4

***Thickness Effects on a Cracked Aluminum Plate with
Composite Patch Repair***

DISSERTATION

Presented to the Faculty of the Graduate School of Engineering

of the Air Force Institute of Technology

Air Education and Training Command

In Partial Fulfillment for the Degree of

Doctor of Philosophy

Specialization in: Aeronautical Engineering

Joel J. Schubbe B.S., M.S.

Captain, USAF

Air Force Institute of Technology

Wright-Patterson AFB, Ohio

June, 1997

Approved for public release; distribution unlimited

***Thickness Effects on a Cracked Aluminum Plate with
Composite Patch Repair***

Joel J. Schubbe B.S., M.S.

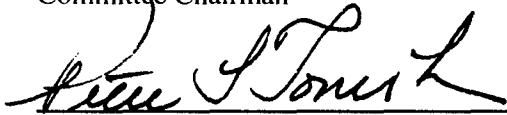
Captain, USAF

Approved:



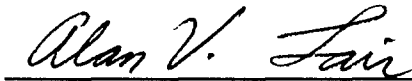
Dr. Shankar Mall
Committee Chairman

6/27/97
Date



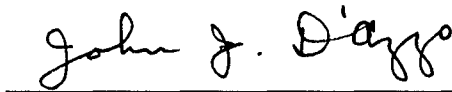
Dr. Peter J. Torvik
Committee Member

27 June 97
Date



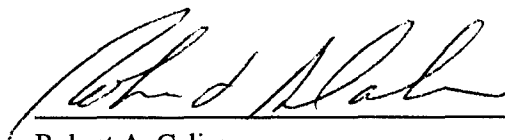
Dr. Alan V. Lair
Committee Member

27 Jun 97
Date



Dr. John J. D'Azzo
Dean's Representative

27 Jun 1997
Date



Robert A. Calico
Dean, Graduate School of Engineering

Dedication

This work is dedicated to my family. Without their support I wouldn't be where I am today
(or anywhere else for that matter).

Acknowledgments

I would like to express my sincere appreciation to the numerous individuals and organizations who had a hand in the completion of my research. This document represents only a small portion of the technical, personal, and general life knowledge gained through this effort. Thanks go out to Wright Laboratory's Flight Dynamics Directorate for sponsorship and encouragement in this study. Secondly, thanks go out to the Materials Directorate for manpower support and equipment use in specimen preparation. I'd especially like to thank MSgt Bryan Cramer for his efforts in patch curing/bonding and for his unique insights on aircraft repair from years of experience on the flightline...an invaluable resource. Mr. John Brausch and Lt. Dom Cicchenelli are to be congratulated on their support in the NDE/NDI arena. I owe a debt of gratitude to my advisor, Professor Shankar Mall, for having confidence in my ability to complete this degree, and for his support and direction when I stumbled. I would also like to thank my other committee members, Professor Peter Torvik, Professor Alan Lair, and, representing the Dean, Professor D'Azzo for their support and time spent in the evaluation of my research. The input was very much appreciated.

Thanks to all the Lab Techs: Jay, Dan, Andy, Charlie, and especially Mark Derriso for all the assistance in getting the 'rubber on the ramp'. Many thanks also go out to Kris Larsen, for sys admin support. Thank you to Jennifer, Kathy, and Karen for all the admin support.

Thanks to my wife, Sherry, and my boys for putting up with me. To HEART BEAT, thanks guys— for keeping me sane! Finally, I'd like to thank God for giving me the opportunity, the strength, the time, and about everything else to accomplish this effort.

Joel J. Schubbe

Table Of Contents

	Page
Dedication	iii
Acknowledgments	iv
List of Figures	x
List of Tables	xxi
List of Symbols	xxiii
Abstract	xxvi
Part: I Introductory Sections	1
1. INTRODUCTION	2
1.1 Overview of Aircraft Repair	2
1.2 Bolted/riveted versus Bonded Repair	4
1.3 Problem Statement/Motivation	6
1.4 Research Objectives	7
2. BACKGROUND	9
2.1 Basic Terminology of Fracture Mechanics	9
2.2 Concepts of Patched Repair	17
2.2.1 Advantages and Disadvantages of Patched Repair	17
2.2.2 Factors Affecting Repair	19
2.2.3 Factors Affecting Crack Growth After Bonded Patched Repair	29

	Page
2.3 The Need for a Generalized Predictive Method	33
2.4 Overview of Previous Research	34
Part: II Experimental Testing	49
3. TEST PROCEDURE	50
3.1 Summary of Research Plan	50
3.2 Experimental Test Apparatus and Procedure	51
3.2.1 Materials, Specimen, and Patch Repair Description	51
3.3 Test Equipment	58
3.3.1 Crack Measurement Systems	58
3.3.2 Test Execution	68
3.4 Data Analysis Techniques	73
3.4.1 Data Sampling/Analysis.	73
3.5 Post-Mortem Examination of Tests	77
3.6 Numerical Approach	77
4. TEST RESULTS AND DISCUSSION	79
4.1 Test Summary	79
4.2 Material Constant Determination	79
4.3 Pre-Test Curvature	84
4.3.1 Curvature Measurement	84

	Page
4.3.2 Residual Stresses and Pre-existent Strains	86
4.4 Effects of Patch Length	89
4.4.1 Initial Curvatures	89
4.4.2 Crack Growth Rates	91
4.4.3 Crack Opening Displacement (COD)	102
4.4.4 Patched/Unpatched Face Crack Growth Rates	107
4.5 Effects of Patch Stiffness Ratio	109
4.5.1 Initial Curvature	114
4.5.2 Crack Growth Rates	116
4.5.3 Crack Opening Displacement (COD)	121
4.5.4 Patched/Unpatched Face Crack Growth Rates	126
4.6 Effects of Patch Width	129
4.6.1 Initial Curvature	129
4.6.2 Crack Growth Rates	130
4.6.3 Crack Opening Displacement	140
4.6.4 Patched/Unpatched Face Crack Growth Rates	144
4.7 Damage Mechanisms	144
4.7.1 Disbond	144
4.7.2 Fracture Surface	153

	Page
4.8 Crack Growth Retardation	154
4.9 Summary of Experimental Observations	158
Part: III Finite Element Modeling (FEM)	161
5. ANALYSIS	162
5.1 Mindlin Plate Model Description	162
5.2 Boundary Conditions	167
5.2.1 Rotation and Displacement Conditions	167
5.2.2 Temperature Condition	168
5.3 Crack Opening Displacement Comparison	170
5.4 Strain Comparison	172
5.4.1 Direct Comparison	172
5.4.2 Out-of-Plane Displacement	176
5.5 Crack Growth Rate Comparison	178
5.6 Disbond Modification	181
5.7 Limitations of the 3-Layer Model	188
5.7.1 Effective Crack Length Modification	189
5.7.2 Empirical Weighting Factor	192
6. SUMMARY, CONCLUSIONS, AND RECOMMENDATIONS	200
6.1 Summary	200

	Page
6.2 Conclusions	201
6.3 Recommendations for Future Research	203
Appendix A. Additional Crack Growth Rate Data	205
Appendix B. Post-Failure Images	208
Appendix C. Repeat Tests	214
Bibliography	217
Vita	221

List of Figures

	Page
Figure 1. Bolted vs. Riveted Repair Strength [6]	5
Figure 2. S-N Life Cycle Plot	11
Figure 3. da/dN vs. Delta K	15
Figure 4. 2-D Lap Joint Illustration	20
Figure 5. Adhesive Load Transfer	21
Figure 6. Neutral Axis Shift	21
Figure 7. Peel and Cleavage Fracture	22
Figure 8. Ultrasound Use Configurations	28
Figure 9. Eddy Current Configuration	30
Figure 10. Thermal Residual Stresses	32
Figure 11. Ratwani's Model Configuration	36
Figure 12. Ratwani's Crack Formulation Parameters	37
Figure 13. Rose Application	41
Figure 14. Sun's Plate/Spring Model	45
Figure 15. Caisheng and Lam's Model Configuration	46
Figure 16. Slicing Method	47

	Page
Figure 17. Specimen Configuration	54
Figure 18. Patch Configurations	56
Figure 19. Mechanical Load System	59
Figure 20. Specimen in Mechanical Load System	60
Figure 21. Optical Crack Measurement System	61
Figure 22. In-Situ Eddy Current System	62
Figure 23. Eddy Current Instrumentation System	63
Figure 24. Crack Opening Displacement Gage	64
Figure 25. AFIT-Built Clip Gage on Specimen Face	65
Figure 26. Infrared Disbond Monitoring	66
Figure 27. Infrared Camera and Instrumentation	67
Figure 28. Calibration Specimen for Eddy Current Technique	70
Figure 29. Unrepaired Specimen Curvature (i.e. no patch)	71
Figure 30. Repaired Specimen Curvature: Specimen 7 (Patch Length = 102 mm)	72
Figure 31. Clip Gage Calibration Curve	75
Figure 32. Patched Specimen Crack Growth Lag	78
Figure 33. Unpatched Specimen Crack Front Progression	78
Figure 34. Baseline Crack Growth Curves - Unrepaired Panels (at 120 MPa)	82
Figure 35. Paris Law Constant Determination for $t=3.175$ mm Plate	84

	Page
Figure 36. Paris Law Constant Determination for $t=4.826$ mm Plate	85
Figure 37. Paris Law Constant Determination for $t=6.350$ mm Plate	85
Figure 38. Comparison of Measured Curvature with Parabolic Curve Fit	86
Figure 39. Radius of Curvature Variation with Plate Thickness and Patch Length	90
Figure 40. Crack Growth vs. Cycles Comparison, 6.350 mm Plate with $S=1.0$, Full Width Repair, Patch Lengths: 102 mm-Specimen 7, 51 mm-Specimen 9	93
Figure 41. Crack Growth Rate, da/dN , Comparison, 6.350 mm Plate with $S=1.0$, Full Width Repair, Patch Lengths:102 mm- Specimen 7, 51 mm- Specimen 9	93
Figure 42. Crack Growth vs. Cycles Comparison, 4.826 mm Plate with $S=1.0$, Full Width Repair, Patch Lengths:102 mm-Specimen 16, 51 mm-Specimen 17	94
Figure 43. Crack Growth Rate, da/dN , Comparison, 4.826 mm Plate with $S=1.0$, Full Width Repair, Patch Lengths:102 mm-Specimen 16, 51 mm-Specimen 17	94
Figure 44. Crack Growth vs. Cycles Comparison, 3.175 mm Plate with $S=1.0$, Full Width Repair, Patch Lengths:102 mm-Specimen 18, 51 mm-Specimen 19	95
Figure 45. Crack Growth Rate, da/dN , Comparison, 3.175 mm Plate with $S=1.0$, Full Width Repair, Patch Lengths:102 mm-Specimen 18, 51 mm-Specimen 19	96
Figure 46. Crack Growth vs. Cycles Comparison - 6.350 mm Plate with $S=1.3$, Full Width Repair, Patch Lengths: 51 mm- Specimen 24, 102 mm-Specimen 25	96
Figure 47. Crack Growth Rate, da/dN , Comparison, 6.350 mm Plate with $S=1.3$, Full Width Repair, Patch Lengths: 51 mm-Specimen 24, 102 mm-Specimen 25	97

	Page
Figure 48. Crack Growth vs. Cycles Comparison - 6.350 mm Plate with S=1.0, 50 mm Wide Repair, Patch Lengths: 51 mm- Specimen 20, 102 mm-Specimen 22	98
Figure 49. Crack Growth Rate, da/dN, Comparison, 6.350 mm Plate with S=1.0, 50 mm Wide Repair, Patch Lengths: 51 mm-Specimen 20, 102 mm-Specimen 22	99
Figure 50. Crack Growth vs. Cycles Comparison - 6.350 mm Plate With S=1.3, 50 mm Wide Repair, Patch Lengths: 51 mm- Specimen 21, 102 mm-Specimen 23	100
Figure 51. Crack Growth Rate, da/dN, Comparison, 6.350 mm Plate with S=1.3, 50 mm Wide Repair, Patch Lengths: 51 mm-Specimen 21, 102 mm-Specimen 23	101
Figure 52. COD Comparison - 6.350 mm Plate, S=1.0, Full Width Repair, Patch Lengths: 102 mm-Specimen 7, 51 mm-Specimen 9	103
Figure 53. COD Comparison - 4.826 mm Plate, S=1.0, Full Width Repair, Patch Lengths: 102 mm-Specimen 16, 51 mm-Specimen 17	104
Figure 54. COD Comparison - 3.175 mm Plate, S=1.0, Full Width Repair, Patch Lengths: 102 mm-Specimen 18, 51 mm-Specimen 19	105
Figure 55. COD Comparison - 6.350 mm Plate, S=1.3, Full Width Repair, Patch Lengths: 51 mm-Specimen 24, 102 mm-Specimen 25	105
Figure 56. COD Comparison - 6.350 mm Plate, S=1.0, 50 mm Wide Repair, Patch Lengths: 51 mm-Specimen 20, 102 mm-Specimen 22	106
Figure 57. COD Comparison - 6.350 mm Plate, S=1.3, 50 mm Wide Repair, Patch Lengths: 51 mm-Specimen 21, 102 mm-Specimen 23	106
Figure 58. Comparison of Eddy Current and Post-Mortem Crack Length Measurements	108
Figure 59. Patched vs. Unpatched Face Crack Lengths-Specimen 7: 6.350 mm Plate with 102 mm long, S=1.0, Full Width Patch	110

	Page
Figure 60. Patched vs. Unpatched Face Crack Lengths-Specimen 9: 6.350 mm Plate with 51 mm long, $S=1.0$, Full Width Patch	110
Figure 61. Patched vs. Unpatched Face Crack Lengths-Specimen 18: 3.175 mm Plate with 102 mm long, $S=1.0$, Full Width Patch	111
Figure 62. Patched vs. Unpatched Face Crack Lengths-Specimen 19: 3.175 mm Plate with 51 mm long, $S=1.0$, Full Width Patch	111
Figure 63. Patched vs. Unpatched Face Crack Lengths-Specimen 16: 4.826 mm Plate with 102 mm, $S=1.0$, Full Width Patch	112
Figure 64. Patched vs. Unpatched Face Crack Lengths-Specimen 17: 4.826 mm Plate with 51 mm, $S=1.0$, Full Width Patch	112
Figure 65. Patched vs. Unpatched Face Crack Lengths-Specimen 25: 6.350 mm Plate with 102 mm long, $S=1.3$, 50 mm wide Patch	113
Figure 66. Patched vs. Unpatched Face Crack Lengths-Specimen 24: 6.350 mm Plate with 51 mm long, $S=1.3$, 50 mm wide Patch	113
Figure 67. Radius of Curvature Dependence on Patch to Panel Stiffness Ratio	115
Figure 68. Crack Growth vs. Cycles Comparison - 6.350 mm Plate With 102 mm, Full Width Repair - Stiffness Ratios: $S=1.0$ -Specimen 7, $S=1.3$ -Specimen 25	117
Figure 69. Crack Growth Rate, da/dN , Comparison, 6.350 mm Plate With 102 mm, Full Width Repair - Stiffness Ratios: $S=1.0$ -Specimen 7, $S=1.3$ -Specimen 25	117
Figure 70. Crack Growth vs. Cycles Comparison - 6.350 mm Plate With 51 mm, Full Width Repair - Stiffness Ratios: $S=1.0$ - Specimen 9, $S=1.3$ -Specimen 24	118
Figure 71. Crack Growth Rate, da/dN , Comparison, 6.350 mm Plate With 51 mm, Full Width Repair - Stiffness Ratios: $S=1.0$ -Specimen 9, $S=1.3$ -Specimen 24	118

	Page
Figure 72. Crack Growth vs. Cycles Comparison - 3.175 mm Plate With 51 mm, Full Width Repair - Stiffness Ratios: S=.46-Specimen 15, S=1.0-Specimen 19, S=1.3-Specimen 28	119
Figure 73. Crack Growth Rate, da/dN, Comparison, 3.175 mm Plate With 51 mm, Full Width Repair - Stiffness Ratios: S=.46-Specimen 15, S=1.0-Specimen 19, S=1.3-Specimen 28	120
Figure 74. Crack Growth vs. Cycles Comparison - 4.826 mm Plate With 51 mm, Full Width Repair - Stiffness Ratios: S=.69-Specimen 12, S=1.0-Specimen 17	121
Figure 75. Crack Growth Rate, da/dN, Comparison, 4.826 mm Plate With 51 mm, Full Width Repair - Stiffness Ratios: S=.69-Specimen 12, S=1.0-Specimen 17	122
Figure 76. COD Comparison - 6.350 mm Plate, 102 mm Long, Full Width Repair, Stiffness Ratios: S=1.0-Specimen 7, S=1.3-Specimen 25	124
Figure 77. COD Comparison - 6.350 mm Plate, 51 mm Long, Full Width Repair, Stiffness Ratios: S=1.0-Specimen 9, S=1.3-Specimen 24	124
Figure 78. COD Comparison - 3.175 mm Plate, 51 mm Long, Full Width Repair, Stiffness Ratios: S=.46-Specimen 15, S=1.0-Specimen 19, S=1.3-Specimen 28	125
Figure 79. COD Comparison - 4.826 mm Plate, 51 mm Long, Full Width Repair, S=.69-Specimen 12, S=1.0-Specimen 17	125
Figure 80. Patched vs. Unpatched Face Crack Lengths-Specimen 12: 4.826 mm Plate With S=0.69, 51 mm, Full Width Repair	126
Figure 81. Patched vs. Unpatched Face Crack Lengths-Specimen 15: 3.175 mm Plate With S=0.46, 51 mm, Full Width Repair	127
Figure 82. Patched vs. Unpatched Face Crack Lengths-Specimen 28: 3.175 mm Plate With S=1.3, 51 mm, Full Width Repair	127
Figure 83. Crack Growth vs. Cycles Comparison - 6.350 mm Plate With S=1.3, 102 mm Long Repair - Patch Widths: 50 mm-Specimen 23, Full Width-Specimen 25	131

	Page
Figure 84. Crack Growth vs. Cycles Comparison - 6.350 mm Plate With S=1.3, 51 mm Long Repair - Patch Widths: 50 mm-Specimen 21, Full Width-Specimen 24	132
Figure 85. Crack Growth Rate, da/dN, Comparison, 6.350 mm Plate With S=1.3, 102 mm Long Repair - Patch Widths: 50 mm-Specimen 23, Full Width-Specimen 25	132
Figure 86. Crack Growth Rate, da/dN, Comparison, 6.350 mm Plate With S=1.3, 51 mm Long Repair - Patch Widths: 50 mm-Specimen 21, Full Width-Specimen 24	133
Figure 87. Crack Growth vs. Cycles Comparison - 6.350 mm Plate With S=1.0, 102 mm Long Repair - Patch Widths: 50 mm-Specimen 22, Full Width-Specimen 7	134
Figure 88. Crack Growth vs. Cycles Comparison - 6.350 mm Plate With S=1.0, 51 mm Long Repair - Patch Widths: 50 mm-Specimen 20, Full Width-Specimen 9	135
Figure 89. Crack Growth Rate, da/dN, Comparison, 6.350 mm Plate With S=1.0, 102 mm Long Repair - Patch Widths: 50 mm-Specimen 22, Full Width-Specimen 7	135
Figure 90. Crack Growth Rate, da/dN, Comparison, 6.350 mm Plate With S=1.0, 51 mm Long Repair - Patch Widths: 50 mm-Specimen 20, Full Width-Specimen 9	136
Figure 91. Crack Growth vs. Cycles Comparison - 3.175 mm Plate with S=1.0, 51 mm Long Repair - Patch Widths: 50 mm-Specimen 26, Full Width-Specimen 19	137
Figure 92. Crack Growth vs. Cycles Comparison - 3.175 mm Plate With S=1.3, 51 mm Long Repair - Patch Widths: 50 mm-Specimen 27, Full Width-Specimen 28	138
Figure 93. Crack Growth Rate, da/dN, Comparison, 3.175 mm Plate With S=1.0, 51 mm Long Repair - Patch Widths: 50 mm-Specimen 26, Full Width-Specimen 19	138

	Page
Figure 94. Crack Growth Rate, da/dN , Comparison, 3.175 mm Plate With S=1.3, 51 mm Long Repair - Patch Widths: 50 mm-Specimen 27, Full Width-Specimen 28	139
Figure 95. COD Comparison - 6.350 mm Plate, S=1.3, 102 mm Long Repair, Patch Widths: 50 mm-Specimen 23, Full Width-Specimen 25	141
Figure 96. COD Comparison - 6.350 mm Plate, S=1.3, 51 mm Long Repair, Patch Widths: 50 mm-Specimen 21, Full Width-Specimen 24	141
Figure 97. COD Comparison - 6.350 mm Plate, S=1.0, 102 mm Long Repair, Patch Widths: Full Width-Specimen 7, 50 mm-Specimen 22	142
Figure 98. COD Comparison - 6.350 mm Plate, S=1.0, 51 mm Long Repair, Patch Widths: Full Width-Specimen 9, 50 mm-Specimen 20	142
Figure 99. COD Comparison - 3.175 mm Plate, S=1.0, 51 mm Long Repair, Patch Widths: Full Width-Specimen 19, 50 mm-Specimen 26	143
Figure 100. COD Comparison - 3.175 mm Plate, S=1.3, 51 mm Long Repair, Patch Widths: 50 mm-Specimen 27, Full Width-Specimen 28	143
Figure 101. Patched vs. Unpatched Face Crack Lengths-Specimen 20: 6.350 mm Plate With S=1.0, 51 mm Long, 50 mm Wide Repair	145
Figure 102. Patched vs. Unpatched Face Crack Lengths-Specimen 21: 6.350 mm Plate With S=1.3, 51 mm Long, 50 mm Wide Repair	145
Figure 103. Patched vs. Unpatched Face Crack Lengths-Specimen 22: 6.350 mm Plate With S=1.0, 102 mm Long, 50 mm Wide Repair	146
Figure 104. Patched vs. Unpatched Face Crack Lengths-Specimen 23: 6.350 mm Plate With S=1.3, 102 mm Long, 50 mm Wide Repair	146
Figure 105. Patched vs. Unpatched Face Crack Lengths-Specimen 26: 3.175 mm Plate With S=1.0, 51 mm Long, 50 mm Wide Repair	147
Figure 106. Patched vs. Unpatched Face Crack Lengths-Specimen 27: 3.175 mm Plate With S=1.3, 51 mm Long, 50 mm Wide Repair	147

	Page
Figure 107. Thermographic Video Pictures of Disbond Growth in Full Width Patch Specimen	149
Figure 108. C-Scan Image of Disbond Growth in Full Width Patched Specimen with Long Crack	150
Figure 109. Disbond Progression in Finite Width Patch: $S=1.0$	151
Figure 110. Disbond Progression in Finite Width Patch: $S=1.3$	152
Figure 111. Comparison of Repaired to Unrepaired Panel Stress Intensity Factors (6.350 mm Thick Panel, $S=1.0$, 102 mm Long, Full Width Repair)	156
Figure 112. Crack Growth Retardation in Finite Width and Full Width Patch Specimens 20 and 22	157
Figure 113. Quarter Model Configuration	163
Figure 114. FEM Quarter Panel Grid ($a=45\text{mm}$, Full Width Patch)	164
Figure 115. FEM Crack Tip Grid Refinement	165
Figure 116. Thermal Curvature Comparison - FEM versus Experimental	169
Figure 117. Tab Configuration for COD Calculations	171
Figure 118. Experimental versus FEM COD Comparison, 6.350 mm Plate with $S=1.0$, 51 mm Long, Full Width Patch	172
Figure 119. Experimental versus FEM COD Comparison, 3.175 mm Plate with $S=1.0$, 102 mm Long, Full Width Patch	173
Figure 120. Experimental versus FEM COD Comparison, 6.350 mm Plate with $S=1.0$, 102 mm Long, Full Width Patch	173
Figure 121. Gage Locations for Strain Measurements	175
Figure 122. Out-of-Plane Curvature - Post-bonding, 0 to 120 MPa, 6.350 mm Plate with $S=1.0$, 102 mm, Full Width Patch	177

	Page
Figure 123. Unpatched Face (UPF) Crack Growth Rate Comparison - Experiment vs. FEM Model Results	179
Figure 124. Patched Face (PF) Crack Growth Rate Comparison - Experiment vs. FEM Model	180
Figure 125. FEM Results Comparison to Specimen 7 Experiment - No Disbond Added	182
Figure 126. FEM Results Comparison to Specimen 18 Experiment - No Disbond Added	182
Figure 127. Experimental vs. Analytical Disbond Configuration	184
Figure 128. Experimental vs. Numerical Calculation of Crack Growth Rates - 35% disbond added at $2a = 120$ mm	186
Figure 129. Experimental vs. Numerical Calculation of Crack Growth Rates - 35% disbond added at $2a = 120$ mm	186
Figure 130. Experimental vs. Numerical Calculation of Crack Growth Rates - 35% disbond added at $2a = 120$ mm	187
Figure 131. Experimental versus FEM Calculation of Crack Growth Rate - with Disbond and Crack Length Adjustment	190
Figure 132. Experimental versus FEM Calculation of Crack Growth Rate - with Disbond and Crack Length Adjustment	191
Figure 133. FEM Model Crack Length Adjustment for Effective Area	193
Figure 134. Weighting Factor Results Comparison to Experiment - 3.175 mm Plate, $S=1.0$, Full Width Repair	195
Figure 135. Weighting Factor Results Comparison to Experiment - 6.350 mm Plate, $S=1.0$, Full Width Repair	196
Figure 136. Weighting Factor Results Comparison to Experiment - 6.350 mm Plate, $S=1.3$, Full Width Repair	197

	Page
Figure 137. Short Crack Growth Rates, da/dN , 3.175 mm Thick Plates, $S=1.0$, Full Width Repairs	205
Figure 138. Short Crack Growth Rates, da/dN , 6.350 mm Thick Plates, 102 mm Long, Full Width Repairs	206
Figure 139. Short Crack Growth Rates, da/dN , 6.350 mm Thick Plates, 51 mm Long, Full Width Repairs	206
Figure 140. Short Crack Growth Rates, da/dN , 6.350 mm Thick Plates, $S=1.0$, 50 mm Wide Repairs	207
Figure 141. Pre-Failure Specimens - Full Width and Finite Width (50 mm Nom)	209
Figure 142. Pre-Failure Specimens - Close-up of Full Width and Finite Width Patches	210
Figure 143. Post-Failure Full Width Repair - Adhesive Surface and Patch	211
Figure 144. Post-Failure Finite Width Repair - 102 mm Long Adhesive Surface and Patch	212
Figure 145. Post-Failure Finite Width Patch - 51 mm Long Adhesive Surface and Patch	213
Figure 146. Repeat Test Comparison - 3.175 mm Thick Panel, 102 mm Long, Full Width, $S=1.0$ Repair	214
Figure 147. Repeat Test Comparison - 6.350 mm Thick Panel, 102 mm Long, Full Width, $S=1.0$ Repair	215
Figure 148. Repeat Test Comparison - 6.350 mm Thick Panel, 102 mm Long, Full Width, $S=1.3$ Repair	216

List of Tables

	Page
Table 1. Patch/Plate Material Properties	28
Table 2. Material Properties	51
Table 3. Aluminum Alloy Composition (Percent Weight-ASTM-B209-92A)	52
Table 4. Patch Configuration Lay-ups	53
Table 5. Example of Square Patch Lay-up	55
Table 6. Test Summary	69
Table 7. Eddy Current System Calibration Results: Gain=4	74
Table 8. Eddy Current Calibration Results: Gain=8	74
Table 9. Repaired Specimen Test Summary	80
Table 10. Baseline Test Plates - Cyclic Life	81
Table 11. Baseline Tests - da/dN vs. Delta K Determination	82
Table 12. Experimentally Determined Paris Law Constants	83
Table 13. Measured Curvature Summary	87
Table 14. Lifespan Increase Summary, Full Width Repair, $S=1.0$	92
Table 15. Percentage Change in Life Cycles with Increasing Patch Length from 51 mm to 102 mm	102
Table 16. Maximum Crack Length Lag between Patched and Unpatched Faces	109

	Page
Table 17. Maximum Patched-Face Crack Length Lag - Stiffness Ratio Comparison	128
Table 18. Percentage Change in Fatigue Life with Change in Patch to Panel Stiffness Ratio Relative to Stiffness Ratio $S=1.0$	129
Table 19. Percentage Change in Fatigue Life with Reduction in Patch Width from 153 mm to 50 mm	139
Table 20. Maximum Patched-Face Crack Length Lag for Finite Width Patch Specimens	144
Table 21. Experimental Strain Comparison with FEM Model on Unpatched Face (UPF) - Specimen 7, $a=13.91$ mm	174
Table 22. Experimental Strain Comparison with FEM Model on Unpatched Face (UPF) - Specimen 9, $a=13.91$ mm	176
Table 23. Life Prediction Results for Weighted 3-Layer Mindlin Model	198
Table 24. Life Prediction Results for Weighted 3-Layer Mindlin Model-Repeat Tests	199

List of Symbols

Symbols

Symbol	Definition
α	Coefficient of Thermal Expansion or LEFM Correction Constant for Geometry
B_{SE}	GE Sigmoidal Curve Parameter
C	Paris Law Parameter (Slope) or Pratt & Whitney Inflection Point Parameters
D	GE Sigmoidal Curve Parameter
δ	Crack Opening Dimension (Ratwani)
Δ	Parameter Range
da/dN	Crack Growth Rate (m/cycle)
E	Young's Modulus (MPa)
f	Frequency (Hz) or Function of ()
h	Parabolic Vertex Coordinate
J_o, J_x	Current Density at Surface, Plane x (A/m ²)
k	Parabolic Vertex Coordinate
K	Stress Intensity Factor or $\frac{1}{\rho}$ (inverse of radius of curvature)
L	Length (mm)
m	Paris Law Constant (Intercept Point)
μ	Magnetic Permeability
N	Number of Cycles to Failure
P	Load (kg), Pressure Distribution, or Distance from vertex to apex of parabola
π	Pi (Radians)
Q	GE Sigmoidal Curve Parameter

r	Radius (Crack tip to point of interest)
R	Stress Ratio
ρ	Density (kg/m^3) or Radius of Curvature
S	Repair Stiffness Ratio
σ	Stress (MPa) or Electrical Conductivity
t	Thickness (mm)
T	Temperature ($^{\circ}\text{C}$)
θ	Plane Rotation (Radians), or Elevation Angle from Crack Plane to Point of Interest
W	Width Parameter
x, y	Length Parameters
∞	Far Field Value
$\#$	Number of ()

Subscripts

Symbol	Definition
a	Half Crack Length, Adhesive Property Values, or Amplitude
app	Remotely Applied Value
c	Critical Value
I	Mode I
II	Mode II
III	Mode III
i, j, k	Counter Indices
$\text{max, min, } m$	Maximum, Minimum, Mean Values
o	Nominal Value

p	Plate Property Values
r	Patch or Repair Property Values
th	Threshold Value

Superscript

Symbol	Definition
c	Leading Node Quantity
u	Extensional Designator
t	Total Designator
θ	Rotational Designator
*	Wildcard Designator for Plate, Adhesive, or Patch Properties

Abbreviations

AFIT	Air Force Institute of Technology
COD	Crack Opening Displacement
CTE	Coefficient of Thermal Expansion
DAS	Data Acquisition System
FAA	Federal Aviation Administration
FEM	Finite Element Model
LEFM	Linear Elastic Fracture Mechanics
MSD	Multi-Site Damage
NDE/NDI/NDT	Non-destructive Evaluation/Inspection/Test
UPF/PF	Unpatched Face/Patched Face

Abstract

Many military and commercial aircraft are flying well beyond their design service lives. Due to budget cuts, a dwindling cash flow has forced the airlines and the U.S. Air Force to extend the lives of current fleet inventories. Through increased emphasis on programs involving advanced maintenance and repair technologies, the fleet owners desire to prolong retirement of current aircraft to reduce costs of replacement. One repair technology of great interest is bonded composite patch repair of cracked aircraft structures. Recent developments in high strength composites and adhesives have brought bonded repair technology to the forefront. However, there is currently a lack of experimental data, especially data characterizing the fatigue crack growth behavior in thick components repaired with bonded composite patches. Further, analytical methods developed to date, have not been validated for thick components. Also, an economical yet accurate predictive method for crack growth in thick components is required.

Therefore, this study involving a hybrid experimental-numerical approach was undertaken with the focus on repairs of cracked, flat aluminum (2024-T3) plates. Three thicknesses (3.175, 4.826, and 6.350 mm) ranging from thin to thick panels were examined. These panels, 508 mm long and 153 mm wide, were repaired with a single-sided composite patch, made of pre-cured unidirectional boron/epoxy, and bonded with FM73 sheet adhesive. Several patch configurations were tested in order to investigate the effects of different parameters of patch design on fatigue crack growth rates. These parameters were patch width (full width-153 mm vs. partial width-50 mm), patch length (51, 68, and 102 mm), and patch to panel stiffness ratio ($S=0.46, 0.69, 1.0, \text{ and } 1.3$). Fatigue tests were conducted at maximum stress of 120 MPa, stress ratio of $R=0.1$ and frequency of 10 Hz. Curvatures induced by residual thermal stresses developed during bonding of the repair, crack growth rates

on patched and unpatched faces, center crack opening displacements, disbond characteristics, and strains at a few locations during fatigue were measured.

Test results showed that crack growth rates increased with an increase of plate thickness in both unrepaired and repaired panels. Bonding of the repairs caused significant thermal residual stresses and an initial curvature in the patched area of the plate. Thin panels experienced more bending due to patch bonding than the thick plates. Variations in patch length affected the curvature of the repaired plate. Radius of curvature in thin plates increased as patch length increased. However, the trend is reversed in thick plates with increase of patch length. Patch to panel stiffness ratio effects showed a reduced crack growth rate with increased stiffness ratio. In all panels, crack growth rate under a finite width patch was lower than that of its full width repair counterpart. Differences in crack growth rate between patched and unpatched faces increased as plate thickness increased. Disbond growth was minimal until one of the following events occurred: (1) the crack grew beyond the uniform thickness area in partial width repairs, or (2) the unpatched face crack grew to the critical crack length of the unrepaired panel in the case of the full width repair.

The analytical part involved a two-dimensional finite element model incorporating three layers of linear elastic 4-noded Mindlin plate elements to model the cracked plate, adhesive, and composite patch. This technique uses a continuum to model the adhesive instead of spring elements (non-continuum body) as employed in previous studies. Constraint equations are used to enforce compatibility conditions along the plate-adhesive and adhesive-patch interfaces. Strain energy release rates, and subsequently Mode I (opening) stress intensity factors, are calculated from the modified crack closure method. The fatigue crack growth relationship (Paris Law) of the unpatched plate is used to calculate crack growth rates using the computed stress intensity factors from the three layer model and experimentally determined material constants.

The predicted fatigue crack growth rates from the analysis agreed very well with experimental counterparts. The present three-layer model accurately predicts crack growth rates in the thin and thick plates for crack lengths up to 50 mm long, respectively. For crack lengths longer than 90 mm, experiments showed increasing growth of disbond in the bondline between the patch and plate. So, these disbonds were included in the three-layer analysis for crack lengths greater than 90 mm. The agreement between the experimental and predicted fatigue crack growth rates did not improve by this incorporation of debond in the analysis. However, the model more accurately characterized the shape of the final experimental growth curves. A crack length correction and an empirical correction factor involving plate thickness, stiffness ratio, and crack length were also developed as attempts to improve analytical results for longer cracks. Results of the three-layer model along with this empirical correction factor demonstrated excellent agreement with experimental data.

Thus this study provided a scientific knowledge-base for efficient, reliable, and better design tools for repair of thick aircraft components with bonded composite patches.

Part: I
Introductory Sections

1. Introduction

1.1 Overview of Aircraft Repair

A distressing trend, well known to current aviators in both the military and civilian communities, is the increasing mean age of the current aircraft fleet. In 1993, the age of 51 percent of the United States Air Force fleet was older than 15 years and 44 percent of the airframes were over 20 years of age [26]. This trend of extended use of aircraft, coupled with incidents such as the Aloha Airlines' disaster [52], prompted efforts by the Federal Aviation Agency, commercial airlines, and the U.S. Air Force to examine maintenance and repair programs for aging aircraft. This review was performed from the perspective of fatigue and corrosion damage, inherent in aging aircraft.

In this age of budget cuts, personnel reductions, and keeping up in the global economy with what the country has, the mission of current research on aging aircraft is to provide the U.S. Air Force and industry with technologies to extend the usable lives and reduce the long-term costs of the current aircraft fleet. Industry and government research organizations are concentrating on life, risk, repair, and dynamic loading analysis of aerospace structures to provide methods for ensuring structural integrity over their extended life span.

It is evident from the emphasis of the many different programs addressing service life of aircraft that the overall philosophy of design, manufacturing, inspection, maintenance, repair, and replacement must undergo a major overhaul. This change in philosophy must account for the age-related failure modes in areas such as propulsion, avionics, structures, and various aircraft subsystems. Fail-safe modes must be designed into systems. The initial design must be expanded to include repair technologies and durability for the unique failure modes (fatigue cracking with multi-site damage (MSD)) associated with extended use. Corrosion effects on fatigue or on joint strengths must be characterized. Along with these new design philosophies, more advanced non-destructive evalua-

tion or inspection (NDE/I) techniques must be developed for detecting and monitoring damage before and after executing a repair. These new philosophies combined with the advent of new analysis tools will give designers and users the means to predict service lives for imperfect components, to determine inspection intervals, and to predict specific types of damage growth for safe, dependable aircraft in the years to come. Most aircraft in the USAF mobility fleet can be expected to be in service 30, 50, 60 years or longer. For example, C-141s are expected to be retired in the year 2003, a 38 year life-span. But, the C-5 fleet is currently expected to last until 2038: 69 years of life! [26]

Due to the extensive age and use of the current aircraft inventory, crack initiation, growth, and fatigue damage is inevitable. The widespread occurrence of this damage reduces the overall safety of the fleet. Once this damage has been detected through the available means such as: ultrasonic, tap tests (composite delamination), eddy current, visual inspection, etc., the repair or replacement of the component must then be addressed. For most aircraft structural components, repair would be the primary choice from both monetary (simple repair cost is usually less than replacement) and convenience (most repairs can be accomplished *in situ* quickly) perspectives.

Most of the previous airframe repairs were designed to restore the static strength of the structure, as dictated by the original design specifications. These repair designs did not account for dynamic loading or fatigue conditions, which might re-initiate the cracks. For these earlier repairs, bolted/riveted-type repairs were chosen due to the ease of fabrication, quick installation, and the non-existence of today's advanced composite materials and adhesives. Composite materials and the advanced adhesives have made bonded composite patch repair technology a reality. Two types of repair which are currently in use for aircraft (bolted/riveted and bonded) are discussed briefly in the following section as an introduction to the present study [6].

1.2 Bolted/riveted versus Bonded Repair

Riveted or bolted panel repair has been the standard method to decrease stresses due to a flaw or to stiffen an underdesigned portion of an in-service aircraft component. But, these repairs often are designed only to account for static load design requirements. Life cycle analyses of these repaired components under fatigue conditions are usually not considered. When bolted or riveted repairs are used, they usually have the following detrimental effects:

- Machined holes weaken the underlying structure and produce multiple stress risers for the initiation of new fatigue damage.
- Bolted repairs, in particular, weaken composite structures, often requiring additional reinforcement to withstand design loads.

Adhesive bonding of aircraft structures is a proven and accepted means for fabrication of many aircraft components. Extensive use of adhesive bonding including use of composite materials can be found in the Fokker Aircraft. Examples of the use of adhesive bonding can also be found in many aircraft components including: fuselage longerons, fuselage skin panel splice areas, and wing stiffeners. In recent years, the advances in adhesive bonding techniques and advanced composites have sparked new interest in repairing cracked aircraft components with bonded composite patches in addition to the fabrication of new fatigue resistant parts [9].

Bonded patch repairs, however, require a stringent cleaning, preparation, and processing procedure, but, when properly designed, can provide an effective alternate load path in the damaged area. This results in reduced localized stress concentrations. Figure 1 from Baker [6] shows a comparison of bolted vs. bonded repair strengths as simulated by a symmetric lap shear joint. Baker conducted a comparison test of a bolted composite/aluminum joint and the same joint bonded with adhesive. Results showed more than a 300 percent increase in strength of the bonded joint over the bolted joint.

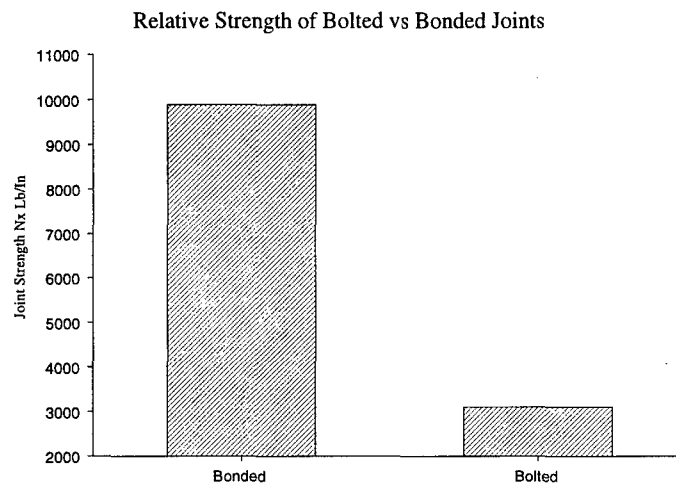
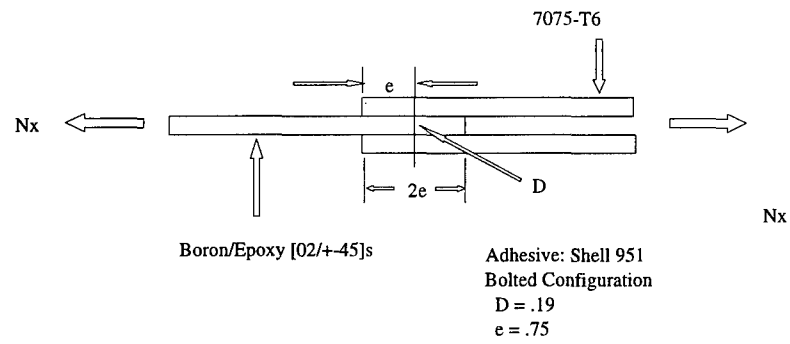


Figure 1. Bolted vs. Riveted Repair Strength [6]

Great success has been achieved in using bonded patches to repair thin panels, such as fuselage skins, damaged by fatigue loading. Currently there are more than 6500 repair patches flying on aircraft as either coupons or actual crack arrestors on fuselage skins [9]. But, the successes of these repairs were dependent on the studies performed by Baker [4, 7, 8], Sun [2, 44, 61, 67], Jones [33, 34, 37–39], Heller [27–29], Ratwani [40, 42, 54], and others [15, 23, 31, 57, 62]. These researchers have investigated the repair of thin panels ($\leq 5\text{mm}$, but mostly in the thickness range of 1–3 mm) with bonded composite patches. All previous works in the thin thickness regime have simplifying assumptions which restrict their validity, and thus usefulness, in the repair of thick components. Assumption of ‘no significant bending’ is one of the conditions commonly used in all previous studies with thin panels which served to simplify the problem greatly. Experiments have shown this assumption to have an insignificant effect on final solutions for most thin panels. It does, however, have a dramatic effect in the thick panel problem. The few experiments that have been performed in this area by Ratwani [42] showed the great differences in crack growth rates between the thin and thick panel experiments. Some analytical work has also been accomplished by previous researchers such as Jones [33] and Caishang and Lam [43] in thick components with asymmetric repairs. Further, these limited research programs, taking the form of analytical models characterizing plates thicker than 5 mm, have not been validated by experimental data. The few available experimental data sets for panels thicker than 5 mm have either neglected bending effects or have attempted to restrict bending by applying stiffeners to the specimens [32, 40]. The specific cause and effect relationships of factors influencing crack growth differences between the repaired thick and thin plates are yet to be determined.

1.3 Problem Statement/Motivation

As will be shown in the next chapter, the review of current studies in the area of bonded composite patches applied to cracked aluminum panels can be summarized as follows:

- Few studies have addressed fatigue characteristics of repaired thick components.
- Those which have investigated this problem have not addressed secondary bending effects or disbonding at the crack tip in a systematic manner.
- There is a need to perform experiments to characterize fatigue crack growth after thick components are repaired with bonded composite patches and to provide data to validate analytical or numerical solutions currently available.
- A simple, inexpensive approach to crack growth prediction in thick components with repairs is needed to reduce inspection intervals and to predict service life of aircraft repairs with more accuracy.
- Development of new analytical tools is an important next step to expand the usefulness of bonded composite repair technology.

This study, therefore, was proposed involving a hybrid experimental-numerical investigation of thick cracked aluminum panels (>5 mm) with bonded composite repairs. Specifically, this study characterized fatigue crack growth behavior in repaired panels of three thicknesses ranging from thin to thick regimes (i.e. from 3.175 mm to 6.350 mm). The influence of panel thickness on fatigue crack growth rate induced by localized bending (due to neutral load axis shift) and thermally induced curvatures (generated during patch adhesion) were also examined. This study involved both experiments and numerical analysis. The effort compared fatigue crack growth in the aluminum panels, as influenced by the repairs, with results from numerical analyses. The uneven fatigue crack growth between front and back faces of the panels is also examined. This study will provide a basic science and knowledge base for development of design tools to estimate post-repair life of thick aircraft components with bonded composite patches. The improvement of these tools is essential in setting inspection intervals in today's damage tolerance methodology.

1.4 Research Objectives

This study's specific objectives can be summarized as follows:

1) Conduct experiments to investigate the fatigue crack growth behavior with three thicknesses of repaired aluminum panels with center crack. These thicknesses were: a) at the upper limit of thin panels (3.175 mm), b) in the transition region between thin to thick regimes (4.826 mm) and c) in the thick regime (6.350 mm). Cracked panels of the above thicknesses were repaired asymmetrically with uniaxial boron/epoxy pre-cured patches. Initial curvatures (due to residual thermal stresses from bonding repairs), fatigue crack growth rates, crack opening displacements, and strains at selected locations were obtained in the experiments. Also, experiments with cracked yet unrepaired panels were conducted to establish baseline data for comparison.

2) Investigate the effects of various parameters of patch configuration on fatigue crack behavior. These were: patch length, patch to panel stiffness ratio, and patch width.

3) Develop a validated analytical/numerical method to predict fatigue crack growth in a repaired aluminum panel of thickness ranging from the thin to thick regimes. Also, use this analytical method to characterize the experimental results.

The specific details of how this study was accomplished are provided in Chapter 3. The next chapter provides the background and literature review relevant to the proposed research.

2. Background

2.1 Basic Terminology of Fracture Mechanics

The separation or fragmentation of a solid body, under the influence of stresses, is called fracture. Although the study of fracture is a vast field, involving disciplines such as: continuum mechanics, materials science, and solid state physics, this study will mainly involve principles from the discipline known as Linear Elastic Fracture Mechanics (LEFM). This study will investigate the propagation of fatigue cracks as affected by different configurations of repaired, cracked aluminum panels representing damaged structure found in aging aircraft. Fracture can be divided into several phases:

- 1) Damage or crack initiation
- 2) Crack growth or nucleation of several cracks
- 3) Crack growth until failure or separation of the material

Damage accumulation can be associated with the material properties of the component such as preexistent flaws, atomic structure, lattice, grain boundaries, etc. on the microscopic level. But when stresses in the material exceed local strengths, a crack forms two free surfaces and begins to propagate. The application of LEFM lends itself to this crack propagation phase and usually does not lend itself to the nucleation problem. Fatigue is the phenomenon of the above mentioned crack nucleation, propagation, and failure under cyclic loading. It is well known that failures under cyclic loading conditions occur at much lower stress levels than under monotonic loading.

Two factors contribute to the recent increase of interest in fatigue. First, the aerospace industry is constantly demanding and using lighter, higher strength materials for airframe structures. Second, it also desires ever-increasing structural performance from these materials. These higher strength

materials are not always better in fatigue resistance. Therefore, the problem of structural fatigue has reached a level of even higher importance.

The traditional method of examining the behavior of a material under cyclic loading is to obtain $S - N$ curves where S represents the stress amplitude and N is the number of applied load cycles to failure, Figure 2. The relationship between S and N is represented by a curve which shows the tendency of the material to fail under fatigue at a given load level. S_L represents a lower limit of this relationship. For a majority of materials, assuming no additional external influences (environment, corrosion, etc.) other than loading, failure of the material will never occur below this S_L load limit. Some additional terms, useful in later discussions are:

Cyclic Stress Range: $\Delta\sigma = \sigma_{max} - \sigma_{min}$

Cyclic Stress Amplitude: $\sigma_a = (\sigma_{max} - \sigma_{min})/2$

Mean Stress : $\sigma_m = (\sigma_{max} + \sigma_{min})/2$

Stress Ratio: $R = \sigma_{min}/\sigma_{max}$

Two common forms of loading mode are examined during most fatigue studies: stress controlled and strain controlled cycling. In stress controlled cycling, the stress level oscillates from σ_{max} to σ_{min} (the extremes of loading stress) and σ_a (stress amplitude) remains constant. Strain-controlled cycling, on the other hand, is controlled by the test extremes being set in terms of maximum or minimum displacement (or strain). Each form of testing has its unique characteristics. Stress controlled tests show forms of cyclic hardening in the material, causing strains to decrease with more cycles. This may happen until crack nucleation or damage has accumulated sufficiently to overcome the effects of strain hardening. Strain controlled tests exhibit the hardening effect as an increased load required to maintain the same strain or displacement as the modulus of elasticity increases. Again, with damage accumulation and increased cycles, the required load levels to maintain the desired controlled strain will decrease.

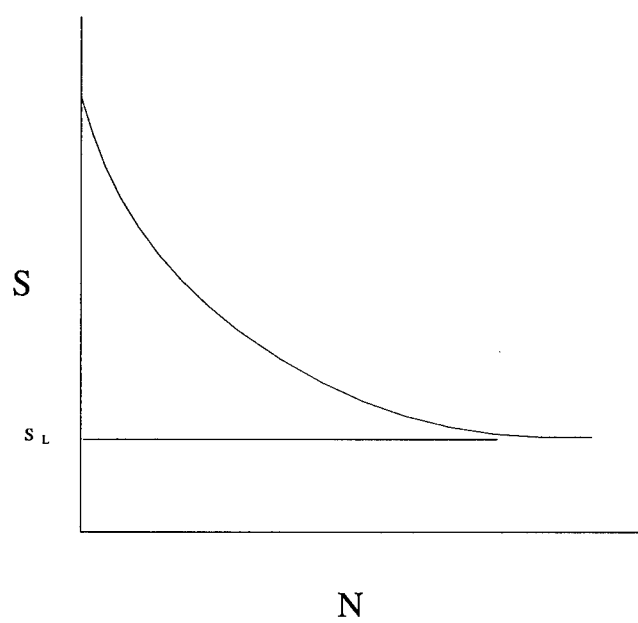


Figure 2. S-N Life Cycle Plot

Assuming all components have inherent flaws (one of the basic assumptions of LEFM), it is possible to predict the growth of these flaws and thus the component's fatigue life. This prediction is the ultimate goal for the prevention of catastrophic failure of cracked or damaged components. Although this study is restricted to constant amplitude fatigue cycling (a first step in these prediction methods), cumulative damage models, such as the Palmgren-Miner [46] rule given below, have been proposed to enable life prediction in a component when exposed to varied stress levels:

$$\sum_{i=1}^k \frac{n_i}{N_i} = \frac{n_1}{N_1} + \frac{n_2}{N_2} + \frac{n_3}{N_3} + \dots + \frac{n_k}{N_k} = 1 \quad (1)$$

where:

- k is the number of discrete stress levels the specimen sees (such as in block spectrum loading)
- N_i are the fatigue lives corresponding to stress levels σ_i
- n_i are the number of cycles carried out at each specific stress level, σ_i

In order to apply LEFM to fatigue, the underlying hypothesis of LEFM must be understood.

The following summarizes the salient aspects of LEFM:

- Cracks or flaws are inherently present in the given system
- A crack is a free, internal, and plane surface in a linear elastic stress field
- Crack growth is characterized by K , the stress intensity factor

From linear elasticity [13], it can be shown that the stress near the crack tip, in an infinite plate, for a Mode I (crack opening) stress field signified by σ , is:

$$\sigma_x = \frac{K}{\sqrt{2\pi r}} \cos \frac{\theta}{2} \left(1 - \sin \frac{\theta}{2} \sin \frac{3\theta}{2} \right) \quad (2)$$

$$\sigma_y = \frac{K}{\sqrt{2\pi r}} \cos \frac{\theta}{2} \left(1 + \sin \frac{\theta}{2} \sin \frac{3\theta}{2} \right) \quad (3)$$

$$\tau_{xy} = \frac{K}{\sqrt{2\pi r}} \cos \frac{\theta}{2} \sin \frac{\theta}{2} \cos \frac{3\theta}{2} \quad (4)$$

$$\sigma_z = 0 \text{ (plane stress)} \quad (5)$$

$$\sigma_z = \nu(\sigma_x + \sigma_y) \text{ (plane strain)} \quad (6)$$

where the x-axis is defined parallel to the crack and the y-axis is defined perpendicular to the crack. The z-axis is defined as orthogonal to the other two axes and through the plate thickness.

The polar stress field near the tip is defined as:

$$\sigma_{r\theta} = \frac{K}{\sqrt{2\pi r}} f(\theta) \quad (7)$$

-or-

$$K = \sigma \sqrt{\pi a} \quad (8)$$

at the crack tip ($\theta = 0$), where r and θ are polar coordinates and K is the stress intensity factor. The following relation can be defined from elasticity where α accounts for crack geometry or modal variations in the crack progression:

$$K = \alpha \sigma \sqrt{\pi a} \quad (9)$$

where a = half of the crack length

σ_{app} = applied stress

α = correction constant or function of crack opening mode, specimen geometry, etc. (this term has the units $m^{-1/2}$ when a is defined in terms of meters.

Timoshenko used the method of conformal transformation to develop the elastic solution for the stresses at an elliptical hole in an infinite plate under a uniaxial load condition perpendicular to the hole's major axis. He showed:

$$\sigma_{max} = \sigma_{app} \left(1 + 2\frac{a}{c}\right) \quad (10)$$

where a and c are defined as the major and minor axes of the ellipse.

The stress concentration factor (S.C.F.) is defined as:

$$S.C.F. = 1 + 2\frac{a}{c} \quad (11)$$

By defining ρ as the radius of curvature on the ellipse, it can be shown that $S.C.F. = 1 + 2\sqrt{\frac{a}{\rho}}$ and $\sigma_{max} = \sigma_{app} \left(1 + 2\sqrt{\frac{a}{\rho}}\right)$. As the ellipse collapses to a crack (i.e. $\rho \rightarrow 0$ and $\sigma_{max} = \lim_{\rho \rightarrow 0} \sqrt{\frac{a}{\rho}}$ or $\sigma_{max} \simeq \lim_{\rho \rightarrow 0} \frac{1}{\sqrt{\rho}}$), the formulation exhibits the square root singularity of the stress riser at the crack tip. The dimensionless $S.C.F.$ can be approximated by $\alpha\sqrt{\pi a}$. Using the well-defined stress intensity factor, K , the inherent stress riser near the crack tip can be characterized and can be used to predict when crack growth will occur.

A common form for presenting data of measured fatigue crack growth rates is the $\Delta K - da/dN$ relationship. This relation is plotted on a log-log scale, where ΔK is the stress intensity factor cyclic range and da/dN is the crack growth rate per cycle. Figure 3 shows a typical representation of this relation on a log-log $\Delta K - da/dN$ plot.

The log-log relationship between ΔK and da/dN characterizes three stages of crack growth:

- Stage I: Threshold crack growth region where the lower asymptotic value defines threshold stress intensity range, ΔK_{th} . This value is affected by microstructure, load ratio (R), and environment
- Stage II: Subcritical, stable crack growth (typically the linear portion of the curve). This stage depends on R , thickness, environment, and a small influence from microstructure
- Stage III: Region of critical crack growth where the upper asymptotic value is the critical stress intensity range, ΔK_c . This region is affected largely by the influence of microstructure, R , thickness, and a small influence from the environment.

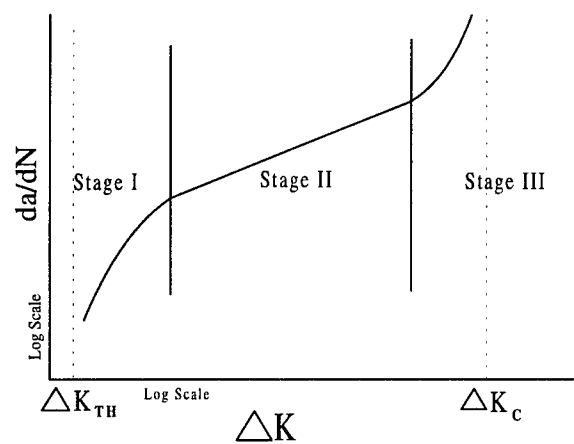


Figure 3. da/dN vs. ΔK

Many mathematical relations have been developed to characterize the relationship between da/dN and ΔK . The power law (crack growth law) used by Paris [46] describes Stage II (linear segment) of the $\Delta K - da/dN$ relation's curve:

$$\frac{da}{dN} = C(\Delta K)^m \quad (12)$$

where C and m are empirical constants defining this portion of the curve through the slope and y-intercept of the linear segment. Stress ratio, R , and the maximum K were also found to influence da/dN , crack growth rate. Attempts by Erdogan, Forman, *et al* [11, 17, 18, 65], respectively, have resulted in the following relationships:

$$\frac{da}{dN} = C(\Delta K)^m (K_{max})^n \quad (13)$$

$$\frac{da}{dN} = \frac{C(\Delta K)^m}{(1 - R)(K_C - K_{max})} \quad (14)$$

Limitations of the Paris, Erdogan, and Forman equations are:

- They address only subcritical (linear) portion of crack growth rate curve
- They are only minimally accurate for variations in load ratio
- They do not address frequency or temperature variations

Due to the scope of this study, the Paris Law crack growth relation was used. (This will be formally stated later.) The application of this simple law, characterizing stage II of the crack progression, is sufficient for most aerospace material applications due to the fact one is mostly interested in predicting growth of existing cracks during reasonably stable growth periods. Other, more general, relations have been developed to characterize additional regions of the $\Delta K - da/dN$ relation. The sinh (hyperbolic sine) relation developed by Pratt and Whitney [65]:

$$\log\left(\frac{da}{dN}\right) = C_1 \sinh[C_2(\log \Delta K + C_3)] + C_4 \quad (15)$$

defines inflection points in the curve, where constants (C_1, C_2, C_3, C_4) are expressed as functions of temperature, frequency, hold-time, and load ratio. The sigmoidal crack growth model, developed at General Electric [64], adds the characteristic of defining lower and upper inflections separately and therefore the log-log $\Delta K - da/dN$ curve need not be symmetric:

$$\frac{da}{dN} = \exp(B_{se}) \left[\frac{\Delta K}{\Delta K_{th}} \right]^C \left[\ln\left(\frac{\Delta K}{\Delta K_{th}}\right) \right]^Q \left[\ln\left(\frac{\Delta K_c}{\Delta K}\right) \right]^D \quad (16)$$

In the realm of the fatigue problem related to patched component repairs, it can be safely assumed that the repaired flaws have already reached the point of subcritical (or possibly critical) growth in the component. The properly designed repair, for a finite number of cycles, will prevent any critical unstable growth rates. Therefore, the main requirement for prediction of crack growth rates is the characterization of stable crack growth kinetics (i.e. within the linear region of the da/dN curve). The stress at the crack tip (or front) is of primary concern since crack growth will initiate at the crack front, being the highest stressed region. Using the crack growth law, a single parameter, the stress intensity factor ($K = f(\Delta K, K_{max}, \text{frequency}, T, R, \text{etc.})$), can be used to characterize the crack growth rate.

2.2 Concepts of Patched Repair

2.2.1 Advantages and Disadvantages of Patched Repair

Bonded patch repairs distribute stresses more effectively than bolted or riveted repairs. The bonded repairs reduce or eliminate stress risers at fastener holes, required for bolted/riveted repair, and increase fatigue life. In most cases, bonded patch repairs exhibit a significantly higher strength to weight ratio over bolted/riveted repairs. Lighter (weight-saving) and thinner (aerodynamic) re-

pairs lead to fuel savings and longer cruise ranges. Patches using composite materials are more adaptable to complex contours or shapes can be optimized to meet the strength and aerodynamic requirements. Composite ply orientations can also be tailored to meet other requirements. Due to the fact that a good adhesive bond acts as a seal to the environment, patches inherently protect the parent material against corrosion. Although some composite materials (graphite/epoxy) can cause a galvanic reaction with the underlying structure, a thin fiberglass insulator can prevent such reactions. With composite materials such as boron/epoxy or glass/epoxy (non-conductors), non-destructive inspection/evaluation (NDI/E) techniques such as eddy current can be used to detect or measure cracks without previous removal of the patch. With the tailorable properties of the composite repair, there is no need to maintain an inventory of large, complex parts on site for repair of aircraft.

Despite bonded patch repair's advantages, there are a few drawbacks. Repairs require a stringent cleaning, preparation, and environmental sequence prior to installation. If any of the preparation steps are left out or not performed properly, it degrades the patch effectiveness (maybe to the point of a dangerously inadequate repair). The number and type of these errors are driven by the training of the applicator and the execution of the process. Proper training and adherence to procedure is a must. Heating required for the adhesion of the patches causes inherent residual stresses in both the patch and the parent material. These stress risers can impact the effectiveness of the repair, dependant on operating conditions of the aircraft. Further, if a new repair has a pre-existing flaw or an old repair needs replacement, it is generally difficult to remove and replace a bonded composite patch. The process requires chemical treatment or mechanical grinding to remove the repair, and these processes can damage underlying material. Installation of these repairs (though effective) can be inconvenient. If an ambient temperature cure adhesive is used, it may take too long to reach proper strength for the desired repair. Other higher temperature cure adhesives require a controlled

thermal environment (thermal blanket, etc.) for cure. The sustained temperatures may damage underlying components or be impractical in some outdoor environments.

2.2.2 Factors Affecting Repair

In Chapter 1 some of the characteristics of bolted/riveted repairs vs. bonded repair were mentioned. In this section some of the major factors, which should be considered when selecting 'bonding' as the repair method, will be addressed. These major factors, each discussed in subsequent sections, are as follows:

- Design
- Surface Preparation
- Patch Material Selection
- Adhesive Selection
- Pre/Post Repair Flaw Inspection

Design. The goal of a repair is to return the component to a state capable of fulfilling its original function. But, structures in older aircraft were not necessarily designed for resisting fatigue damage (i.e. durability and damage tolerance approach). Replaced or repaired components should not only meet previous static strength requirements, but must also meet newer, more stringent fatigue and strength guidelines. Therefore, the replacement or repair must be accomplished without further degradation of the parent structure. It must also either arrest or substantially retard future crack growth, while still maintaining static strength.

By examining a simple 2-D lap joint, the principal loading factors in bonded repair design can be explained. See Figure 4 for an illustration of the lap joint. Upon initial examination it is seen that the plate is subjected to pure tensile loading and the composite repair subjected to the same condition. The adhesive bond layer, between the plate and repair, is the principal player in the transfer of tensile load from the plate to the alternate load path in the composite patch. This load transfer is accomplished through a distribution of shear stresses in the adhesive layer. See Figure

5 for a free-body diagram of the loads involved. Further examination of the lap joint displays the eccentricity of the neutral axis through the bondline and the subsequent induced bending of the plate and repair. See Figure 6 for the induced bending effects caused by the neutral axis shift.

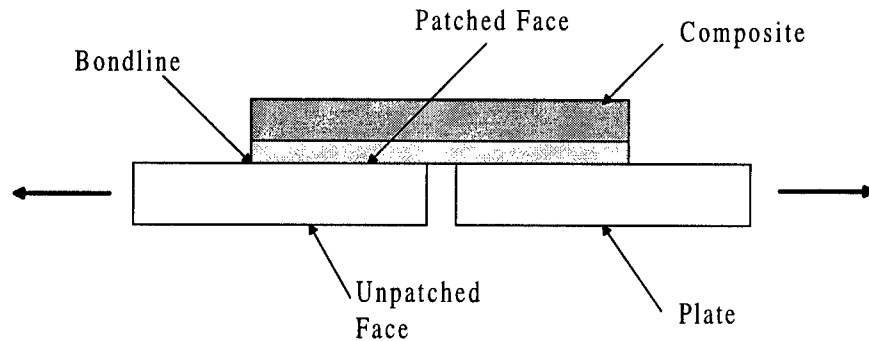


Figure 4. 2-D Lap Joint Illustration

Load conditions on the adhesive include forces normal to the adhesive plane in addition to the shear forces. Forces in this direction cause unwanted deformation and possibly failure of the adhesive in its weakest orientation. Two common modes of adhesive bondline failure, caused by these normal forces, are peel and cleavage. See Figure 7 for pictorials of these failure modes.

Application of double-sided repairs, tapering of the patch ends, or increasing overlap length can reduce or minimize these failure modes at the edges of the patch. This, in turn, reduces the chances of catastrophic bondline failure or “disbonding” of the patch from its edges, but induced bending at the crack face is difficult to characterize. Effects of this induced bending, especially as the neutral axis shift increases with thicker components, are not well understood.

Several basic Rules of Thumb [20] have been suggested to improve the likelihood of success for a repair design. These include:

- Use a repair material whose static strength is greater than or equal to the parent material
- Use a double-sided repair, when possible, to reduce bend effects in the repair

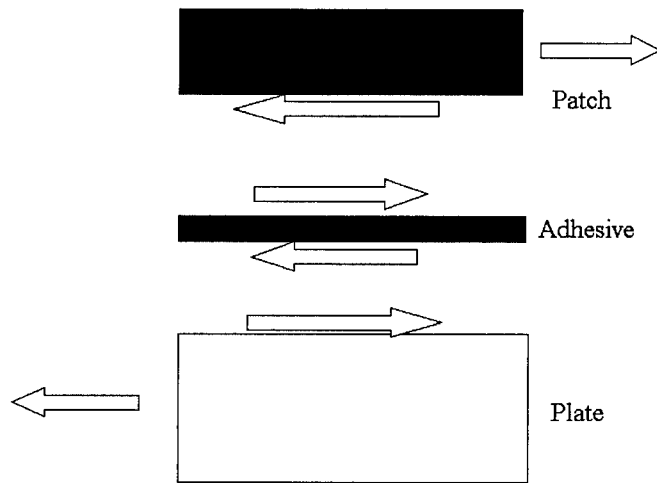


Figure 5. Adhesive Load Transfer

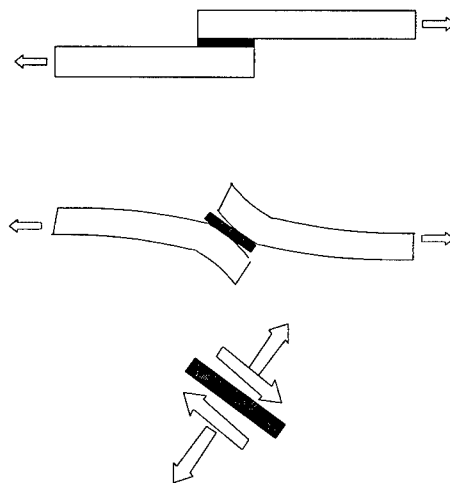


Figure 6. Neutral Axis Shift

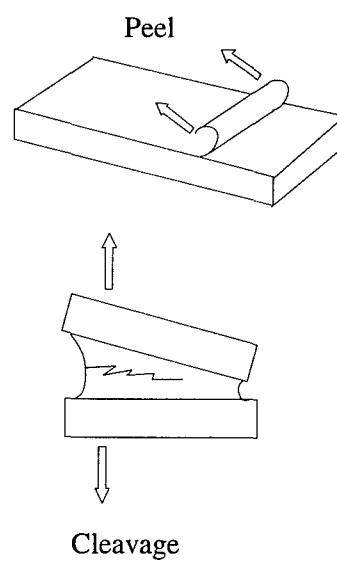


Figure 7. Peel and Cleavage Fracture

- Maintain a minimum overlap length of 30 times the thickness of the repair for double sided repair case (100 times for single sided)
- Maintain a patch to panel stiffness ratio of $E_r t_r / E_p t_p \geq 1$, where E_p and E_r are the moduli of the panel and patch, respectively. Also, t_p and t_r are the thicknesses of each, respectively
- Taper the edges of the repair in the directions expected to experience significant loads

Surface Preparation. According to Baker [4], durability of the adhesive bond is the most critical aspect of the bonded repair technology. Durability of the repair and thus the patched component is largely determined on the pre-treatment (surface preparation) of the metal surface. Primary considerations of these pre-treatments are simplicity and safety. With this in mind, Baker mentioned the following required features:

- The repair must incorporate a highly durable bond for the given environment
- No noxious chemicals should be used, due to possible closed repair areas or close handling
- Fabrication and curing should be accomplished as close to ambient temperature as possible
- The repair must resist or discourage corrosion or stress corrosion cracking
- The repair process must not produce electrical sparking, due to fuel tanks, etc.
- The overall process must be non-specific, applicable to several adherends

Results achieved by Baker [6] in adhesive peel tests show that an optimal combination of grit-blasting the surfaces, applying anodizing/coupling agents, and the application of primers, greatly enhances the durability of these patch bonds. Specifically, this study (as described in Chapter 3) will use this methodology for preparing specimens with a process of alumina grit-blasting, application of silane-coupling agents, and application of an epoxy primer before applying the patches.

Patch Material Selection. Selection of the patch material is the next item of discussion. Obviously, material selection has a large impact on the ease of use, availability, workability, and performance of the repair. Three main high strength composite systems have been examined by various researchers [4, 20, 45]. Analytical and numerical studies have been accomplished for thin skin repairs using Graphite/Epoxy, Boron/Epoxy, and hybrid fiber-metal laminates (such as *GLARETM*). See Table 1 for material properties of these composite systems.

Due to a better match of coefficients of thermal expansion with the aluminum panels, fiber-metal laminates reduce the effects of stresses caused by bonding and thermal cyclic fatigue [22]. However, both the fiber-metal laminate and the Graphite/Epoxy, being conductive, possibly preclude the use of eddy current or similar inspection techniques. These techniques are important to examine crack growth under the patches after repair. Boron/epoxy, being non-conductive, allows monitoring of the crack growth through the patch by the eddy current technique. It also doesn't create the problem of galvanic corrosion between the patch and aluminum, a problem present with graphite/epoxy. Boron/epoxy, a high strength and high stiffness composite, allows the use of thinner repairs. Making the repair thinner, as mentioned before, reduces the effect of the repair on aerodynamics. It also has the added benefit of reducing the amount of bending induced by the neutral load axis shift. Neutral axis shift is dependent on both patch stiffness and the thickness of the repair. The boron/epoxy system has been a favorite of the Australian Aeronautical and Maritime Research Laboratory (AMRL) for repairs of Royal Australian military aircraft. Baker [4], one of the big contributors to development of this technology, has described other positive aspects of the boron/epoxy system:

- Good combination of strength and stiffness
- Non-conductive, avoids galvanic corrosion (seen in graphite repairs)
- Higher coefficient of thermal expansion than graphite. Reduces thermal residual stresses caused during cure
- Better fiber alignment than graphite due to larger fiber diameter

Drawbacks to Boron/Epoxy include:

- More costly
- Less available
- Less workable (due to larger fiber diameter)

Boron/epoxy was chosen as the candidate composite system in this study. It was chosen for its number of positive features and its non-conductive property which allowed inspection of the patched crack by the eddy current technique.

Adhesive Selection. Adhesive selection is dependent on these factors:

- Must have good strength and toughness in the operating temperature range (i.e. -50°C to approximately 80°C - for many aircraft applications)
- Must have resistance to humidity (porosity, weakened bonds) and/or aircraft fluids (chemical degradation)
- Bonding ability must be compatible with chosen surface preparation agents/process
- Must have the lowest possible cure temperature (optimize for operating temperature range)

Strength and toughness specifically relate to the adhesive's shear strength and modulus. Higher shear modulus adhesives reduce stress intensity factors in the cracked plate. Lower modulus adhesives allow greater deformation in the adhesive layer and allows greater crack opening displacements, higher tip stresses, and increased crack growth rate in the plate. The increased deformation before failure allows high shear strain adhesives to improve the durability of the patch/plate bond. But, these same adhesives do not transfer load as efficiently as the more stiff bonding agents do; the high shear strain adhesives increase the crack tip stresses.

Operating temperature was mentioned as one of the criteria for choosing the adhesive. High temperature cure adhesives become more brittle at very low temperatures and low temperature cure adhesives become more plastic at high temperatures. Choosing a cure temperature as close as possible to operating temperature will minimize thermal residual stresses in both the patch and plate when the repair is in service. Thermal cyclic stresses also have an effect on crack growth rate. Therefore, it is important to minimize any contribution made by these residual stresses to the operating stress levels. Applying high cure temperatures to the structure can also have detrimental effects on the underlying components within the aircraft structure. High temperature equipment may not be avail-

able for field repair situations. This situation results in a desire for higher strength low temperature cure adhesives which can withstand a variety of environments.

Three types of adhesives are used on a regular basis for bonded structures: (1) foam, (2) paste, and (3) film. Foam adhesives provide the advantage of filling voids in the bondline by expanding during the curing process. This type of adhesive is usually used on rough or damaged bondlines. Paste adhesives come in a one or two-part mixture and are prepared (mixed) and spread manually using a spatula or another knife edge instrument. Two-part paste adhesives, which use chemical curing agents rather than heat as catalysts, reduce the need for refrigerated storage of the adhesives and the inconvenience of applying heat during cure. They do however tend to be less uniform and human error causes inaccuracies when mixing and spreading the adhesive. These inaccuracies can cause significant variations in the bondline and therefore increase the stresses and the probability of bondline failure. Film adhesives, though they are the most expensive, are conveniently found in tape or sheet form. They require refrigerated storage and require heated and/or pressurized cure cycles. Ease of application and uniformity of the bondline are its strong points.

Most film-type epoxy adhesives, with a moderate cure temperature, fill the first three characteristic requirements mentioned above. Experience and demonstrated performance from the many Australian repair projects (Baker, *et al.* [8, 32]), as well as availability, directed the choice of film adhesive FM-73 for this study. Baker has shown FM-73 to cure sufficiently at temperatures as low as 80°C . This resulted in reducing (minimizing) thermal residual stresses at the crack caused by the inherent mismatch of expansion coefficients between the patch and the plate. Denney [16] has also shown that this adhesive demonstrates successful repair, durability, and repeatability characteristics for this type of study.

Pre/Post Repair Flaw Inspection. All three of the previous factors, surface preparation, patch selection, and adhesive selection, play an important part during pre/post repair inspection. Obvi-

ously, measurements of crack length, taken optically, are not an option after a patch is applied. How can the condition of the patch and the plate after repair be determined? Ultrasonic techniques are proven methods for determining disbond growth between the patch and plate or delamination within the patch itself. Figure 8 shows the general configuration for the detection of flaws using ultrasound techniques. Ultrasound cannot determine the crack length in the panel, through the patch, unless an assumption is made that the disbond between patch and plate grows self-similarly with the crack. In this case, the disbond length would be approximately equal to the crack length. In destructive evaluation or post-mortem examination, Baker [7] showed an alternate method for measuring disbond size using the oxidized surface condition of the plate. Within the disbanded region, he removed patches with heating and the disbanded region was visible due to oxidation of the parent material's surface. (This method is destructive in nature and is not an option on permanently repaired aircraft.) Evaluation using the X-ray technique may be another Non-Destructive Test (NDT) option, but its use on places of the aircraft where there is limited access to the hidden face of the component could be a problem.

The eddy current technique is a proven, viable method for detecting cracks in aircraft structures, given certain conditions [25]. Although the eddy current method has not yet been generally used as a field inspection method after structural repairs, sufficient evidence exists to warrant its further investigation [60]. When eddy current testing is applied, alternating current is applied to a sensing coil within the instrument. This alternating current produces an alternating magnetic field which, when placed near a metal conductor, causes current to flow in the metal conductor (the specimen) by mutual inductance. The 'eddy' current in the conductor will generate a secondary magnetic field, which induces a current in the sensor coil. This mutual inductance causes a change in the impedance of the coil. The impedance signals sensed by the search coil are the information characterizing the test object. Any change in the fields, due to a disruption of the eddy currents (i.e. a crack,

Table 1. Patch/Plate Material Properties

	Boron/Ep	Graphite/Ep	Fib-Met Hybrid	2024-T3 Al
$E_L(\text{GPa})$	210	138	65.6	72.4
$E_T(\text{GPa})$	25	8.96	50.7	72.4
ν	0.168	0.30	0.33	0.33
$\text{CTE } (\alpha_L) 10^{-6}/^\circ\text{C}$	4.5	-0.3	17.9	22.7
$\sigma_{ult} \text{ (MPa)}$	1590	1447	390	324

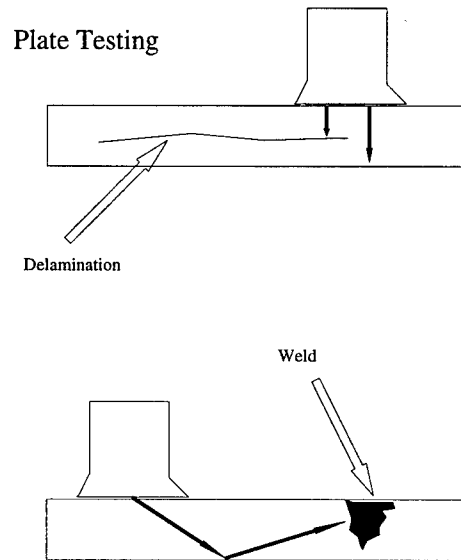


Figure 8. Ultrasound Use Configurations

inclusion, thickness change, etc.), is detected by a change in impedance at the sensor coil. See Figure 9 for a schematic of the eddy current technique. Depth of penetration for eddy current testing is important when determining crack lengths through varied thicknesses of patches. Eddy current density changes magnitude with distance from the surface of the specimen. This value at a depth x is:

$$J_x = J_0 \exp(-x \sqrt{(\pi f \mu \sigma)}) \quad (17)$$

where:

J_0 = current density at surface in A/m^2

f = frequency in Hz

μ = magnetic permeability = $4 \times 10^{-7} H/m$ (defined for non-magnetic materials)

x = depth from surface in m

σ = electrical conductivity in ohm/m

The frequency of probe used for given patch and panel thickness must be optimized to increase the accuracies of the measurements. Prior to conducting the experiments a standard for calibration was developed to determine the optimum frequency of probe and determine accuracies of the data compared with the standard measurement technique, the travelling optical microscope.

The specific eddy current equipment and procedures used in this study are discussed in Chapter 3.

2.2.3 Factors Affecting Crack Growth After Bonded Patched Repair

Examining the basic Linear Elastic Fracture Mechanics (LEFM) relations, as applied to the crack repair problem, there are several factors that have significant impact on K_I , opening stress intensity factor, and da/dN , fatigue crack growth rate. In general, it can be seen from LEFM that

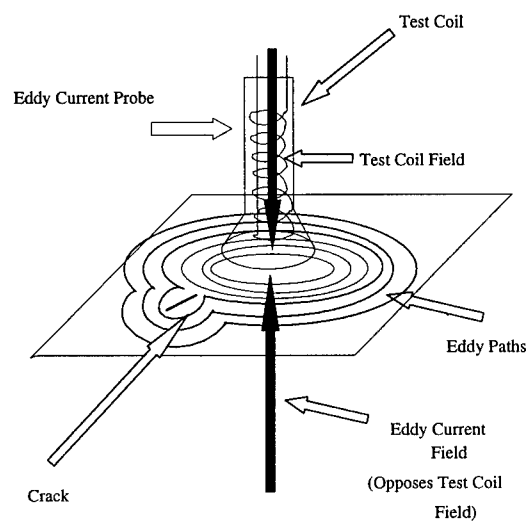


Figure 9. Eddy Current Configuration

load or stress are related to K_I by the relationship, $K_I = \sigma\sqrt{\pi a}$. Crack length, a , also influences K_I through this relation. Subsequently, da/dN (crack growth rate per cycle) is determined by the Paris Law, $da/dN = C(\Delta K)^m$.

Other factors, specific to the present patch repair problem, affecting crack growth rate, are:

- Thermal Residual Stresses
- Bond Quality
- Secondary Bending

Thermal residual stresses are induced by the bonding of two materials with different thermal expansion coefficients. Before the composite patch is bonded to the component to be repaired, each part, plate and patch, is stress-free. But, during the curing process of the bonding, each part must be heated to an elevated cure temperature (80° to $120^\circ C$). Each part expands freely according to its individual coefficient of thermal expansion (CTE). When cooling, the parts are linked by the cured adhesive but there is a mismatch of contraction rates between the aluminum structure and the composite patch. This mismatch results in the plate being in tension and the patch being in compression after cooldown to ambient conditions. Figure 10 displays this phenomenon.

The effect is more pronounced as the cooldown, or change in temperature, ΔT , increases. The resulting thermal residual stresses not only affect K_I by increasing or decreasing the applied stress and stress range, they can also directly cause fatigue during environmental temperature changes. Fredell, et al. [19] has proposed investigating this aspect of repair durability, as influenced by cold-thermal fatigue. Residual stresses also impact the durability of the repair through their effect on adhesive shear stresses. Stresses in the adhesive bond layer are increased due to the mismatch between the patch and plate. These stresses can initiate disbonds, weaken or degrade adhesive properties, or cause existing imperfections to grow from cyclic fatigue loading. Thus, it is advisable to have an adherend with a cure temperature as close as possible to the operating temperatures of the repair, as discussed in Section 2. Another method for reducing the effects of residual stresses is to restrict the

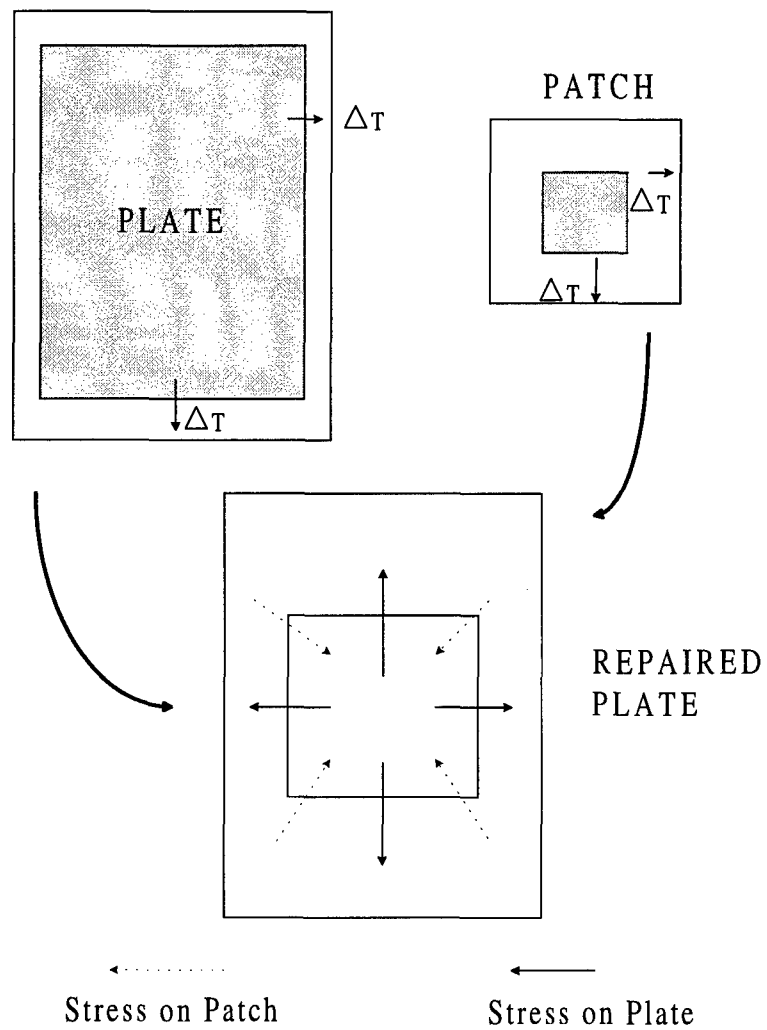


Figure 10. Thermal Residual Stresses

deformation of the parent material during the cure process. An example of how this occurs would be the presence of stringers or longitudinal stiffeners restricting the bending of fuselage skin material during *in situ* repairs. These understructure components causing displacement constraints in the proximity of the repair result in a reduction of material expansion of the skin during the heating process.

Some characteristics of the bondline will now be discussed. Other than the properties of the composite patch itself, adhesion of the patch to the parent material is probably the single most important component of patch quality and durability. Adhesive bondline variables such as surface preparation quality, thickness, type, or uniformity, all affect resulting local shear stresses and strains in the bondline. This, in turn, influences the presence, initiation, or growth of disbonds. Surface preparation was discussed in Section 2 and won't be addressed again here. Thickness, type, and uniformity of the adhesive bondline are influenced by the choice of adhesive used and method of application.

Patch and bondline quality can degrade over time due to direct damage, disbond growth, or absorption of moisture from the environment. These effects can degrade perceived properties of the repair thus causing the bonded patch to be less effective for resisting further crack growth.

2.3 The Need for a Generalized Predictive Method

The prediction of fatigue crack growth behavior in metallic structures is a highly involved and complex process. The complexity is further compounded when these structures are repaired with bonded composite patches. Despite this complexity, there is a need to establish a generalized approach, of sufficient accuracy, to model crack growth rates after repair. A generalized approach should ideally do the following:

- 1) provide results for a wide range of plate and/or component thicknesses

- 2) characterize thermal residual stresses and associated bending
- 3) model the secondary bending effects which result from the neutral axis shift inherent in thick panel repair
- 4) provide a simple, economical, and accurate method to predict the stress intensity factors
- 5) provide a simple, economical, and accurate method to predict the fatigue crack growth rates

The following sections briefly review the literature which documents research toward this generalized predictive method.

2.4 Overview of Previous Research

Several experimental studies have been performed through the efforts of many researchers; Baker [4, 7, 8], Jones [34, 37], Ratwani [42], Roach [55], and Belason [9, 10]. A large segment of the experimental testing was conducted by Baker at the Australian AMRL [7, 8, 32]. These studies included: characterization of crack retardation in thin plates after repair, examination of debond growth, and some studies (mostly numerical) of specific large component repairs of the F-111 aircraft. Baker's specimen configuration was unique in that it attempted to restrict or eliminate bending during preparation and testing. The specimens were asymmetrically repaired, but were assembled and tested two at a time with the unrepaired faces bonded to a honeycomb inner layer to restrict out-of-plane bending. Baker's assumption was (to a large extent) that, in actual skin application of repairs, local stiffening by components (i.e. spars, longitudinal stiffeners, etc.) would prevent bending. Baker's [4] results show, for thin sections, crack growth rate (da/dN) was relatively constant within the repaired area for constant amplitude loading tests of thin panels. These results were verified by Denney [16]. Baker also developed, from experimental data and Rose's technique (discussed later), an efficient two-step method [6] to incorporate bending in thin aluminum panels with bonded composite patches. Results from this method are good for thin panels but their accuracy is

reduced for thicker sections. Adhesive variations and disbond growth were examined and an analytical model for the thin skin repair was developed to predict disbond shape. Baker also conducted tests to examine debond growth characteristics of different adhesives at elevated temperatures [4,7].

Ratwani also conducted experiments, both in the thin and thick plate regime. He also developed an empirically weighted analytical model for repaired structure. Ratwani's experiments dealt with thin to thick sections and 3-dimensional cases such as corner cracks or reinforced bolt holes [40,42]. His thick panel experiments were conducted on specimens with a dual crack configuration (i.e. two cracks and two repairs in each specimen), in an attempt to gather more data per test case. The effects of bending were assumed to be negligible for these tests. Bending, in the form of a large correction, was reinstated in the model through an empirical correction factor. This approach was used when significant discrepancies were noted in comparisons with thick panel experimental data. Ratwani used a semi-analytical method assuming the form of the through-the-thickness stress distribution and using a strip model approach. Models of the thick plate were used to determine back face stress intensity factors for plates with one-sided repair. The approach to the problem used a complex variable method which reduced the original analytical problem to a solution, for a set of integral equations, achieved through numerical means. He then used an empirical correction to account for differences from the experimental data. The results from the semi-analytical model, compared with a series of experimental data (different plate thicknesses versus constant patch thickness), predicted K_I reasonably well for thin sheets. But, the results of the model became increasingly less accurate as sheet thickness of the comparisons increased. Figures 11 and 12 show the geometric relationships used by Ratwani in his semi-analytical approach to solve for $K_y(z)$, the stress intensity factor as it varies through the thickness of the specimen. His formulation of the problem detailed a cracked metal plate with a bonded patch under uniform tensile loading. The crack opening, $\delta = f(x)$, where $\delta = \delta_{max}$ @ $x = 0$ and $\delta = 0$ @ $x = a$, half of the crack length. Without the patch

the $\delta_{max} = \frac{4\sigma_{\infty}a}{E_1}$, where E_1 is the Young's Modulus of the plate and thickness effects on stress distribution are neglected.

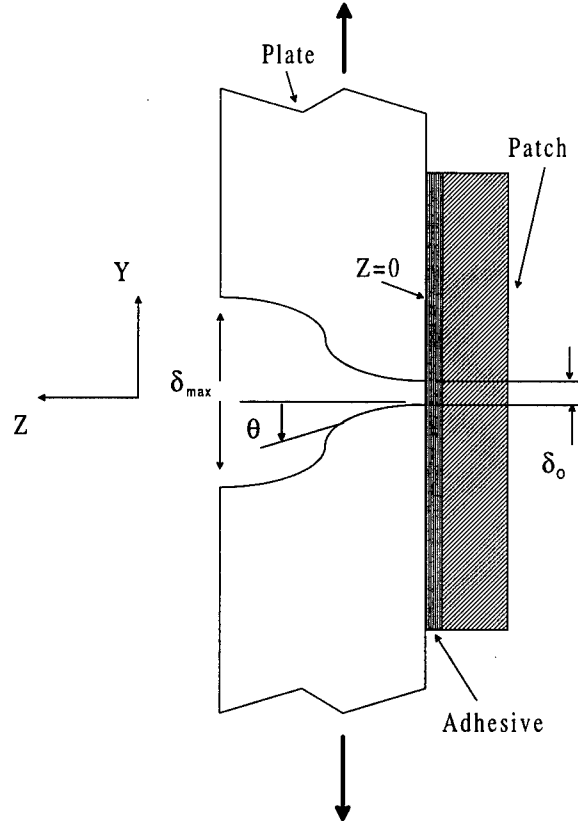


Figure 11. Ratwani's Model Configuration

He showed, by examining the effect of repair on the crack opening, that:

$$\delta_o = \frac{4(\sigma_{\infty} - \sigma_o)a}{E_1} \quad (18)$$

where σ_o is the stress transferred to the patch (stress decrease due to application of the patch). Ratwani defined θ as the rotation angle of the crack face about the x-axis. Ratwani assumed the angle $\theta(z) = 0$ everywhere for 'thin' plates and for 'thick' plates; $\theta(z) = 0$ and $\frac{d\theta}{dz} = 0$ for $z = 0$ and for $z \rightarrow \infty$. He then used a slicing method where the thickness of the specimen is divided

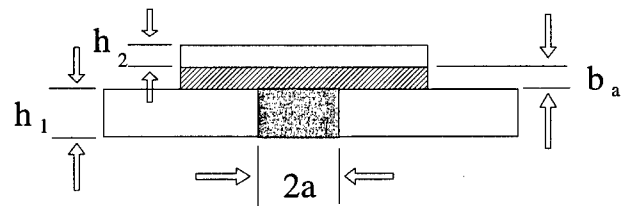


Figure 12. Ratwani's Crack Formulation Parameters

into 'n' slices of 'b' thickness, i.e. $z = nb$. He assumed the magnitude of crack opening nearest the repair is given by the unrepaired crack opening formula as given in the previous paragraph. He also assumed the crack opening profile was a piecewise linear function of 'z' (through the thickness dimension). Therefore, equations for $\theta(z)$ and the crack opening displacement at the patch/plate interface is given by thin plate analysis:

$$\delta_k = \delta_o + b \sum_{i=1}^k \theta_i \quad (19)$$

and

$$\delta_k = \frac{4(\sigma_\infty - \sigma_k)a}{E} \quad (20)$$

with

$$\sigma_k = \sigma_o - \frac{bE}{4a} \sum_{i=1}^k \theta_i \quad (21)$$

thus: $K_k = (\sigma_\infty - \sigma_k)\sqrt{\pi a}$ at the kth slice and the total load per unit width transferred to the patch can be defined as T where:

$$T = nb\sigma_o - \frac{b^2E}{8a} \sum_{k=1}^n \left[2 \sum_{i=1}^k \theta_i - \theta_k \right] \quad (22)$$

Ratwani found that the calculated unpatched face stress intensity factor with his empirical corrections was accurate to predict the fatigue life of repaired structure [42], given his assumptions of restricted bending.

Roach [55], at Sandia National Laboratory's aging aircraft NDI validation center, focused on application and operation issues of patch doublers (large patches which cover entire sections of structure) applied to the L-1011 aircraft. He conducted static ultimate tests and fatigue tests at stress

levels from 21 to 139 MPa. Roach was successful in restoring ultimate design strengths in 2024-T3 aluminum components and in arresting the growth of 12.7 mm long cracks in 1.8 mm thickness panels.

Under the direction of Boeing, Belason [10] (from TEXTRON Specialty materials) showed the usefulness of boron/epoxy patches for arresting crack growth, using two-sided thin section repairs and stop-drilling, in 7075-T6 aluminum. He additionally showed static strength was restored and fatigue crack reinitiation was eliminated in 1.6 mm thickness aluminum panels, for the applied stress range from 21 to 139 MPa.

Fredell, *et. al.* [19–23] has conducted extensive experimentation with a hybrid fiberglass/epoxy-aluminum composite repair for thin fuselage skins. A reduction in thermal residual stresses resulting from bonding was seen. The reduction was due to the better coefficient of thermal expansion match between this hybrid composite patch and the parent material.

Denney conducted tests at the Air Force Institute of Technology examining the impact of imperfectly bonded repairs of thin panels (1 mm) [16]. Denney's tests showed the capability of repeatable fatigue test results and the utility of thermographs used as an *in situ* means of monitoring debond growth during tests.

In addition to the previous experimental studies, many analytical studies involving repaired structures were also reported. Jones, *et. al.* [28, 29, 32–37, 39, 53], have developed both analytical and complex numerical models for design of repairs. The analytical models that have been developed were targeted for thin panel repair designs. The complex three-dimensional finite element models were designed for thicker component repairs. The main drawback to these models was their uniqueness to each individual repair and the computational complexities of the 3-dimensional finite element method. One initial attempt to analytically model a plate repaired with a bonded patch was developed by Rose [56]; this model is commonly referred to as the Rose Model. It was based on

the inclusion formulation for isotropic plates with isotropic reinforcements by Muki and Sternberg [47]. Rose modelled a plate with a semi-infinite crack repaired with reinforcing sheets bonded to its faces. The model was then extended to a crack of finite size. Rose applied the inclusion analogy to estimate the reduction in crack extension force when the cracked plate was repaired by reinforcing patches. Rose began with an uncracked plate. The reduction in stress at the crack location was determined by treating the reinforced region as an inclusion with a higher stiffness than the surrounding material. This higher stiffness inclusion was then treated as an entity with the combined properties of the two parent materials. See Figure 13. He then introduced a crack to the inclusion (in the reduced stress field) and estimated the crack extension force using results from a formulation for the upper bound of G_x (the strain energy release rate) when reinforcements cover the whole plate. Rose then compared the effect of applied stresses on these cases to the change in G_x . Rose also addressed the effect of bending due to asymmetric patching of the thin panel. With the assumption of an infinite strip repair and slender beam theory, an induced moment was calculated and applied to the repaired and unrepaired regions.

In the early 1980's Jones, *et al* [33,35,37–39] used finite element and other numerical methods to validate analytical methods of Rose and others for determining K_I in a general case. They also worked to validate K_I determinations made for specific applications of repair to the Mirage III aircraft [8]. This work included two-dimensional finite element models for thin-skin double-sided repairs as well as three-dimensional models for thick sections. A limited number of experimental data sets were generated from these applications. Results of Baker's work on Mirage and F-111 [5, 8] (i.e. repairs to 'in-service' aircraft) have been used to 'calibrate' these numerical models. Two-dimensional numerical models did not incorporate or allow out-of-plane deformations caused by the patch. Thus, they were limited to the thin skin cases where limited bending occurs.

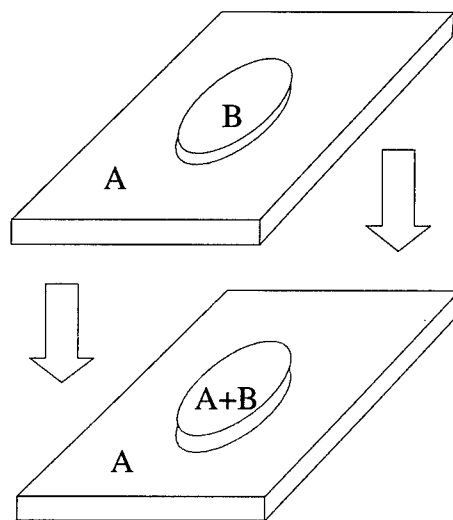


Figure 13. Rose Application

To maintain low-cost and simplicity in the models, yet still provide reasonable predictions for design of bonded patches, most of the previous analytical methods in this direction involve simplified two-dimensional approaches which were calibrated or verified using only limited experimental or three-dimensional model results. Heller [27], in 1993, developed a thick plate model (three-dimensional finite element) which compared well with the experimental data from tests of repaired plates up to 3.15 mm thickness. The drawback of three-dimensional numerical models, such as these, lies in the large number of elements (computationally expensive) required to prevent skewed or unreasonably high aspect ratio elements in, or near, the thin adhesive layer.

Sun, *et. al.* [2], in turn, developed a two-dimensional finite element model using Mindlin plate elements for the patch and the panel. These Mindlin plate element layers were used in conjunction with spring elements modeling the adhesive layer. The shear spring elements were connected to each of the Mindlin plate layers through displacement constraint equations which satisfied the Mindlin plate assumptions. Then, to calculate the stress intensity factor, the indirect crack closure method was employed. The crack closure method was first introduced by Rybicki and Kanninen [58]. Sun, *et. al.* modified it to include the rotational effects in the two-dimensional Mindlin plate elements. The resulting modified crack closure method, as applied to a cohesive crack (crack in a plate), was based on Irwin's [30] crack closure integral which states that the energy absorbed to extend a crack tip by an amount Δa is equal to the work required to close the crack to its original length. The calculation of the stress intensity factor range, ΔK , of a cohesive crack from finite element calculations, uses contributions from both the central plane (mid-plane) displacements and the rotations determined by the 2-dimensional elements. The strain energy release rate (or crack driving force) G is defined as the force per unit crack extension. The extensional strain energy release rates

for Mode I (opening) and Mode II (sliding) are given by:

$$G_I^u = \lim_{\Delta a \rightarrow 0} \frac{1}{2\Delta a} F_y^c \cdot \Delta v^c, \quad (23)$$

$$G_{II}^u = \lim_{\Delta a \rightarrow 0} \frac{1}{2\Delta a} T_x^c \cdot \Delta u^c \quad (24)$$

The contribution to the Modes I and II strain energy release rates, due to rotation of the cross-sections, are given by:

$$G_I^\theta = \lim_{\Delta a \rightarrow 0} \frac{1}{2\Delta a} M_y^c \cdot \Delta \theta_y^c, \quad (25)$$

$$G_{II}^\theta = \lim_{\Delta a \rightarrow 0} \frac{1}{2\Delta a} M_x^c \cdot \Delta \theta_x^c \quad (26)$$

The rotational contribution to the strain energy release rates from a four-noded Mindlin plate element is based on Young and Sun's [67] cracked plate configuration. The superscript 'u' denotes contributions due to displacements at the mid-plane of the element. Δa is the virtual crack extension and is equal to the length of the first element ahead of the crack tip. Δu^c and Δv^c are the crack opening displacements at the first node ahead of the crack along the x and y axes, respectively. T_x^c and T_y^c are the forces in the x and y directions required to close the crack. Each of these reaction forces are accurately estimated for the crack tip as long as the elements are sufficiently small. Similarly, for rotational contributions, $\Delta \theta_x^c$ and $\Delta \theta_y^c$ are the relative crack rotations along Δa about the x and y axes. M_x^c and M_y^c are the moments about the x and y axes required to hold the crack closed. Thus, for Mode I, the total strain energy release rate becomes:

$$G_I^t = G_I^u + G_I^\theta. \quad (27)$$

In a linear elastic continuum, the stress intensity factor and strain energy release rate are related by combining Westergaard's representation and Irwin's crack closure integral, yielding:

$$K_I^2 + K_{II}^2 = \frac{GE}{\beta}, \quad (28)$$

where β is equal to unity for plane stress and equal to $1 - \nu^2$ for plane strain. E is defined as Young's modulus. The stress intensity factors in Equation 28 decouple if no interaction between Modes I

and II is assumed. The equation is then reduced to:

$$K_I = \left(\frac{G_I E}{\beta} \right)^{\frac{1}{2}}. \quad (29)$$

Figure 14 shows Sun's basic model configuration of the plate with repair. His method allowed the adhesive layer to be modeled without its 'thinness' dictating highly skewed or poor aspect ratio elements. This overcame the computational expense required for a three-dimensional finite element model of this repair. Sun then compared the results of this two-dimensional model to results from three-dimensional finite element models and found a good correlation with repaired, thin plate results. Despite his success the model still showed increasingly poorer results when compared with thick 3-D models. Sun showed that the bending correction factors for asymmetric repairs, used by Rose and Ratwani, could introduce a large error, especially when the patch had a much higher modulus than the plate.

Naboulsi and Mall [49] extended Sun's method one step further. They used the two-dimensional Mindlin elements to model all three layers of repair problem on thin plates (<3mm). This included the plate, adhesive, and patch. The method allowed the adhesive layer to be modeled as a continuum. The extension from Sun's model allows the economical approach, in a two-dimensional model, to more closely approximate experimental or three-dimensional finite element model results. Further, it provides the means to realistically model other aspects of the adhesive continuum such as: thermal effects, progressive damage, and material property distributions. More details of this model are discussed in Part II: Finite Element Modeling. Use of this modelling technique for thick plates provided analytical results which are then compared to the experimental results of this study.

In 1993, Lam and Caisheng, *et. al.* [14,43] pursued yet another approach. The method involved a pseudo-analytical method for repaired thick sections based on the principles of anisotropic elasticity, classical laminated plate theory, and slicing methods developed in 1982 by Saff and Sanger [59] (for determining K_I in isotropic plates). Figures 15 and 16 show the basic configurations used for

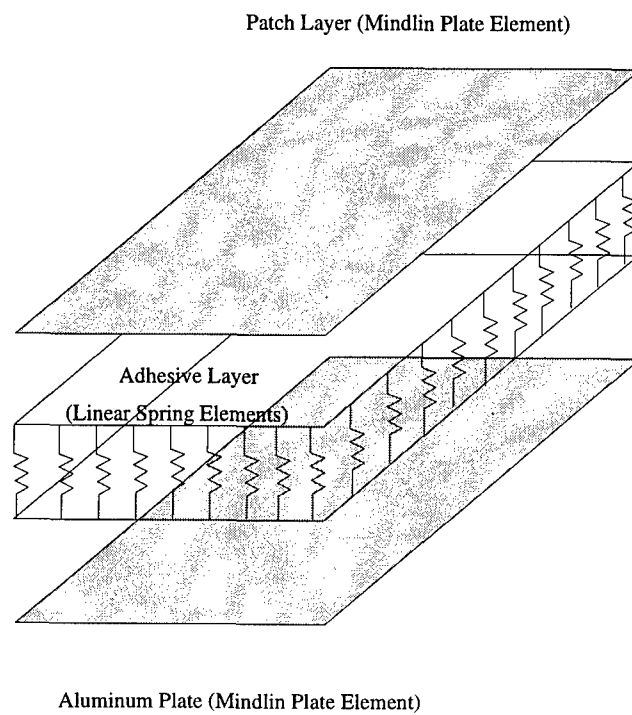


Figure 14. Sun's Plate/Spring Model

this technique. Caisheng and Lam used this slicing method by: (1) reducing the patch/plate problem to a two-dimensional lap joint (Figure 15) and (2) applying St. Venant's principle of equivalent loads to achieve a single anisotropic plate under shear with moment loads. The problem may then be solved using superposition principles and the properties of the anisotropic lay-up of the patch(es) and plate. Obviously this solution only gave the solution for the uncracked panel. But, then they used the slicing method to divide the panel into orthogonal horizontal and vertical slices (Figure 16) to determine K , the stress intensity factor, for the aluminum panel with a crack. Each series of slices were coupled analytically with the introduction of a pressure distribution $P(x, z)$ on each respective face of the crack. In this manner, a three-dimensional problem was reduced to multiple two-dimensional models and they were solved simultaneously. Their results compared favorably with three-dimensional finite element results and available experimental results (up to 3.1 mm plate thickness).

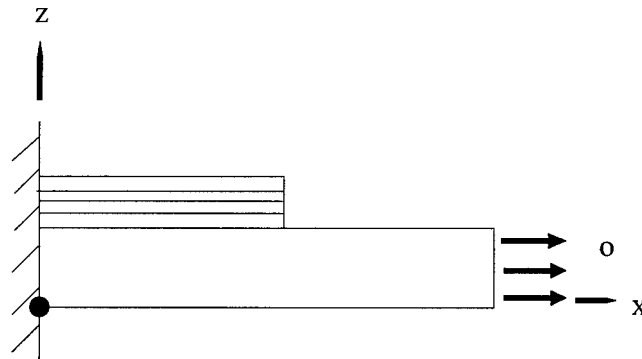


Figure 15. Caisheng and Lam's Model Configuration

In summary, it was evident that in the case of thin skin repair, models examined in the previous studies correlate well with experiments. But, a generalized approach to model the fatigue crack

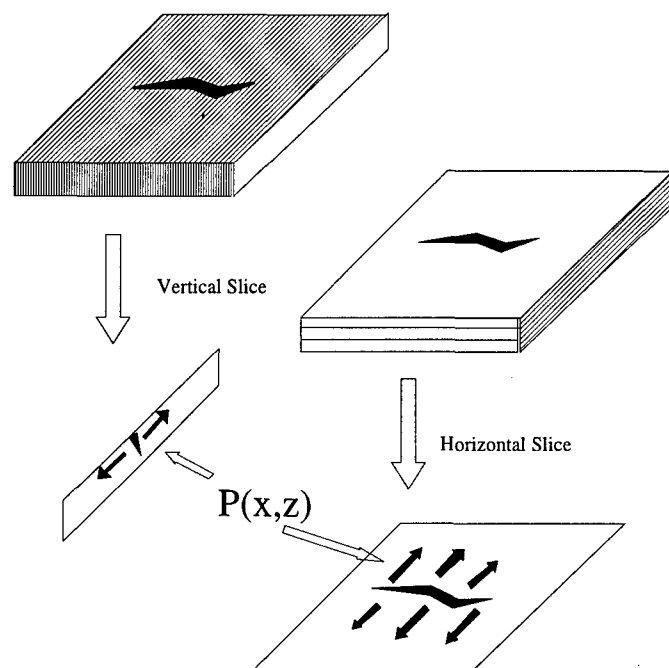


Figure 16. Slicing Method

growth rates in repaired, thick panels has yet to be found. Further, there are few experiments characterizing repaired thick plates/components.

This study was undertaken to conduct a hybrid experimental-numerical investigation characterizing panel thickness effects on crack growth after the repair of aluminum aircraft components with bonded composite patches. Fatigue crack growth behavior was systematically investigated with respect to different patch configurations. Results of the numerical investigation validated an analytical method to predict fatigue crack growth rates over a range of thicknesses for repaired flat structures.

Part: II
Experimental Testing

3. Test Procedure

3.1 Summary of Research Plan

This study examined and characterized the fatigue crack growth response of cracked aluminum (thin and thick) panels repaired with a bonded composite patch. It also involved a combination of both experiments and analysis.

The first phase of this study was an experimental part, involving the investigation of the effects of panel thickness and patch size on fatigue crack growth rate in repaired panels with bonded composite patches. Fatigue crack growth changes were observed as they were influenced by neutral axis shift, out-of-plane bending and other geometric effects. A test system was developed to measure crack growth on both faces of the repaired plate (unpatched and patched) during fatigue testing. This allowed the research to document the uneven crack growth due to the asymmetry of repair. The strains at selected locations on the specimens were measured. Three panel thicknesses were investigated to determine the effect of component thickness on the crack growth rate in panels repaired with one-sided adhesively bonded boron/epoxy composite patches.

The analytical part of this study involved the development of a numerical technique to predict crack growth rates in repaired components. The hybrid experimental-numerical model developed in this study uses a 2-dimensional (2D) approach to model a 3-dimensional (3D) problem. This 'pseudo-3D' approach uses 2D Mindlin plate elements in three layers to simulate a 3D solution. Each layer's displacements are governed by Mindlin plate theory and by linear constraint equations which ensure compatibility among the patch, adhesive, and repaired plate interfaces. This approach allows the designer to produce a simple, economical solution for the stress intensity factor at the crack tip. This model, combined with the empirical weighting factor developed in this study, and the Paris Law, allow accurate fatigue crack growth rate predictions for repaired thin and thick panels.

3.2 Experimental Test Apparatus and Procedure

This section details the test equipment and procedures used in the experimental phase of this program.

3.2.1 Materials, Specimen, and Patch Repair Description

Material used for the center-cracked plate specimens was 2024-T3 sheet (unclad) and 2024-T351 plate (unclad) aluminum. The composite patch was composed of a boron/epoxy system. Material properties for the plate material and composite patch are shown in Table 2. Alloy chemical composition for the aluminum is shown in Table 3.

Table 2. Material Properties

	2024-T3/T351 Al [1]	Boron/Epoxy [10] (Single Ply $\nu_f = 0.5$)
E (GPa)	72.4	200
σ_{ult} (MPa)	441	1550
σ_y (MPa)	290	-
ν	.33	.168

All specimens were cut from the aluminum sheet such that the longitudinal (load) axis was aligned with the grain (rolled direction). Each specimen, measuring 508 mm long by 153 mm wide, was configured as shown in Figure 17. Each specimen was machined with a center crack (starter notch). This ultra-narrow notch was electric-discharge machined (EDM) to serve as a starter crack in the specimens. The starter notch initially measured 12.7 mm long and was pre-cracked to 25.4 mm long before testing (baseline) or repair with the boron/epoxy patches. This pre-cracking process was accomplished to ensure that the effect of the machined starter notch is removed. It is also to ensure that subsequent crack growth rate data is not affected by the pre-crack load history [3]. Pre-cracking was accomplished by cycling the specimens at a frequency of 10 Hz with a K_{max} of less than or equal to the K_{max} during actual testing. Fatigue testing of the repaired specimens was accomplished at constant maximum load (P_{max}), or σ_{max} , of 120 MPa. This load is sufficiently above

Table 3. Aluminum Alloy Composition (Percent Weight-ASTM-B209-92A)

	Minimum	Maximum
Cu	3.8	4.9
Mg	1.2	1.8
Mn	0.30	0.90
Si	-	0.50
Fe	-	0.50
Zn	-	0.25
Cr	-	0.10
Ti	-	0.15

the nominal aircraft design load (90 MPa) to provide a reasonable safety margin for underdesigned components. A load ratio of $R=0.1$ at 10 Hz, slowed to 1 Hz during data acquisition of strain and center crack opening displacement measurements, was used to fatigue all specimens. The slower cycles, comprising less than 2% of the total cycles, served a dual purpose. First, it allowed sufficient time for the data system to accomplish needed tasks such as data collection and minor load adjustments. Second, the slower cycles provided 'markers' for striation analysis by scanning electron microscope (SEM) or optical analysis, allowing measurements of crack growth after the test. Crack growth data by post-mortem examination of the tested specimens was used to validate patched-face crack measurements taken by the eddy-current technique.

Patches were configured to isolate various parameters which might influence fatigue crack growth in the specimens. All patches had unidirectional lay-up, $[0^\circ]^n$ (n equal to the number of plies) with fibers in load direction. Different patch lengths, widths, and stiffness ratios were examined. Again, the patch to panel stiffness ratio, S , is defined as:

$$S = \frac{E_r t_r}{E_p t_p} \quad (30)$$

where E is Young's Modulus, t is the plate or patch thickness, and r and p are subscripts designating the repair patch and plate, respectively. Table 4 details the number of plies and the calculated stiffness ratios for the finite number of plies in each case.

Table 4. Patch Configuration Lay-ups

t_p	# Plies	Targeted S	Actual S
3.175	9	1.0	1.045
4.826	14	1.0	1.069
6.350	18	1.0	1.045
3.175	11	1.3	1.276
6.350	22	1.3	1.276
3.175	4	.46	.464
4.826	9	.69	.687

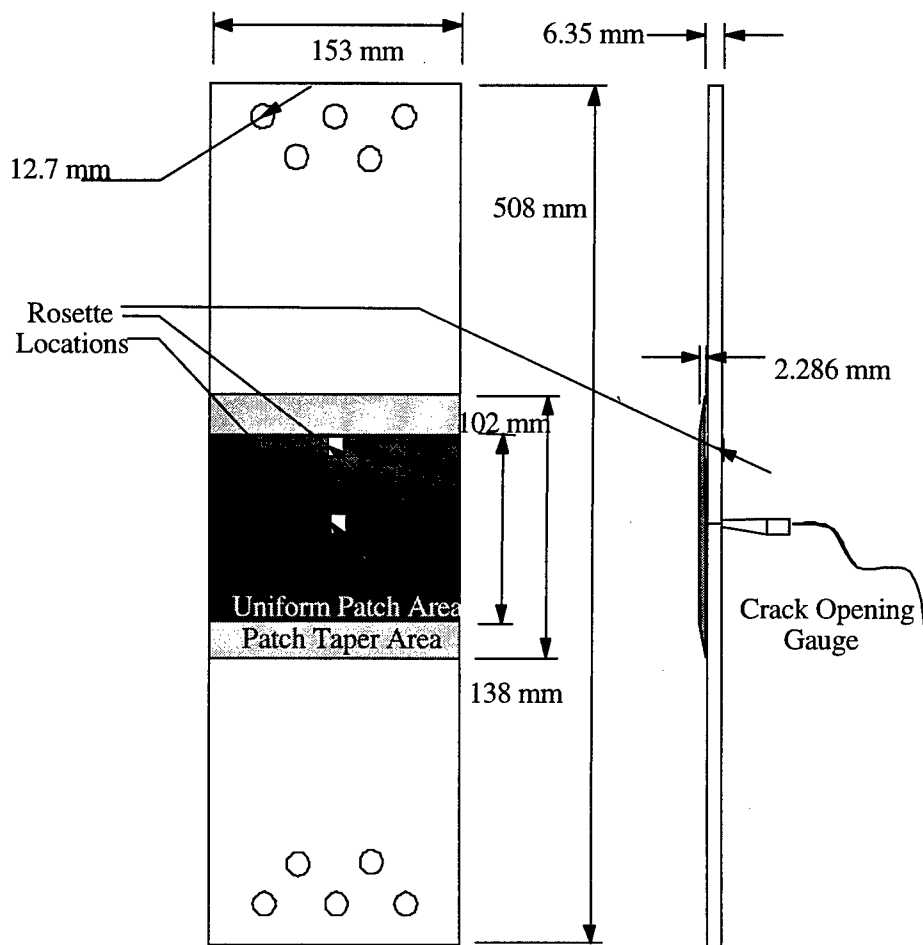


Figure 17. Specimen Configuration

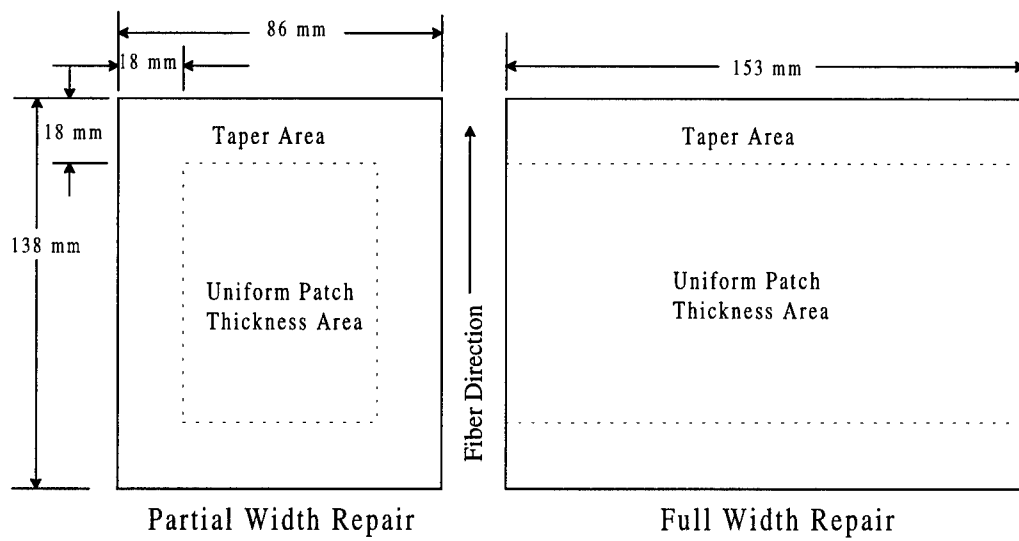
Patches were rectangular in shape. All patches were configured in a decreasing ply size orientation (from bond surface to top) with cover plies. Edge tapers of patches had a constant nominal length of 18 mm with uniform ply drop-off dependent on the number of plies. See Table 5 and Figure 18 for the schematic view of the patch lay-up. The full width repairs had tapers on the longitudinal ends (loading direction) only. Finite width patches had tapers on four sides. Patch stiffness ratios were referred to by the rounded numbers such as: $S=1.0$, 1.3, etc. Patch sizes (lengths and widths) were referred to by the size of the uniform patch thickness area (i.e. excluding tapers) in this study.

Table 5. Example of Square Patch Lay-up

Ply #	Length (mm)	Width (mm)
1	75	75
2	75	75
3	63	63
4	63	63
5	51	50
6	51	50
7	75	75
8	85	85
9 (cover-ply)	87	87

Patch Cure. Patches were pre-cured using a portable autoclave (porto-clave) at Wright Laboratory. The pre-curing process enhances the storability of the patch prior to bonding for repair. The cure process for the patches was as follows:

- Place uncured patch in porto-clave, layered with Teflon sheets above and below. This is to prevent sticking of the patch and allow proper adhesive flow.
- Double bag debulk in the porto-clave - 30 minutes Room Temperature ($RT=21^{\circ}C$).
- Apply 40 psi positive pressure.
- Release vacuum (vacuum dump).
- Start heating cycle ramp-up $2.77^{\circ}C/\text{min}$ to $121^{\circ}C$.
- Hold at temperature for 60 minutes.
- Ramp to cool-down $\leq 8.4^{\circ}C/\text{Min}$ to ambient temperature.
- Release pressure and remove.



Side View
(NOT TO SCALE)

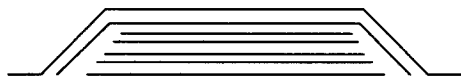


Figure 18. Patch Configurations

Plate Surface Preparation. Plates were treated, prior to the bonding of patches, using field/base level surface preparation techniques. Preparation was conducted in an area on each plate corresponding to the patch size to be used for the repair. Steps in preparation of the surfaces included:

- Solvent degreasing.
- Grit blasting (mechanical abrasion) of adherends.
- Silane agent preparation.
- Wetstanding procedure (silane application).
- Primer application and cure.

Methyl Ethyl Ketone (MEK) was used as a degreaser on the aluminum surfaces by wiping and repeating with clean aerospace wipes until no residue remained. MEK wiping was also conducted on the patch surface before bonding. Grit blasting of the aluminum to the prescribed surface quality was accomplished using an aluminum oxide grit (50 micron). Excess abrading dust was blown off the surface using gaseous nitrogen. Silane preparation was accomplished through a one hour hydralization/mixing process of 1 ml silane agent (Dow Corning Z640) to 99 ml distilled water. The wetstanding procedure is accomplished by evenly applying the silane mixture to the patch area, keeping the full surface area wet for 10 minutes, then drying the area immediately again, using gaseous nitrogen. The silane treated panels were then dried/heated in a 93°C oven for one hour, followed by application of a degreasing primer (American Cyanamid BR127) and cured for 30 minutes at room temperature, then cured at 121°C for one hour to protect the surface from contaminants.

Patch Adhesion. Patches were bonded to the prepared aluminum surfaces using the following procedure:

- FM73 sheet adhesive is cut to size and applied to the back surface of the patches
- Patch with adhesive is applied to the prepared surface.
- Patch and plate (with adhesive) are cured in porto-clave with the same cure cycle as the patch.

3.3 Test Equipment

The following test equipment systems were used in this study:

- Mechanical Load System
- Crack Measurement Systems
- Strain/Curvature Measurement Systems
- Computer Controller/Data Acquisition System

See Figures 19 and 20 for the mechanical load system layout. The mechanical load system consists of the following components:

- 100 kip MTS 810 Servohydraulic Testing Machine
- MTS 458.20 Controller
- MTS 458.90 Waveform Generator
- Zenith microcomputer (IBM 486 compatible Z-433D+) with *LABVIEWTM* software

LABVIEWTM was used as the control software for the mechanical system during testing of the specimens. A signal giving frequency, amplitude, and waveform was sent by the software to the function generator, which then sent, in turn, the commands to the MTS servohydraulic controller. The controller then loaded the specimen with the hydraulic actuator with control feedback from the load cell (during load controlled testing). In addition to control feedback, this output from the load cell also provided the signal for data acquisition of applied load measurements.

3.3.1 Crack Measurement Systems

The following systems were used for measuring crack length (thus producing crack length vs. number of cycles comparisons):

- Gaertner travelling telemicroscope with digital readout (See Figure 21): This system provided optical crack length measurements on the unpatched face of the specimen.
- *In situ* Eddy current crack imaging system (See Figures 22 and 9): The *in situ* eddy current test system was on-loan from Wright Laboratory to measure patched face crack growth. (The PHASEC 2.2 eddy current system used NORTEC multi-frequency probes (50-100kHz) and a Krant-Kramer Branson Andscan eddy current scanner with color imaging capability). Figure 23 displays a photograph of the ANDSCAN system with computer and probe instrumentation.

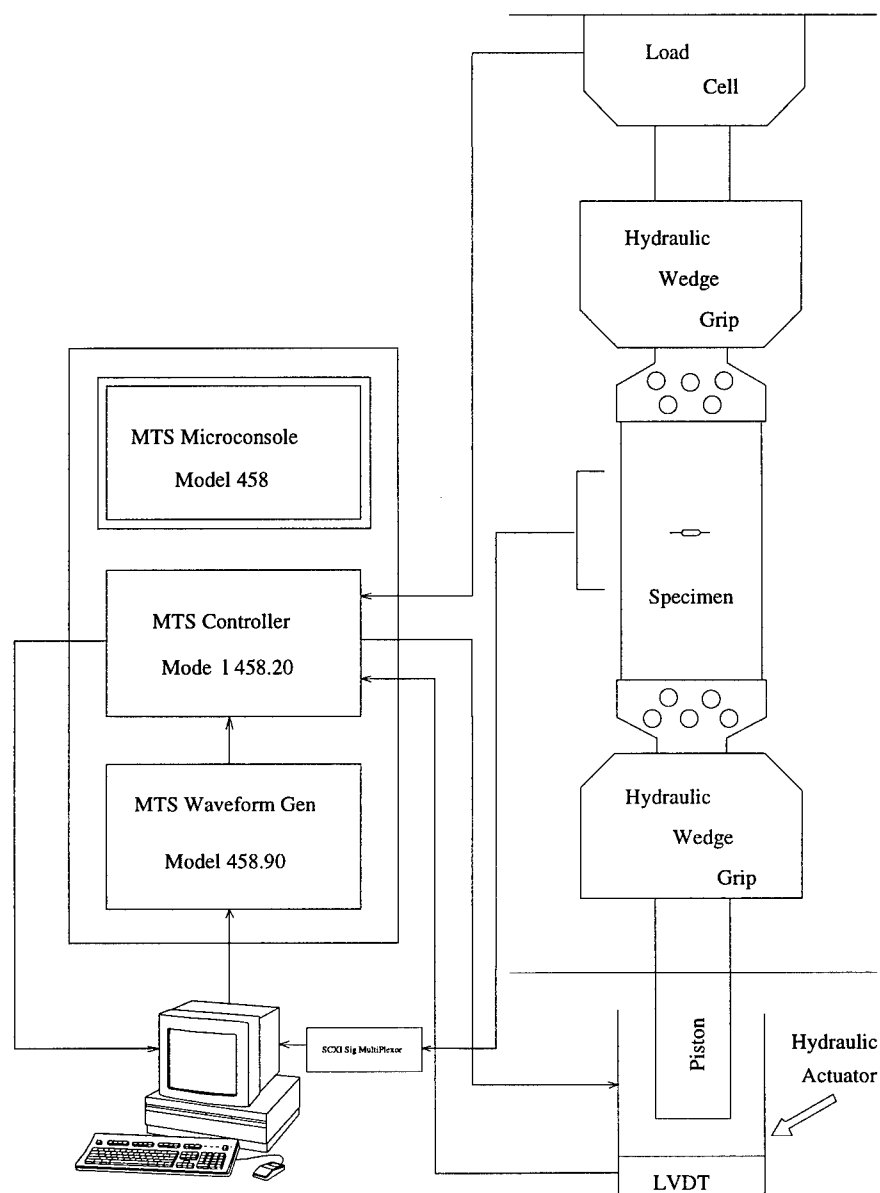


Figure 19. Mechanical Load System

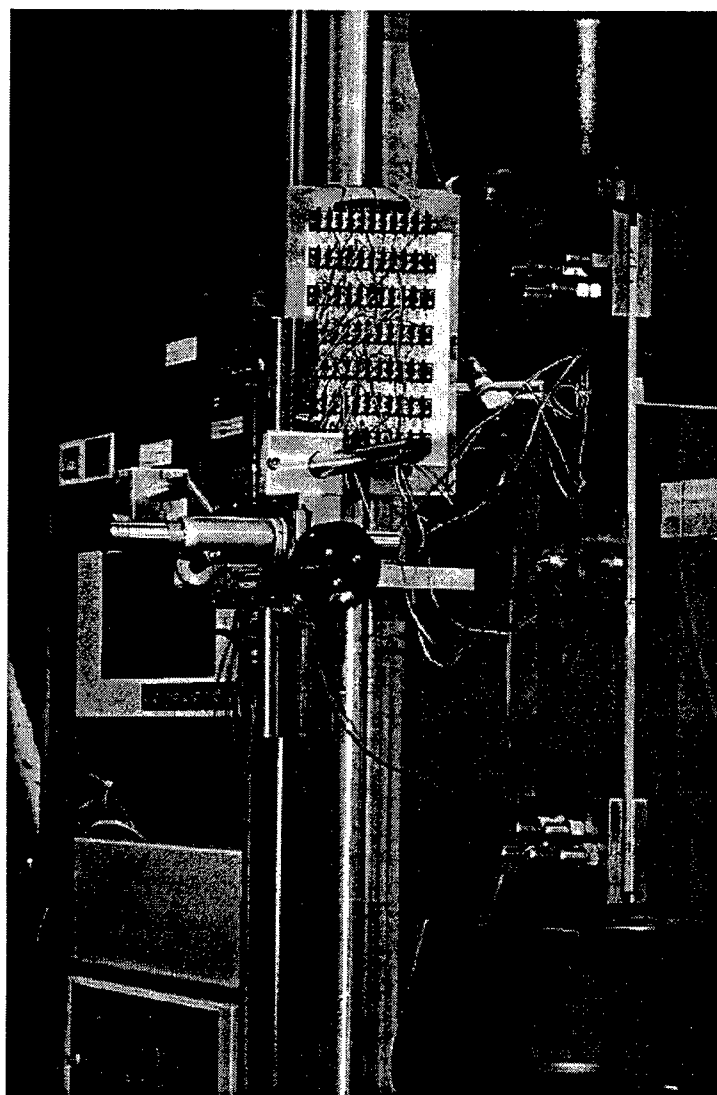


Figure 20. Specimen in Mechanical Load System

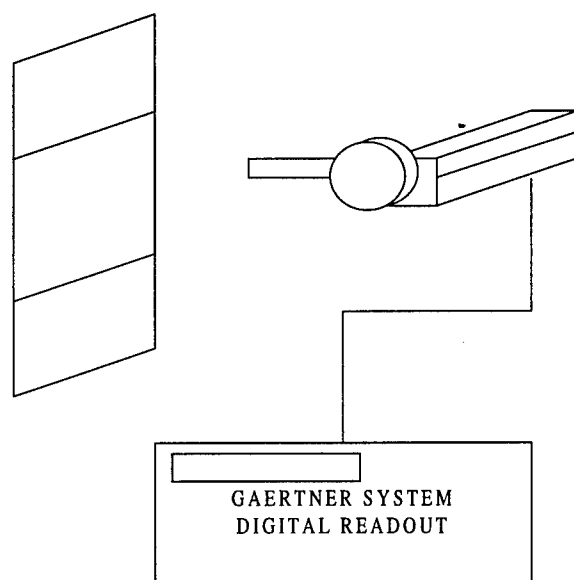


Figure 21. Optical Crack Measurement System

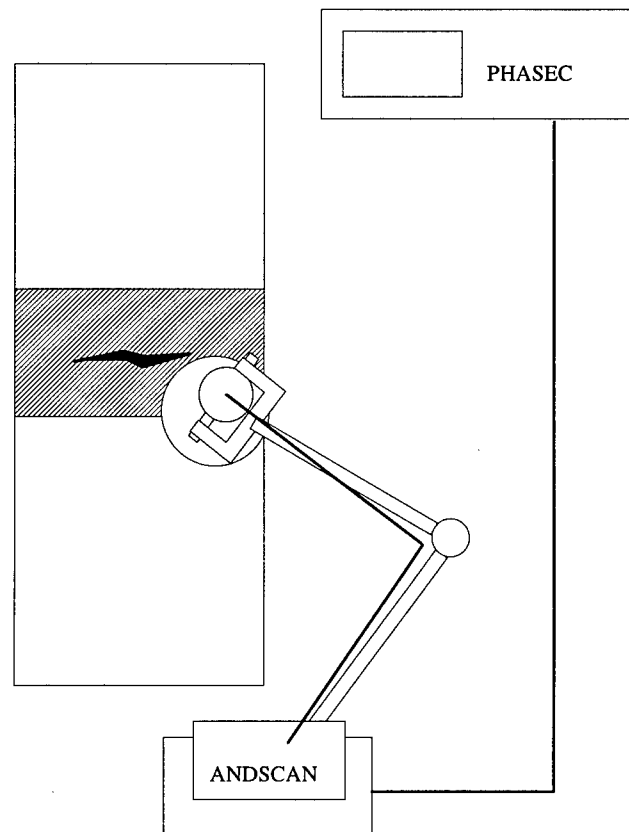


Figure 22. In-Situ Eddy Current System

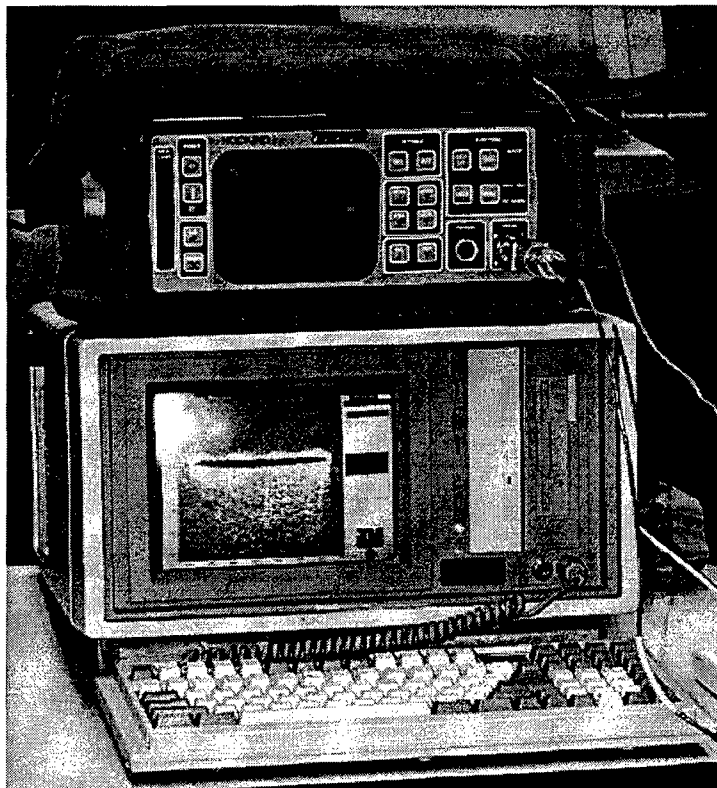


Figure 23. Eddy Current Instrumentation System

In addition to the crack length measurement systems, Micro-Measurement 120 Ohm strain gage rosettes (locations shown in Figure 17) and an AFTT-built crack opening gage (shown in Figures 24 and 25) were used. These instruments determined surface strains within the patched area and the center crack opening displacement, respectively. An infra-red (IR) thermographic camera and video system were used to monitor patch integrity (i.e. monitored disbond growth under the patches). Figures 26 and 27 detail the IR system set-up.

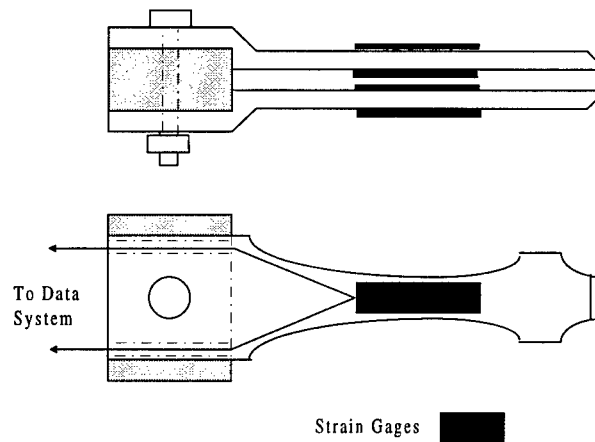


Figure 24. Crack Opening Displacement Gage

Photomicroscopy was used for the striation analysis and post-test patched face crack growth measurements. Lower frequencies encountered during data acquisition cycles (strain/COD data was acquired at 1 Hz) provided striation 'marking'. This allowed visualization of patched vs. unpatched face crack lengths after failure of the specimens. Analysis of these lengths (and subsequently crack growth rate differences across the thickness of the panels) provided additional insight to the effect of panel thickness on the uneven crack propagation. Using the lengths measured at the surfaces, crack lag on the patched face was used in a correction of the numerical results in Chapter 5.

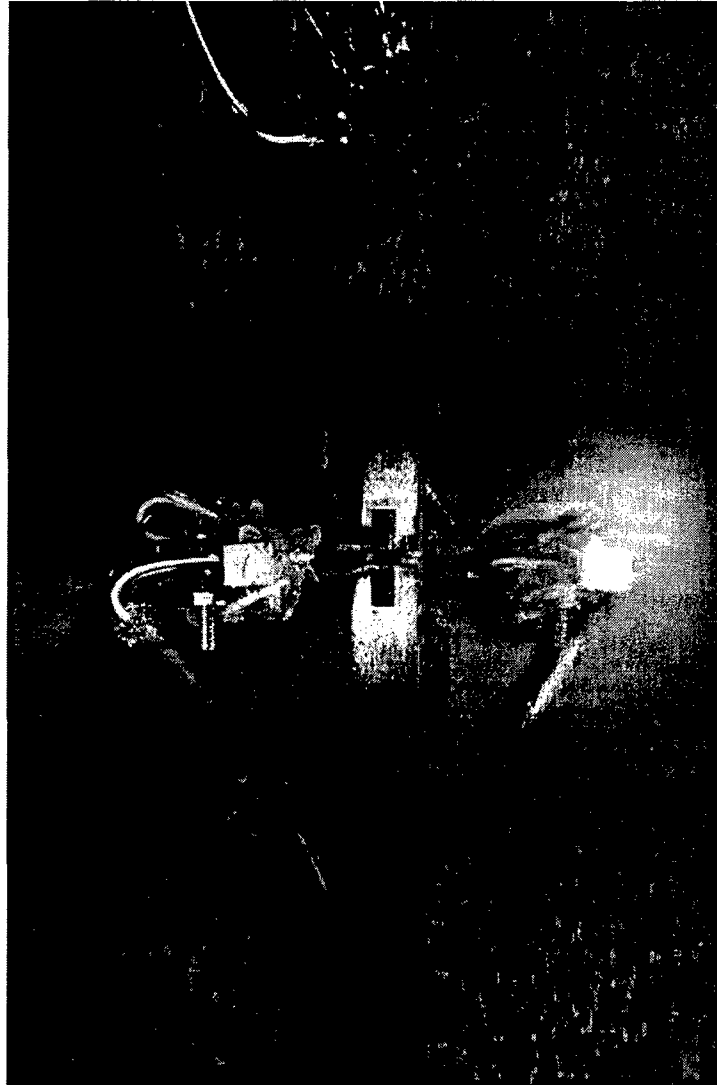


Figure 25. AFIT-Built Clip Gage on Specimen Face

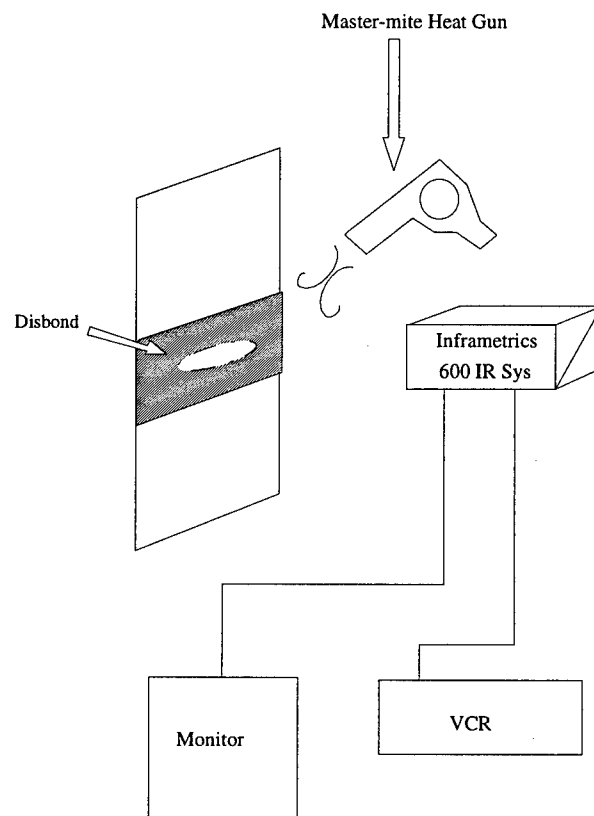


Figure 26. Infrared Disbond Monitoring

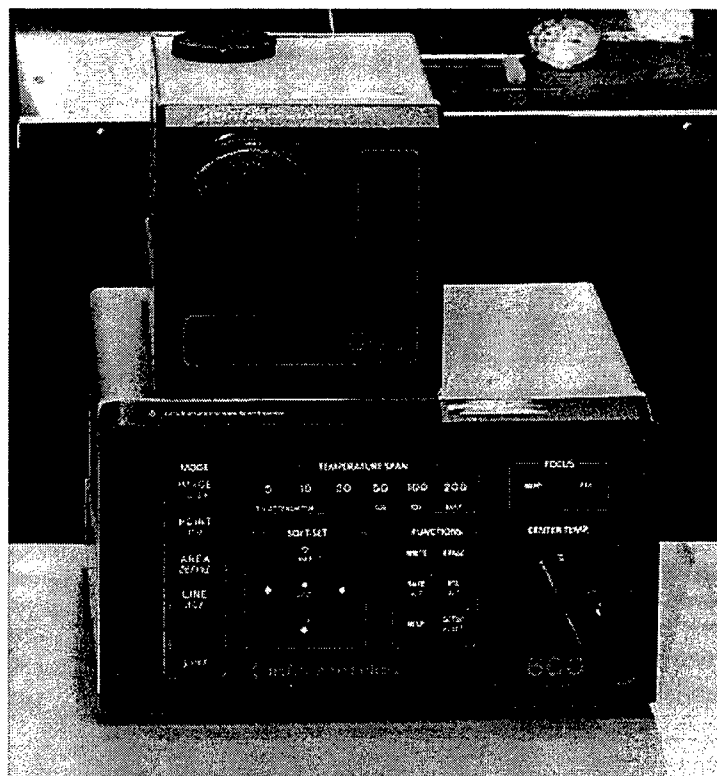


Figure 27. Infrared Camera and Instrumentation

Specimen preparation was a tedious, labor intensive process and most steps were accomplished using off-site equipment (Air Force Wright Laboratory). Off-site equipment and supplies included: grit blaster, preparation chemicals, and porto-clave (for pre-curing patches and final adhesion of patches to plate specimens).

3.3.2 Test Execution

The test matrix was designed to investigate the effects of various patch configuration parameters on fatigue crack growth rate after repairing a structure. The test matrix is shown in Table 6. Besides these (28 specimens), the series of tests included a baseline calibration specimen for use of the eddy current technique and six additional specimens repeating selected configurations of these tests (See Appendix C).

The first segment of repaired specimen tests were preceded by the preparation of the calibration specimen and fatigue testing of six unrepaired baseline plates with a 25.4 mm long pre-crack. The single calibration specimen, used for calibration of the eddy current test system, was a 6.350 mm thick plate of the same dimensions as the other test specimens. However, this specimen had six center notches, machined by electric-discharge machining. Three notches were initially 12.7 mm long and the other three were initially 19.0 mm long. Figure 28 shows the location of the notches on the specimen. The specimen was then fatigued to pre-crack these six notches. Due to the differences in the initial lengths of these notches, different final crack lengths were achieved, as was desired for the calibration. A full width (153 mm wide) patch was designed for the calibration specimen to contain three patch thicknesses (9, 14, and 18 plies) which provided the different repair thicknesses for $S=1.0$ on 3.175 mm, 4.826 mm, and 6.350 mm thick plates. Refer again to Figure 28 for an illustration of this patch layout. Using the three patch thicknesses and the six different crack lengths, the eddy current system was used at different frequencies and gains to measure the crack lengths.

Table 6. Test Summary

Specimen #	Thickness of Panel, t (mm)	Stiffness Ratio, S	Length of Repair, (mm)	Width of Repair, (mm)
1	3.175	No Repair	-	-
2	4.826	No Repair	-	-
3	6.350	No Repair	-	-
4	3.175	No Repair	-	-
5	4.826	No Repair	-	-
6	6.350	No Repair	-	-
7	6.350	1.0	102	Full Width ¹
8	6.350	1.0	68	Full Width
9	6.350	1.0	51	Full Width
10	4.826	0.69	102	Full Width
11	4.826	0.69	68	Full Width
12	4.826	0.69	51	Full Width
13	3.175	0.46	102	Full Width
14	3.175	0.46	68	Full Width
15	3.175	0.46	51	Full Width
16	4.826	1.0	102	Full Width
17	4.826	1.0	51	Full Width
18	3.175	1.0	102	Full Width
19	3.175	1.0	51	Full Width
20	6.350	1.0	51	50
21	6.350	1.3	51	50
22	6.350	1.0	102	50
23	6.350	1.3	102	50
24	6.350	1.3	51	Full Width
25	6.350	1.3	102	Full Width
26	3.175	1.0	51	50
27	3.175	1.3	51	50
28	3.175	1.3	51	Full Width

¹Note: Full Width = Panel Width = 153 mm

Then, by comparing measurements of the crack length (under the repair), taken by the eddy current technique, to the measurements taken optically prior to the repair, the optimal frequency and gains were established for use in this study

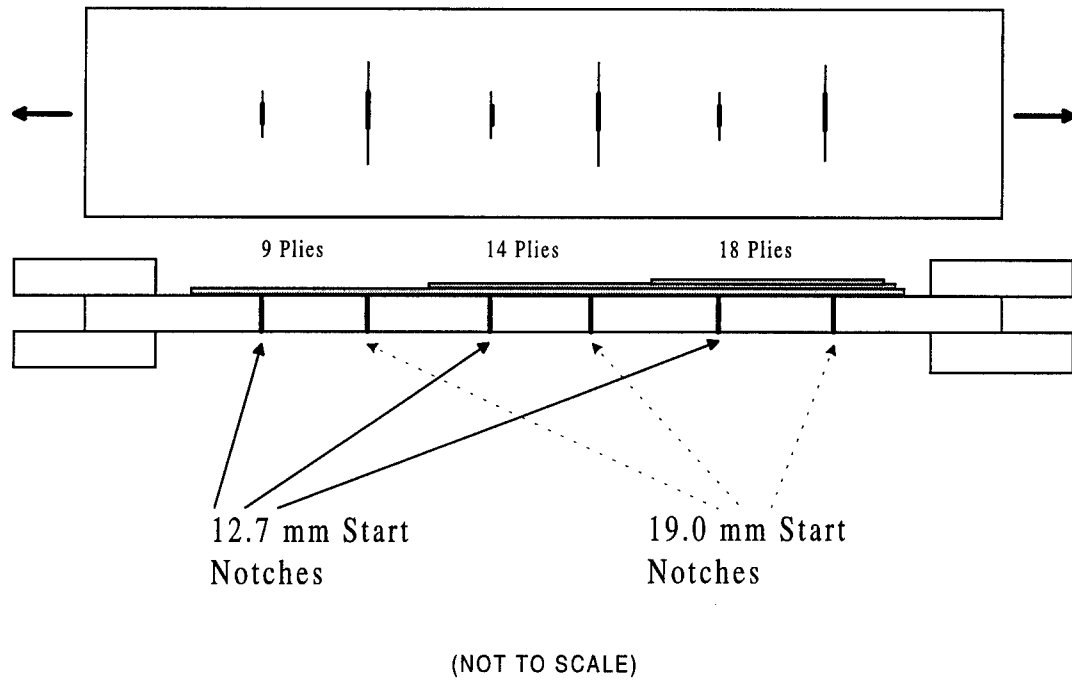


Figure 28. Calibration Specimen for Eddy Current Technique

Two unrepaired baseline plates for each thickness, were tested to failure. One plate at each thickness was tested in a range of different values of P_{max} to determine C and m , material constants. These constants were required for the baseline Paris Law crack growth relation (i.e. $da/dN = C(\Delta K)^m$), used for the analytical prediction of crack growth rates, da/dN , of the plate. The other specimen at each thickness was tested at a constant P_{max} to determine the baseline fatigue life and crack length versus cycle relation (crack length, $2a$ vs. number of cycles, N).

Subsequent testing involved patched specimens (Table 6) where patched and unpatched face crack lengths, unpatched face crack opening displacement, and strains on patch and panel faces, with full width and finite width patches, were measured. These tests provided empirical data for validation of the numerical modeling of crack growth rates. Out of plane displacements (initial curvature) of the patched specimen, prior to testing, were measured to within ± 0.05 mm using a 3-D digitizing arm. These profiles were used to establish induced thermal curvatures developed during bonding. Refer to Figures 29 and 30 for examples of these digitized curvature measurements. These data were required to validate the boundary conditions used in the numerical method. The method includes the bending effects due to the thermal CTE mismatch during bonding cure of the patch to the plates. All the above tests were conducted with three thicknesses of panels, 3.175, 4.826, and 6.35 mm.

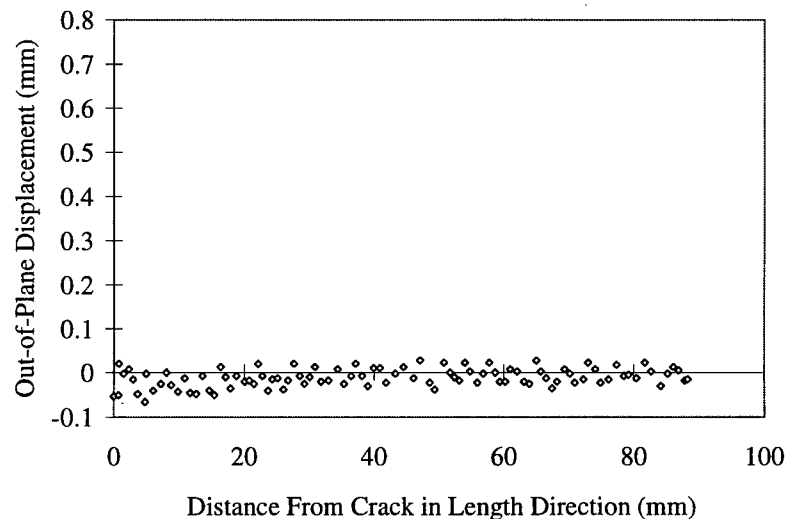


Figure 29. Unrepaired Specimen Curvature (i.e. no patch)

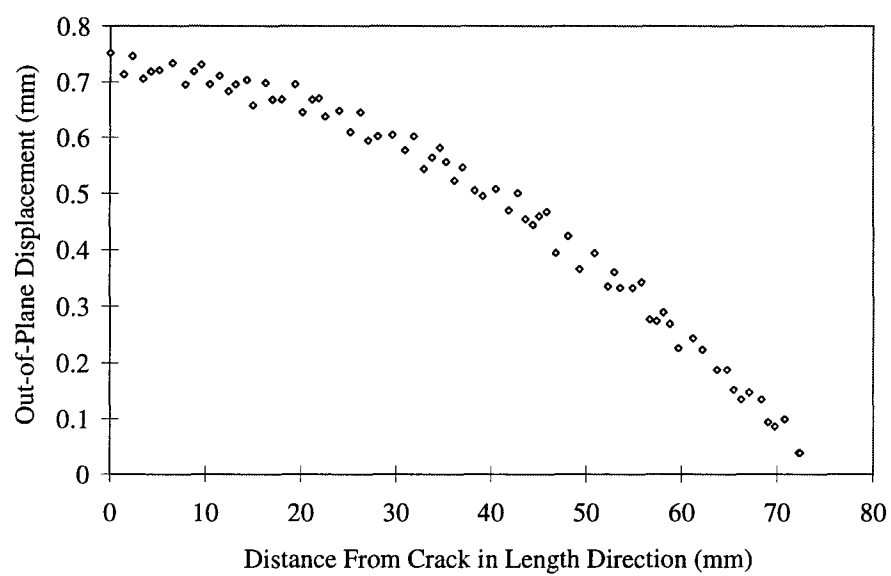


Figure 30. Repaired Specimen Curvature: Specimen 7 (Patch Length = 102 mm)

3.4 Data Analysis Techniques

3.4.1 Data Sampling/Analysis.

Calibrations: Systems which had to be calibrated prior to test were as follows:

- Eddy Current System
- Flaw Opening Gage (clip gage)
- Strain Gauge System

The eddy current system was calibrated using a blind calibration technique and conducted by the Air Force Materials Lab. This calibration was performed on a specimen prepared from a 6.350 mm thick plate with six separate pre-cracks of differing lengths and three different patch thicknesses, as mentioned previously. Crack lengths were measured optically (prior to repair) by the author and the specimen was sent to the Air Force Materials Lab for re-measurement of the cracks using the ANDSCAN system with the eddy current technique. The desired location of the crack length measurement was on the patched surface of the plate. Depth of penetration of the eddy currents is dependent on the probes' frequencies. Therefore, from the results of the tests, a NORTEC eddy current probe with a frequency range of 50-100kHz was chosen. Results of the two calibration measurement series and comparison to actual (optically measured) crack length measurements are shown in Tables 7 and 8. Results of the first calibration measurement series (shown in Table 7), using a gain equal to four, showed excellent results for the 9 and 14 ply patch thicknesses. A second measurement series, shown in Table 8, was necessary to refine the 18 ply thickness measurements and increased the gain to 8. From these results of calibration of the eddy current system, a gain of 4 was chosen for the 4.826 and 3.175 mm thickness repaired specimens and a gain of 8 was chosen for the 6.350 mm thickness specimens.

The clip gauge design (Figure 24) design originally used by University of Dayton Research Institute at the Air Force Materials Lab in compact tension specimens. The design was modified

Table 7. Eddy Current System Calibration Results: Gain=4

Patch Thickness	18 Ply	14 Ply	9 Ply
Trial 1	49.886	49.733	61.646
Trial 2	51.943	49.174	62.255
Trial 3	49.124	50.089	61.519
Trial 4	49.886	51.791	62.433
μ (Mean)	50.210	50.197	61.963
σ (Standard Deviation)	1.210	1.128	0.449
Optical (Reference)	53.302	50.399	61.875
Error	3.092	0.202	0.088
% Error	5.8%	0.40%	0.14%

Table 8. Eddy Current Calibration Results: Gain=8

Patch Thickness	18 Ply
Trial 1	52.680
Trial 2	54.737
Trial 3	53.619
Trial 4	55.677
μ (Mean)	54.718
σ (Standard Deviation)	1.306
Optical (Reference)	53.302
Error	0.876
% Error	1.64%

to miniaturize the gauge and optimize the gauge length and range for these tests. Gauge specifications meet ASTM test standards for CT specimen tests. Knife edge tabs of titanium, bonded to the specimen surface, were designed to match the configuration of ASTM standards for notch size in CT specimens. The gauge was machined and built at AFIT. It was calibrated (using MTS calibration equipment) for range, accuracy, and linearity. Figure 31 shows the calibration curve of the clip gage (voltage output versus displacement relationship). This output voltage was read by the data acquisition system (DAS) and was converted to center crack opening displacement (mm) and strain (mm/mm) during the data acquisition process.

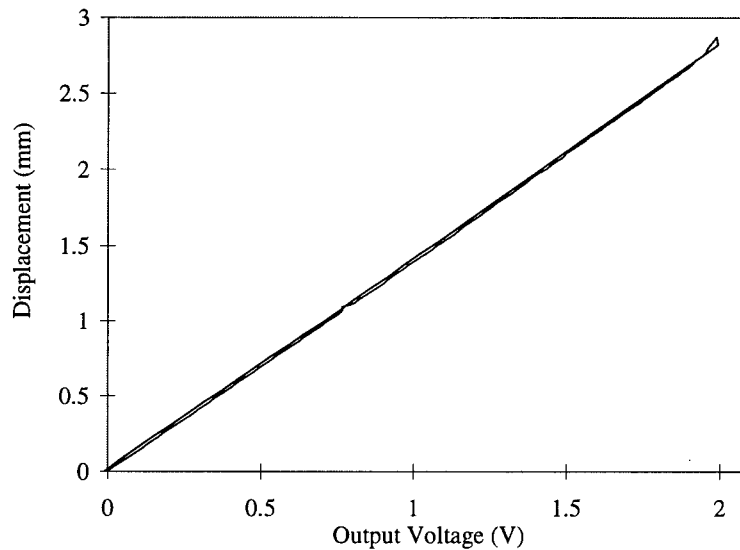


Figure 31. Clip Gage Calibration Curve

Sampling Intervals: ASTM Standard E 647 recommends crack length data sampling at the following intervals:

- $\Delta a \leq 0.04W$ for $0.25 \leq a/W \leq 0.40$
- $\Delta a \leq 0.02W$ for $0.40 \leq a/W \leq 0.60$
- $\Delta a \leq 0.01W$ for $a/W \geq 0.60$

The variable Δa is the crack growth interval between measurements, a is the half crack length and W is the specimen width. Minimum Δa should ideally be ten times the precision of the measuring instrument (i.e. optical, eddy current, etc.). These standards were followed during the tests in this study.

Data Reduction: ASTM Standard E 647 recommends crack length versus fatigue cycle, i.e. a vs. N , data from constant load (P_{max}) tests be reduced by using either a secant or incremental polynomial method. The secant method involves fitting a line between two consecutive points on the a vs. N curve. The incremental polynomial method uses sets of several consecutive points ($set = 2n + 1$ points) and fits a second order polynomial to these sets for determination of da/dN , the crack growth rate per cycle. For example, if ' n ' equals three, using the above sampling intervals, the method would be a 'seven-point-fit'. To be able to include the majority of the data acquired during testing, a three-point least squares fit [41] was used to develop da/dN curves in this study.

The next section describes briefly the computational tools which were used in the acquisition and reduction of data. Also, the computational tools to generate analytical models are discussed.

LABVIEWTM, a commercial data acquisition package, was used with the MTS test stand to control loading and frequency, to acquire loads, to acquire strain data from strain gages/ flaw gage, and to monitor test cycle counts. This package was designed for on-screen graphical programming of the Data Acquisition System (DAS), providing maximum flexibility in the types of tests being run. In this case, there were up to 20 active strain channels selected from 3 to 7 rosettes, 1 surface flaw clip gage multiplexed to the DAS, plus the MTS test stand load cell readings. These totalled 22 channels from which data was acquired during each data acquisition cycle (DAC). Due to a reduction of strain instrumentation in the later tests, this was reduced to 9 or 6 channels, plus the clip gage, dependant upon the necessity of eddy current data for each test. Note here that certain rosette

placements obscured eddy current probe measurements. Therefore, space limitations interfered with being able to get a full range of eddy current measurements on some smaller patch configurations.

3.5 Post-Mortem Examination of Tests

Two main features of the specimens were examined after the tests, in detail, to provide insight to crack growth behavior during its progression. First, as mentioned earlier, the fracture surface crack fronts were measured to determine the crack shape and area, as well as patched and unpatched face crack lengths. Figures 32 and 33 show the differences observed, using photomicroscopy, between the crack growth lag on the patched face of the patched specimen and the relatively straight crack front of the unrepaired specimen.

The fracture surface was examined for any unusual crack propagation characteristics to include plane transitions. Scanning electron microscopic (SEM) imaging was used to examine individual crack fronts and failure characteristics of the fracture surface. Results of these examinations are discussed in Section 4.7 - Disbond and Surface Observations. Second, the adhesive surface (or residue), left behind after final disbonding of the repair, was examined for disbond shape, rate changes, and final mode of failure. Marks left in the adhesive layer provided information about the disbond shape in latter stages of crack growth and verified information gained through debond images captured during the tests (thermography and C-Scans).

3.6 Numerical Approach

PATRAN V was used as the pre- and post-processor for the 'pseudo-3-D' finite element comparisons to experimental data. ABACUS was used as the solver for finite element models generated in this study. Details of these models are further discussed in Part II: Finite Element Modeling.

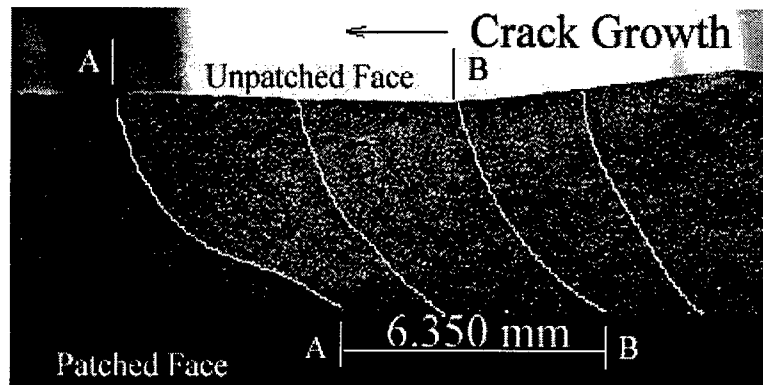


Figure 32. Patched Specimen Crack Growth Lag

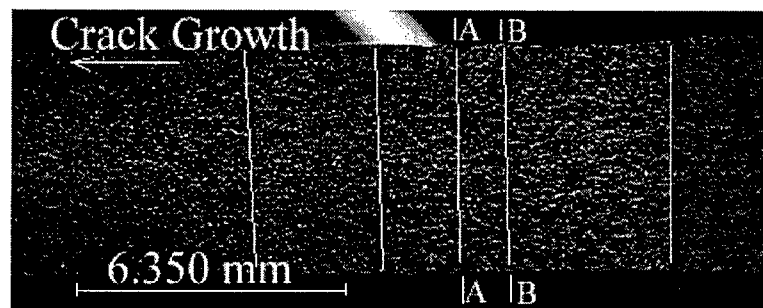


Figure 33. Unpatched Specimen Crack Front Progression

4. Test Results and Discussion

The purpose of this chapter is to present the results of the experimental test portion of this study and the discussion related directly to these tests. A total of twenty-eight unique tests and six repeat tests were performed on a variety of cracked plates with no repair, full-width repairs, finite-width repairs, repairs of different lengths, and repair patches with different patch-to-panel stiffness ratios, S , on three different thickness aluminum panels.

Chapter 4 is divided into nine sections. Each section contains a presentation of representative results and related discussion.

4.1 Test Summary

Table 6, in Chapter 3, details the tests accomplished during the course of this study. The study included one calibration specimen, six baseline plates (i.e. with no repairs), and 22 repaired plates (28 total test specimens: 10 specimens of 3.175 mm thick, 7 specimens of 4.826 mm thick, 11 specimens of 6.350 mm thick). Six additional tests were conducted to verify the range of data scatter experienced and determine the repeatability of test results. Patches on the repaired specimens included: 16 of full width (153 mm), 6 of partial width (50 mm), 8 of 102 mm length, 3 of 68 mm length, 11 of 51 mm length, 3 with stiffness ratio, $S=0.46$, 3 with $S=0.69$, 10 with $S=1.0$, and 6 with $S=1.3$ (see Table 6). Table 9 summarizes cyclic life results for the repaired specimens in the study.

4.2 Material Constant Determination

The first series of tests conducted in this study, Specimens 1 through 3, were to establish baseline data for the crack growth versus fatigue cycle relationship and fatigue life at 120 MPa, $R=0.1$, and 10 Hz for each thickness. Specimens 4 through 6 were then tested to establish baseline data for da/dN , crack growth rate, vs. ΔK (the stress intensity factor range relationship or Paris Law)

Table 9. Repaired Specimen Test Summary

Specimen #	t_p (mm)	S Ratio	Initial Crack Length, 2a (mm)	Patch Length/Width (mm)	Cycles to Failure	% Life Increase ¹
7	6.350	1.0	26.748	102/full	36100	413
8	6.350	1.0	25.824	68/full	38046	435
9	6.350	1.0	25.073	51/full	34350	393
10	4.826	0.69	25.428	102/full	55755	488
11	4.826	0.69	25.531	68/full	46499 ²	N/A
12	4.826	0.69	25.809	51/full	49750	435
13	3.175	0.46	25.325	102/full	64943	464
14	3.175	0.46	25.704	68/full	92350	445
15	3.175	0.46	25.575	51/full	64850	462
16	4.826	1.0	25.541	102/full	75125	658
17	4.826	1.0	25.273	51/full	65698	575
18	3.175	1.0	26.500	102/full	104200	744
19	3.175	1.0	25.301	51/full	88175	629
20	6.350	1.0	25.440	51/50	34697	397
21	6.350	1.3	25.340	51/50	38694	442
22	6.350	1.0	25.315	102/50	39600	452
23	6.350	1.3	26.002	102/50	37600	430
24	6.350	1.3	25.431	51/full	50249	575
25	6.350	1.3	25.903	102/full	43600	499
26	3.175	1.0	25.164	51/50	75338	538
27	3.175	1.3	25.608	51/50	77076	550
28	3.175	1.3	25.333	51/full	99721	712

¹This is the increase relative to unrepaired specimens.

²Specimen 11 failed in the bolted grip fixture due to flaw propagation from a bolt hole. Data from this test should be used with this consideration.

where:

$$\Delta K = \Delta \sigma \sqrt{\pi a} \quad (31)$$

The $\Delta \sigma$ is the applied stress range and a is the half crack length of the center cracked specimens. Baseline cyclic lives and crack growth curves for the first three specimens are shown in Figure 34 and Table 10. Denney [16] showed a high degree of repeatability in the crack growth curves for 1 mm thick specimens with and without repairs. A few replicate tests were also conducted in this study to demonstrate repeatability of the test method and these tests showed less than 20% variation in life-span for the patched cases. See Appendix C for details of these tests.

Table 10. Baseline Test Plates - Cyclic Life

Specimen #	Thickness (mm)	Initial Crack Length, 2a (mm)	Cycles to Failure
1	3.175	25.326	14011
2	4.826	25.212	11425
3	6.350	25.744	8746

Results from tests of specimens 4, 5, and 6 were used to determine material constants C and m , in the Paris Law, for each plate thickness. The constants are the result of a power curve fit to the log-log plots of da/dN vs. ΔK . The constant C is the y-axis (crack growth rate) intercept point of this curve (at x-axis where $\Delta K=1$) and m is the slope of the linear portion of the curve. The curve-fit equation for this portion is of the form:

$$\frac{da}{dN} = C(\Delta K)^m \quad (32)$$

or better known as the Paris Law relation. The values for C and m , with Equation 32 were used later for the determination of the crack growth rates, da/dN , of the repaired specimens. This was accomplished with finite element model results and stress intensity factors calculated from the modified crack closure method. Table 11 shows the initial crack lengths and applied stress ranges used in determining the da/dN vs. ΔK log-log plots.

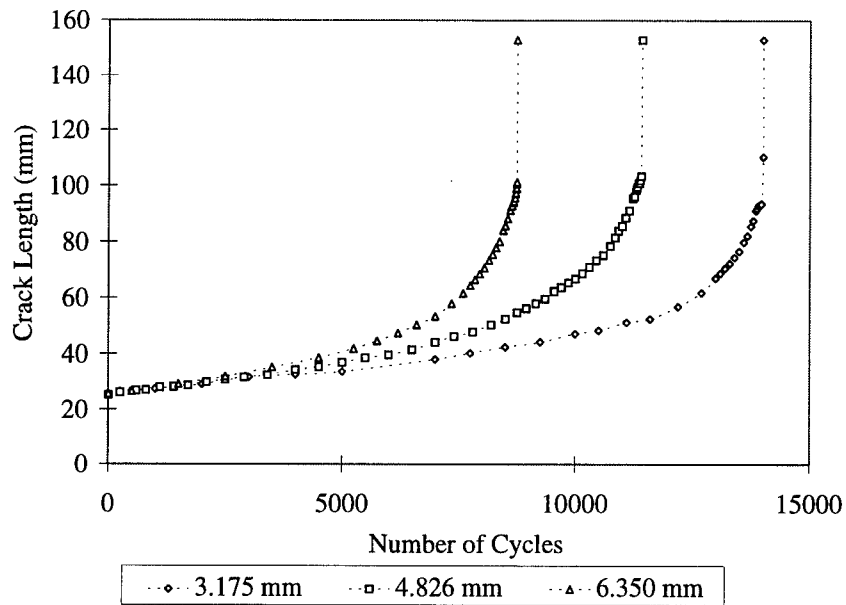


Figure 34. Baseline Crack Growth Curves - Unrepaired Panels (at 120 MPa)

Table 11. Baseline Tests - da/dN vs. Delta K Determination

Specimen #	Thickness (mm)	Initial Crack Length, $2a$ (mm)	Applied Stress Range
4	3.175	25.755	80 - 140 MPa
5	4.826	25.154	80 - 140 MPa
6	6.350	25.379	80 - 140 MPa

Each specimen was fatigued at progressively higher applied stress levels as the crack progressed. By conducting the testing starting with a short crack at lower load and slowly progressing to a longer crack at higher load, the complete range of the da/dN vs. ΔK log-log curve, as associated with this study, was characterized. Figures 35 through 37 show the results of these tests and their corresponding curve-fits. The experimentally determined Paris Law constants are provided in Table 12. When used with ΔK (stress intensity range), in the units of MPa, the Paris Law and these constants give da/dN (crack growth rate) in units of m/cycle. It should be noted here that these constants are for the specific load range, load ratio, plate thicknesses, and frequencies used in this study. In general, the experimentally derived constants were found to be consistent with the range of constants determined by Baker [4, 7]. The Damage Tolerant Design Handbook [24] shows values of C , in the same unit system, ranging anywhere from 10^{-9} to 10^{-13} for 2024-T3 aluminum. The exact values are dependent upon specific load conditions (frequency, R (load ratio), ΔK). It was found that the constants in this study also had a dependence on specimen thickness. This feature was also seen by Broek and Schijve [12] during testing of different thickness unrepaired plates.

Table 12. Experimentally Determined Paris Law Constants

Specimen #	Thickness, t (mm)	C	m
4	3.175	$1.152e-12$	3.917
5	4.826	$7.685e-12$	3.412
6	6.350	$10.267e-12$	3.408

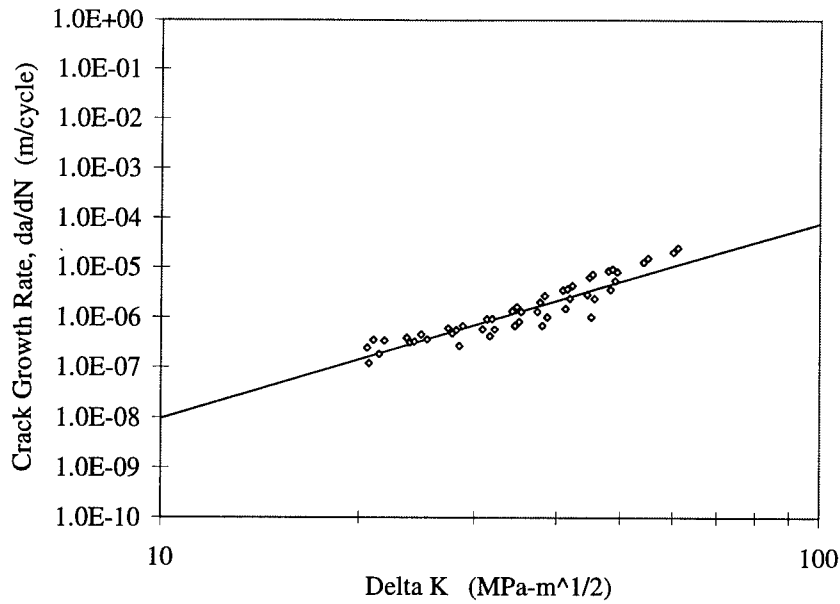


Figure 35. Paris Law Constant Determination for t=3.175 mm Plate

4.3 Pre-Test Curvature

4.3.1 Curvature Measurement

The initial curvature of each specimen was measured and verified as 'flat' (i.e. no initial curvature) prior to repair, as shown by the earlier example in Figure 33. The deviations from 'flat' (or initial curvature), measured as out-of-plane displacements after repair patches were bonded to the plates, were then plotted and the resulting data points were fitted with a parabolic curve of the equation:

$$x = h \pm \sqrt{4P(y - k)} \quad (33)$$

The parabolic parameters, h and k , define the coordinates of the parabola's vertex, P is the distance from the vertex to apex and the parabola's axis is the y-axis. For comparison purposes, each fit was optimized for the range of points, on the plates, falling within ± 25 mm of the crack location, along

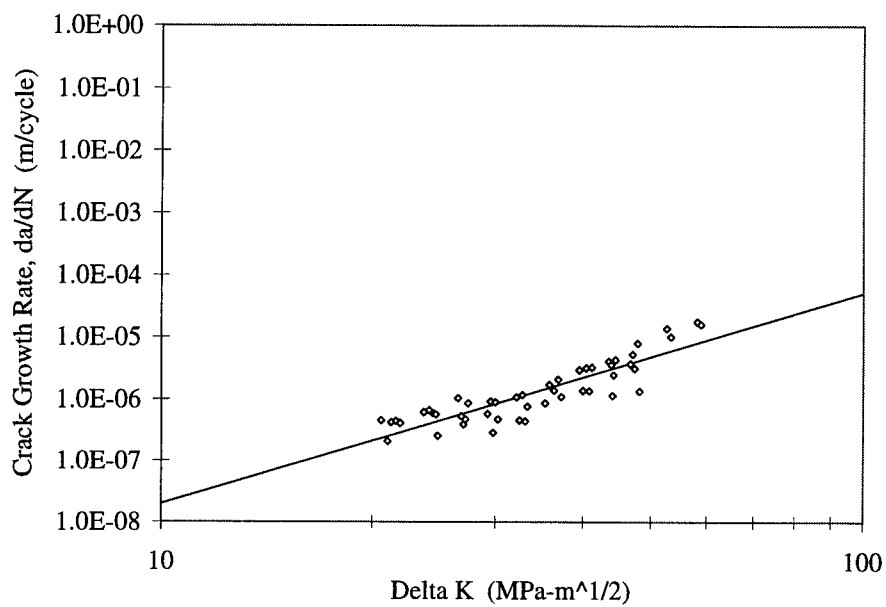


Figure 36. Paris Law Constant Determination for $t=4.826$ mm Plate

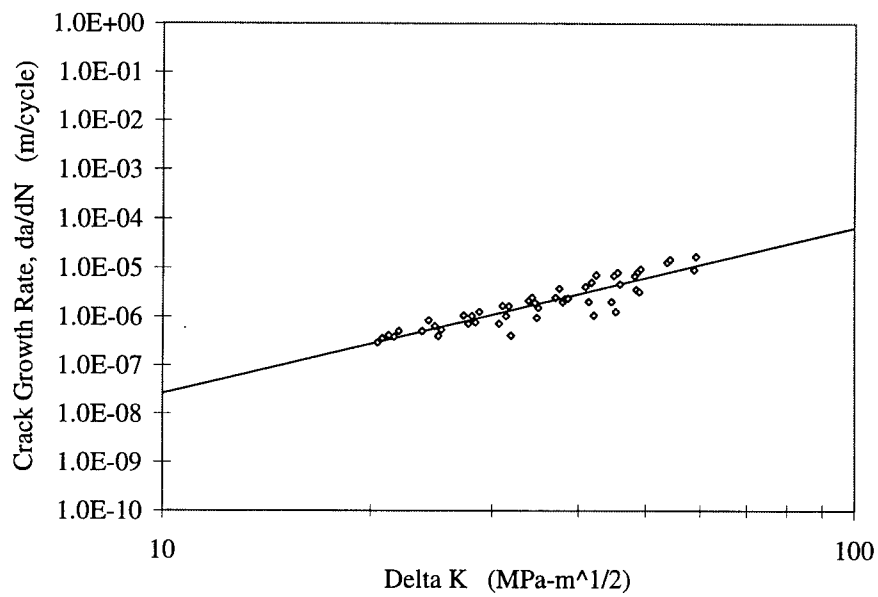


Figure 37. Paris Law Constant Determination for $t=6.350$ mm Plate

the centerline of the panel. Figure 38 shows an example of the curve-fit compared to the measured out-of-plane displacements. Radius of curvature, ρ , is defined as $\frac{1}{K}$, where:

$$K = \frac{|y''|}{[1 + (y')^2]^{\frac{3}{2}}} \quad (34)$$

Using Equation 33 and solving for the radius of curvature, ρ , we find:

$$\rho = 2P \left[1 + \left(\frac{x-h}{2P} \right)^2 \right]^{\frac{3}{2}} \quad (35)$$

Table 13 summarizes the radii of curvature after repair for all specimens. The 6.35 mm plates had approximately twice the radii of the 3.175 mm plates and radii for the 4.826 mm plates fell approximately mid-way between these two.

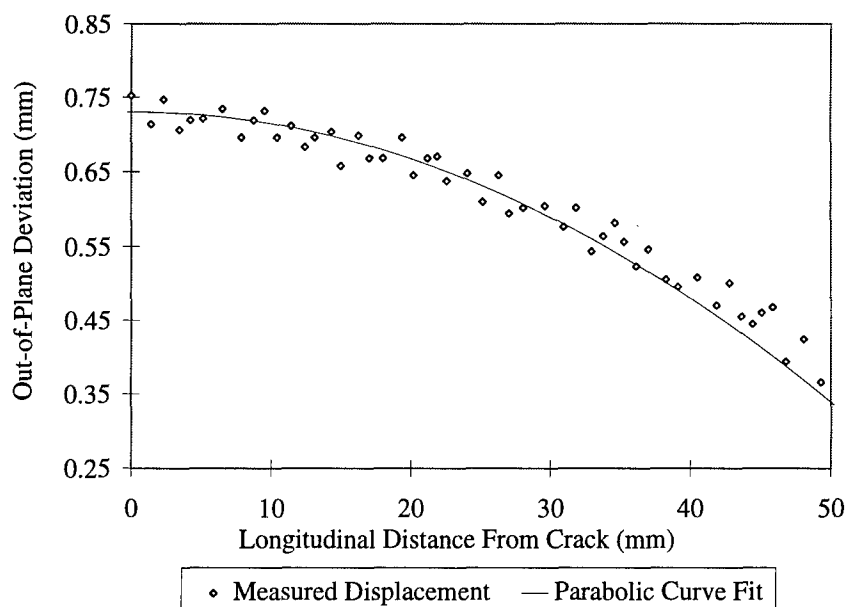


Figure 38. Comparison of Measured Curvature with Parabolic Curve Fit

4.3.2 Residual Stresses and Pre-existent Strains

The bonding process of adhesively-bonded composite repair and the inherent coefficient of thermal expansion (CTE) mismatch of the two dissimilar materials is the direct cause for residual stresses and thus the curvatures in the repaired area of the specimens. The much higher CTE of

Table 13. Measured Curvature Summary

Specimen #	Plate Thickness, t (mm)	Radius of Curvature (mm)
7	6.350	3125
8	6.350	3543
9	6.350	3672
10	4.826	2734
11	4.826	2474
12	4.826	2571
13	3.175	1767
14	3.175	1594
15	3.175	1653
16	4.826	2423
17	4.826	3321
18	3.175	1986
19	3.175	1792
20	6.350	2840
21	6.350	3125
22	6.350	3594
23	6.350	3630
24	6.350	3506
25	6.350	3429
26	3.175	1698
27	3.175	1906
28	3.175	1537

aluminum plate over that of the boron/epoxy patch causes the patched surface of the plate to be under tension while the patched surface of the repair is under compression. The resulting curvature follows the shape characteristics of the beam, subjected to uniform shear stress applied to one side. The fact that the thinner plates had the higher curvature is consistent since the maximum deflection of a beam is governed by a cube of thickness or the moment of inertia. This dependence decreases the maximum deflection under a given shear load with increase in the thickness. But, as plate thickness increases, so do surface stresses for a given deflection. This stress is dependent upon the distance of the surface from the neutral axis of the plate. An additional point to be noted is that these parabolic initial curvatures are caused by the residual stresses after bonding the patch, and this causes the crack on the patched face to open and the unpatched face to close. Dependent upon specimen thickness this may actually cause the unpatched face crack to be under compression.

Two additional effects of the curvature should be noted here. First, one must consider the specimen curvature before loading and the out-of-plane displacement under loading. Second, one must consider the effect these displacements (due to initial curvature and loading) have on the neutral axis after repair and thus the influence of the asymmetric repair on stresses within the specimen. The amount of out-of-plane displacement and bending directly impacts the stress intensity factor of the crack tips, giving a stress which varies through the thickness of the specimen. This bending also effects the rotation of the fracture surface and thus the crack opening displacement. The extent to which these factors affect crack growth rate are discussed in the subsequent sections.

4.4 Effects of Patch Length

4.4.1 Initial Curvatures

Figure 39 shows the measured radius of curvature for three thicknesses of specimens with full width patches (153 mm), for patch to panel stiffness ratio $S=1.0$, and three patch lengths. It also shows the trend for an $S=0.46$, full width patch on a 3.175 mm thickness panel. Trends from these curves show an inverse relationship between patch length and localized radii of curvature, caused by thermal residual stresses in 6.350 and 4.826 mm plates. For the 6.350 mm plate, a 14.9 % smaller radius of curvature is seen for the 102 mm long patch over that of the 51 mm short patch. In the case of the 4.826 mm plate, a 27% smaller radius is seen for the longer patch. Note that a smaller radius is the same as increasing the localized curvature. For these 'thick' plates, the trends agree with two-dimensional beam theory; increased patch length produces a decreased radius of curvature.

The thin plates (3.175 mm) had a smaller radius of curvature than those of the thick plates (4.826 and 6.350 mm). However, the 3.175 mm plates show a 10.8% larger radius for the longer repair. The trend for the plate thickness changes coincides with beam theory; increased plate thickness results in increased radius of curvature. On the contrary, the data trend for increased patch length on the 3.175 mm plates does not coincide with the expected trend from two-dimensional beam theory. Two-dimensional beam theory dictates increased patch length should decrease radius of curvature. But, in practice, methods for the application of patches on thin panels dictate that a larger patch should be used to reduce bending (increased radius of curvature results in increased patch length). This seems to contradict both two-dimensional beam theory [63] and Rose's bending stiffness [6] (decreased radius of curvature results in increased patch length). Numerical results showed transverse bending, due to the transverse CTE mismatch between the uniaxial patch and the aluminum, induces a saddle shape in the specimen. This addition of transverse bending and the re-

sulting change in geometry influence longitudinal bending differently in the thick and thin repaired panels. The thick panels demonstrated proportional decreases in both transverse and longitudinal radii of curvature with increased patch length. The change in longitudinal radius of curvature in the thin panels was inversely proportional to the amount of change in transverse radius. The resulting curvatures are due to the coupled effects of the bending in an anisotropic laminated plate. An increase in the longitudinal bending stiffness of the thin panel increases the longitudinal radius produced by the longer patch, as expected from two-dimensional beam theory. The theories referred to earlier are insufficient for characterizing the repair effects on curvature. Therefore, prediction of thermal and mechanical bending effects must be accomplished using a more rigorous method than two-dimensional beam theory. The numerical method shown in Chapter 5 demonstrates good predictions of the resulting curvatures.

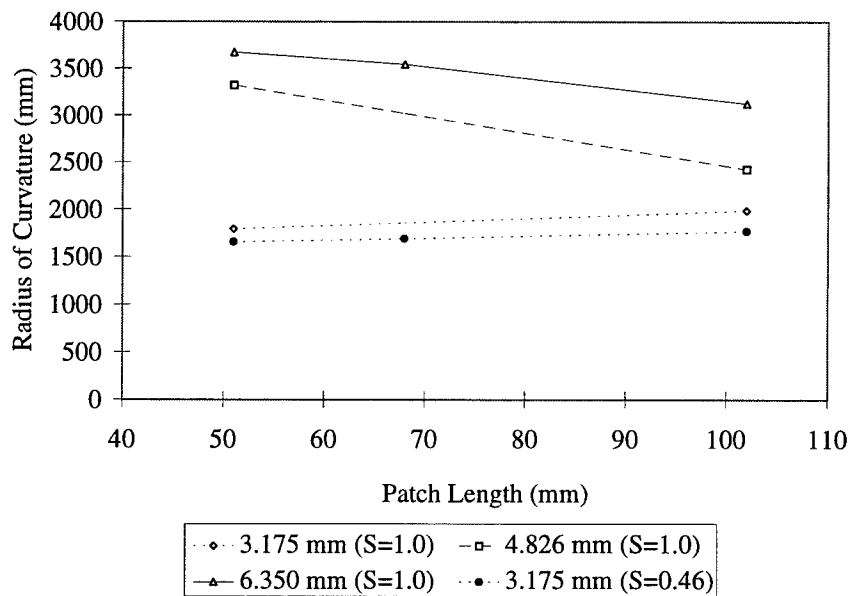


Figure 39. Radius of Curvature Variation with Plate Thickness and Patch Length

4.4.2 Crack Growth Rates

The figures in this chapter present crack growth rates, da/dN , vs. crack length, $2a$, data over the entire width (or up to failure) of the specimens. Additional figures with a more magnified scale (i.e. for shorter crack lengths in greater detail) can be found in Appendix A. Table 14 summarizes increases in the life-span (fatigue life) of the repaired panels over those of the unrepaired baseline specimens. Increase in thickness of the specimens decreased life-spans of both the unrepaired and repaired specimens. Baseline (unrepaired) tests showed a factor of 1.6 times longer life in the thin (3.175 mm) vs. thick (6.350 mm) specimens (see Figure 34). Repaired thin panels had approximately 2.9 times longer life than repaired thick specimens when similar repairs (i.e. same stiffness ratio) were applied.

For the thick panels at stiffness ratio $S=1.0$, increases observed in fatigue life over the baseline plates were 3.93, 4.35, and 4.13 times for the 51, 68, and 102 mm long patches, respectively. Comparison of the long patch (102 mm) to the short patch (51 mm) performance on the thick plate showed only a 2.5% difference in total life-span (Figure 40). This is significantly less than the increase in life seen for the thinner plates as discussed later. This small difference can be due to data scatter or due to the effect of debond differences at very long crack lengths as discussed later.

Crack growth rates, when the crack length was less than the critical crack length of the unrepaired specimen, was moderately higher for the longer patch on thick panels. Crack growth rates for the long (102 mm) and short (51 mm) repairs on the 6.350 mm plates are compared in Figure 41. The most dramatic changes in growth rate occurred when the crack length, $2a$, was 100 mm. This length corresponds to the critical crack length of the unrepaired plates which is approximately 103 mm. At this crack length, the crack growth rate slows for the longer repair. This phenomenon was more pronounced in the lower stiffness ratio patches but it was still evident in the higher stiffness

ratio patches. This effect could be due to the significant increase in debond growth at the crack.

This issue is discussed further in Section 4.7-Disbond Observations.

Table 14. Lifespan Increase Summary, Full Width Repair, $S=1.0$

	Plate Thickness, t			
		3.175 mm	4.826 mm	6.35 mm
Patch Length, L	102 mm	7.44	6.58	4.13
	68 mm	NT	NT	4.35
	51 mm	6.29	5.75	3.93

Note: Fatigue life extension relative to baseline specimens.

(NT = Not Tested)

Current patch design guidelines suggest that by increasing the patch length, one can decrease the rate of debond and bending, and thus increase the life-span.. For the 4.826 mm thick panel, with stiffness ratio 1.0, Figure 42 shows that longer patch had a moderate impact on the reduction of fatigue life. Increases in life-span were 5.75 and 6.58 times baseline unrepaired panel life for the 51 and 102 mm repairs, respectively. Comparison of the long (102 mm) patch to the short (51 mm) patch showed an increase of 14.3% in fatigue life.

Figure 43 shows the crack growth rate curves for the 4.826 mm thickness specimens with $S=1.0$, full width repairs. In this case, however, it can be seen that the longer patch has a lower growth rate throughout the life-span of the specimen. This differs from the trend seen in the 6.350 mm thick plate tests (Figure 41). Similar to the 6.350 mm plates, one sees a decrease in crack growth rate for a short period when the crack grows beyond the critical crack length of the unrepaired, 4.826 mm thick specimen.

For the thin specimen, 3.175 mm thick, a trend similar to the 4.826 mm thick specimens was seen. Increases in life-span were 6.29 and 7.44 times that of baseline unrepaired specimens for the 51 and 102 mm long patches, respectively. Figures 44 and 45 compare life curves and crack growth rates for the $S=1.0$, full width repairs on thin plates. Comparing the long patch (102 mm)

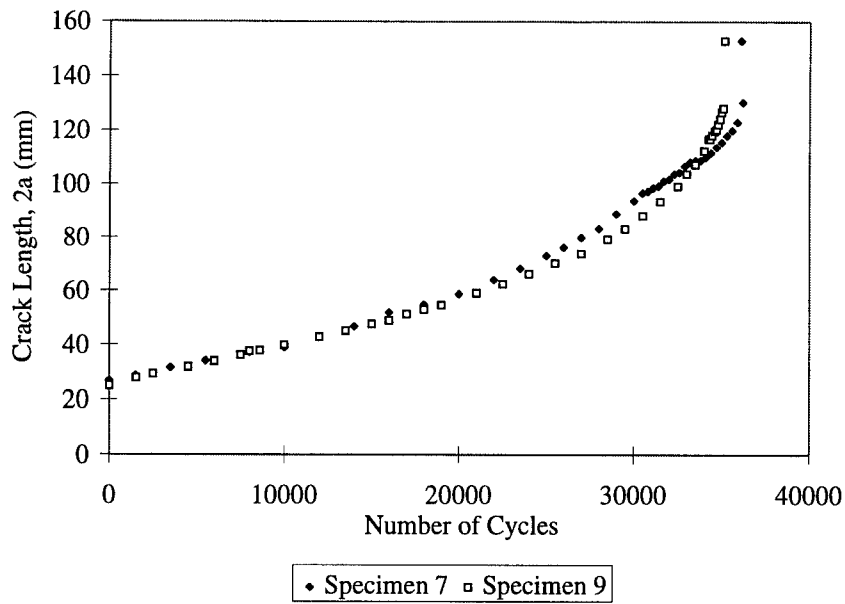


Figure 40. Crack Growth vs. Cycles Comparison, 6.350 mm Plate with $S=1.0$, Full Width Repair, Patch Lengths: 102 mm-Specimen 7, 51 mm-Specimen 9

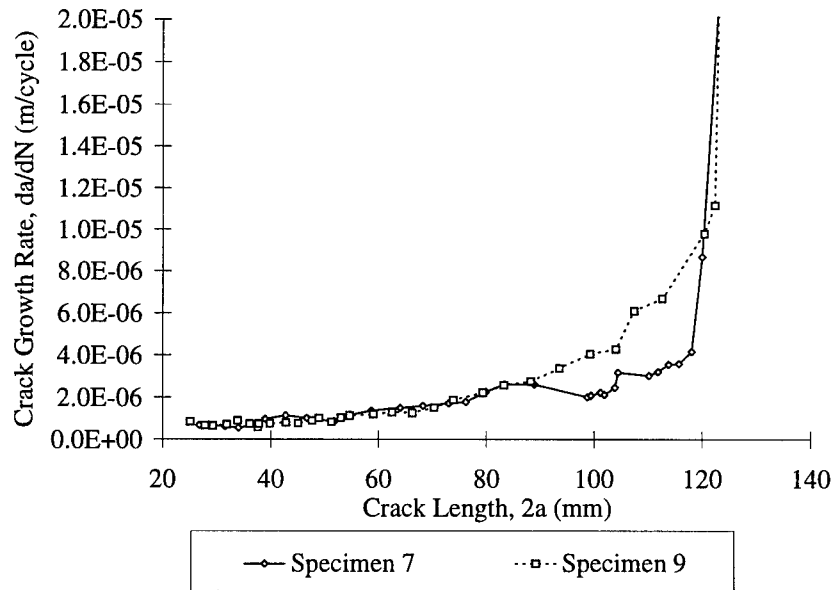


Figure 41. Crack Growth Rate, da/dN , Comparison, 6.350 mm Plate with $S=1.0$, Full Width Repair, Patch Lengths: 102 mm- Specimen 7, 51 mm- Specimen 9

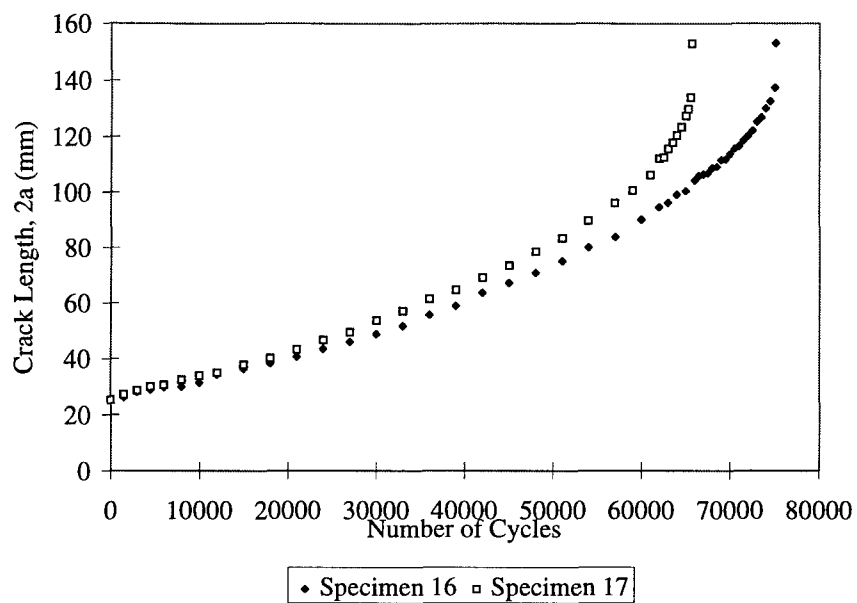


Figure 42. Crack Growth vs. Cycles Comparison, 4.826 mm Plate with $S=1.0$, Full Width Repair, Patch Lengths:102 mm-Specimen 16, 51 mm-Specimen 17

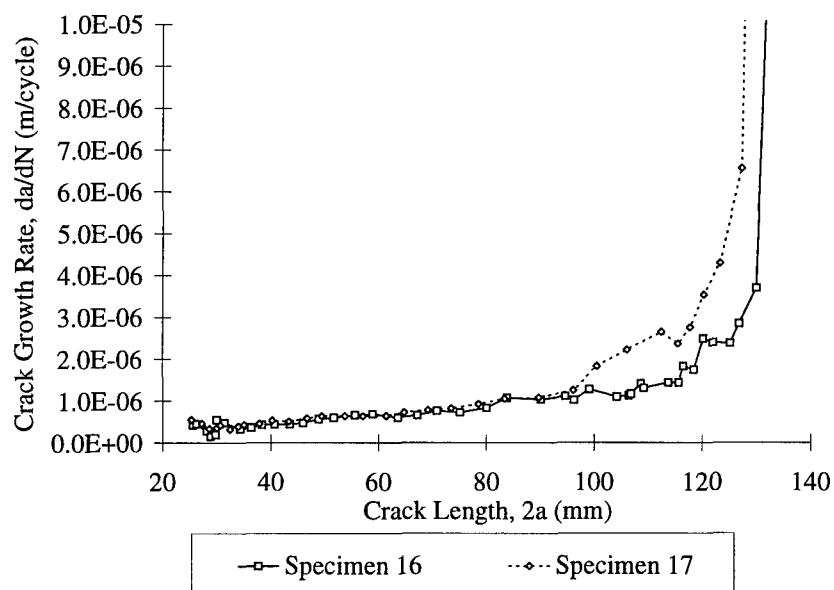


Figure 43. Crack Growth Rate, da/dN , Comparison, 4.826 mm Plate with $S=1.0$, Full Width Repair, Patch Lengths:102 mm-Specimen 16, 51 mm-Specimen 17

performance to the short patch (51 mm), an 18.3% increase in life over the short patch was realized with the longer patch.

Crack growth rates did not show any large difference between these specimens due to patch length. After the crack grew to the unrepaired critical crack length, crack growth rates became much more erratic, most likely due to simultaneous crack and adhesive layer disbond growth as discussed later. Overall, the longer patch length shows a definitive improvement in fatigue life over the shorter patch in this thin plate case.

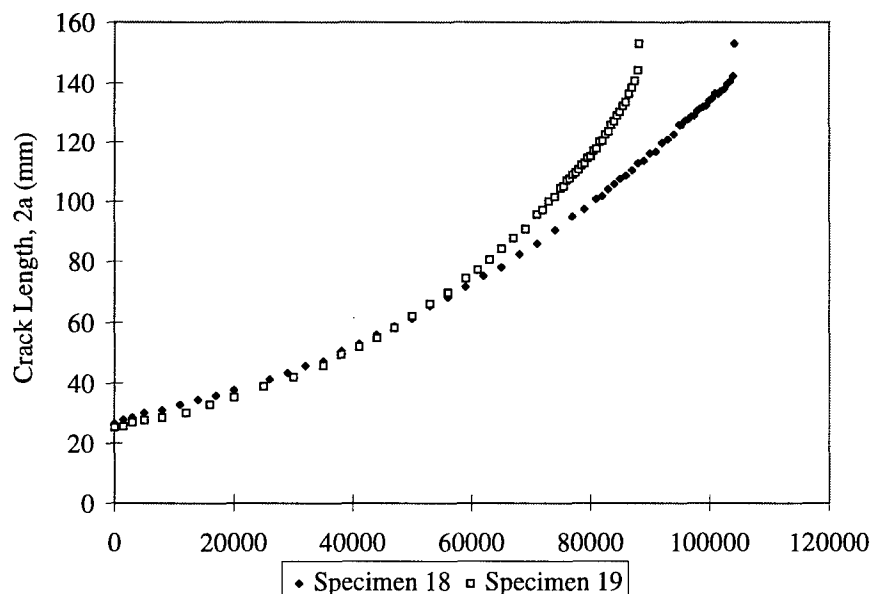


Figure 44. Crack Growth vs. Cycles Comparison, 3.175 mm Plate with $S=1.0$, Full Width Repair, Patch Lengths:102 mm-Specimen 18, 51 mm-Specimen 19

Examining the influence of patch length on higher stiffness ratio, $S=1.3$, and full width repairs, Figures 46 and 47 show a 13.2% decrease in fatigue life for the longer patch repair and a consistently higher growth rate for the longer patch. The most likely cause for this is the larger initial curvature associated with this high stiffness patch repair. It should be noted that the crack growth rates for both these repairs show erratic behavior again at crack lengths exceeding 100 mm (Figure 47).

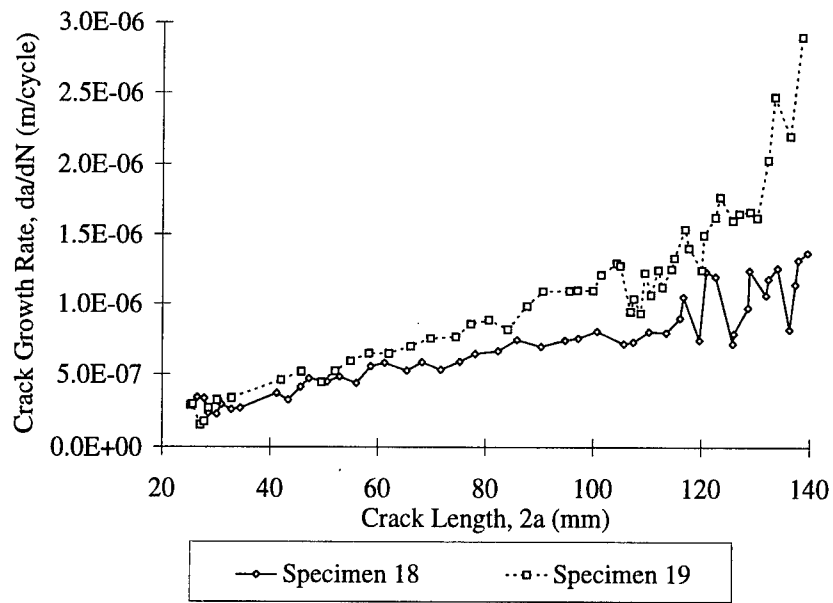


Figure 45. Crack Growth Rate, da/dN , Comparison, 3.175 mm Plate with $S=1.0$, Full Width Repair, Patch Lengths: 102 mm-Specimen 18, 51 mm-Specimen 19

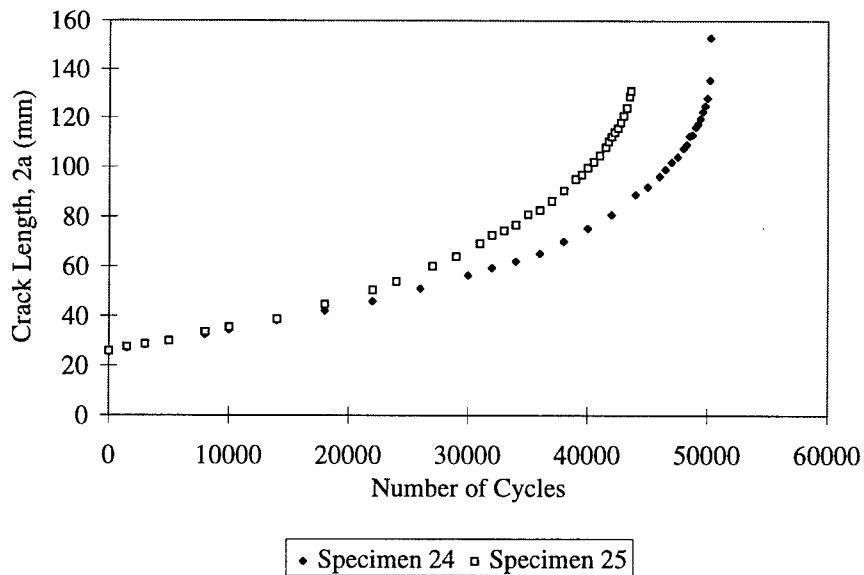


Figure 46. Crack Growth vs. Cycles Comparison - 6.350 mm Plate with $S=1.3$, Full Width Repair, Patch Lengths: 51 mm- Specimen 24, 102 mm-Specimen 25

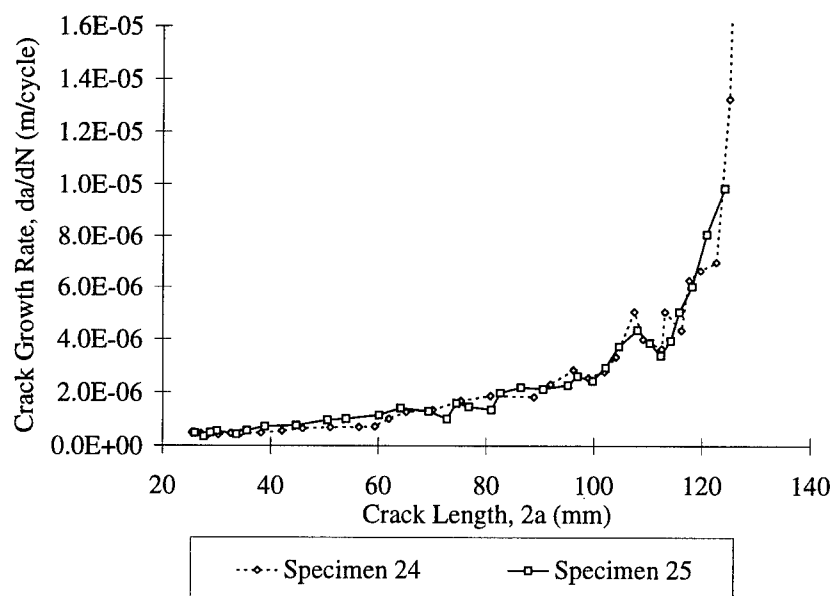


Figure 47. Crack Growth Rate, da/dN , Comparison, 6.350 mm Plate with $S=1.3$, Full Width Repair, Patch Lengths: 51 mm-Specimen 24, 102 mm-Specimen 25

Examining effects of patch length on finite width repairs (50 mm wide with stiffness ratio $S=1.0$), Figure 48 shows an increase in life of 14.1% for the longer versus the shorter patch repair. In this case the longer patch shows a reasonably consistent crack growth rate increase until 100 mm, Figure 49. In the case of the shorter patch, one sees obvious changes in the crack growth rate for the region of the patch edge taper and again at the region where the crack grows beyond the patched area. The specimen with the short repair actually had a crack length, at failure, shorter than the crack length at failure of the baseline specimen, but its fatigue life was extended relative to the baseline specimen. Debond growth was also relatively extensive when compared to the full width repair just before failure.

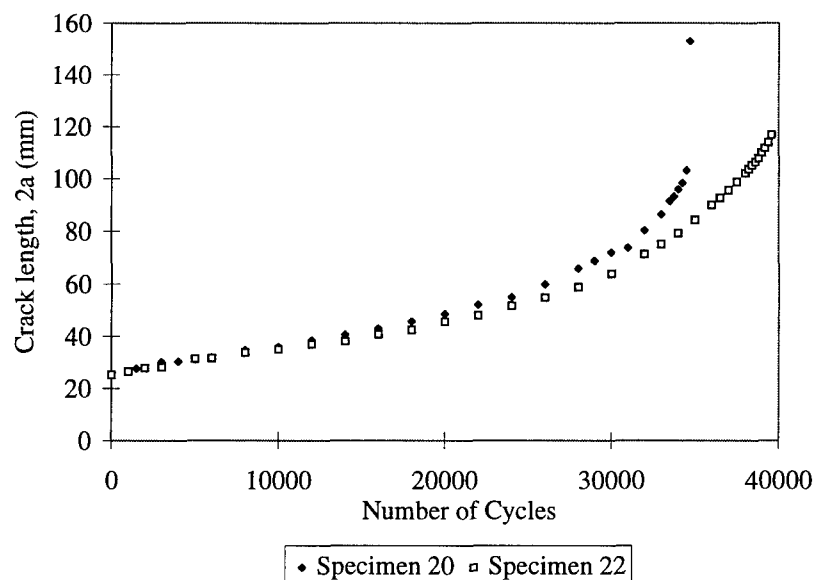


Figure 48. Crack Growth vs. Cycles Comparison - 6.350 mm Plate with $S=1.0$, 50 mm Wide Repair, Patch Lengths: 51 mm- Specimen 20, 102 mm-Specimen 22

For the higher stiffness ratio, $S=1.3$, patches with 50 mm width, it is seen once again that the longer patch has a shorter life span than the short patch by 2.8%. This is a smaller difference than that with the full width patch cases. However, the longer patch in this case has a consistently longer

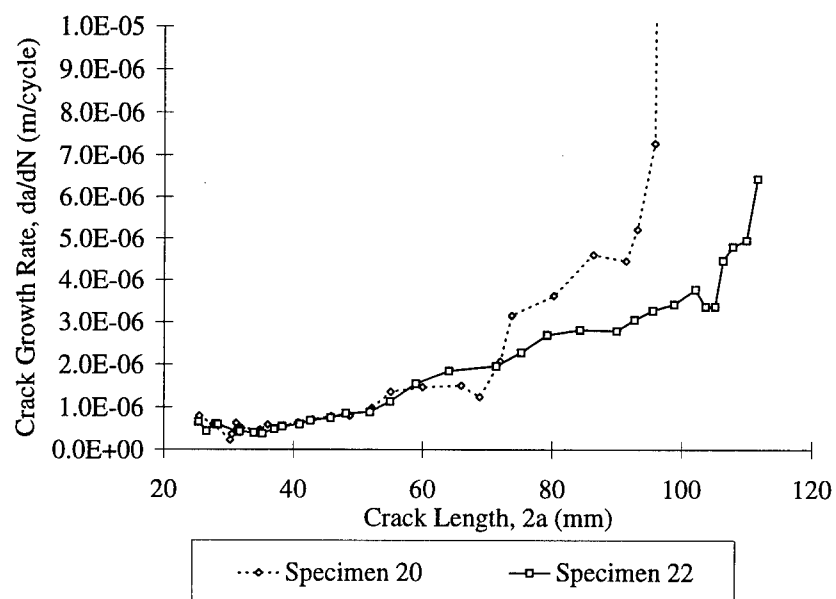


Figure 49. Crack Growth Rate, da/dN , Comparison, 6.350 mm Plate with $S=1.0$, 50 mm Wide Repair, Patch Lengths: 51 mm-Specimen 20, 102 mm-Specimen 22

crack length at a given cycle count and a higher growth rate until the crack grew beyond the patched area, Figures 50 and 51. At this point, the growth rate with the longer patch slows and outlived the short patch. This was because the long patch debond area was smaller relative to the patch size and does not fail catastrophically. Again, debond in the short patch was a large factor in the failure of the short patch repaired panel.

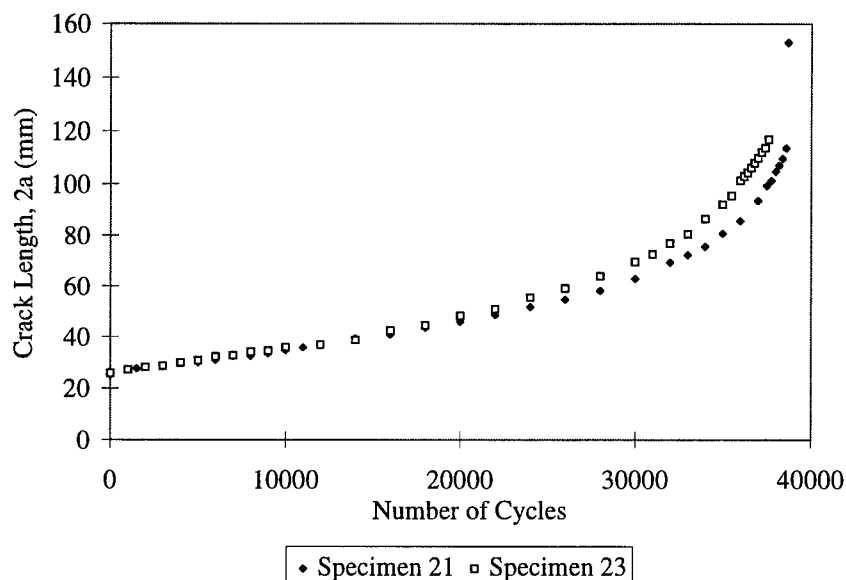


Figure 50. Crack Growth vs. Cycles Comparison - 6.350 mm Plate With $S=1.3$, 50 mm Wide Repair, Patch Lengths: 51 mm- Specimen 21, 102 mm-Specimen 23

In general, the amount of increase in life-span with increasing patch length becomes less and less as the thickness of the specimen is increased. See Table 15 for a summary of percentage life increases due to increasing patch length. The increase in life realized by lengthening patches is maximum in the thinner specimens with $S=1.0$. There is only a nominal increase in life with longer repairs at stiffness ratio $S=1.0$ with the 6.350 mm plates. At a stiffness ratio of $S=1.3$, it can be seen that the increase in length consistently decreases overall life by increasing crack growth rate. An

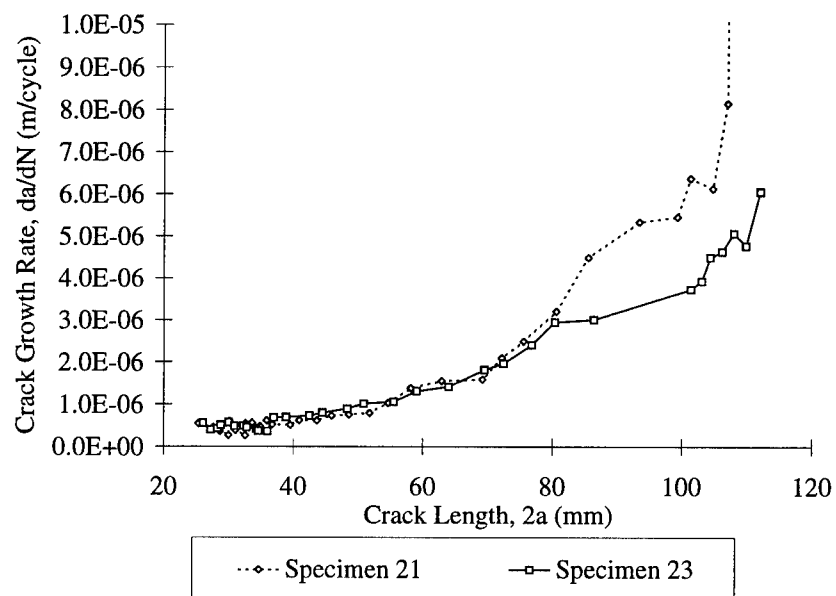


Figure 51. Crack Growth Rate, da/dN , Comparison, 6.350 mm Plate with $S=1.3$, 50 mm Wide Repair, Patch Lengths: 51 mm-Specimen 21, 102 mm-Specimen 23

increase in patch length, therefore, does not necessarily mean an increase in repair efficiency (i.e. an increase of life) for thick components.

Table 15. Percentage Change in Life Cycles with Increasing Patch Length from 51 mm to 102 mm

	Plate Thickness (mm)		
	3.175	4.826	6.350
Full Width, S=1.0	18.3	14.3	2.5
Full Width, S=1.3	14.1	-	(13.2)
Finite Width, S=1.0	-	-	(2.8)

Note: () denotes a decrease or negative percentage effects.

Bending, due to the bonding of the patch to the panels, causes changes in the crack tip stresses for plates of different thicknesses. A longer patch causes increased stresses due to bending in the thick panels. Therefore, there is less benefit to an increase of patch length for thick repairs, and increases in patch length can shorten life-spans, as was shown for higher stiffness ratio and finite width patches. Thus, the current guidelines for thin plate repairs are not directly applicable to thick plate repairs.

4.4.3 Crack Opening Displacement (COD)

Figure 52 shows the comparison of CODs for the two patch lengths (51 and 102 mm). For the 6.350 mm plate, center crack opening displacement (COD) was smaller for the shorter, 51 mm, patch when crack length was short. At longer crack lengths, the panel with the 51 mm repair had a larger crack opening displacement than that of the specimen with the 102 mm patch. This increased COD of the 51 mm patch specimen is consistent with the increased rate of crack growth seen and the shorter life span of the short patch, as discussed earlier.

In the 4.826 mm thick specimens, no significant difference was seen in COD for the different patch lengths, Figure 53. The 3.175 mm plates showed small differences in COD due to change in patch length up to a crack length of about 90 mm, as shown in Figure 54. At longer lengths, COD of

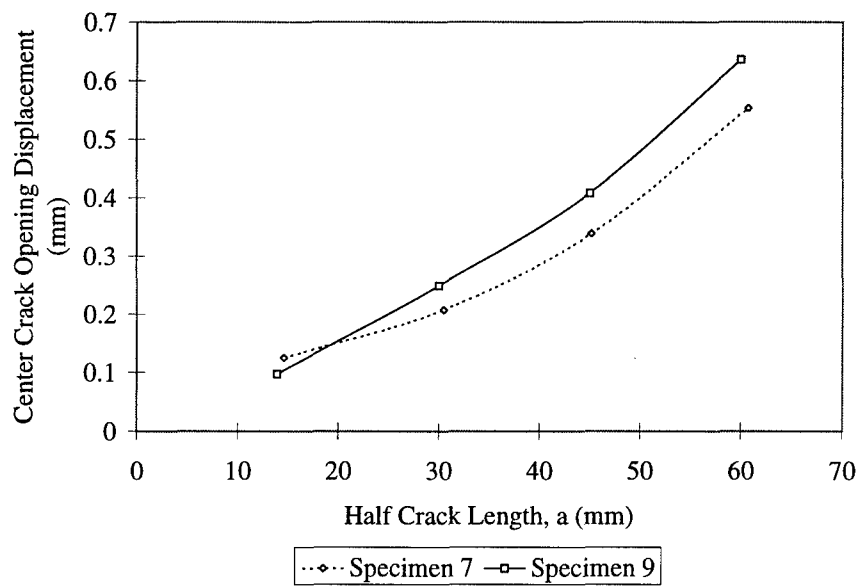


Figure 52. COD Comparison - 6.350 mm Plate, $S=1.0$, Full Width Repair, Patch Lengths: 102 mm-Specimen 7, 51 mm-Specimen 9

the 51 mm patch exceeded the that of the 102 mm patch significantly and increases until specimen failure.

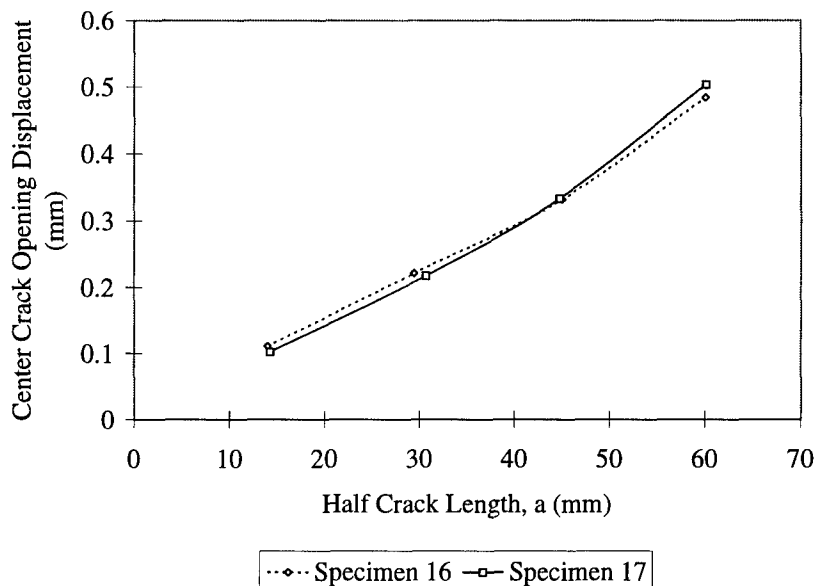


Figure 53. COD Comparison - 4.826 mm Plate, $S=1.0$, Full Width Repair, Patch Lengths: 102 mm-Specimen 16, 51 mm-Specimen 17

Figure 55 shows only a slight increase in the COD of the short patch over that of the long patch for the 6.350 mm plates at stiffness ratio $S=1.3$. This increase is almost unchanged at different crack lengths for this stiffness ratio.

The 6.350 mm plates with $S=1.0$ and finite width (50 mm nominal) patches show a steady divergence between COD of the long vs. short patches, with the shorter patch displaying a larger COD, Figure 56. These tend to diverge much faster as the crack exceeds 100 mm in length. When examining the 6.350 mm plates with the finite width, $S=1.3$ patches, no difference is noted between the CODs until the crack reaches approximately 90 mm, then these curves diverge rapidly, Figure 57.

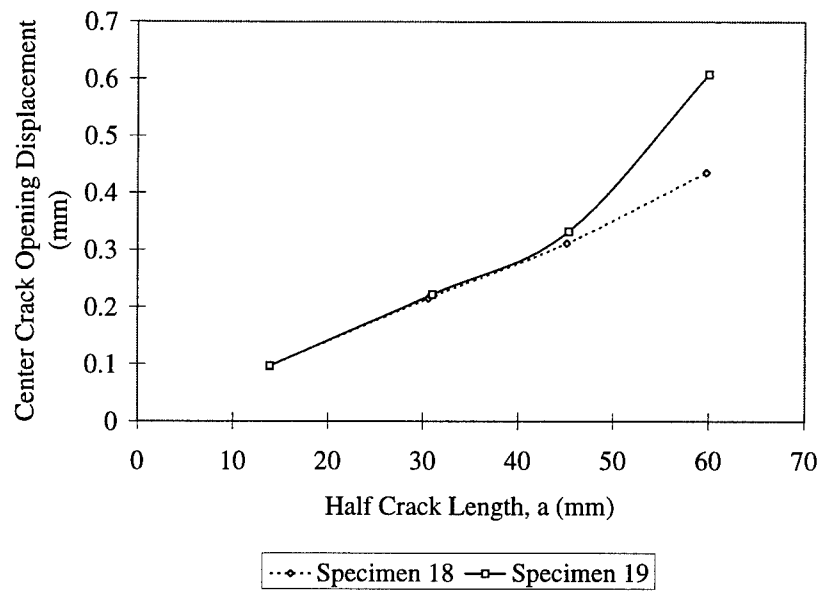


Figure 54. COD Comparison - 3.175 mm Plate, $S=1.0$, Full Width Repair, Patch Lengths: 102 mm-Specimen 18, 51 mm-Specimen 19

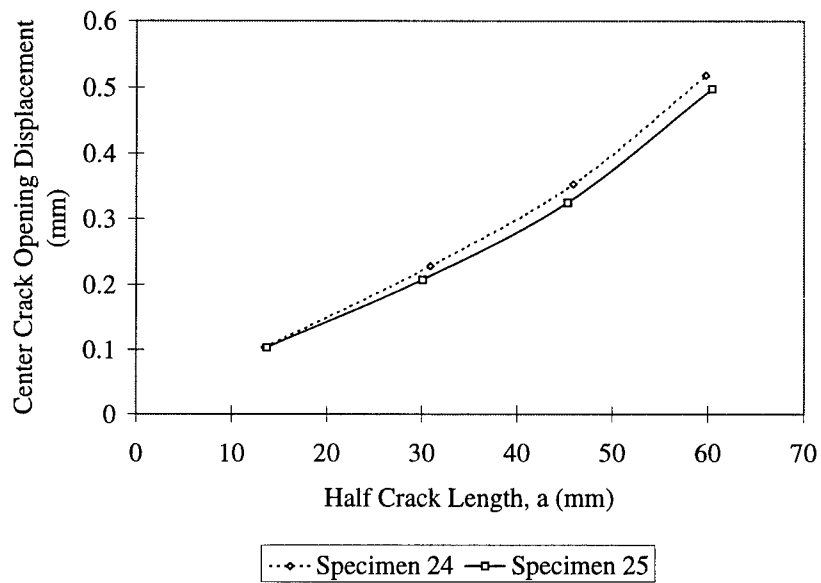


Figure 55. COD Comparison - 6.350 mm Plate, $S=1.3$, Full Width Repair, Patch Lengths: 51 mm-Specimen 24, 102 mm-Specimen 25

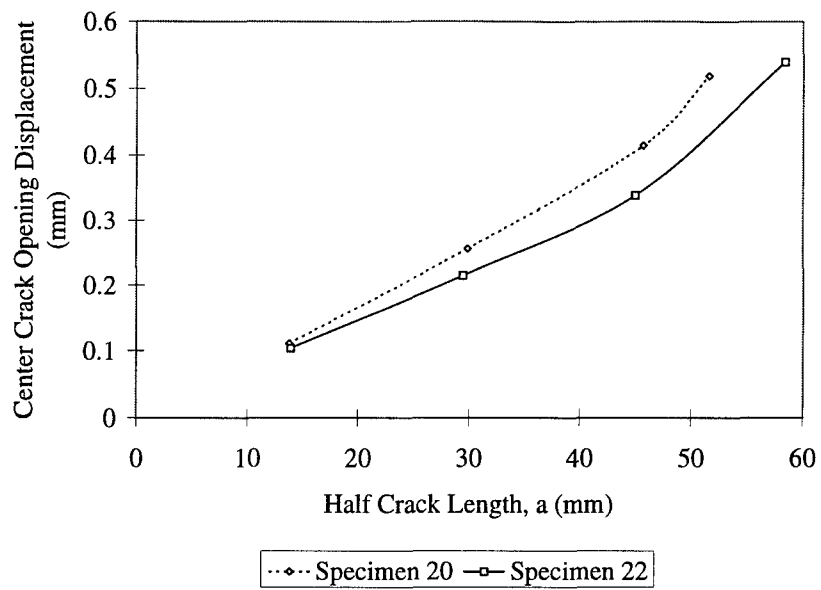


Figure 56. COD Comparison - 6.350 mm Plate, $S=1.0$, 50 mm Wide Repair, Patch Lengths: 51 mm-Specimen 20, 102 mm-Specimen 22

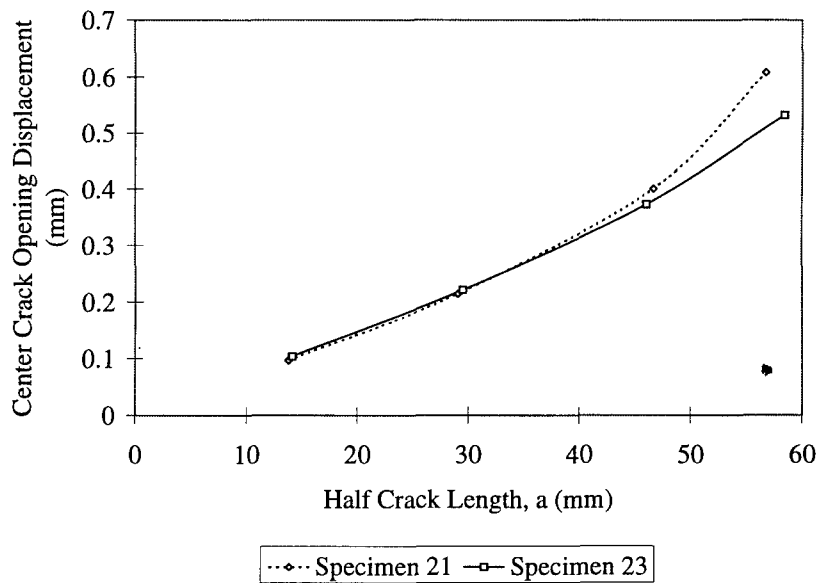


Figure 57. COD Comparison - 6.350 mm Plate, $S=1.3$, 50 mm Wide Repair, Patch Lengths: 51 mm-Specimen 21, 102 mm-Specimen 23

The COD measurements are, in general, a good indication of the specimens' bending during loading. Trends from examination of the CODs for differing patch lengths show a general trend that a larger COD is associated with the shorter patch. Longer patches tend to exhibit less bending during fatigue loading and therefore less crack opening displacement on the unpatched specimen face. Larger bending leads to higher stress intensity factors at the crack tips which, in turn, leads to higher crack growth and shorter fatigue lives. Therefore, the variation in COD with patch length is generally consistent with the previous discussion about the variation of crack growth rate and fatigue life with patch length. In the case of the thick plates, however, a longer patch tends to produce more thermally induced curvature which causes more compressive stresses on the unpatched face crack opening. These induced stresses may offset some tensile stresses during cycling, thus decreasing the magnitude of COD in thick plates with a longer patch.

4.4.4 Patched/Unpatched Face Crack Growth Rates

Figure 58 shows an example of the comparison of the crack lengths on the patched face (PF) obtained from the eddy current technique and the post-mortem examination of the specimen's fracture surface. As can be seen, the measurements taken with the eddy current technique correlated well with the post-mortem measurement of the patched face crack length on the fracture surface. This, as shown in Figure 58, allowed the verification and confidence in the measurements taken with the eddy current technique used in this study. For the thin specimens, eddy current measurements of the crack length on the patched face was the only available data. This was due to the fact that the fracture surface of the thin specimens rubbed or abraded during test and the crack front was indistinguishable on the post-test fracture surface.

Figures 59 through 66 show the lag which occurred between patched and unpatched face crack lengths during fatigue of several specimens. Portions of the curves which lack data for certain

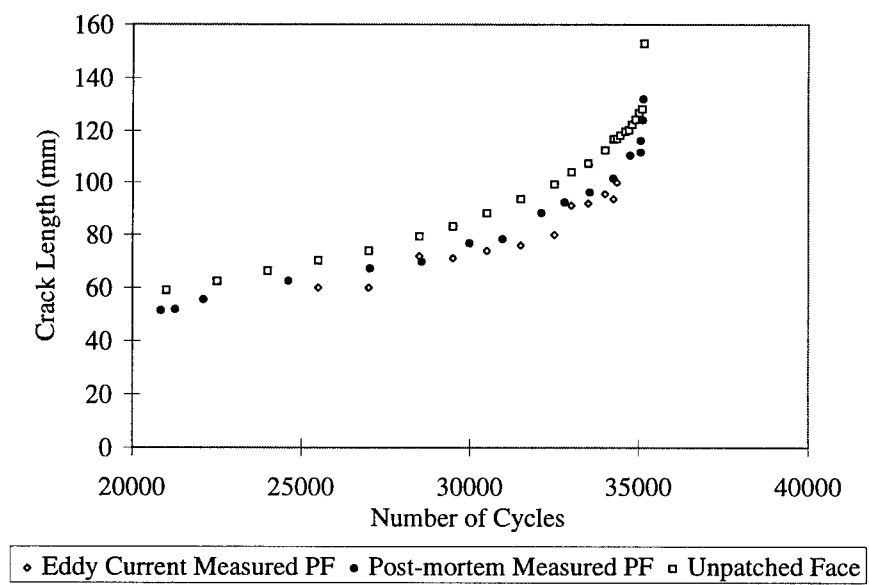


Figure 58. Comparison of Eddy Current and Post-Mortem Crack Length Measurements

crack lengths were due to strain gage placement which obscured readings from the eddy current technique. The location of strain gages applied to the specimens for surface strain measurements covered areas of the patch with instrumentation, making them unusable for measurements taken by the eddy current technique.

In summary, monitoring of the specimens' patched face crack growths, using the eddy current technique, showed a significantly greater crack growth lag between the patched and unpatched faces of the thicker specimens with short patches. This is also consistent with the crack growth rates and the amount of COD and bending observed. Maximum patched face crack length lag, for full width repairs, tends to occur near a crack length of 100 mm. This difference between patched and unpatched face crack lengths tends to stabilize or reduce slightly (patched face crack 'catching up') after this point during the tests. The thinnest plates, 3.175 mm, show a smaller difference in crack lag with the variation of patch lengths. This difference for the thin plates is, in general, on the order of 1-3 mm, as compared to a 10 mm difference for the thicker plates. The maximum lag is given in Table 16.

Table 16. Maximum Crack Length Lag between Patched and Unpatched Faces

Specimen #	Plate t (mm)	Patch L (mm)	Max Lag (mm)
7	6.350	102	13.241
9	6.350	51	23.282
18	3.175	102	6.333
19	3.175	51	7.253
16	4.826	102	7.896
17	4.826	51	6.036
24	6.350	51	21.520
25	6.350	102	11.597

4.5 Effects of Patch Stiffness Ratio

Tests were performed at different patch to panel stiffness ratios, S , to examine their effects on crack growth rates. The aim of this section was not to fully characterize the whole range of stiffness

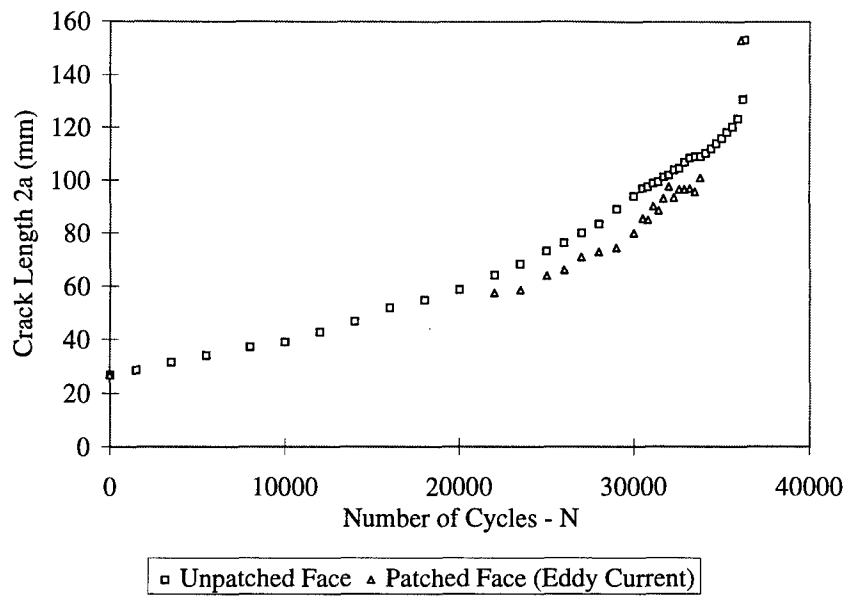


Figure 59. Patched vs. Unpatched Face Crack Lengths-Specimen 7: 6.350 mm Plate with 102 mm long, S=1.0, Full Width Patch

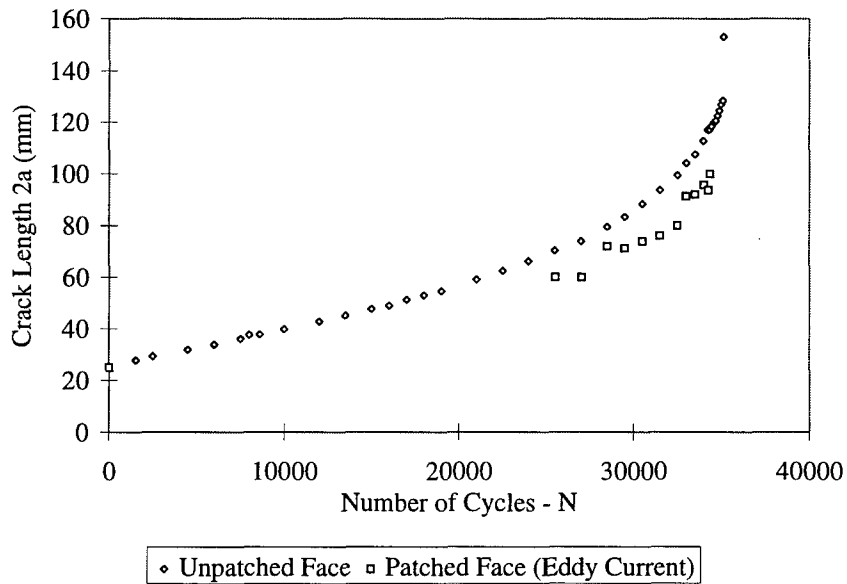


Figure 60. Patched vs. Unpatched Face Crack Lengths-Specimen 9: 6.350 mm Plate with 51 mm long, S=1.0, Full Width Patch

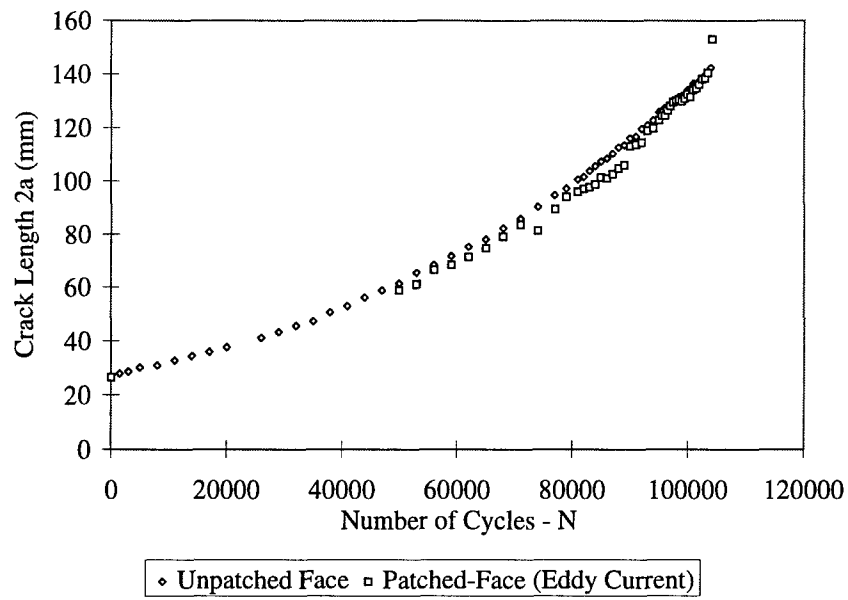


Figure 61. Patched vs. Unpatched Face Crack Lengths-Specimen 18: 3.175 mm Plate with 102 mm long, $S=1.0$, Full Width Patch

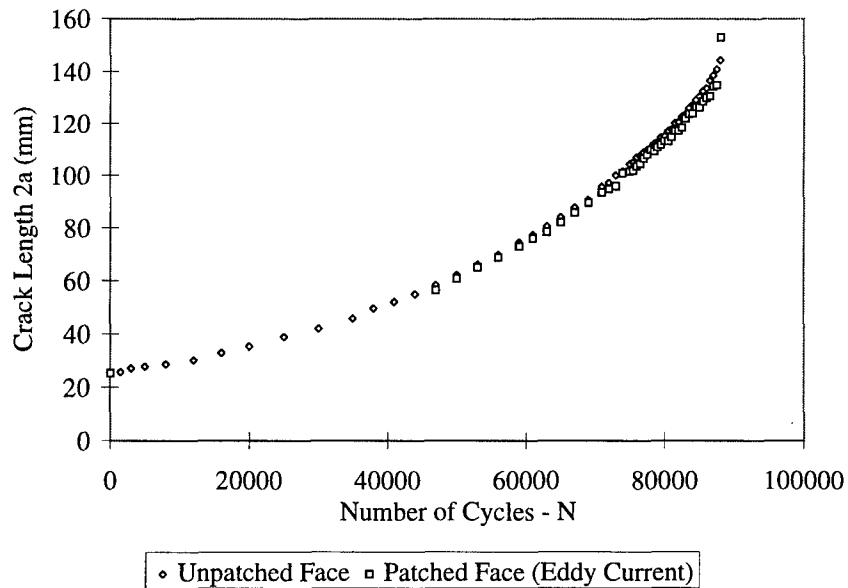


Figure 62. Patched vs. Unpatched Face Crack Lengths-Specimen 19: 3.175 mm Plate with 51 mm long, $S=1.0$, Full Width Patch

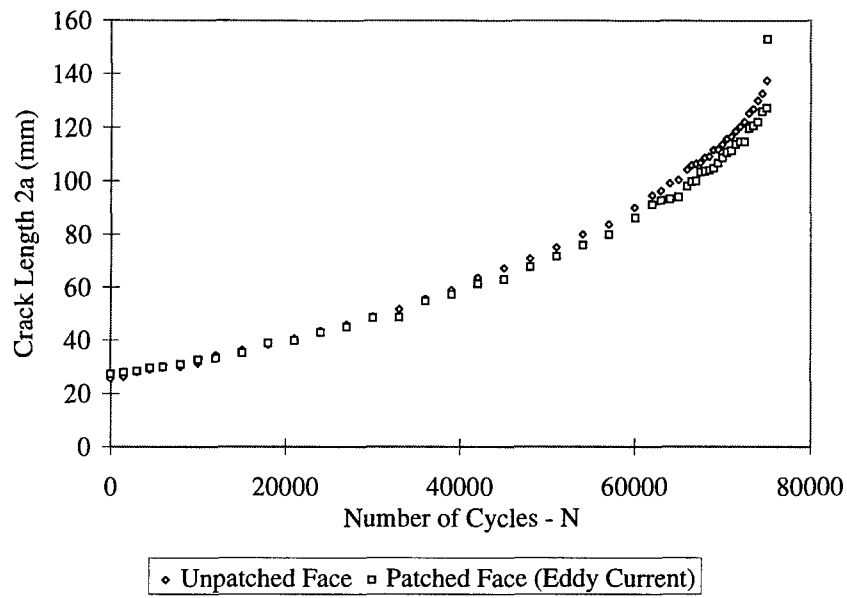


Figure 63. Patched vs. Unpatched Face Crack Lengths-Specimen 16: 4.826 mm Plate with 102 mm, S=1.0, Full Width Patch

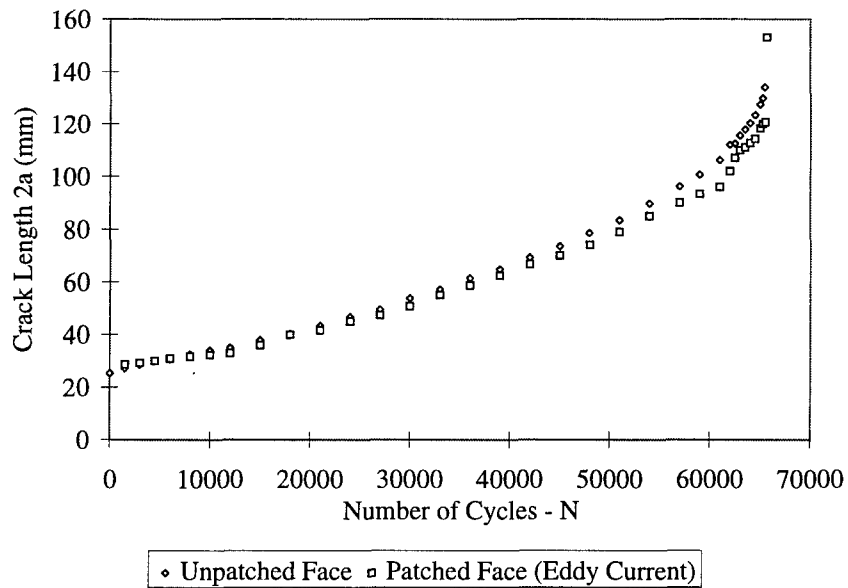


Figure 64. Patched vs. Unpatched Face Crack Lengths-Specimen 17: 4.826 mm Plate with 51 mm, S=1.0, Full Width Patch

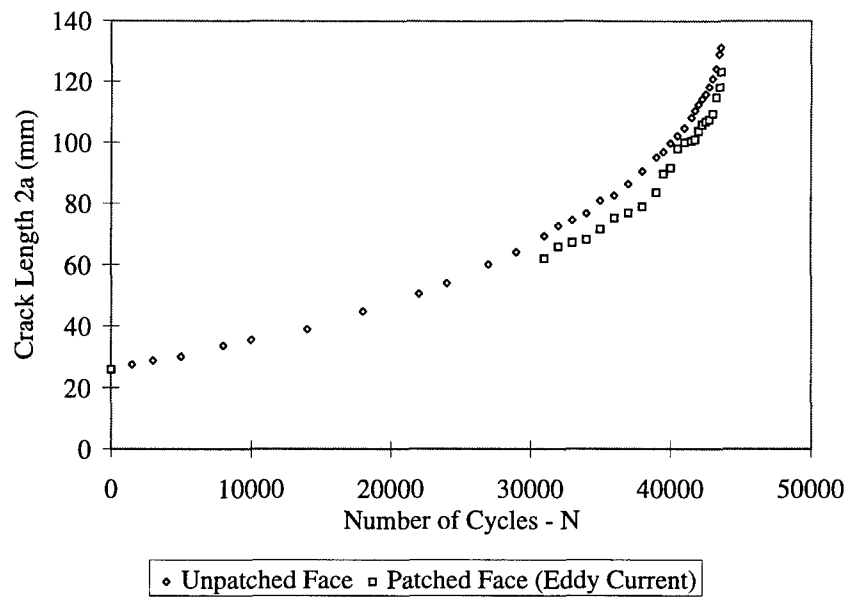


Figure 65. Patched vs. Unpatched Face Crack Lengths-Specimen 25: 6.350 mm Plate with 102 mm long, $S=1.3$, 50 mm wide Patch

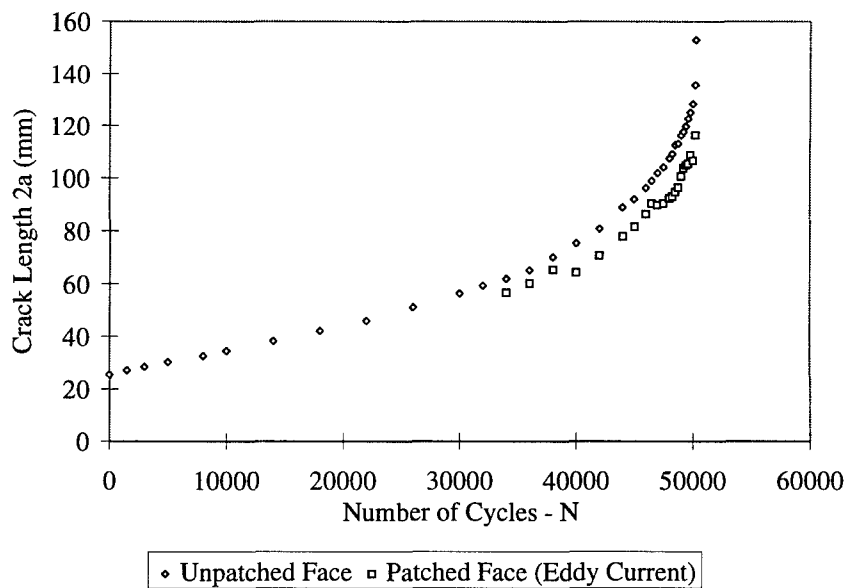


Figure 66. Patched vs. Unpatched Face Crack Lengths-Specimen 24: 6.350 mm Plate with 51 mm long, $S=1.3$, 50 mm wide Patch

ratios on post-repair crack growth, but to examine a few representative cases. Panels with 3.175 and 4.286 mm thickness were tested with patches of stiffness ratios $S=0.46$ and $S=0.69$, respectively, in addition to $S=1.0$. Tests were also conducted on 3.175 and 6.350 mm thickness panels with repairs of stiffness ratio $S=1.3$. A few of these cases have been discussed earlier while examining the effects of variations in patch length and width.

4.5.1 Initial Curvature

Table 13 compares the radii of curvature for all specimens. Figure 67 shows radii of curvature as a function of stiffness ratio. Stiffness ratio change from $S=1.0$ to $S=1.3$ for the 6.350 mm plates with long patches (102 mm) increased radius of curvature 9.7% above that of the $S=1.0$ repair. This comparison for the short patch repairs (51 mm) for the same stiffness change showed a 4.5% decrease in radius of curvature. It should be noted here that due to the bending direction, this decrease in radius results in the stresses on the unpatched face being more compressive.

Examining the results from 3.175 mm plate with $S=0.46$, 1.0, and 1.3, short (51 mm) repairs, it was seen that $S=0.46$ had a 7.7% smaller radius of curvature than the $S=1.0$ repair. The $S=1.3$ repair also had a smaller radius, 14.2% less than the $S=1.0$ repair. This limited data on the effect of patch stiffness ratio shows the possible existence of an optimized patch length which minimizes curvature for the short patch at or near $S=1.0$. If this is true for this configuration or others, a means to reduce the residual stresses might exist. The 4.826 mm panels were also examined with $S=0.69$ and $S=1.0$. Measurements showed the $S=0.69$ repair resulted in a 22.6% smaller radius of curvature than the $S=1.0$, 51 mm long repair. Long patch (102 mm) repairs on the 3.175 mm panels resulted in an 11% smaller radius for the $S=0.46$ specimen over that of the $S=1.0$ specimen. The $S=0.69$ repairs on the 4.826 mm plates showed a 12.8% larger radius than the $S=1.0$ specimen.

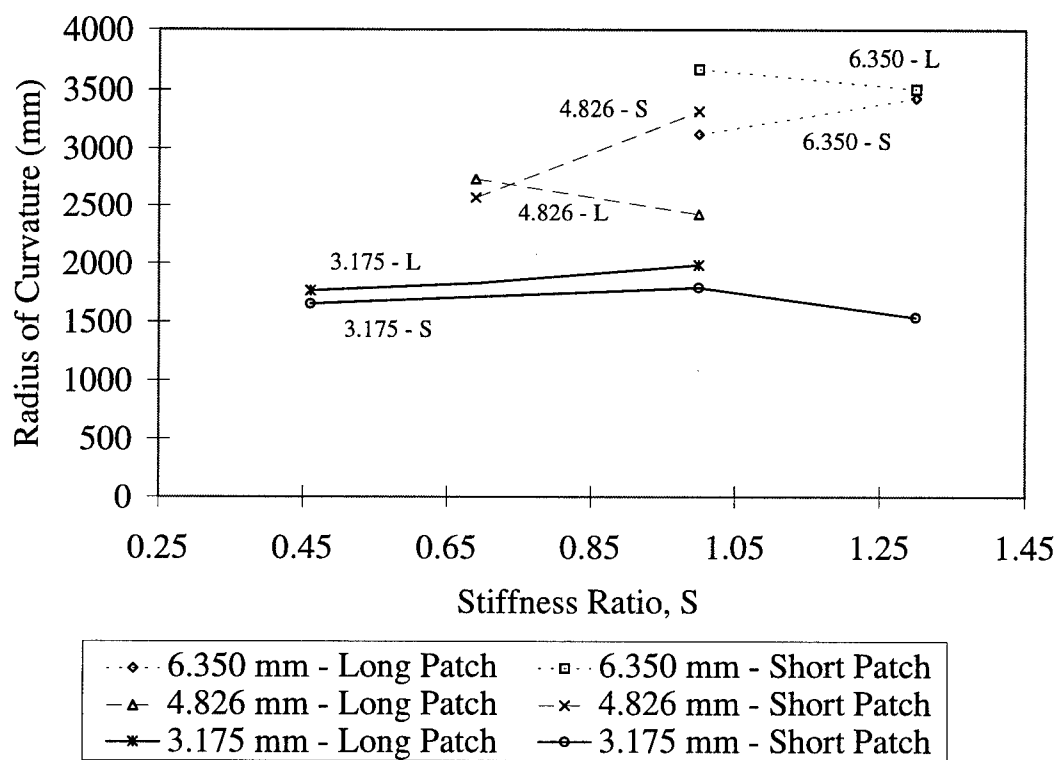


Figure 67. Radius of Curvature Dependence on Patch to Panel Stiffness Ratio

In summary, limited data was collected to investigate the effects of stiffness ratio on radius of curvature and this interrelationship is discussed above. More work, however, is required before any comprehensive trend can be established.

4.5.2 Crack Growth Rates

Figure 68 shows the comparison of crack growth rates in Specimens 7 and 25, i.e. 6.350 mm thick plates with $S=1.0$ and 1.3 and with 102 mm long repairs. The $S=1.3$ repair showed 20.8% increase in life-span over the $S=1.0$ case. Figure 69 compares the crack growth rates, da/dN , for these two specimens, and consistently slower growth was seen with $S=1.3$ repair than that with $S=1.0$ for cracks less than 100 mm long. For longer than a 100 mm crack, the $S=1.0$ repair results for growth rate fell below the $S=1.3$ repair rate, but, the $S=1.0$ rate was greater than the $S=1.3$ rate again before failure. The phenomenon of reduced crack growth rate after the crack grew beyond the $2a=100$ mm point, seen in the $S=1.0$ specimen's case, was not as prevalent in the $S=1.3$ specimen. The likely cause of these differences was a decreased debond rate and decreased plate plasticity (plastic zone growth) when incorporating the stiffer patch. The increased stiffness patch caused more consistent, stable crack growth without exhibiting the crack growth retardation as discussed in Section 4.8.

Examining the results of Specimens 9 and 24 in Figures 70 and 71, a 46.3% increase in life-span was observed with the application of a 51 mm, $S=1.3$, full width repair compared to that with the $S=1.0$ repair. Specimen 24 displayed a smaller initial radius of curvature and thus was likely to have relatively more initial compressive stresses on the unpatched face at the beginning of the test. The differences in initial crack growth rate between Specimens 9 and 24 (Figure 71) is consistently greater than that between Specimens 7 and 25 (Figure 69).

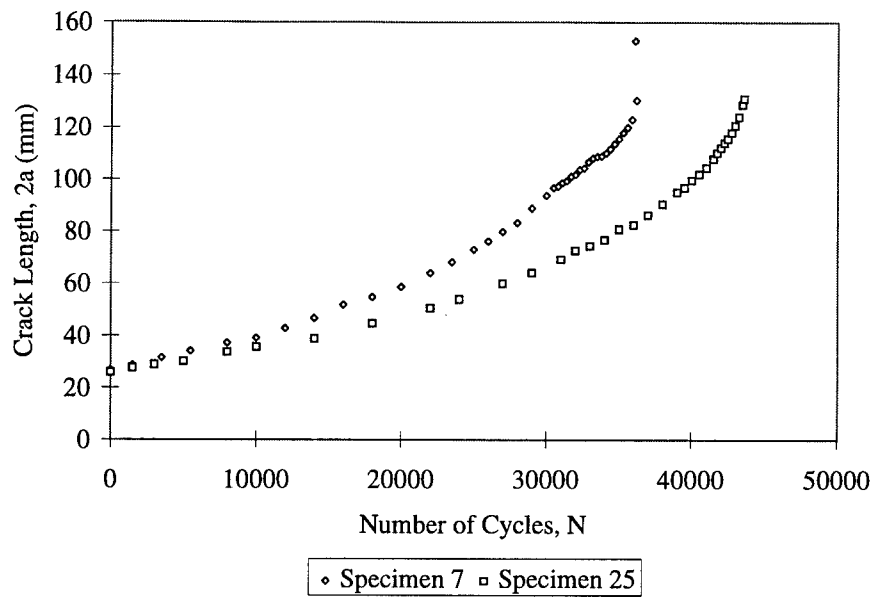


Figure 68. Crack Growth vs. Cycles Comparison - 6.350 mm Plate With 102 mm, Full Width Repair
- Stiffness Ratios: $S=1.0$ -Specimen 7, $S=1.3$ -Specimen 25

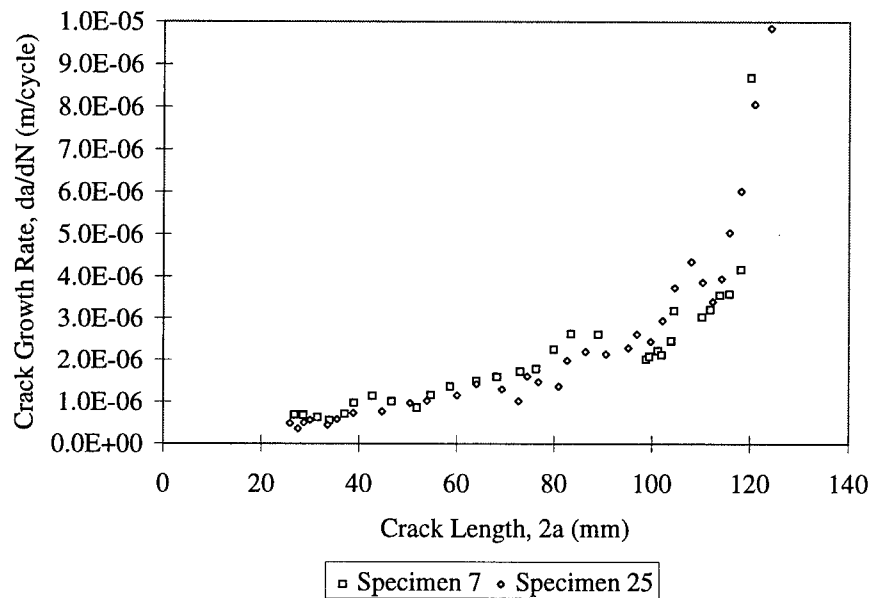


Figure 69. Crack Growth Rate, da/dN , Comparison, 6.350 mm Plate With 102 mm, Full Width Repair - Stiffness Ratios: $S=1.0$ -Specimen 7, $S=1.3$ -Specimen 25

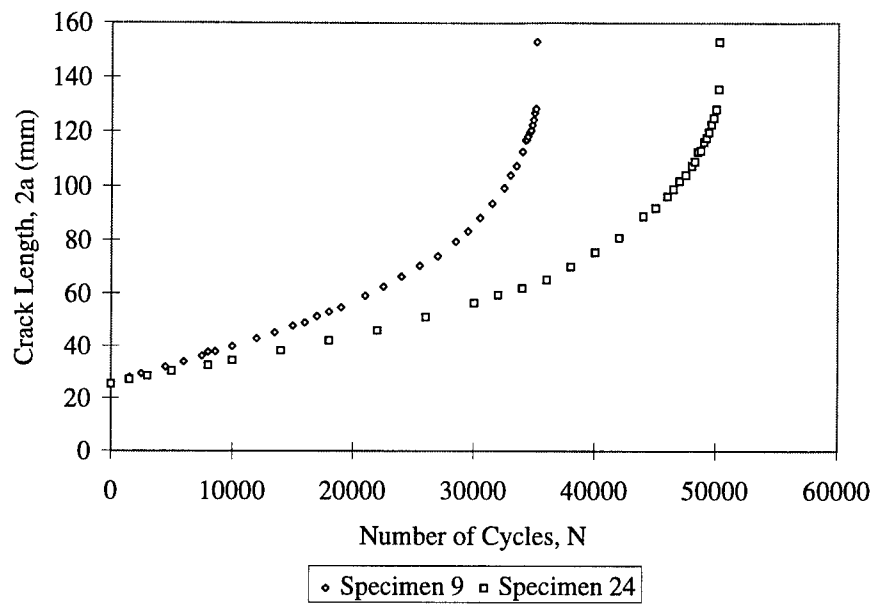


Figure 70. Crack Growth vs. Cycles Comparison - 6.350 mm Plate With 51 mm, Full Width Repair
- Stiffness Ratios: $S=1.0$ - Specimen 9, $S=1.3$ -Specimen 24

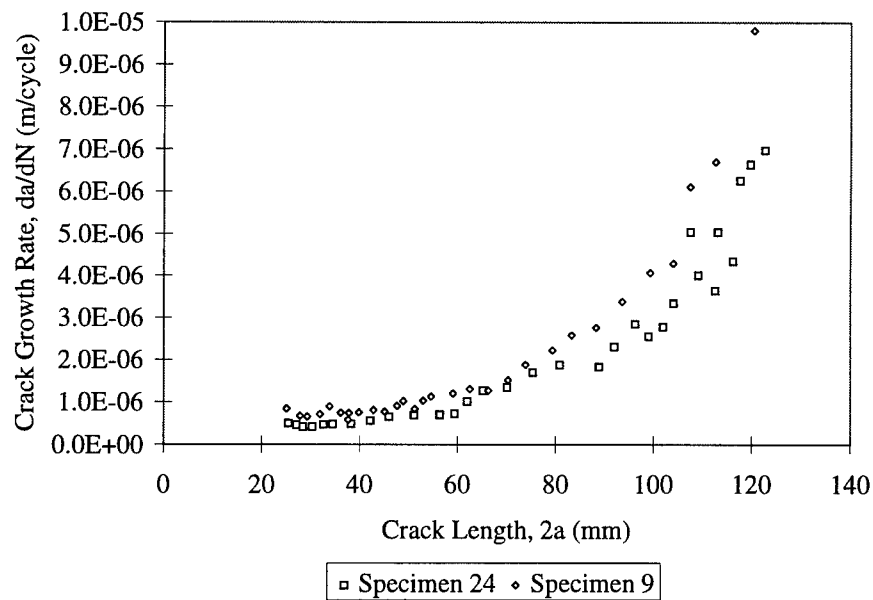


Figure 71. Crack Growth Rate, da/dN , Comparison, 6.350 mm Plate With 51 mm, Full Width Repair
- Stiffness Ratios: $S=1.0$ -Specimen 9, $S=1.3$ -Specimen 24

Figures 72 and 73 display the crack growth behavior for the range of $S=0.46$ to $S=1.3$ short (51 mm) repairs on the 3.175 mm plates. Life-span for the $S=1.3$ repair over that of the nominal $S=1.0$ repair, in Figure 72, exhibits an increase of 13.1% and a decrease of 26.5% for the $S=0.46$ repair case relative to that of $S=1.0$. The long patch repairs on the same thickness showed a 37.7% decrease in life-span for the $S=0.46$ case over that of the $S=1.0$ case. A smaller increase in life than what was seen for the thick plate, was seen with increased stiffness of the repairs on the 3.175 mm plates. The trend shown in Figure 73 shows increasing growth rate with decreasing stiffness ratio. The $S=0.46$ repair test displayed erratic crack growth behavior when reaching the unrepaired panel critical crack length of $2a=100$ mm.

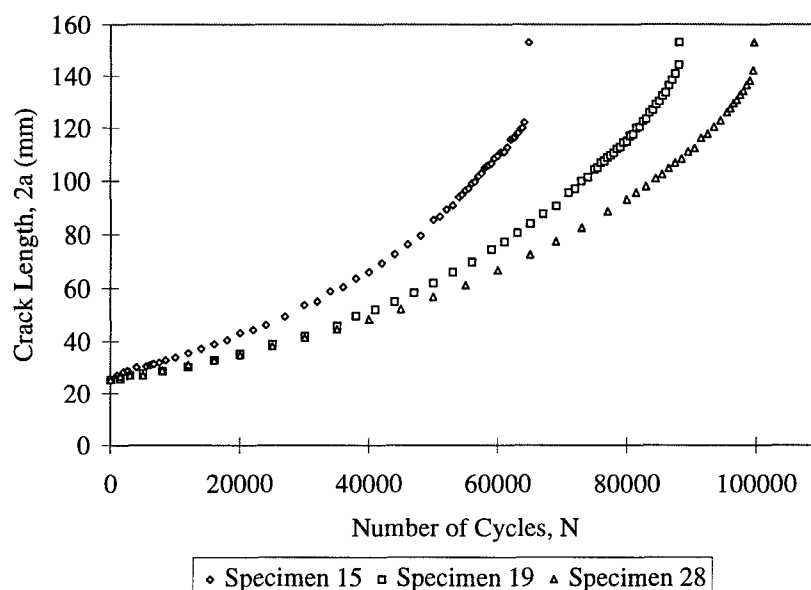


Figure 72. Crack Growth vs. Cycles Comparison - 3.175 mm Plate With 51 mm, Full Width Repair - Stiffness Ratios: $S=0.46$ -Specimen 15, $S=1.0$ -Specimen 19, $S=1.3$ -Specimen 28

A 24.3% decrease in life-span, due to a decrease in stiffness ratio, is shown by the comparison of Specimen 12, $S=0.69$, with Specimen 17, $S=1.0$, in Figure 74. Though not displayed, a similar decrease of 25.8% was seen for the long repair, i.e. Specimens 10 vs. 16. Figure 75 displays again

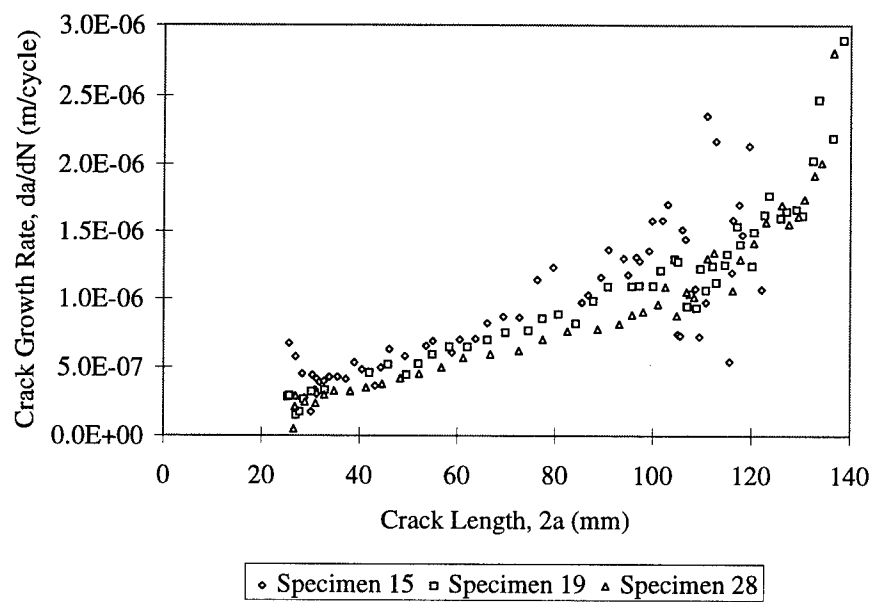


Figure 73. Crack Growth Rate, da/dN , Comparison, 3.175 mm Plate With 51 mm, Full Width Repair
 - Stiffness Ratios: $S=.46$ -Specimen 15, $S=1.0$ -Specimen 19, $S=1.3$ -Specimen 28

the erratic behavior of crack growth rate of the $S=1.0$ specimen after unrepaired panel critical crack length, $2a=100$ mm.

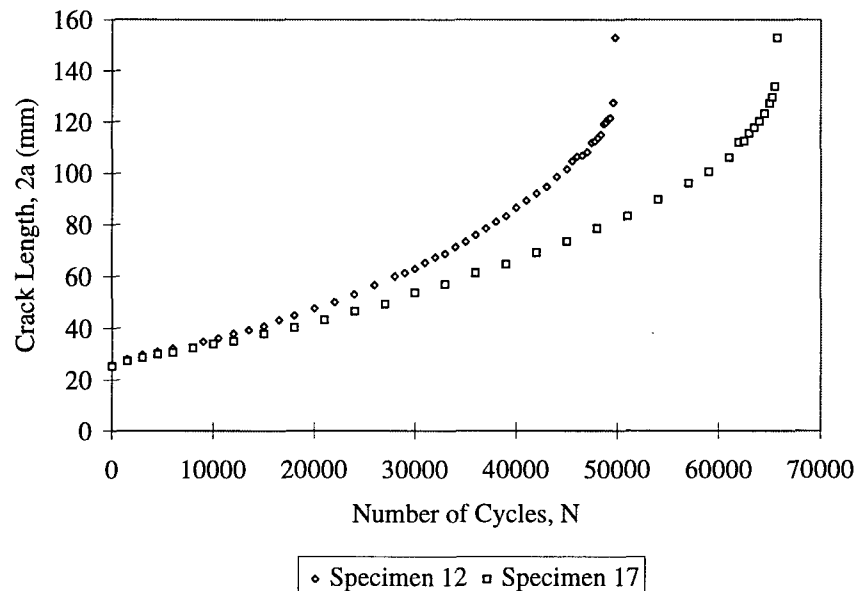


Figure 74. Crack Growth vs. Cycles Comparison - 4.826 mm Plate With 51 mm, Full Width Repair - Stiffness Ratios: $S=.69$ -Specimen 12, $S=1.0$ -Specimen 17

4.5.3 Crack Opening Displacement (COD)

This section discusses the effects of repair stiffness on the magnitude of crack opening displacement. Increased repair stiffness cases showed a generally linear relationship between COD and crack length. Although most of these relationships are relatively linear up to crack lengths of 90-100 mm, the $S=1.0$ repairs' COD diverged more from the linear relationship when crack length exceeded unrepaired plate critical crack length for 120 MPa applied load. This increasing non-linearity is caused by the increased bending, higher stress intensity factors at the crack tips, and is consistent with the higher growth rates associated with increasing disbond size when the crack is long.

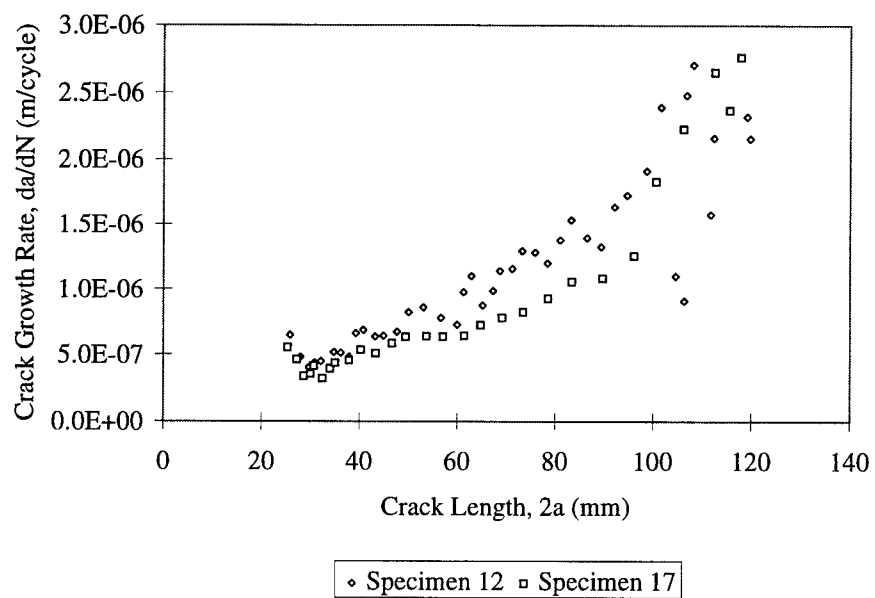


Figure 75. Crack Growth Rate, da/dN , Comparison, 4.826 mm Plate With 51 mm, Full Width Repair
 - Stiffness Ratios: $S=.69$ -Specimen 12, $S=1.0$ -Specimen 17

Figures 76 and 77 show comparisons of COD with stiffness ratio changes for the thick plate (6.350 mm). For the long repairs (102 long), the higher stiffness ratio gave only a nominal improvement (reduction) of COD at long crack lengths (Figure 76). Thus, this amount of stiffness change would only cause a small change in stresses induced by bending. For the short repair, increase in the stiffness ratio causes more reduction of the COD magnitude which results in a greater reduction of crack growth rate (Figure 77).

The COD for the 3.175 mm plates, repaired with $S=0.46$, $S=1.0$, and $S=1.3$ patches, are very similar until the crack reaches about $2a=100$ mm, Figure 78. However, the $S=1.3$ repair COD differs greatly from others beyond this point. Little difference was noted between the $S=1.0$ and $S=1.3$ CODs until the crack in the specimen grew beyond the unrepaired critical crack length (103 mm), but from that point, the $S=1.0$ and $S=0.46$ CODs diverge from the COD data for the $S=1.3$ repair. This large increase in COD with $S=0.46$ and 1.0 is supported by the crack growth data through erratic behavior. The stiff repair displays a reasonably smooth growth curve over the entire range of crack growth. The thinner repairs (i.e. smaller S) allow much greater bending and thus exhibit erratic crack growth rates which is most likely caused by simultaneous disbond and crack growth or plastic zone growth at the crack tips due to unstable crack progression. The 4.826 mm thickness panel displays similar trends as those by the 3.175 mm panel, as shown in Figure 79.

In summary, increase in stiffness ratio causes a reduction in COD and a reduction in bending especially with the thinner plates. The reduction in COD by changing $S=1.0$ to $S=1.3$ for thick plates (6.350 mm) is about 0.1 mm, whereas the reduction for the same increase in stiffness ratio for thin plates (3.175 mm) is about 0.2 mm.

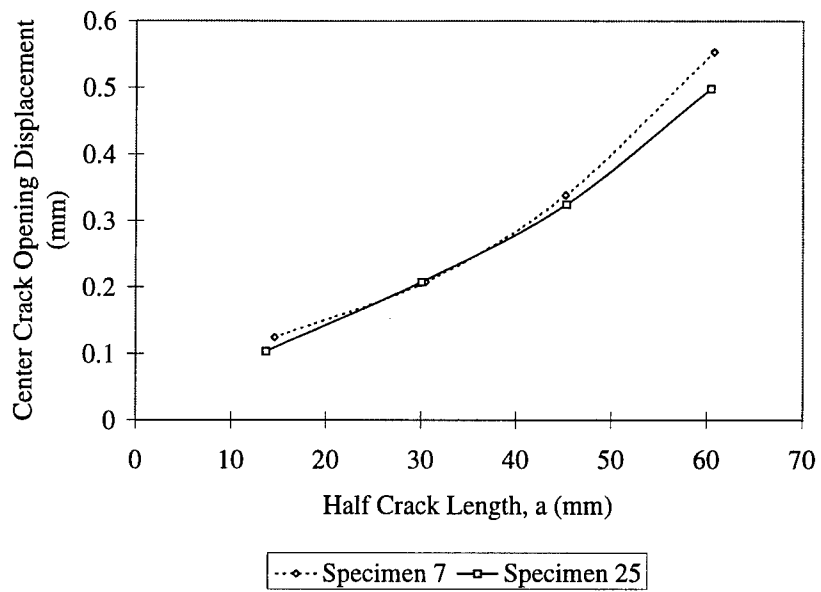


Figure 76. COD Comparison - 6.350 mm Plate, 102 mm Long, Full Width Repair, Stiffness Ratios: S=1.0-Specimen 7, S=1.3-Specimen 25

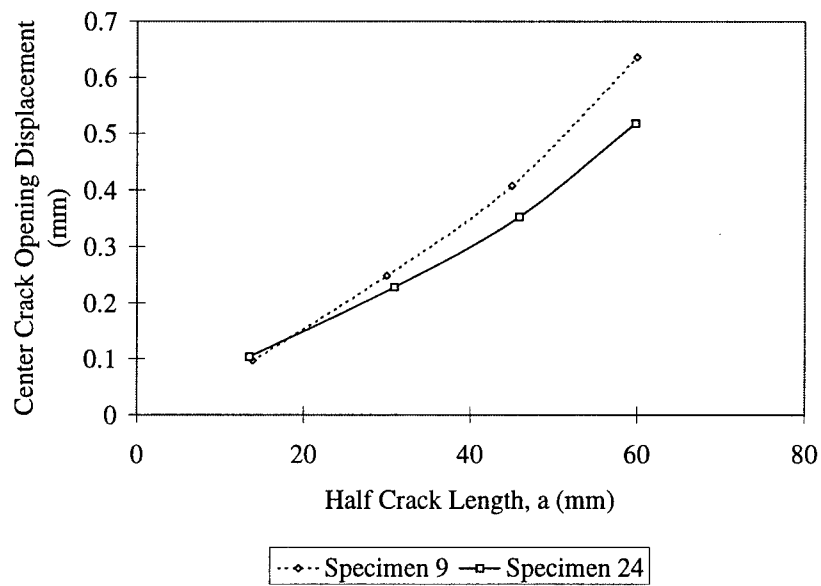


Figure 77. COD Comparison - 6.350 mm Plate, 51 mm Long, Full Width Repair, Stiffness Ratios: S=1.0-Specimen 9, S=1.3-Specimen 24

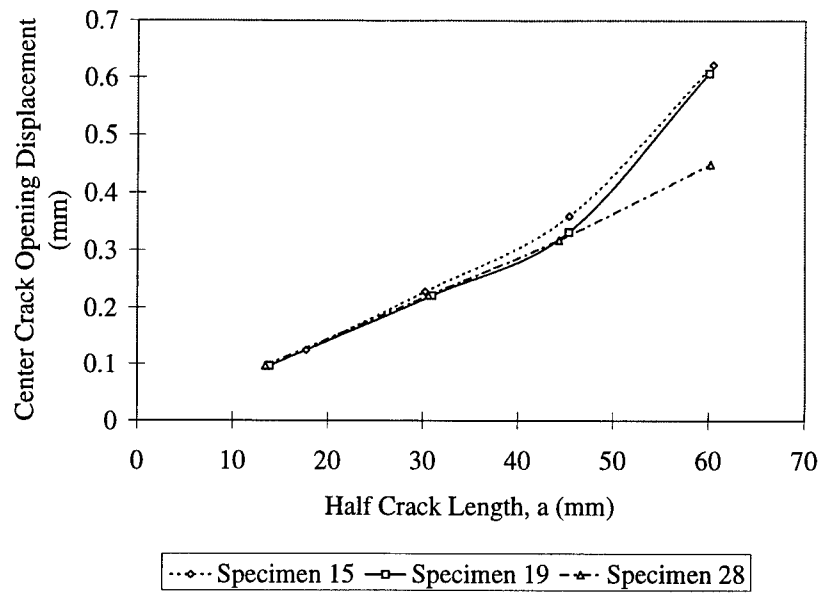


Figure 78. COD Comparison - 3.175 mm Plate, 51 mm Long, Full Width Repair, Stiffness Ratios: S=.46-Specimen 15, S=1.0-Specimen 19, S=1.3-Specimen 28

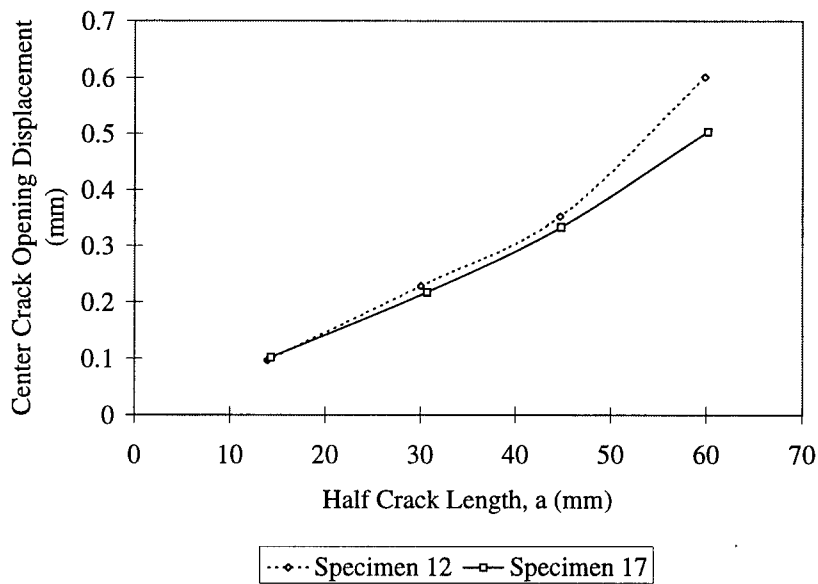


Figure 79. COD Comparison - 4.826 mm Plate, 51 mm Long, Full Width Repair, S=.69-Specimen 12, S=1.0-Specimen 17

4.5.4 Patched/Unpatched Face Crack Growth Rates

Increase in stiffness ratio for all specimens decreased the amount of lag in the crack growth between the unpatched and patched faces. This demonstrates, again, the decrease in bending under loading with increase in stiffness, and thus the stress intensity factor and crack growth rates decreased in these tests. Figures 80 to 82 show the crack length on the patched faces measured by the eddy current technique compared to the unpatched face crack length for the different specimens. Table 17 summarizes the effect of stiffness ratio on the maximum lag of patched face crack growth relative to the unpatched face. The most significant patched face crack lag difference, influenced by stiffness ratio, was observed in the thin (3.175 mm) plates when comparing stiffness ratio $S=1.0$ results to those of $S=0.46$.

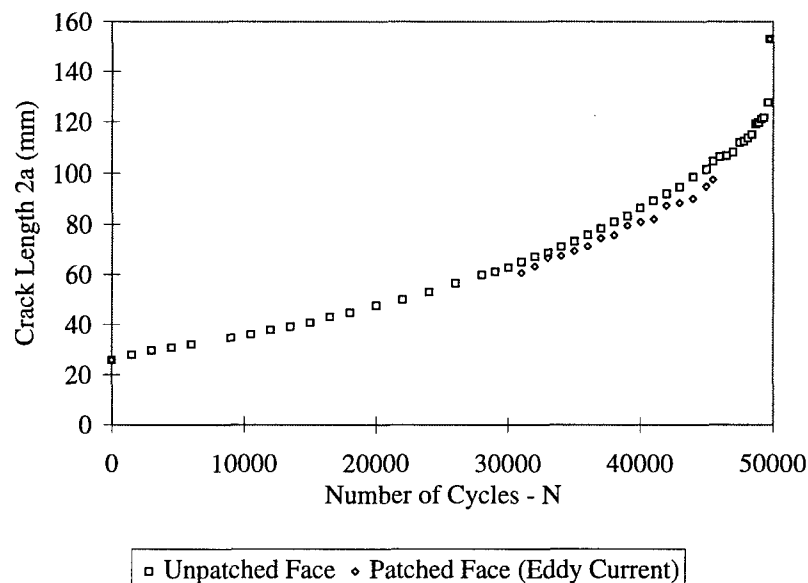


Figure 80. Patched vs. Unpatched Face Crack Lengths-Specimen 12: 4.826 mm Plate With $S=0.69$, 51 mm, Full Width Repair

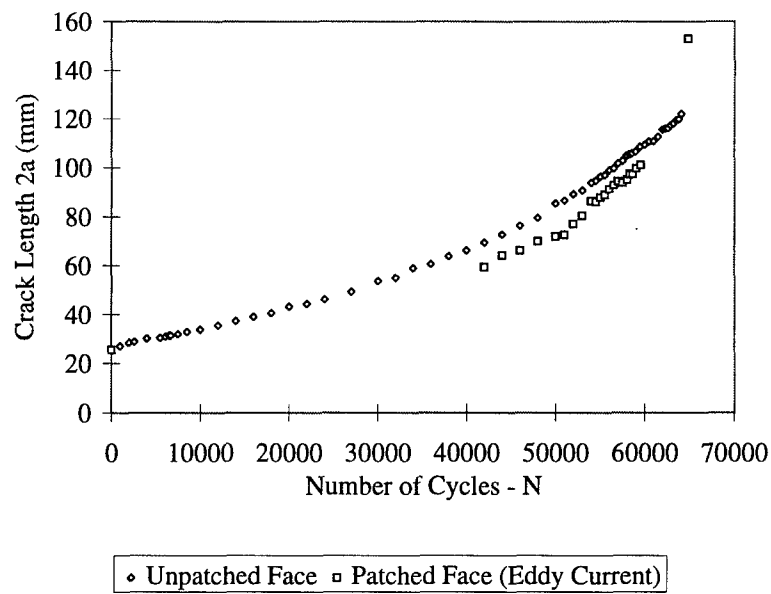


Figure 81. Patched vs. Unpatched Face Crack Lengths-Specimen 15: 3.175 mm Plate With $S=0.46$, 51 mm, Full Width Repair

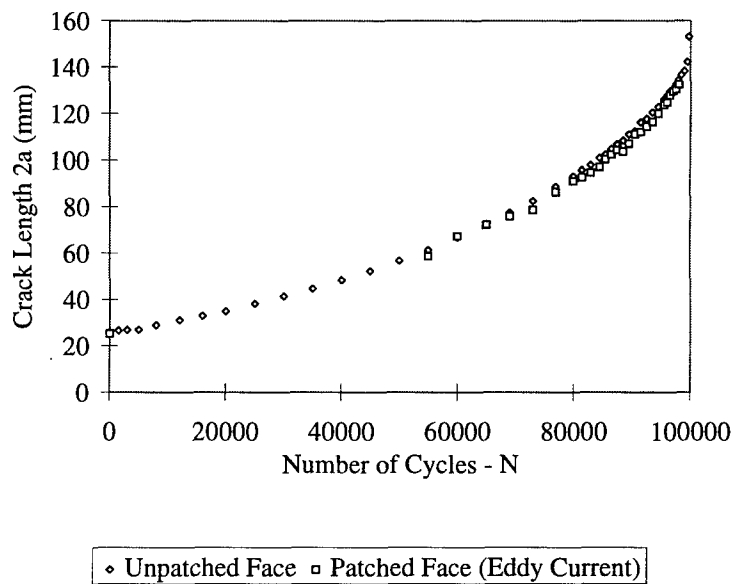


Figure 82. Patched vs. Unpatched Face Crack Lengths-Specimen 28: 3.175 mm Plate With $S=1.3$, 51 mm, Full Width Repair

Table 17. Maximum Patched-Face Crack Length Lag - Stiffness Ratio Comparison

Specimen #	Plate t (mm)	Stiffness Ratio, S	Patch L (mm)	Max Lag (mm)
7	6.350	1.0	102	13.241
25	6.350	1.3	102	11.597
9	6.350	1.0	51	23.282
24	6.350	1.3	51	21.520
15	3.175	0.46	51	14.136
19	3.175	1.0	51	6.036
28	3.175	1.3	51	4.532
12	4.826	0.69	51	7.282
17	4.826	1.0	51	7.253

Table 18 summarizes the effects of stiffness ratio on life-span of the repaired panels tested. Higher stiffness ratio patches showed consistently longer life-spans and decreased crack growth rates for each of the thicknesses and patch lengths examined.

Table 18. Percentage Change in Fatigue Life with Change in Patch to Panel Stiffness Ratio Relative to Stiffness Ratio $S=1.0$

Patch Characteristics	Plate Thickness (mm)		
	3.175	4.826	6.350
Length = 102 mm, $S=1.3$	-	-	20.8
Length = 51 mm, $S=1.3$	13.1	-	46.3
Length = 51 mm, $S=0.46$	(26.5)	-	-
Length = 102 mm, $S=0.46$	(37.7)	-	-
Length = 51 mm, $S=0.69$	-	(24.3)	-
Length = 102 mm, $S=0.69$	-	(25.8)	-

Note: () Denotes a decrease in fatigue life.

4.6 Effects of Patch Width

Cracked plates repaired with finite width patches, 50 mm wide (measured over the width of the patch where its thickness is uniform), were tested, and their results were compared with their counterparts from the full width (153 mm wide) patches. Also, two patch lengths, 51 and 102 mm long, were tested with 3.175 mm and 6.350 mm thickness plates to examine the effect of patch length on these narrower patches.

4.6.1 Initial Curvature

On examination of the effect of narrower patches on post-repair plate curvature, two trends were seen. First, for the long (102 mm), finite width (50 mm) patch on the thick plates (with $S=1.0$ and $S=1.3$), there was a increase of 5-15% in radius of curvature over the full width configuration, i.e. with the reduction in patch width. Second, with shorter and narrower patches, there was a consistent 10-20% decrease in radii for both the $S=1.0$ and $S=1.3$ repairs. Magnitudes of these changes were approximately two times, in the $S=1.0$ specimens, over those for the $S=1.3$ specimens.

The magnitude of the radius change in the 3.175 mm specimen with the narrower patch of $S=1.0$ is even smaller with approximately a 5% decrease in radius, but follows the same trend as the thicker panels. The highest stiffness, finite width patch, at $S=1.3$ on the 3.175 mm plate, resulted in a 24% increase in radius of curvature. In these finite width patch cases, the decreases seen in radius caused increased crack growth before the crack grew beyond the uniform thickness area of the patch. Increased radii, seen in the long repairs, caused the growth rates for these specimens to be less than their full width counterparts, as seen in the next section. This indicates that in the case of finite width repairs, minimizing thermal residual stresses and thus initial curvature by adjusting the length of the patch can reduce growth rates and extend specimen life. This is most likely due to the reduction in out-of plane bending associated with the straightening of the specimen during loading.

4.6.2 Crack Growth Rates

There are two ways to compare specimen life or crack growth rates when the results from the specimens with finite width patches are examined. First, crack growth results for the finite width patches must be compared to full width repair results up to the crack length equal to the width of the finite patch. Results from all finite width repairs, in this respect, showed that the crack growth rates were slightly less than those from their full width counterparts. This was due to the smaller amount of induced bending seen when bonding the smaller patches to the plates. Though crack growth rates were reduced within this area, rates were still similar to crack growth rates of the full width specimen tests. Secondly, crack growth behavior up to failure must be compared. These results are discussed in the following sections.

On comparing finite width patches with their full width counterparts on the thick (6.350 mm) plates, it was seen that the finite width patches with $S=1.3$ had shorter life-spans to failure than their full width counterparts for both long and short repairs. Figures 83 and 84 show 13.8% and

23.0% decreases in life-spans for the $S=1.3$, finite width repairs, on the thick plates relative to full width repairs. Further, crack growth rates for these finite width repairs were consistently equal to or slightly less than their counterparts for the full width repairs when within the uniform thickness area of the patch. But, once the crack progresses into the patch taper, the crack growth rates for the finite width patch quickly increased beyond the full width patch specimen crack growth rates, as should be expected. Figures 85 and 86 display these rate curves for comparison.

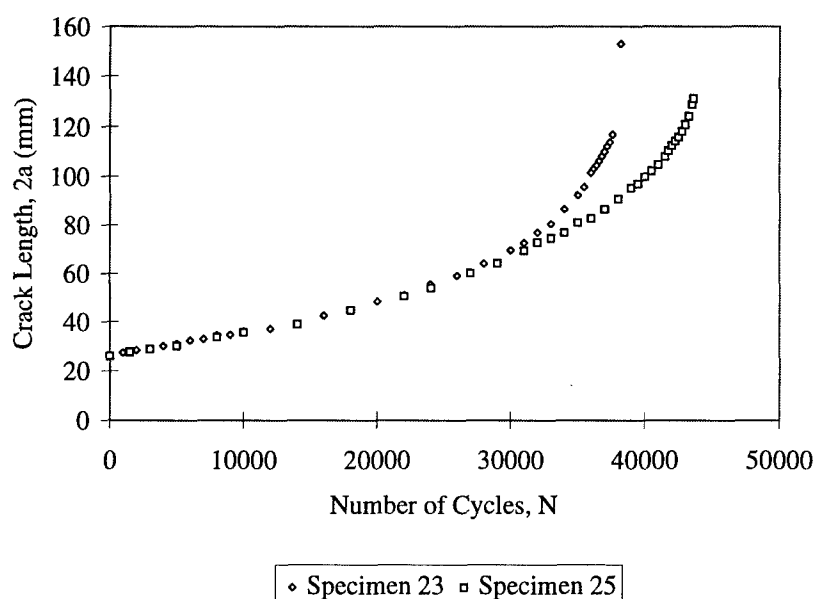


Figure 83. Crack Growth vs. Cycles Comparison - 6.350 mm Plate With $S=1.3$, 102 mm Long Repair - Patch Widths: 50 mm-Specimen 23, Full Width-Specimen 25

Figures 87 and 88 display the results of the $S=1.0$ repairs on Specimens 22 (6.350 mm thick and 102 mm long, 50 mm wide repair) and 20 (6.350 mm thick and 51 mm long, 50 mm wide repair) compared to their full width repair counterparts. In contrast to the previous $S=1.3$ repairs, the $S=1.0$ finite width repairs' life-spans equaled or exceeded that of the full width repairs. A 9.7% increase and only a 1.0% decrease in life-span to failure was observed in the results for Specimens 22 and 20, respectively, over the full width test results. Figures 89 and 90 show the crack growth

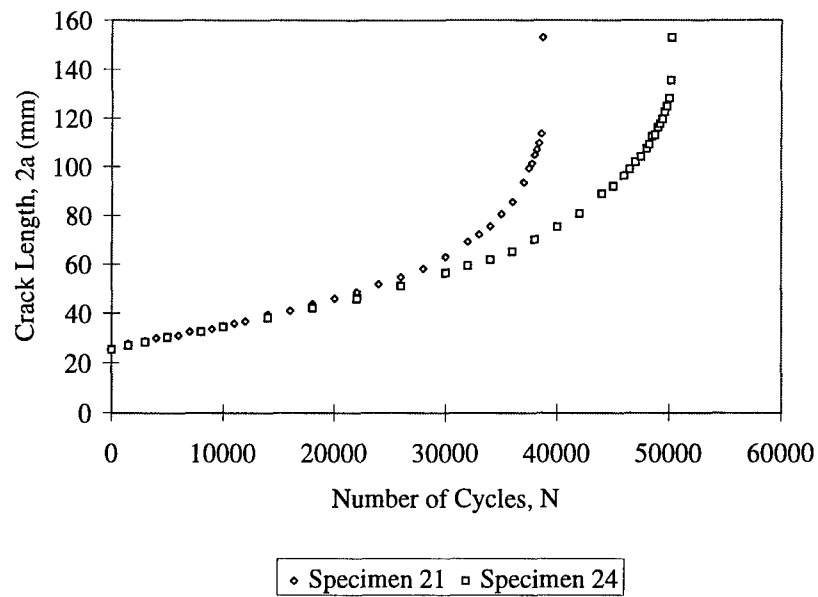


Figure 84. Crack Growth vs. Cycles Comparison - 6.350 mm Plate With $S=1.3$, 51 mm Long Repair - Patch Widths: 50 mm-Specimen 21, Full Width-Specimen 24

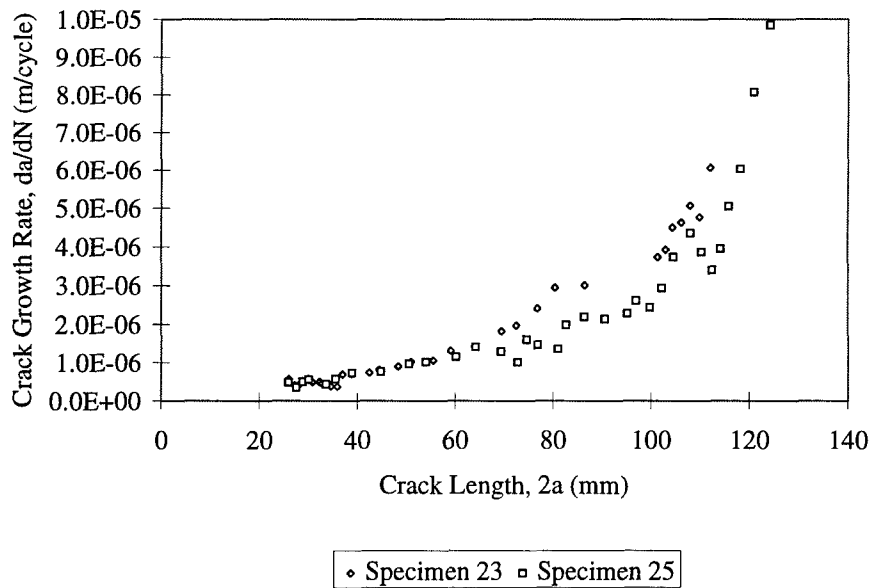


Figure 85. Crack Growth Rate, da/dN , Comparison, 6.350 mm Plate With $S=1.3$, 102 mm Long Repair - Patch Widths: 50 mm-Specimen 23, Full Width-Specimen 25

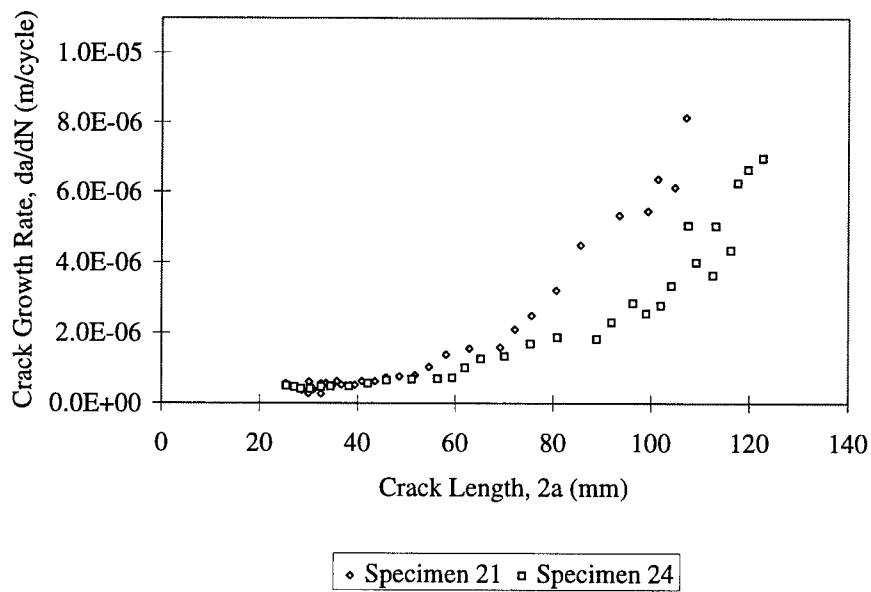


Figure 86. Crack Growth Rate, da/dN , Comparison, 6.350 mm Plate With $S=1.3$, 51 mm Long Repair - Patch Widths: 50 mm-Specimen 21, Full Width-Specimen 24

rate in these specimens which is lower in the finite width patch than in the full width patch in the early stages of crack growth. As the crack progresses beyond the uniform patch thickness area and taper section, finite width growth rate quickly increases to greater than that of the full width repair. Thus, a lower crack growth rate was seen for the $S=1.0$, finite width repairs on thick plates before the crack grows beyond the uniform patch thickness area. Then retardation of crack growth rate was seen due to overloads on the unpatched face crack which provided this increased life-span to failure of the finite width repair exceeding that of the full width patched specimens. On the other hand, for repairs on the 6.350 mm thick plates, with $S=1.3$, full width repairs exhibit significantly longer life-spans than finite width patches.

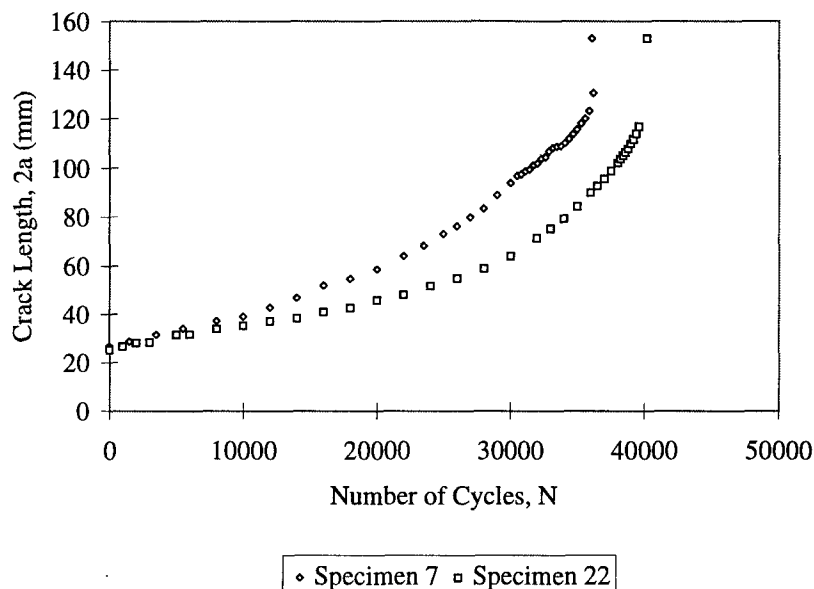


Figure 87. Crack Growth vs. Cycles Comparison - 6.350 mm Plate With $S=1.0$, 102 mm Long Repair - Patch Widths: 50 mm-Specimen 22, Full Width-Specimen 7

Crack length versus fatigue cycles relationships for the finite width patches, on 3.175 mm specimens, shown in Figures 91 and 92, were approximately the same as those in the full width patch test results, when compared within the uniform patch thickness area. Comparisons of the

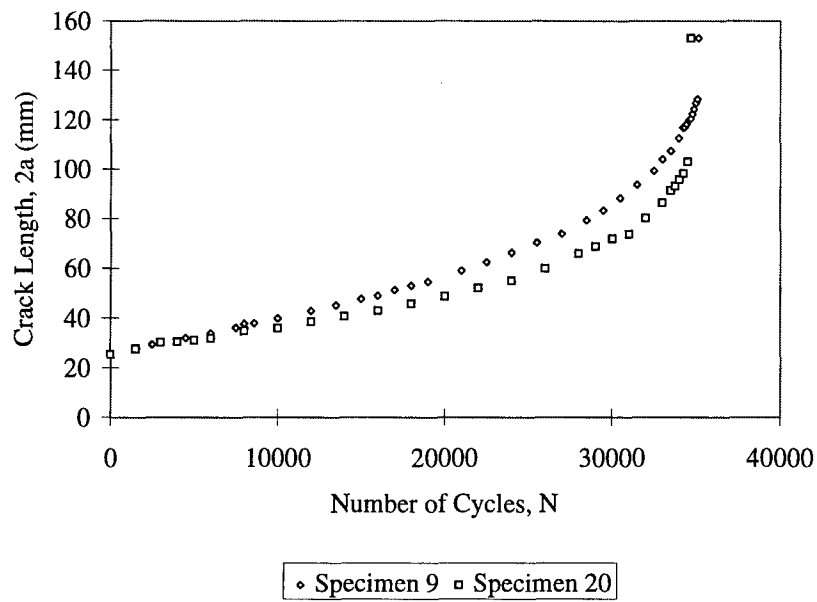


Figure 88. Crack Growth vs. Cycles Comparison - 6.350 mm Plate With $S=1.0$, 51 mm Long Repair - Patch Widths: 50 mm-Specimen 20, Full Width-Specimen 9

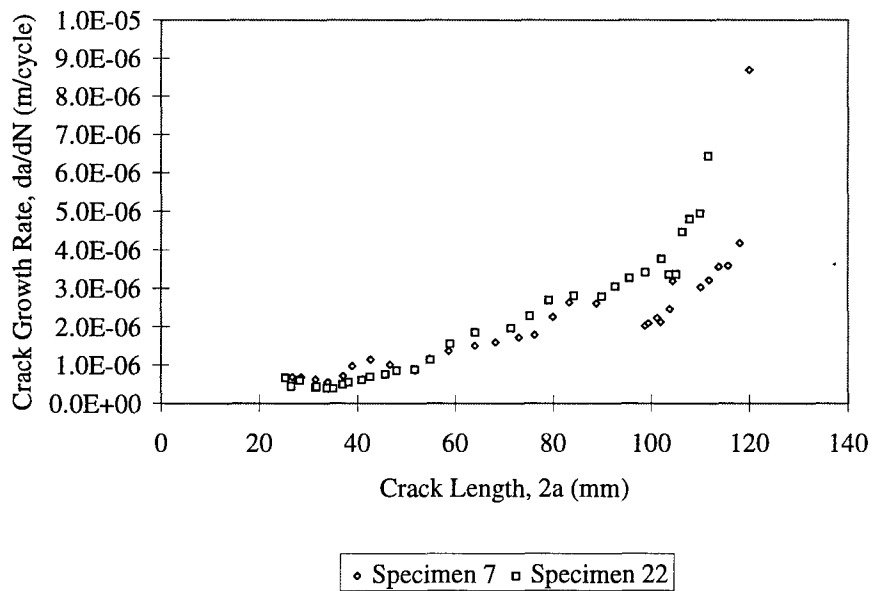


Figure 89. Crack Growth Rate, da/dN , Comparison, 6.350 mm Plate With $S=1.0$, 102 mm Long Repair - Patch Widths: 50 mm-Specimen 22, Full Width-Specimen 7

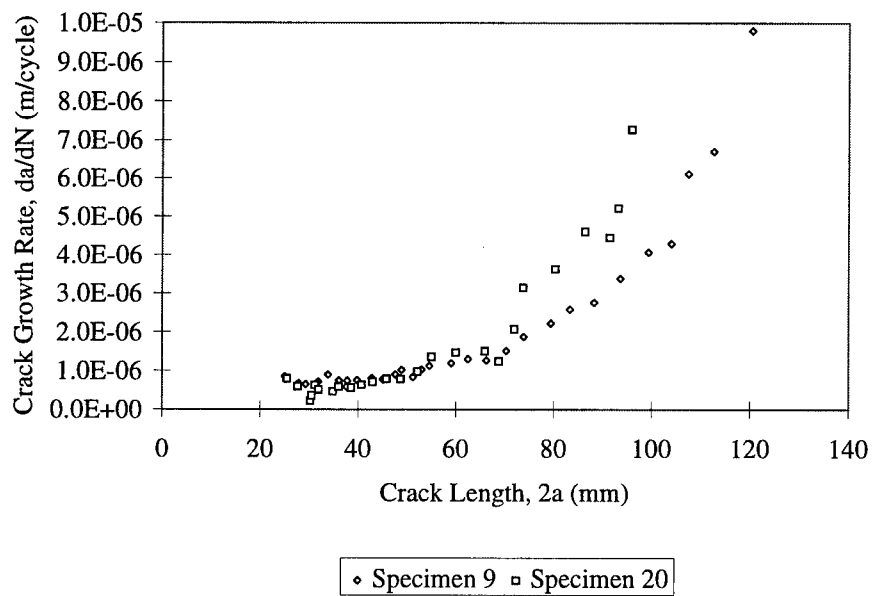


Figure 90. Crack Growth Rate, da/dN , Comparison, 6.350 mm Plate With $S=1.0$, 51 mm Long Repair - Patch Widths: 50 mm-Specimen 20, Full Width-Specimen 9

cycles to failure with full width patch counterparts show that the finite width patch specimens have shorter life-spans for all cases. Further, the crack growth rates for the repaired 3.175 mm plates, shown in Figures 93 and 94, are essentially equal between full width and finite width repairs while the crack is within the uniform patch thickness area, and the rates for the finite width patches tend to increase dramatically once the crack has progressed beyond this area.

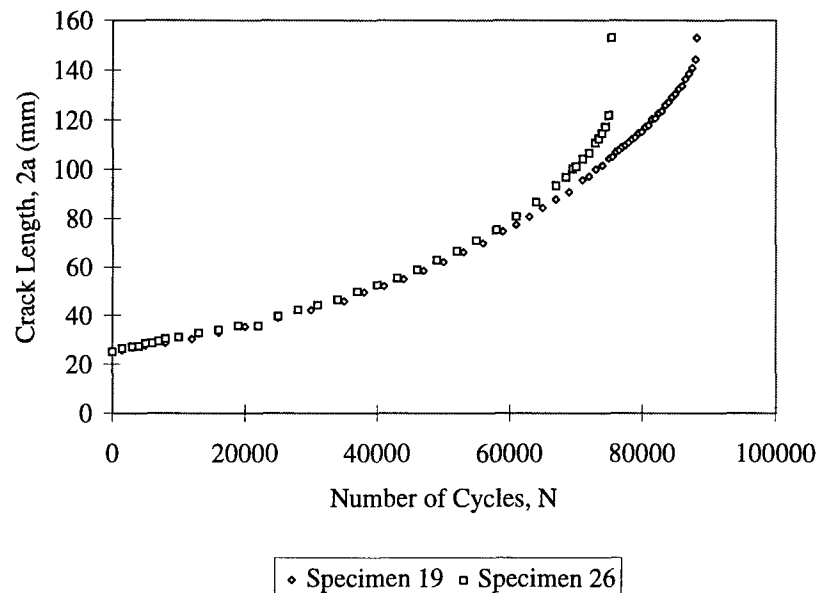


Figure 91. Crack Growth vs. Cycles Comparison - 3.175 mm Plate with $S=1.0$, 51 mm Long Repair - Patch Widths: 50 mm-Specimen 26, Full Width-Specimen 19

Summarizing this section, it was shown that reduction in patch width, in general, decreases specimen life-span to failure due to rapid increases in crack growth rate after the crack grows beyond the patch. Further, it was also seen that within the uniform thickness area of the patches, growth rates for cracks repaired with the finite width patches grew at an equivalent rate, or slightly slower, than the cracks in thick plates repaired with full width patches. Table 19 summarizes life-span changes due to change in patch width.

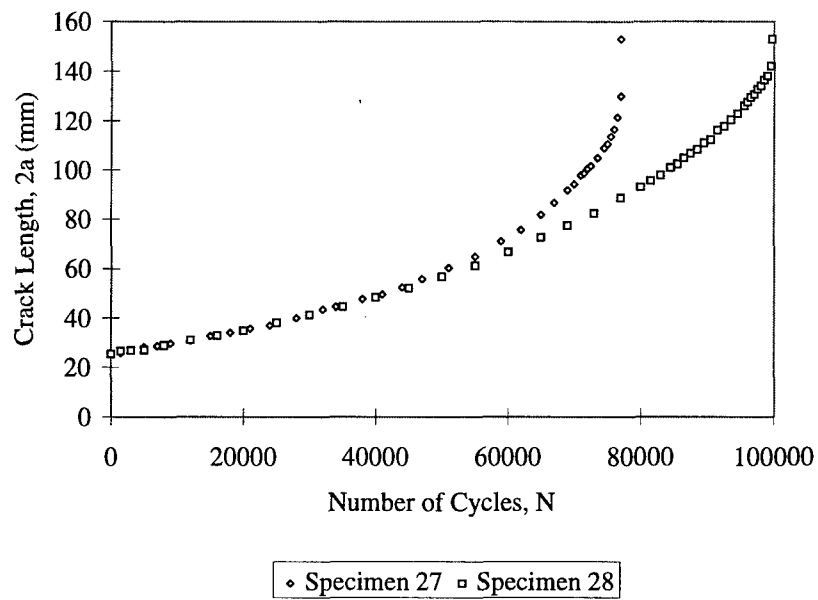


Figure 92. Crack Growth vs. Cycles Comparison - 3.175 mm Plate With $S=1.3$, 51 mm Long Repair - Patch Widths: 50 mm-Specimen 27, Full Width-Specimen 28

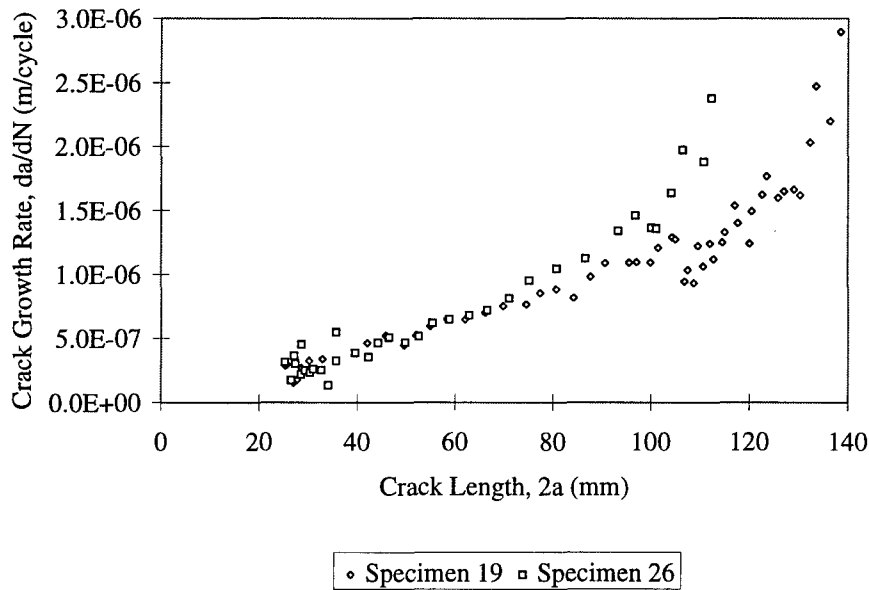


Figure 93. Crack Growth Rate, da/dN , Comparison, 3.175 mm Plate With $S=1.0$, 51 mm Long Repair - Patch Widths: 50 mm-Specimen 26, Full Width-Specimen 19

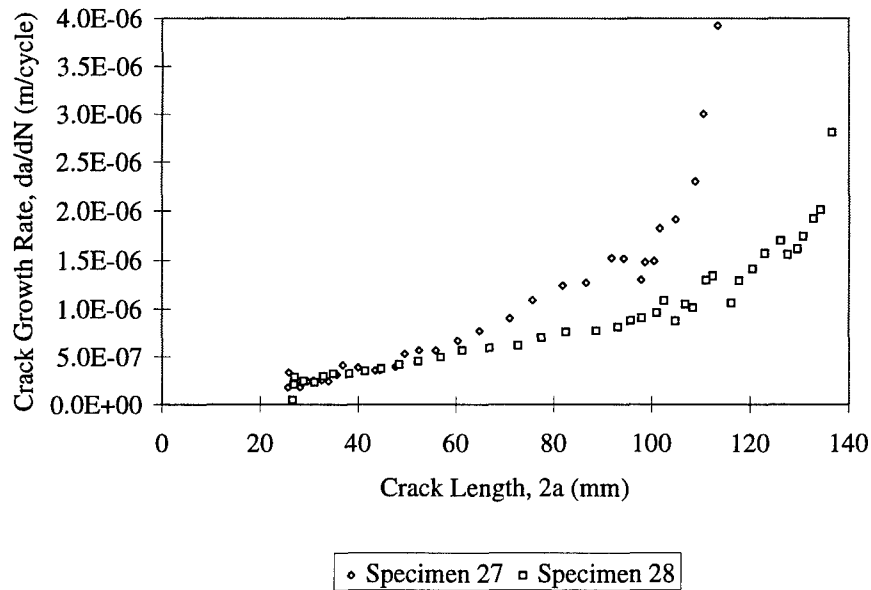


Figure 94. Crack Growth Rate, da/dN , Comparison, 3.175 mm Plate With $S=1.3$, 51 mm Long Repair - Patch Widths: 50 mm-Specimen 27, Full Width-Specimen 28

Table 19. Percentage Change in Fatigue Life with Reduction in Patch Width from 153 mm to 50 mm

Patch Characteristics	Plate Thickness (mm)	
	3.175	6.350
Length = 102 mm, $S=1.0$	-	9.7
Length = 51 mm, $S=1.0$	(14.6)	(1.0)
Length = 102 mm, $S=1.3$	-	(13.8)
Length = 51 mm, $S=1.3$	(22.7)	(23.0)

4.6.3 Crack Opening Displacement

Crack opening displacement (COD) for the $S=1.3$ specimens, shown in Figures 95 and 96, are higher for finite width patches than for the full width repairs. Specimens repaired with short (51 mm long) patches have a much faster increase in COD in the later stages of cycling. This is the result of the high percentage of area in the short patches which has debonded from the specimen. The increased amount of bending associated with the disbond causes increased compliance of the specimen and in turn more bending due to the asymmetry of the repair. Crack opening displacements for the $S=1.0$ finite width repairs did not differ significantly from their corresponding full width repairs, demonstrating that there is only a small difference in the bending due to changes in patch width in these specimens. Increased material, due to a more stiff patch, may account for the greater reduction in COD for $S=1.3$ repairs. The change from a full width $S=1.3$ stiffness patch to a finite width patch of the same stiffness creates a larger increase in compliance of the specimen, especially outside the finite width patch area, than a similar change in specimens with $S=1.0$ repairs. Figures 97 and 98 illustrate these minor differences.

Figures 99 and 100 present the COD data for finite width repairs on 3.175 mm plates. As would be expected from the above cases, the $S=1.3$ finite width repair COD diverges faster from its full width counterpart's results than the $S=1.0$ finite width repair. For the $S=1.0$ patch case, it was seen that the curves track closely to one another until the crack length exceeded $2a=100$ mm long. When the crack length reached this point, the full width patch COD actually opens to a greater value than the finite width patch repaired specimen. This increase in COD for the full width specimen is an indicator of the increased bending associated with the larger patch at long crack lengths.

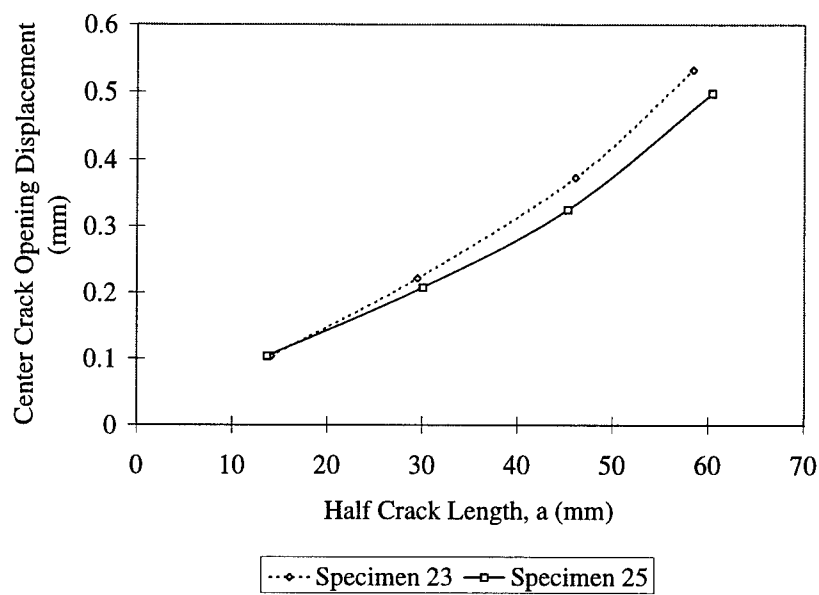


Figure 95. COD Comparison - 6.350 mm Plate, S=1.3, 102 mm Long Repair, Patch Widths: 50 mm-Specimen 23, Full Width-Specimen 25

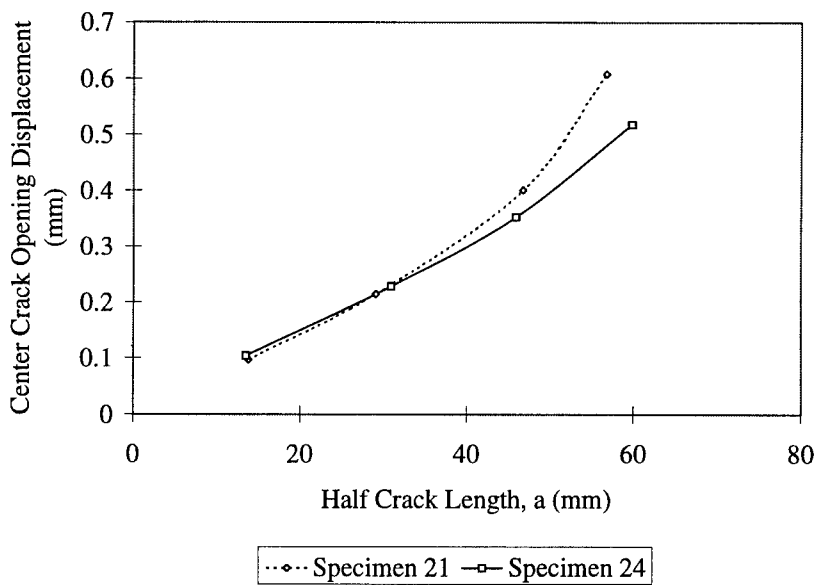


Figure 96. COD Comparison - 6.350 mm Plate, S=1.3, 51 mm Long Repair, Patch Widths: 50 mm-Specimen 21, Full Width-Specimen 24

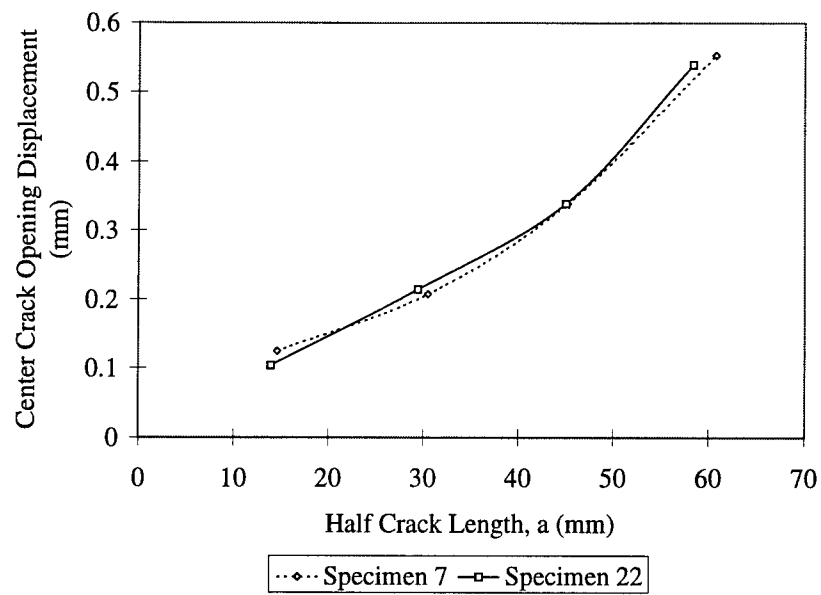


Figure 97. COD Comparison - 6.350 mm Plate, $S=1.0$, 102 mm Long Repair, Patch Widths: Full Width-Specimen 7, 50 mm-Specimen 22

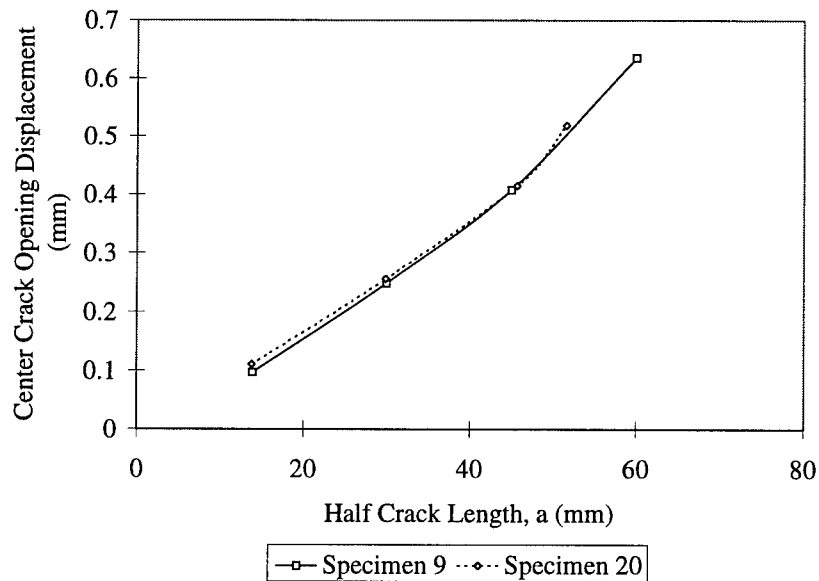


Figure 98. COD Comparison - 6.350 mm Plate, $S=1.0$, 51 mm Long Repair, Patch Widths: Full Width-Specimen 9, 50 mm-Specimen 20

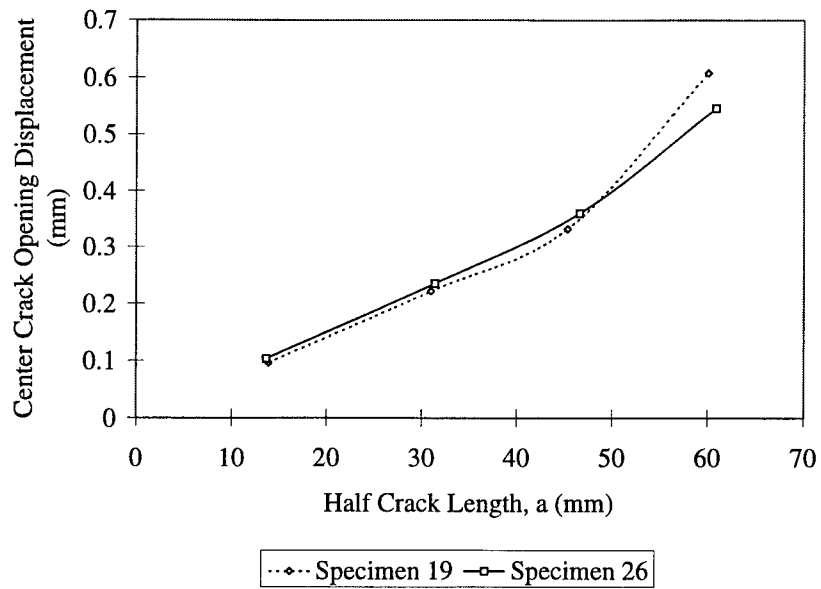


Figure 99. COD Comparison - 3.175 mm Plate, $S=1.0$, 51 mm Long Repair, Patch Widths: Full Width-Specimen 19, 50 mm-Specimen 26

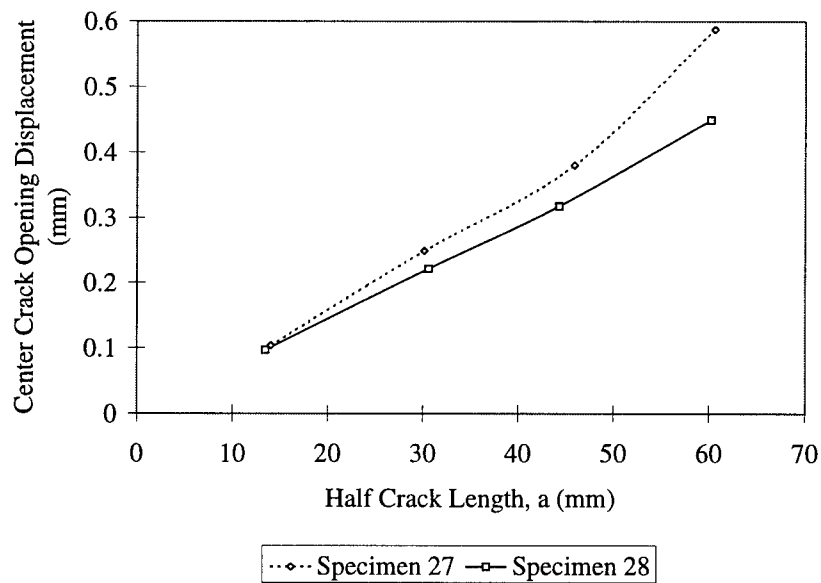


Figure 100. COD Comparison - 3.175 mm Plate, $S=1.3$, 51 mm Long Repair, Patch Widths: 50 mm-Specimen 27, Full Width-Specimen 28

4.6.4 Patched/Unpatched Face Crack Growth Rates

Figures 101 through 106 show the patched face crack growth data from the eddy current technique for the specimens repaired with finite width patches. These are shown for cracks within the uniform patch thickness area. Examination of the fracture surfaces after test showed the maximum lag between patched and unpatched face crack growth occurs when the crack reaches the patch taper area. Since lag measurements could not be obtained for crack growth within the patch taper area, lag measurements, taken at the point where the crack enters the patch taper will be used in the comparison to the full width patched face lag results. Every finite width patch case showed a significantly smaller (on the order of 17-40% smaller) crack lag than for the full width repair. This is consistent with the lower crack growth rates of the finite width patches within the uniform thickness patched area. The case of the long, $S=1.3$, finite width repair was an exception to this observation, where a similar amount of lag was noted as compared to its full width counterpart. This exception indicates that bending of the plates or rotation of the crack faces were similar for these two cases. Table 20 gives the values of the maximum crack lag measured for the finite width patched specimens.

Table 20. Maximum Patched-Face Crack Length Lag for Finite Width Patch Specimens

Specimen #	Plate t (mm)	Stiffness Ratio, S	Max Lag (mm)
20	6.350	1.0	6.406
21	6.350	1.3	3.808
22	6.350	1.0	2.955
23	6.350	1.3	18.682
26	3.175	1.0	1.262
27	3.175	1.3	1.835

4.7 Damage Mechanisms

4.7.1 Disbond

The growth of disbond was monitored during tests using infra-red (IR) thermography. These images were video-taped to examine disbond initiation and growth, and provide insight to the ef-

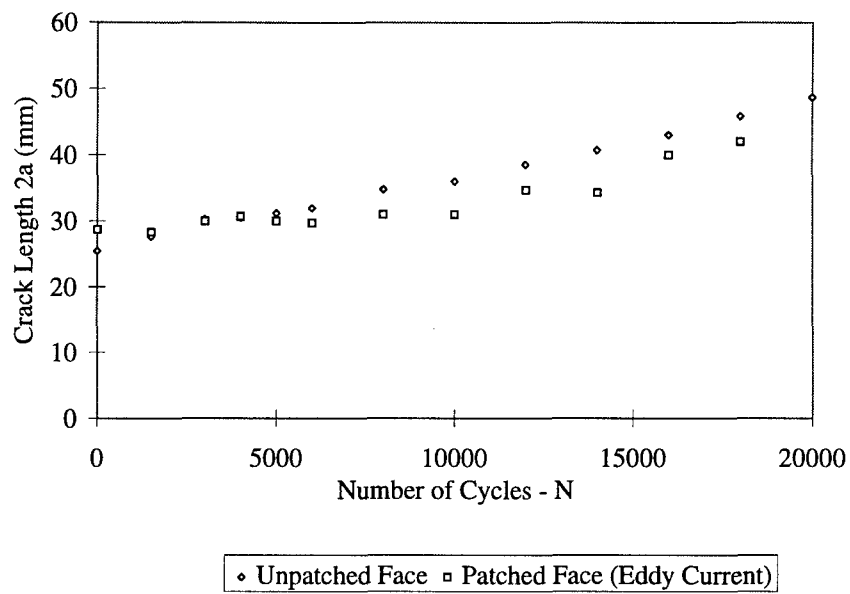


Figure 101. Patched vs. Unpatched Face Crack Lengths-Specimen 20: 6.350 mm Plate With $S=1.0$, 51 mm Long, 50 mm Wide Repair

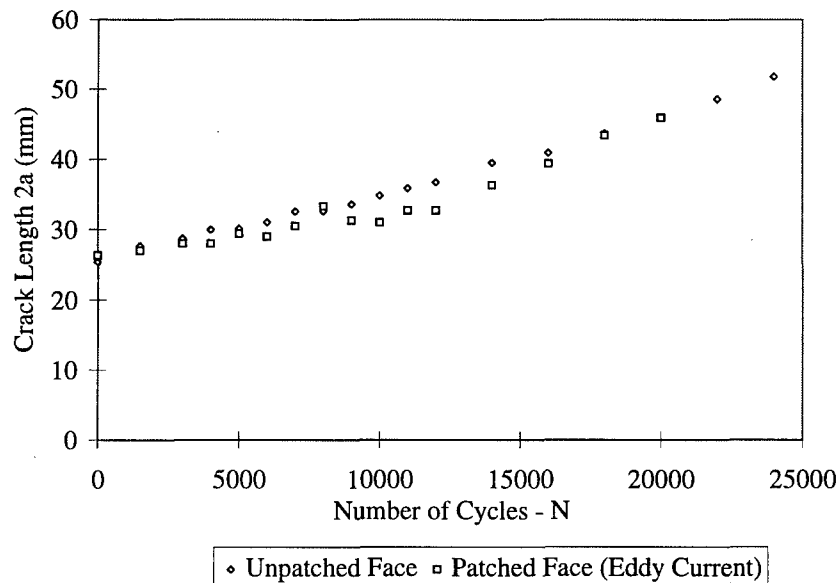


Figure 102. Patched vs. Unpatched Face Crack Lengths-Specimen 21: 6.350 mm Plate With $S=1.3$, 51 mm Long, 50 mm Wide Repair

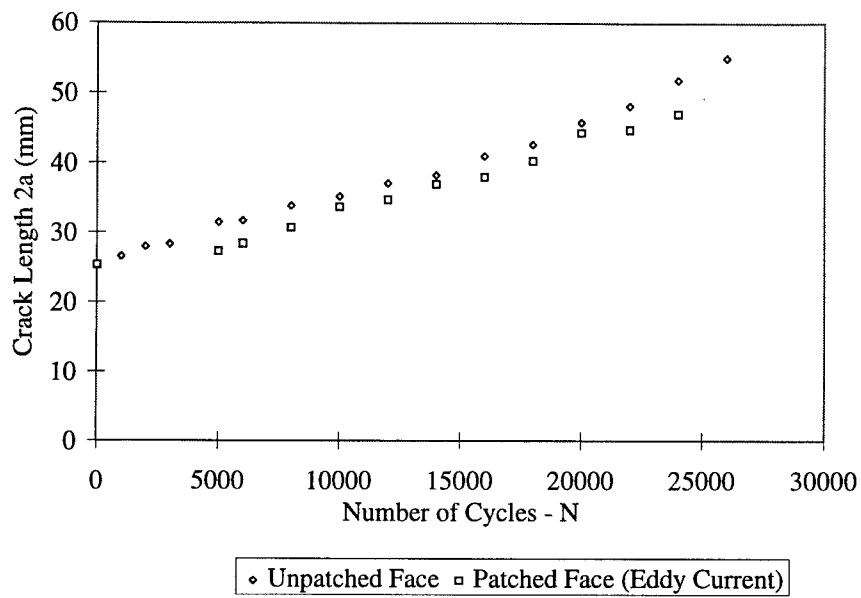


Figure 103. Patched vs. Unpatched Face Crack Lengths-Specimen 22: 6.350 mm Plate With S=1.0, 102 mm Long, 50 mm Wide Repair

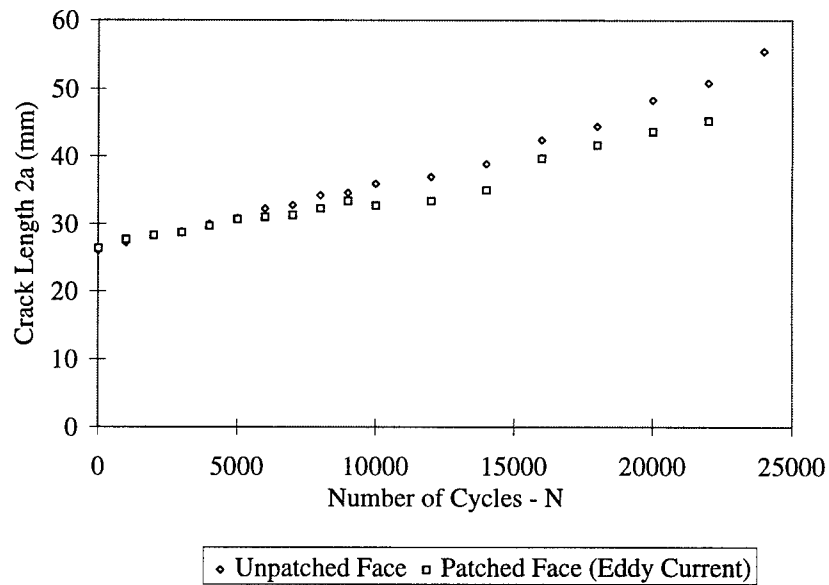


Figure 104. Patched vs. Unpatched Face Crack Lengths-Specimen 23: 6.350 mm Plate With S=1.3, 102 mm Long, 50 mm Wide Repair

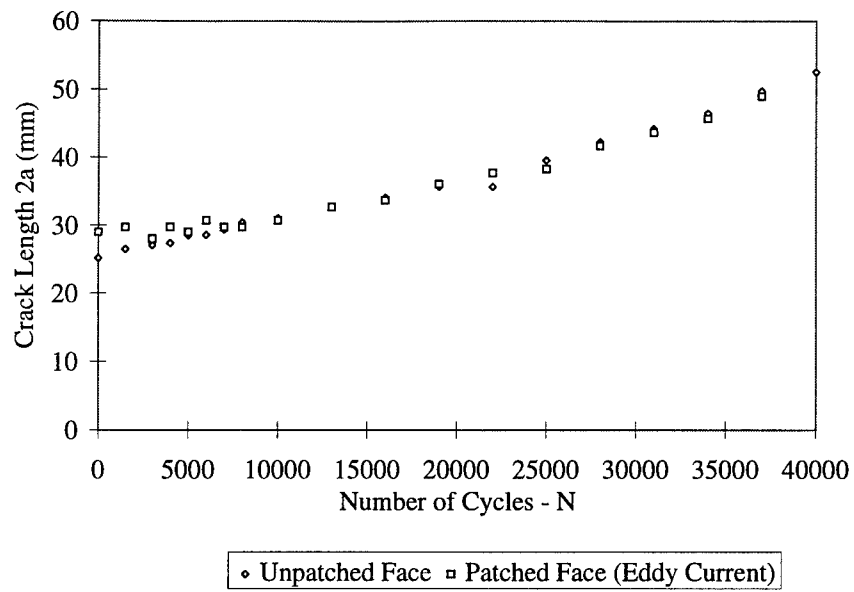


Figure 105. Patched vs. Unpatched Face Crack Lengths-Specimen 26: 3.175 mm Plate With S=1.0, 51 mm Long, 50 mm Wide Repair

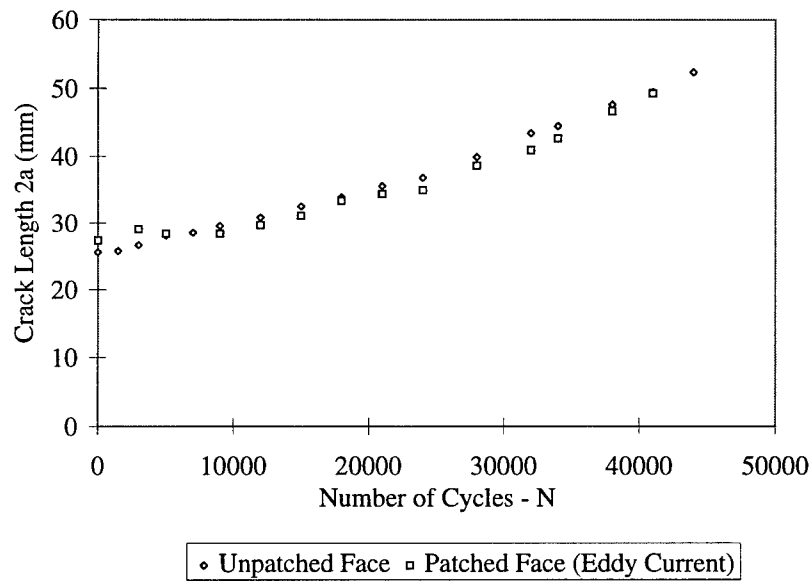


Figure 106. Patched vs. Unpatched Face Crack Lengths-Specimen 27: 3.175 mm Plate With S=1.3, 51 mm Long, 50 mm Wide Repair

fects of disbond on crack growth. Figure 107 illustrates the progressive growth of a disbond in a full width patch specimen, taken with the IR camera, recorded on video, and digitally captured by computer for examination. The images, starting with no disbond at $2a=89.5$ mm, show a disbond closely related to the crack shape at $2a=109.8$ mm. In the subsequent images, the disbond continues to progress with the crack in the width direction, but begins to rapidly increase in size perpendicular to the crack orientation. These records of disbond growth provided insight to when the disbond began to grow, its relation to crack size and its size at failure of the specimen. The information from these images was used to determine the disbond modification to the finite element models as discussed in Chapter 5. A limited number of ultra-sonic images (C-scans) were taken to validate the IR thermography results acquired during testing. This validation process gave higher confidence in the *in-situ* thermographs which were the preferred method of monitoring disbonds during testing. As was expected, the additional handling of the specimens during C-scans caused instrumentation damage (i.e. loss of strain gages, tabs etc.). Therefore, the *in-situ* nature of the thermography allowed a better qualitative, non-interference monitoring of the disbond growth of the patch-specimen interface during testing. Figure 108 shows a C-scan of the disbond growth when the crack growth was within 1% of the cycles to failure. Figure 108 can be compared with the final image ($2a=134.2$ mm) in Figure 107 to verify the validity of the thermographic technique.

Results of the thermographs and C-scans of the patched areas showed no detectable disbonds in the taper or edge areas of the patch in any specimens during testing, even at long crack lengths. Further, instrumentation wiring, strain gages, clip gage tabs, and FM73 adhesive, bled onto the unpatched side of the specimen, can be seen in the C-scanned image (Figure 108). These irregularities should not be confused with the disbond area.

Figures 109 and 110 show how disbond growth progressed during tests of 6.35 mm panels with finite width patches at the two stiffness ratios: $S=1.0$ and $S=1.3$. Very little disbond growth

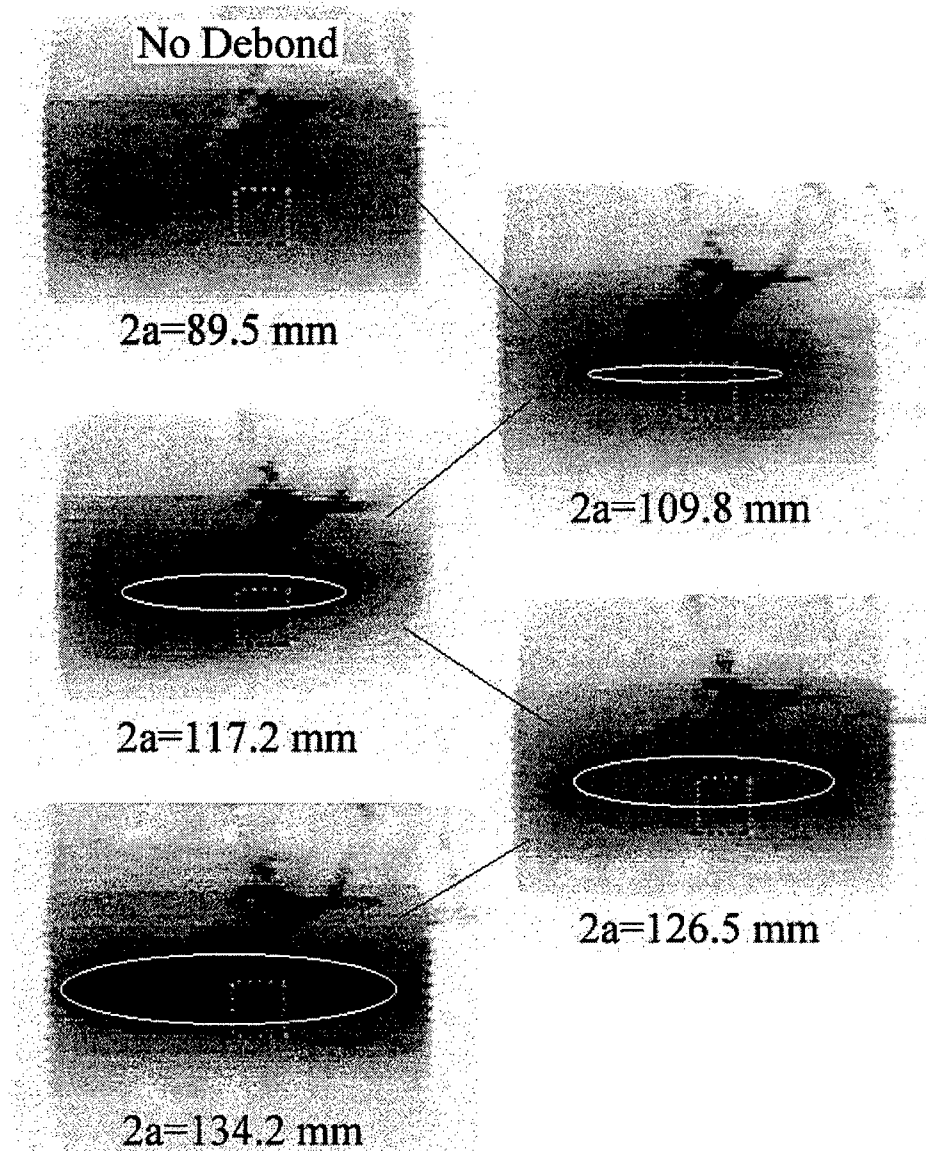


Figure 107. Thermographic Video Pictures of Disbond Growth in Full Width Patch Specimen

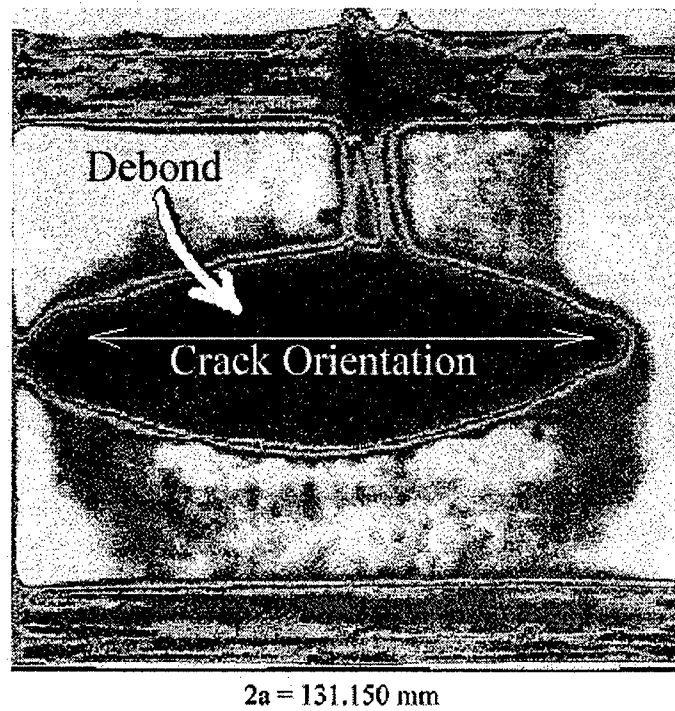


Figure 108. C-Scan Image of Disbond Growth in Full Width Patched Specimen with Long Crack

was observed until the crack reached the patch taper ($2a = 50$ mm) and did not grow appreciably until the crack grew beyond the patch edges ($2a = 86$ mm). Although disbond growth in these two different patch lengths were generally similar, the size of the disbond in the smaller patch specimen can be attributed to the earlier failure of the 51 mm long patches. As the crack grows beyond the patch edge, disbond growth accelerates and due to the fact the disbond size is approximately the same in both these patches, i.e. the area of patch disbanded from the specimen is much higher (2 times) in the short patch, the short patch adhesive layer fails (disbonds) sooner, causing earlier failure of the specimen.

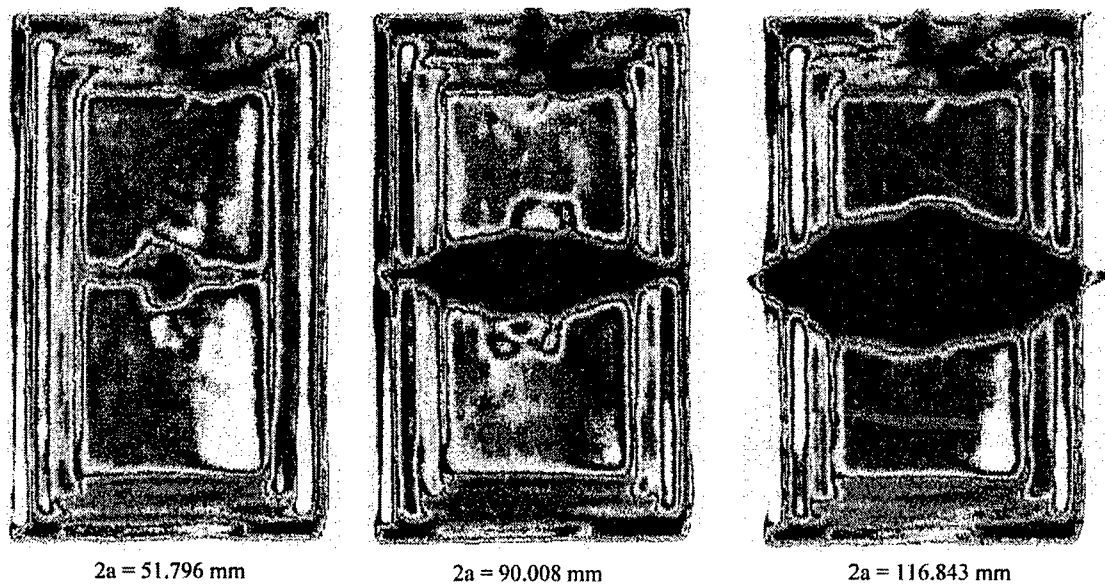


Figure 109. Disbond Progression in Finite Width Patch: $S=1.0$

Findings from the examination of debond growth in all specimens tested in this study show a consistent growth pattern of the debond (i.e. size and shape), regardless of patch size and stiffness ratio. Significant debond growth (away from the immediate area of the crack) occurs only when change in patch thickness occurs (i.e. in taper portion), or when the crack reaches a length where it would grow unstable in the unrepaired specimen. (The unrepaired specimens failed catastrophically

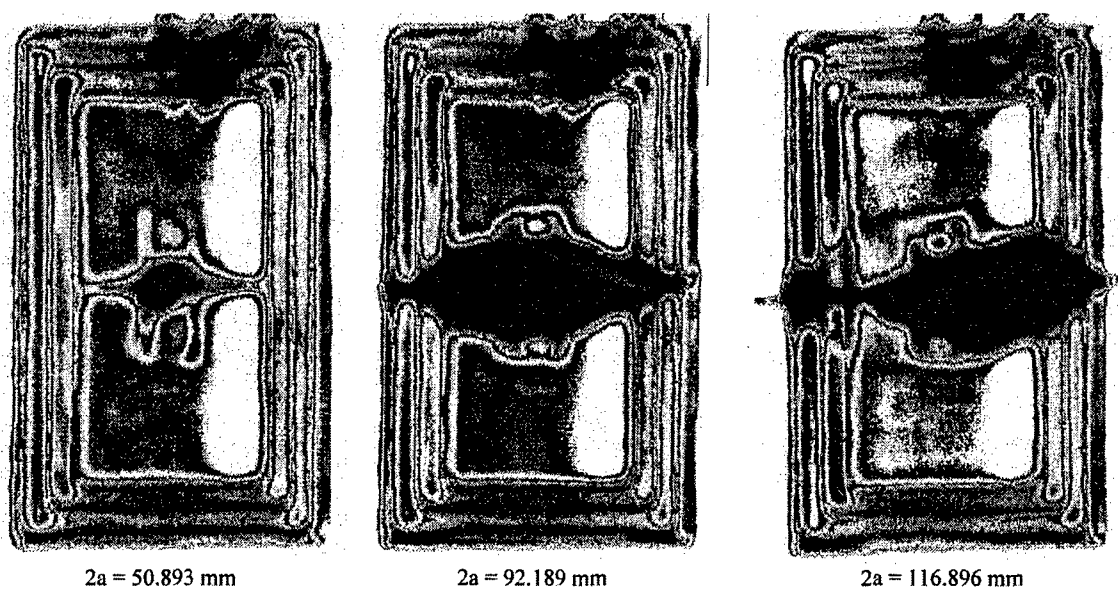


Figure 110. Disbond Progression in Finite Width Patch: $S=1.3$

at crack lengths of approximately $2a=100$ mm during cycling. This means that at this crack length, the maximum load of 120 MPa on the specimen creates a condition where the stress intensity factor at the crack tips exceeds the critical stress intensity factor, K_C . This stress intensity factor causes the crack to grow unstably (i.e. it progresses to failure). The consequences of this unstable growth and the associated disbond will be discussed further in Section 4.8 - Crack Growth Retardation.) Little or no debonding was discovered at patch edges regardless of patch size. Debond effects on crack growth indicated a greater impact due to the percentage of debond area relative to patch size rather than the size and configuration of the patch itself. Debond growth tended to be greatest in the crack length range from 90 mm to failure of the specimens. This range was also where the greatest changes in crack growth rates and COD occurred.. It can be assumed that the debonding of the patch at this point had a significant impact on these results through increased compliance of the specimen and increased bending.

4.7.2 Fracture Surface

Post-mortem examinations of the fracture surfaces were conducted to gather any additional information about the mode of failure and crack progression. These examinations included photographic imaging of the fracture surface, optical microscopic examination, and scanning electron microscopic (SEM) images. Examination of the fracture surface showed a crack front which started as straight through the specimen with a flat fracture surface. During the course of the test this straight crack front would become increasingly non-uniform and the surface would become slanted to 45° from flat. This transition from flat to taper indicates a plane stress condition which is dominant throughout all of the tests. Calculations of strain energy release rates in Chapter 5 are, therefore, based upon the plane stress assumptions.

Patched face crack lags behind the unpatched face crack which is consistent with measurements earlier in the chapter. This lag continues to increase until the $2a=100$ mm crack length, at which point the rate of crack growth on the unpatched face slows and the patched face crack length 'catches up' somewhat. Again, this can be explained by the unpatched face crack tip reaching critical stress intensity and being prevented from growing unstably by the bridged crack on the patched face. Instead the unpatched face crack growth rate, having experienced an overload, slows for a period of time and the patched face crack length increases at a faster rate. This phenomenon known as 'retardation' is discussed in the following section.

4.8 Crack Growth Retardation

As was discussed in the previous sections, crack growth retardation occurred near the unrepaired plate critical crack length in all specimens. This crack length, approximately $2a=100$ mm, was measured in the unrepaired baseline tests as the crack length where the maximum applied stress of 120 MPa caused the unrepaired specimen to fail suddenly during cycling. Using the relation for calculating stress intensity factor for a center-cracked finite width plate:

$$K = \sigma \sqrt{\pi a} \left(SEC \left(\frac{a}{W} \right) \right)^{\frac{1}{2}} \quad (36)$$

where K is the stress intensity factor, σ is the applied stress, a is the half crack length, and W is the specimen width. The calculated results for this, in a panel of thickness 6.350 mm, are shown in Figure 111. Also shown in the figure is the point at which the unrepaired specimens generally failed. The calculated stress intensity factors for the unpatched face, midplane, and patched face from the finite element method in Chapter 5 are also shown in this figure for the corresponding repaired panel. Note that near this critical length of $2a=100$ mm, the unpatched face stress intensity factor, K , exceeds the critical K_G value for the unrepaired specimen. It is this phenomenon, where the unpatched face K is greater than K_G and there remains portions of the thickness where K is less

than K_C , when crack growth retardation occurs in the patched specimens. This same phenomenon was also observed at other locations in specimens with finite width patches. In these cases, the retardation of crack growth rate was observed when the crack approached the location where the patch thickness changes or where the patch taper terminated. As is seen in Figure 112, test results showed that at near $2a=100$ mm for the full width patches, and near $2a=50, 86,$ and 100 mm in finite width patches, a reduction in the rate of increase of crack growth rate is seen. After this drop in rate, the crack eventually resumed its previous growth rate acceleration. In the thinner plates and when a higher stiffness ratio repair was used, this drop was less prominent, but it was still observed in all cases.

The above mentioned crack growth retardation is akin to the changes in growth rate observed when a component experiences a stress overload. In an overload scenario, the crack tip plastic zone is suddenly expanded in size when the crack opens under overload. When the crack again closes, the elastic material surrounding the plastic zone imparts residual compressive stresses on the expanded plastic region. Crack growth slows until the crack has grown past this area of compressive stress, after which it resumes its normal growth curve trend.

In the case of the present repaired specimens, data indicates that near the unrepaired panel critical crack length, or at locations where there are large changes in localized stress due to any changes in patch configuration, the patch and larger amount of uncracked material on the patched face carries suddenly significantly higher load. The unrepaired specimen would have failed at this point but the patch bridges the crack in the repaired specimen, reducing the stress level below K_C on a significant portion of the crack front. Further, due to the increased load on the adhesive interface, the existing disbond progresses at a faster pace, thus increasing compliance of the specimen. This increased compliance allows greater bending and an increased load on the unpatched face. Increased load, in turn, causes the crack to open significantly at the tip, producing a stress overload and a suddenly

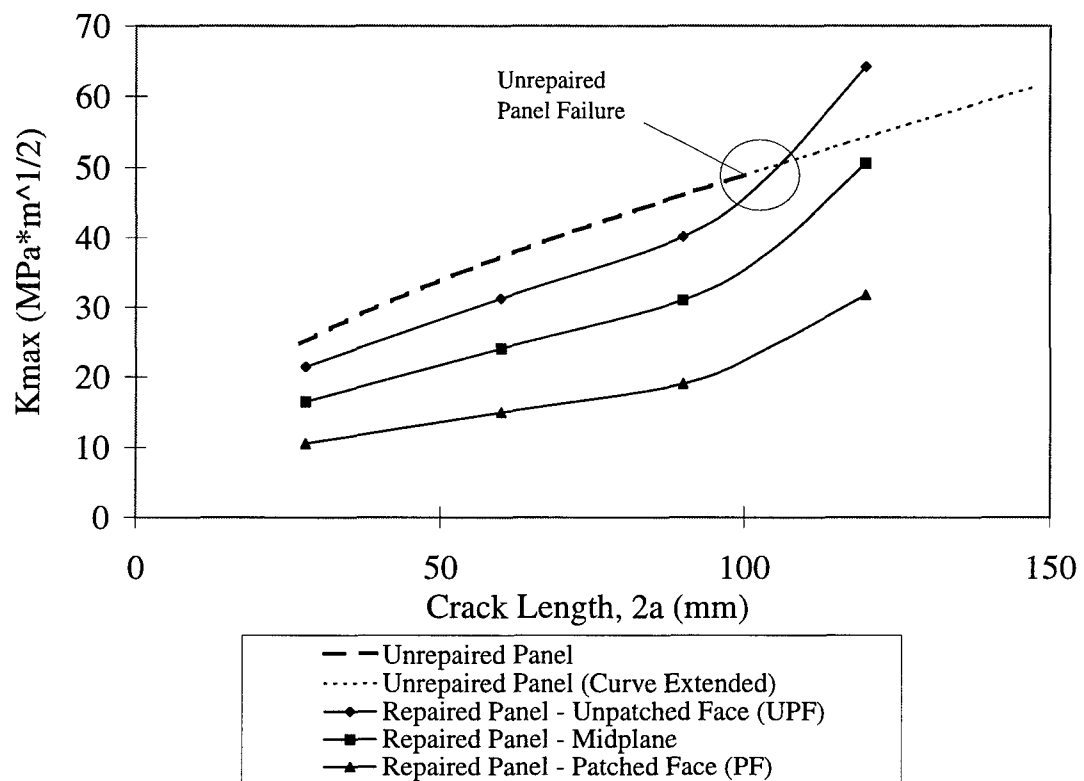


Figure 111. Comparison of Repaired to Unrepaired Panel Stress Intensity Factors (6.350 mm Thick Panel, $S=1.0$, 102 mm Long, Full Width Repair)

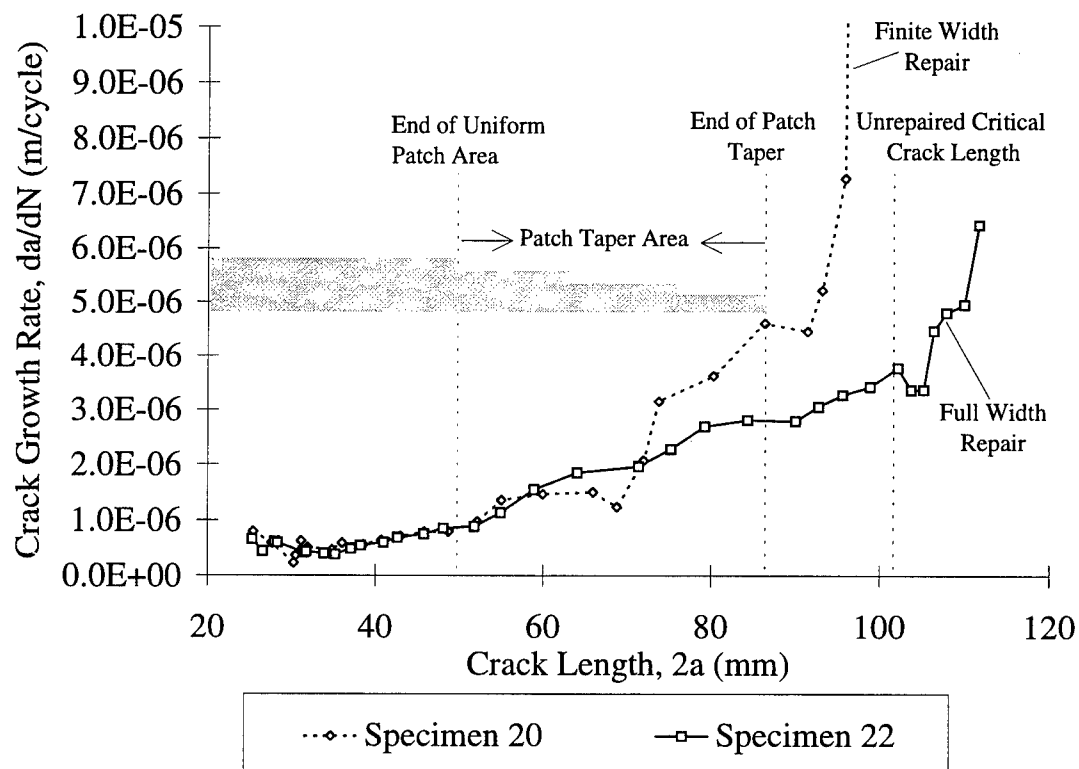


Figure 112. Crack Growth Retardation in Finite Width and Full Width Patch Specimens 20 and 22

increased plastic zone size at the crack tip. At this point the crack growth slows on the unpatched face until the crack had progressed through the area of residual compressive stress. Crack lengths at the midplane and patched face, not having undergone the stress overload, progress at a normal pace, thus 'catching up' occurs in relation to unpatched face crack growth. In some cases, this retardation phenomenon caused thinner patch repairs to outlive thicker repairs. Though this might seem advantageous for increasing life-span, it is a much more complicated problem, especially if it is to be included in the analysis.

4.9 Summary of Experimental Observations

This section briefly summarizes experimental observations as discussed in detail above.

Bonding patches caused thermally induced curvature in the plates. This study confirmed the previous findings that an increase in the length of patches on 'thin' plates reduces initial thermal curvatures in the specimens. Increase in patch length, however, caused increased initial curvature in 'thick' specimens. Patch length affected life-spans in the following manner: (1) longer patch provided longer life for thin plates, (2) a small increase was seen in the fatigue life of thick plates by increasing the patch length with $S=1.0$, (3) life-span was reduced for thick plates by increasing patch length with $S=1.3$. The changes in patch length had little effect on crack opening displacement for thick panels, but reduced COD in thin plates. Little or no change was observed in the amount of the lag in patched versus unpatched face crack lengths due to patch length variations for thin plates. Longer patches created a larger crack lag between patched and unpatched faces in the thick plates.

Variations in patch to plate stiffness ratio showed initial curvature trends that were inconclusive. This was due to insufficient data. There is possibly some optimal stiffness ratio where initial thermally induced curvature is minimum. For the thin and thick plates, this seemed to be near stiffness ratio, $S=1.0$. Higher stiffness ratio patches produced increased life-span in both the thin and thick

repaired plates. The benefit of this increase was much greater in the thick than in the thin plates. COD vs. crack length curves showed a linear relationship with increased stiffness ratio, which indicates less bending during loading of the specimens at longer crack lengths. This results in reduced stress levels at the crack tips and longer life-spans in these specimens. More benefit was observed from the reduction of COD in the thin plate repairs than in the thick plates with the increase of stiffness ratio. Stiffness ratio changes investigated in this study did not show any noticeable effect on lag in patched versus unpatched face crack lengths.

Plates repaired with a finite width patch had less initial curvature than that in full width patch due to reduced thermal stresses. Within the uniform thickness patch area, the repaired, thin plate crack growth rates were nominally the same as these with the full width repairs. With thick plate repairs ($S=1.3$), the finite width patch had greater crack growth rate than that of the full width repair. With thinner repairs ($S=1.0$), crack growth rates were the same or slightly lower than with full width repairs, resulting in longer lives. COD for cracks within the patch area showed little difference between finite width and full width repairs. The largest crack lag, resulting from bending stresses, was observed at the points just before crack growth retardation occurred for the unpatched face. This was near $2a=100$ mm (the unrepaired panel critical crack length) for the full width repairs or, for the finite width repairs, where there was a change in patch thickness.

Debond size and growth were dependent on crack size rather than on patch configuration. The disbonds noted in this study grew initially only in the immediate vicinity of the crack itself. Debond changes occurred when the crack reached the point where the patch's thickness changed or where the crack would have grown unstable if the patch were not present (i.e. beyond the unrepaired panel critical crack length). Debond had greater effect on crack growth only when the debond size covered a large portion of the uniform patch area and then the patch begins to debond quickly. Observations during this study show that thin patches and thickness changes in the taper area actually have a

short-lived beneficial effect by creating an 'overload' phenomenon. The overload occurs when the unpatched face crack experiences a stress intensity factor higher than the unrepaired panel's K_{IC} . This results in unstable crack growth suddenly on the unpatched face, creating a large compressive stress area at the crack tip of the unpatched face. The crack progresses slower through this area due to this compressive stress, then recovers its original growth rate when past the compressive stress area.

In general, plate thickness, t , and patch to plate stiffness ratio, S , were found to be the most influential factors governing crack growth rates and life-span for the repaired aluminum plates with composite patches in this study.

Part: III
Finite Element Modeling (FEM)

5. Analysis

This chapter presents the analytical part of this study. The analysis involved the finite element technique to supplement and/or model the results of experiments shown in Chapter 4. Also, the validity and limitations of this modelling method, along with its capability to predict the fatigue behavior in a thick plate repaired with a bonded patch, is investigated.

5.1 Mindlin Plate Model Description

The analysis used in this study is a two-dimensional (2D) finite element analysis consisting of three layers of 2D Mindlin plate elements to model the repaired plate, the adhesive, and the composite patch. Due to symmetry, only a quarter of the repaired panel configuration is modeled. The model with a full-width patch consists of 4700 four-noded Mindlin plate elements; 1700 in the plate, 1500 in the adhesive layer, and 1500 in the repair. Refinement in the crack tip area consists of 0.05 mm square elements, ten leading the crack tip, ten trailing the crack tip, and ten deep from the line of symmetry in Regions 4 and 5 (see Figure 113). Figures 114 and 115 show the FEM model crack tip grid refinement and overall grid configuration, respectively.

Naboulsi and Mall [48–51] demonstrated the usefulness of this modelling technique by comparing its results with the thin (1 mm) repaired panel experimental data and previous analytical results by Sun [61, 66, 67]. The uniqueness of this three layer method is how the adhesive layer is modelled. The adhesive layer is modeled here as an elastic continuum replacing the previous method used by Sun, et al. [61, 66, 67], who used spring elements (non-continuum). The reason for using the three layer model is to provide an economical 2D numerical solution to a three-dimensional (3D) problem, yet minimize the inherent differences between the 3D and 2D model solutions.

The 4-noded Mindlin plate elements were used with transverse shear capability for each of the layers. Constraint equations were then used to enforce compatibility conditions at each of the bonded

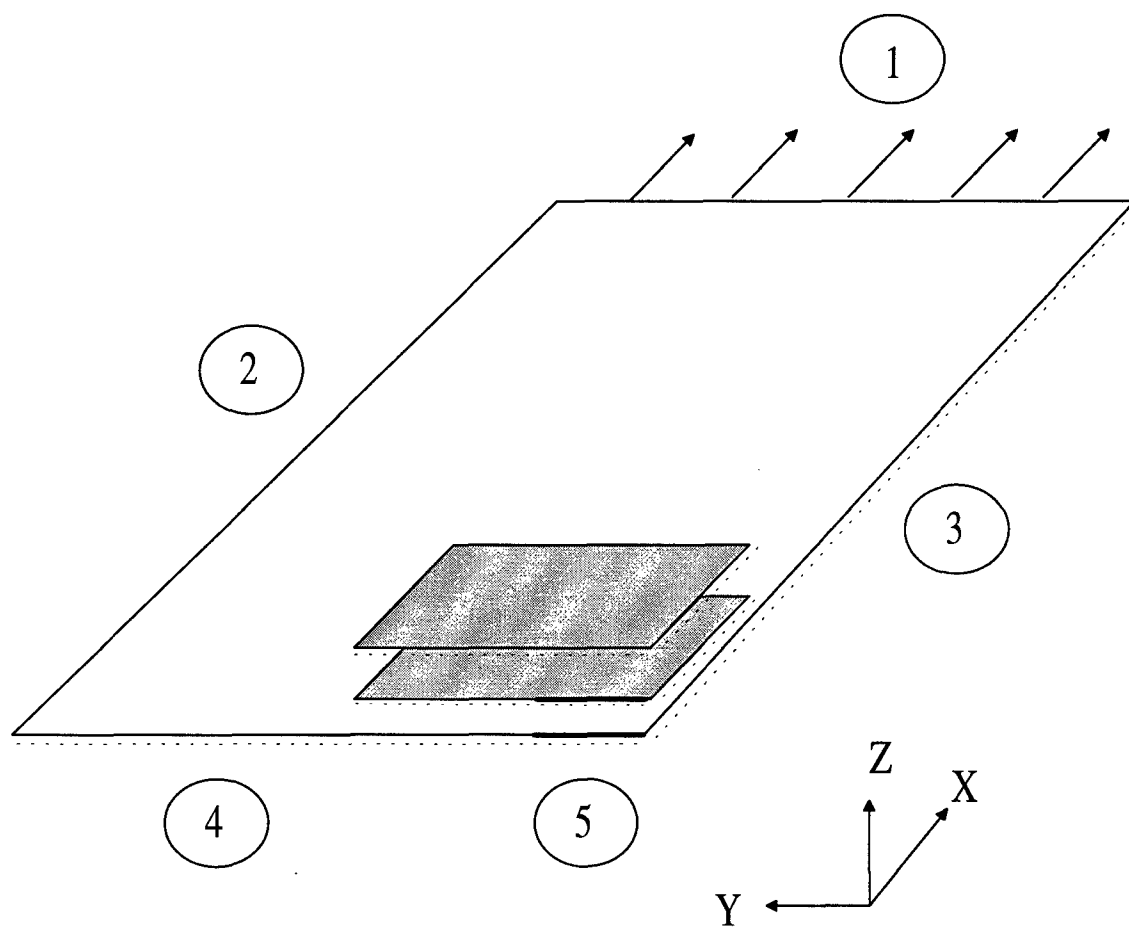


Figure 113. Quarter Model Configuration

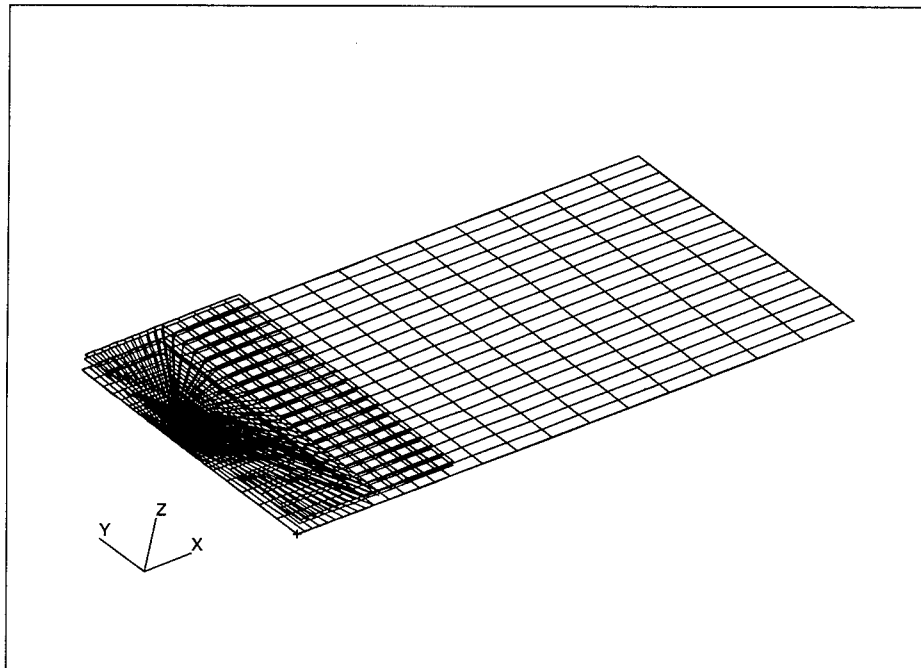


Figure 114. FEM Quarter Panel Grid ($a=45\text{mm}$, Full Width Patch)

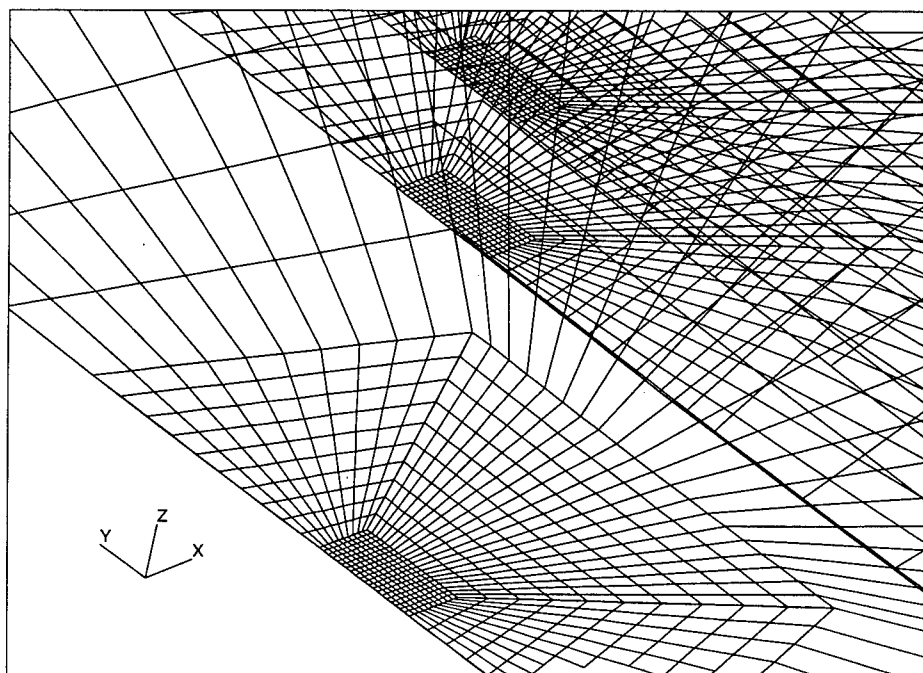


Figure 115. FEM Crack Tip Grid Refinement

interfaces, based on the Mindlin plate theory. This allowed the model to enforce the displacement constraints for bending in unsymmetrically repaired panels, as well as the bilinear displacement constraints of symmetric repairs.

Mindlin plate theory assumes a linear displacement field through the plate thickness:

$$\begin{aligned} u_x &= \bar{u}_x + z\bar{\theta}_y \\ u_y &= \bar{u}_y + z\bar{\theta}_x \\ u_z &= \bar{u}_z \end{aligned} \quad (37)$$

where \bar{u}_x , \bar{u}_y , and \bar{u}_z are defined as the mid-plane displacements in the x , y , and z directions, respectively. $\bar{\theta}_x$ and $\bar{\theta}_y$ are the rotations of the plate cross-section about the x and y axes, respectively. Axes x and y are in the plane of the plates, and the x -direction is the loading direction for the uniaxial load condition. ' z ' was the axis in the thickness direction of the plates. Each of the three layers (cracked plate, adhesive, and patch) were assumed to have a linear displacement field (relative to the mid-plane displacements) throughout the thickness of the individual layers and thus each layer must satisfy the following equations:

$$\begin{aligned} u_x^* &= \bar{u}_x^* + z^*\bar{\theta}_y^* \\ u_y^* &= \bar{u}_y^* + z^*\bar{\theta}_x^* \\ u_z^* &= \bar{u}_z^* \end{aligned} \quad (38)$$

where the superscript $*$ represents p , a , or r , denoting plate, adhesive, or repair patch, respectively. z^* represents the z -coordinate through the thickness of each plate element defined as:

$$-\frac{h^*}{2} \leq z^* \leq \frac{h^*}{2} \quad (39)$$

with h defined as the thickness of each individual plate and ' $*$ ' representing p , a , or r for plate, adhesive, or repair. In addition to compatibility constraints, geometric constraints at the interfaces were also enforced. For example, where the z -coordinate of the plate matches the z coordinate of

the adhesive, $z^p = z^a$, the displacement field's constraint equations at the interface are:

$$u_x^p = u_x^a \quad (40)$$

$$u_y^p = u_y^a$$

$$u_z^p = u_z^a$$

and subsequently, where the z-coordinates match at the adhesive-repair interface, $z^a = z^r$, the displacement field's equations are:

$$u_x^a = u_x^r \quad (41)$$

$$u_y^a = u_y^r$$

$$u_z^a = u_z^r$$

As was discussed in Background - Overview of Previous Research (Chap 2 Section 2.4), the finite element model allowed calculation of the strain energy release rate, G , of the specimens' midplane crack tips by the indirect modified crack closure method [58]. By assuming a decoupling of Mode I crack opening from Mode II in the strain energy relation, the strain energy release rates, G_I , at the patched and unpatched surfaces was calculated. This was done by using the through-the-thickness linear displacement assumption of the model. This was the case for the self-similar crack growth in the present study. In turn, the stress intensity factor, K_I , was calculated from G_I for Mode I fatigue crack growth at the patched (patched face - PF) and unpatched (unpatched face - UPF) surfaces.

5.2 Boundary Conditions

5.2.1 Rotation and Displacement Conditions

The three layer model uses a quarter plate configuration (refer to Figure 113 for this schematic) due to symmetry of the specimen and loading conditions. Symmetry lines in the figure are shown

by dotted lines. Along the gripped end of the specimen (Region 1), displacements in the x-axis (load axis), u_x , were free, displacement of y-axis and z-axis were restricted to $u_z^p = u_y^p = 0$, and rotations were restricted to $\theta_y^p = 0$, to simulate the bolted/clamped configuration of the test machine grips. All boundary conditions along the free edge of the plate and free edges of the adhesive/repair (Region 2) were unconstrained. Displacements on the longitudinal symmetry axis of the specimen (Region 3 - parallel to the load direction) were constrained only in the y-direction, $u_y = 0$. Rotations along the same edge are restrained in both the x- and z- directions by $\theta_x^p = \theta_z^p = \theta_x^a = \theta_z^a = \theta_x^r = \theta_z^r = 0$. The uncracked plate portion of the transverse edge of the specimen (Region 4) had the x-direction displacements restrained for all layers, $u_x^p = u_x^a = u_x^r = 0$. Rotations about the y- and z-axes were restrained for all layers in the uncracked region, $\theta_y^p = \theta_y^a = \theta_y^r = \theta_z^p = \theta_z^a = \theta_z^r = 0$, due to symmetry. In the cracked region of the transverse edge of the model (Region 5), the plate and adhesive were assumed 'cracked' and the resulting edges are free surfaces, therefore only the repair layer x-displacement and rotations about the y- and z-axes were restricted, $u_x^r = \theta_y^r = \theta_z^r = 0$.

5.2.2 Temperature Condition

Temperature change during the cool-down period of patch bonding was simulated in the analysis as $\Delta T = -100^\circ C$ to characterize the cool-down phase of bonding the repair to the plate. Figure 116 shows the typical results of this temperature change calculation from finite element analysis in terms of out-of-plane displacement (z-direction), and these are compared with the corresponding experimental data. This clearly shows an excellent agreement, thus ascertaining the importance of modeling the thermal effects in bonded patch repair in an attempt to capture all physical aspects of the problem. This temperature profile was subsequently used throughout the modelling in this study.

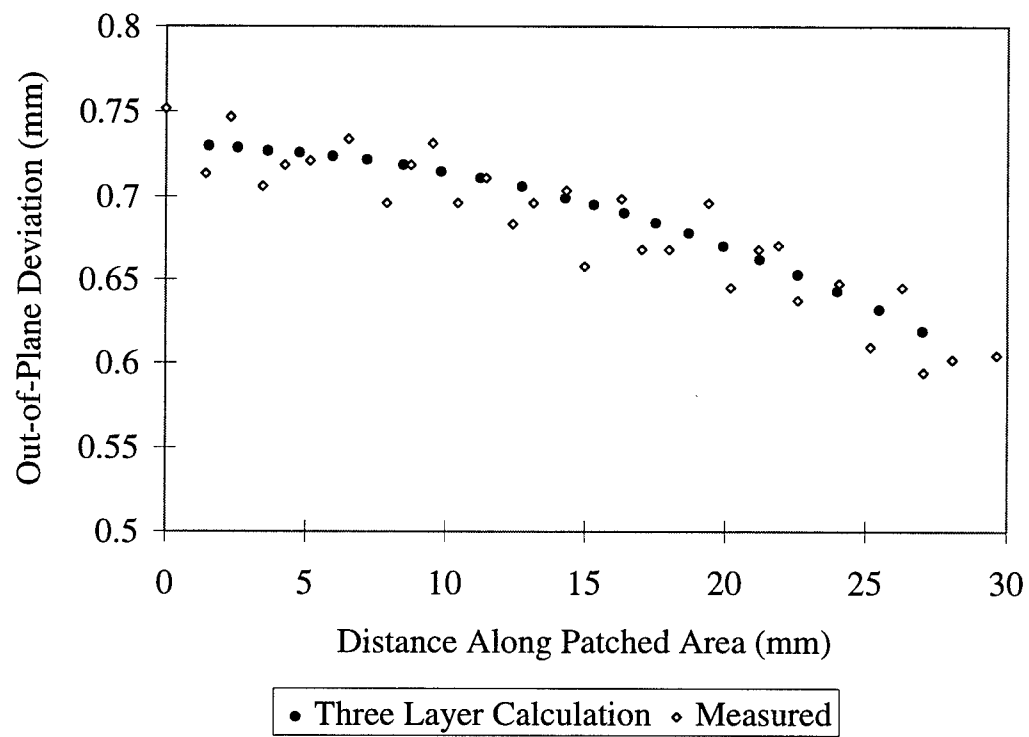


Figure 116. Thermal Curvature Comparison - FEM versus Experimental

5.3 Crack Opening Displacement Comparison

A detailed comparison of analytical and experimental center crack opening displacement (COD) was undertaken in order to ascertain the validity of the three-layer technique. Figure 117 shows the configuration of the bonded titanium tabs on the specimen surface to allow the clip gage to measure center crack opening displacement. Due to the thickness of the tabs (0.794 mm thick), measurements of COD data were consistently made at a distance of slightly less than 1 mm from the actual surface of the specimens.

In order to make proper comparisons of the measured data to the calculated values, the following assumptions were made to adjust the computed values of COD from the numerical model at the unpatched face (linearly extrapolated from the mid-plane) to values for the displacements at the tab tips. The Mindlin plate surfaces in the numerical model are assumed to displace linearly relative to the mid-plane and the displacements in the plane of the tab tips were extrapolated using the same method by using the following formula:

$$2v_{eff} = 2 \left[\frac{\bar{u}_x}{2} + \sin(\theta_y) \cdot \left[\frac{t_p}{2} + t_{tab} \right] \right] \quad (42)$$

where $2v_{eff}$ was defined as the measured COD at the tab tips, \bar{u}_x was the plate's mid-plane, x-direction displacement, θ_y was the rotation about the y-axis at mid-plane, t was the thickness of the repaired aluminum plate, and the quantity t_{tab} was the thickness of the applied tab. The calculated values for Δv (the differences between v , COD on the unpatched surface, and v_{eff} , COD at the tab tips) were approximately 11-14% of $2v_{eff}$ for the thin plates (3.175 mm) and 7.5-8.5% for the thick plate (6.350 mm) specimens, dependent on the tab thickness. Since the calculated COD (at the tab tips), $2v_{eff}$, could then be compared directly to the experimental measurements, this comparison was used, in part, to assess the FEM model's adequacy. Figures 118 and 119 show the comparisons of COD for two extreme cases of the thickest and thinnest plates. Excellent agreements between experimental measurements and computed values are seen for crack lengths up to $2a = 90$ to 100

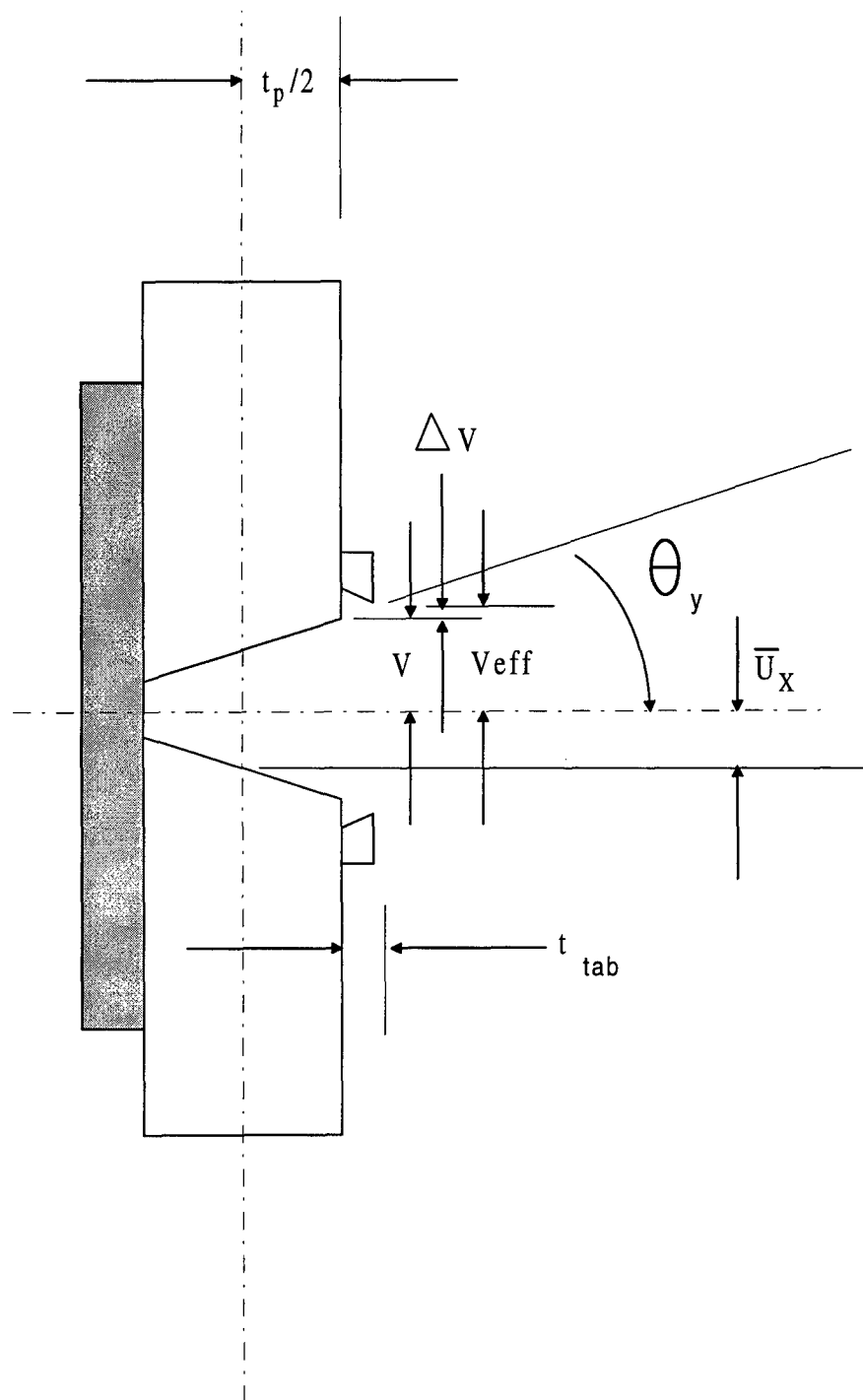


Figure 117. Tab Configuration for COD Calculations

mm long. As mentioned in Chapter 4, debond growth was observed in all tests when crack grew beyond 90~100 mm in length. Figure 120 shows an example of the improvement to the calculated COD curve for crack length $2a=120$ mm when a disbond modification was included in the analysis (this is discussed further in Section 6). This modification shows that with the disbond growth being modeled, the Mindlin plate three-layer model provided an excellent representation of the center crack opening displacement as well as the overall modelling of repaired panels tested in this study.

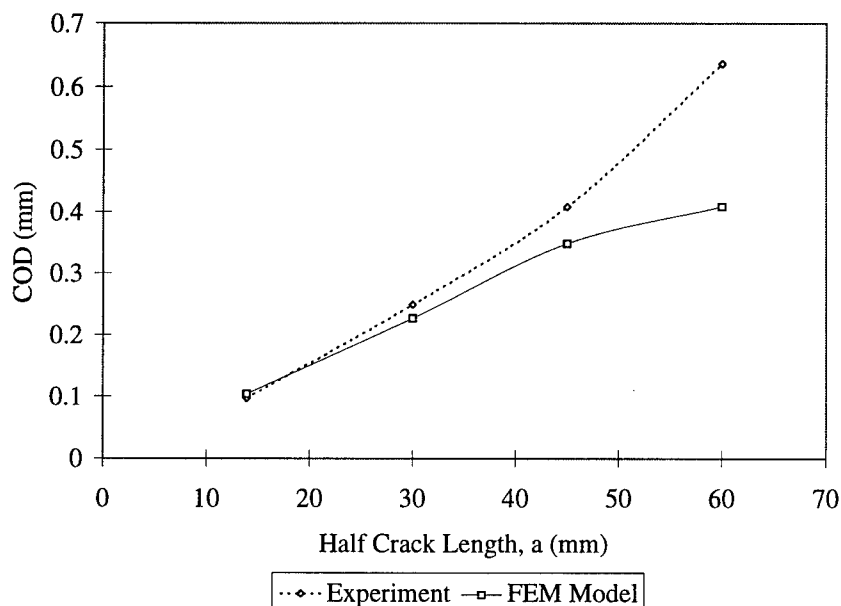


Figure 118. Experimental versus FEM COD Comparison, 6.350 mm Plate with $S=1.0$, 51 mm Long, Full Width Patch

5.4 Strain Comparison

5.4.1 Direct Comparison

As was discussed in Chapter 3, strain measurements were taken at selected locations on the specimens for comparison with FEM model results. Although surface strains in the tests (as influenced by non-linear through the thickness stresses) were not expected to correspond directly to

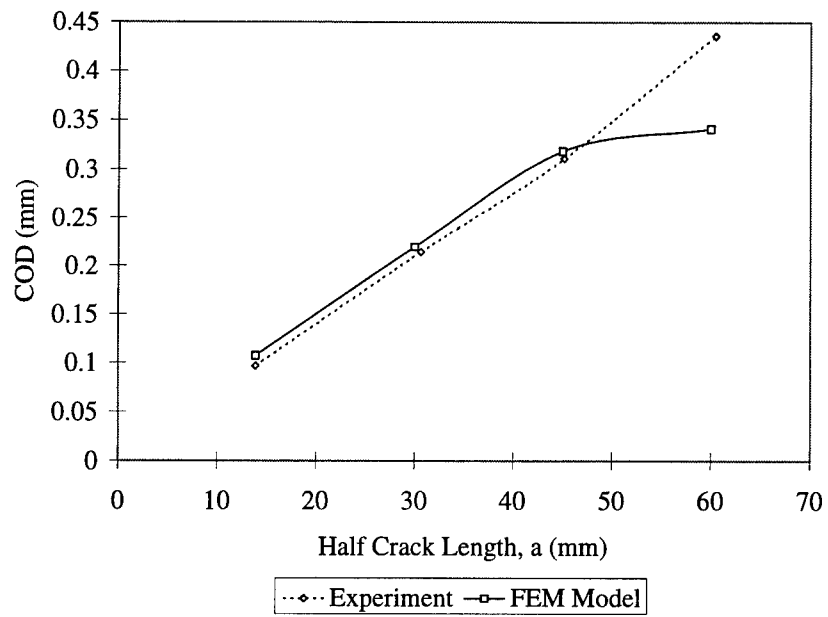


Figure 119. Experimental versus FEM COD Comparison, 3.175 mm Plate with S=1.0, 102 mm Long, Full Width Patch

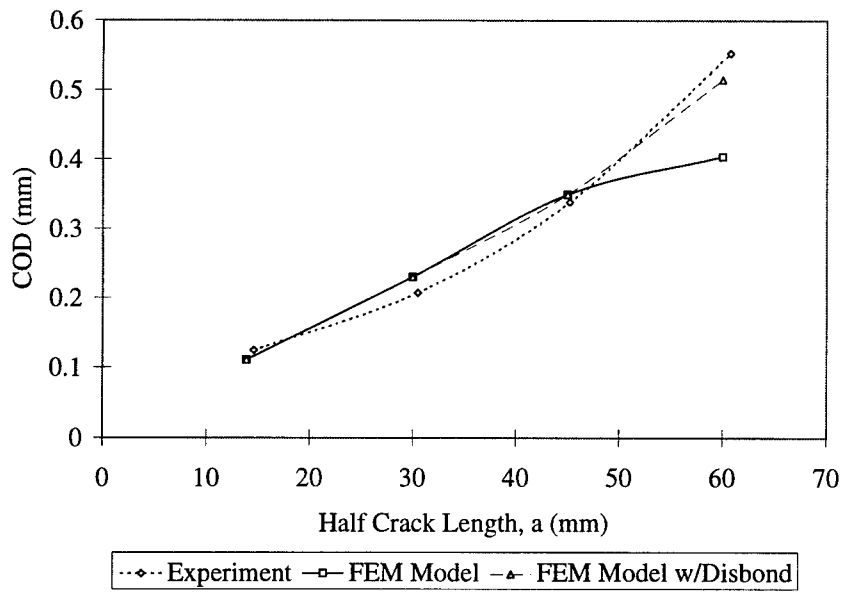


Figure 120. Experimental versus FEM COD Comparison, 6.350 mm Plate with S=1.0, 102 mm Long, Full Width Patch

calculated values, these values were used to provide an additional check of the models' boundary conditions. Figure 121 provides a schematic of the gage locations, (as positioned in the majority of tests), on the plate side (unpatched face - UPF) and the patch side (patched face - PF), on the specimens where strains were measured. Maximum strains were plotted for the locations on the plate side of the specimens (locations 1, 2, and 4) and the patched side (location 3) in Tables 21 and 22 along with calculated strains from the three layer model. Although not a perfect match, the strains calculated by the FEM model are generally in agreement with experimental counterparts for locations 1 and 4. At location 2, the strains did not match in direction but were similar in magnitude. After examination of both the model results and the physical movements of the experimental specimens during test, it was found location 2 was unfortunately chosen near an inflection point of the specimen's curvature. This point was very close to the location where the specimen's curvature changes from concave to convex and any slight error in positioning of the gage, or the fact that averaged element strains are being read from the model, would cause large errors due to the much higher strain gradients in these areas. Strain calculations for the patch side were similar to those on the plate side, however, with slightly more error between experimental and analytical strain values on the patched face. Analytical strain at location 3 (over the crack opening) on the patch side had good agreement with its experimental counterpart and errors ranging from only 5-30% from experiment. (Location 3 on the plate side is the location of the COD clip gage whose results were in excellent agreement with analysis, as noted in the previous section.)

Table 21. Experimental Strain Comparison with FEM Model on Unpatched Face (UPF) - Specimen 7, $a=13.91$ mm

Location	Experiment Strain (mm/mm)	FEM Strain (mm/mm)
1	0.000818	0.00134
2	0.000115	-0.000225
4	0.000588	0.000630
3 (PF)	-0.00100	-0.00136

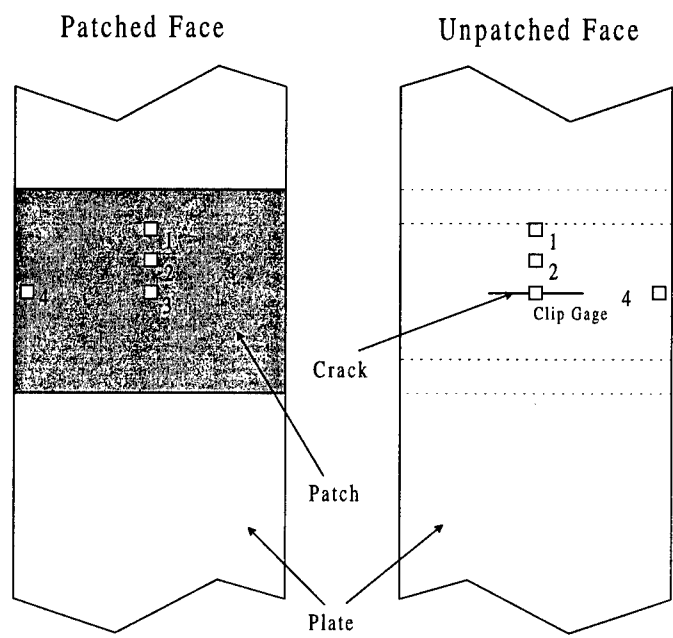


Figure 121. Gage Locations for Strain Measurements

Table 22. Experimental Strain Comparison with FEM Model on Unpatched Face (UPF) - Specimen 9, $a=13.91$ mm

Location	Experiment Strain (mm/mm)	FEM Strain (mm/mm)
1	0.000873	0.000843
2	-0.0000440	0.000418
4	0.000470	0.000600
3 (PF)	-0.000800	-0.000678

In general, experimental strain measurements compared to the FEM model calculations were not as accurate as the COD comparison. The strain comparison did, however, provide valuable insight to the relative out-of-plane specimen movement during loading. This is discussed next.

5.4.2 Out-of-Plane Displacement

In the process of examining strain measurements and making comparisons to the FEM models, out-of-plane displacement calculations were examined to determine the out-of-plane movement of the patched area of the repaired panel during the loading. Previous analytical models have assumed that any curvature in the repaired specimen developed from bonding of the patch was quickly removed (or overcome) by the load applied to the specimen during test [40, 57, 61]. In other words, the specimen and patch supposedly straightened at reasonably low loading levels and therefore it was assumed that the specimen could be modeled as initially straight. This assumption may approximate the conditions for the thin specimens. At the very least, it can be assumed that the unpatched area of the plate straightens along the load axis during loading for all thicknesses. But, the patched area of a thick repaired plate never straightens and the stresses are significant. Figure 122 shows the calculated shape of a specimen's centerline at different load levels. The plots were generated by taking the FEM displacement results at different load levels and combining the data in the chart by establishing the patch end as a pivot point. This presentation does not show the full movement of the repaired area of the plate but instead shows the shape characteristics and movement within the

patched area relative to the patch end. A saddle shape was the general shape common to all plates (though most prominent in the full width patched plates) and was also significant enough to be seen visually during experimental testing. The saddle shape is caused by the combination of bending induced by the neutral axis shift in the cracked area and the transverse buckling effect in the uncracked area of the patched specimen.

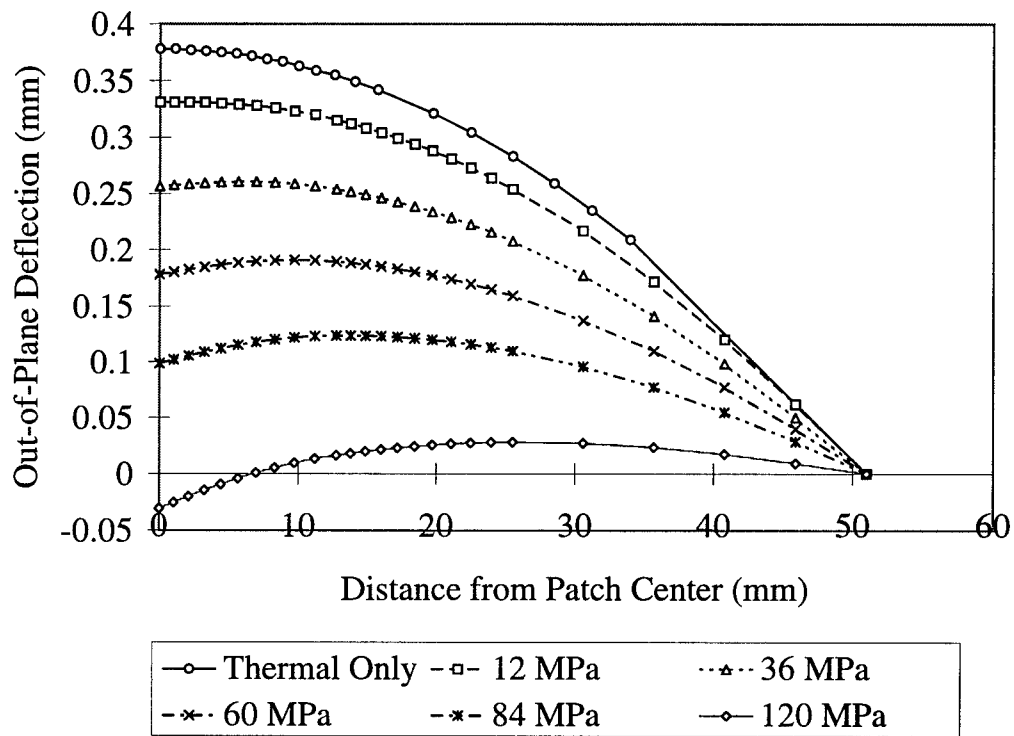


Figure 122. Out-of-Plane Curvature - Post-bonding, 0 to 120 MPa, 6.350 mm Plate with S=1.0, 102 mm, Full Width Patch

Figure 122 shows that the patched area of the repaired specimen never totally straightens under even full load, and the actual crack face rotation changes from a small positive θ_y rotation, initially after bonding, to a negative rotation at full load. This 'pop-through' effect, rapidly changing curvatures shown in Figure 122, and through the thickness non-linearities explain why it was difficult

to get good strain comparisons. Particularly, this was even more difficult at some transition points in the patched plate curvature during test. Any minor discrepancy in the actual placement of gages versus the position where the calculated value was read (near saddle transition points) was amplified. The errors even provided discrepancies with the opposite magnitude reading, especially when strains were small or when the curvature was changing from convex to concave shape. It should be noted here that strain gage location 2 (Figure 121) was in this transition region.

5.5 Crack Growth Rate Comparison

Crack growth rate values, da/dN , were estimated using the calculated stress intensity factor ranges, ΔK , and the Paris Law of fatigue crack growth (using material constants C and m , determined experimentally) for each plate thickness, as discussed in Chapter 4. Results for the predictions of unpatched face (UPF) crack growth rates showed good agreement with measured values of growth rate for cracks less than $2a = 50mm$ length for all specimens. In some cases accurate predictions were accomplished for cracks up to $2a = 80mm$ long. An example of these predictions is shown in Figure 123. On the other hand, Figure 124 shows an example comparison between analytical and experimental da/dN results on the patched face (PF). It is easily seen that the model underpredicts the crack growth rates determined from the experiment at the patched face. Calculations of the patched face crack growth rate using this three layer model configuration assume displacements at the surfaces of the plate to be linearly related to the midplane. From examination of the crack front (in Chapter 3-Post-mortem Examination of Tests), it is evident that the crack front is not only skewed from a uniform through-crack profile (i.e. lag exists between unpatched and patched face crack lengths), but also it is not straight (linear). This limitation of the model can be attributed to the numerous linear assumptions in the elements and in the constraint relations. It also can be attributed to lack of knowledge characterizing the crack tip opening and crack tip debonding at the

patched face. At the micro-mechanical level this limitation is serious when trying to predict crack initiation. But, application of the model at the macro-mechanical level does allow accurate predictions of curvature, plate stresses, and unpatched face crack growth. In reality, the unpatched face crack length (the longest crack with the highest stresses) is the critical parameter for predictions in the durability and damage tolerance approach as applied to the repaired plate. The UPF crack consistently has a longer crack length than the PF crack. Tolerance intervals for inspection, required for damage and durability tolerance, should be conservative in nature and therefore should be based on the unpatched face crack length and growth rates. Therefore, the remaining discussion of this chapter will examine the capability of the three layer model to predict the unpatched face crack growth rates for a cracked panel repaired with a composite patch.

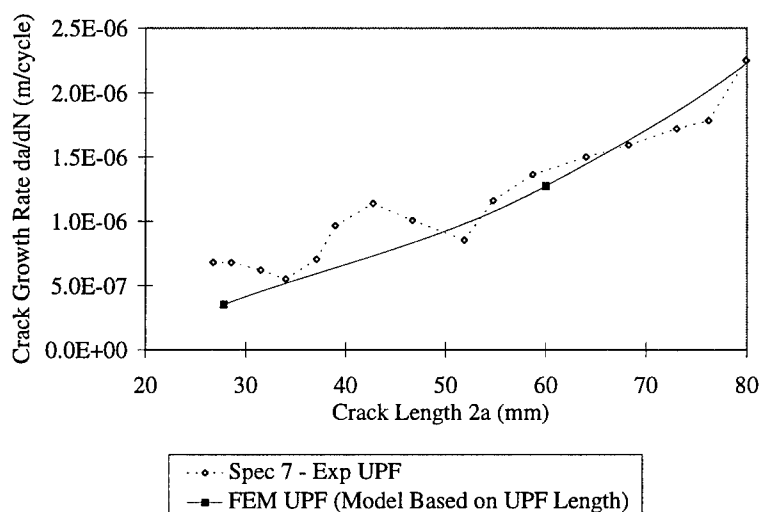


Figure 123. Unpatched Face (UPF) Crack Growth Rate Comparison - Experiment vs. FEM Model Results

In general, comparisons of all of the numerical models to experimental data exhibited consistent, accurate results to crack lengths of at least $2a = 50mm$. To illustrate the comparisons made in

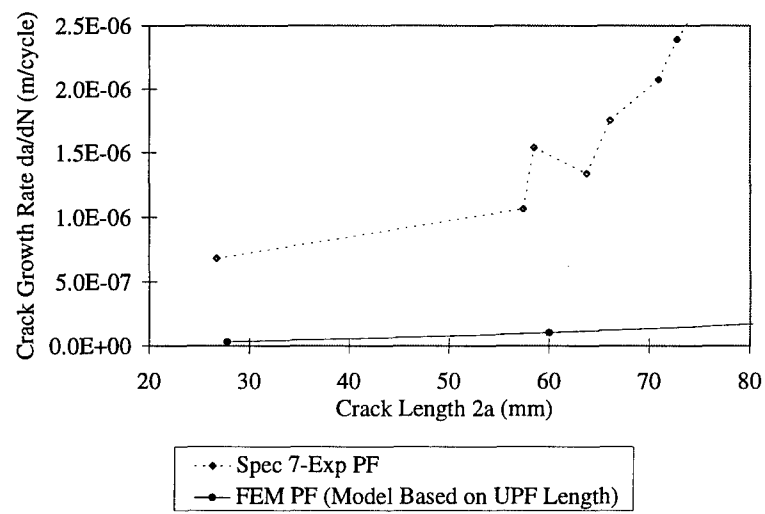


Figure 124. Patched Face (PF) Crack Growth Rate Comparison - Experiment vs. FEM Model

this study, several cases, representing the wide range of experiments, were chosen to demonstrate the comparisons made between numerical and experimental results. Specimens 7 and 18 were chosen to represent the range of thicknesses, i.e. the thickest (6.350 mm) and thinnest (3.175 mm) specimens (best and worst case), respectively. The results for these predictions bound the accuracies of predictions for all other cases modeled. Specimen 25 (6.350 mm thick, $S=1.3$) was chosen as an additional comparison with the final model results to illustrate the results of the higher patch stiffness case. Figures 125 and 126 display the results for FEM models with a fully integral (i.e. no disbond) patch. These initial curves show the accuracy of the model for predicting crack growth rates for Specimen 7, up to a crack length of $2a = 80mm$. The model is accurate to $2a = 50$ to $60mm$ for Specimen 18. Beyond these lengths, the predicted crack growth rates for the numerical prediction are consistently higher than the experimental counterparts (conservative in nature). Differences between the analytical and experimental results in the thin panel are partly due to slight transverse buckling in the more compliant thin panel and a higher amount of plasticity associated with the crack tip. Due to these initially encouraging results of this modeling technique, modifications were attempted to further improve the model's performance. The first of these modifications was to incorporate a disbond between the repair and the plate as observed in the later stages of crack growth in all specimens. This modification is discussed in the next section.

5.6 Disbond Modification

The FEM model initially assumed an integral bond (i.e. no disbond) between the patch and plate as discussed above. Experimental monitoring of the disbond growth showed noticeably larger disbond growth occurs after a crack length of approximately $2a=90mm$. By $2a=100$ to 120 mm, the growth was approaching an area which could be approximated by a disbond equal to the full width of the patch. Naboulsi and Mall had some successes with modelling the full width debond

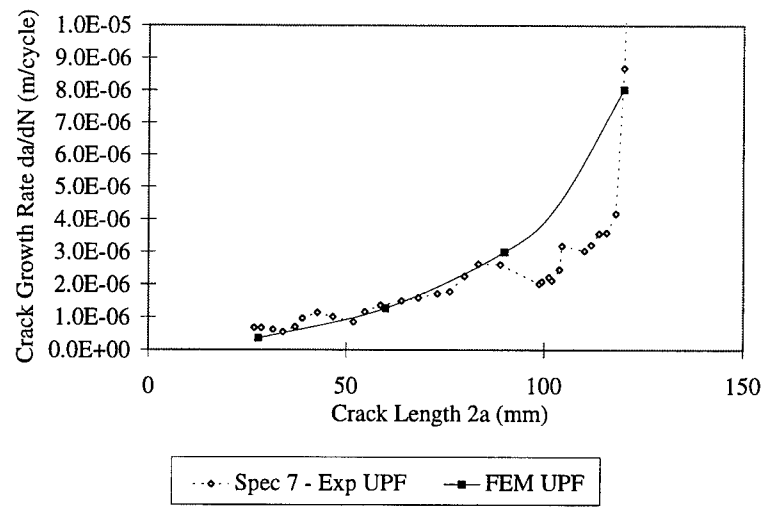


Figure 125. FEM Results Comparison to Specimen 7 Experiment - No Disbond Added

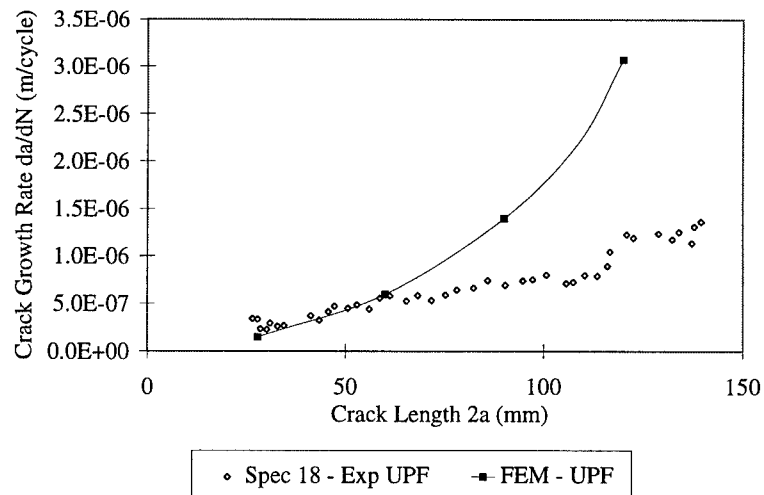


Figure 126. FEM Results Comparison to Specimen 18 Experiment - No Disbond Added

on thin plates (1 mm) [51] which were tested by Denney [16]. Given the fact that the disbond at crack length $2a=90$ mm was negligible and the disbond at $2a=120$ mm was approaching maximum size, it can be assumed that the transition between the integral patch result curve and the disbond modified curve occurs between these points. Therefore, the FEM models for the $2a=120$ mm crack length (102 mm long repairs) were modified to incorporate a full width strip disbond of 35% of the uniform thickness patched area. This approach, using a rectangular disbond area, was used as a simplified first attempt at incorporating the disbond in the three layer model. How this was accomplished is described in subsequent paragraphs. Due to the results from this approach and the size of the disbond in the model, this method was deemed appropriate for this investigation. See Figure 127 for an illustration of the observed (experiment) vs. FEM (analytical) disbond. This area method of approximating the disbond may only be accurate for the large disbond cases. For intermediary steps, refining the curves, a rectangular or elliptical disbond area could be used, the area of which would be determined from experimental observations. The percentage of area (35%) for the disbond was based on the size of debond seen in the experiments with a 102 mm long repair. The same size disbond was observed and used for modifying the short (51 mm) patch models, but, the resulting disbond area was 70% of the uniform thickness patch area. Results showed that disbond of the patches from the repaired specimens caused significant changes in the predictions of COD, specimen deformation, and crack growth rates.

The disbond was incorporated by eliminating the constraint equations of the adhesive to the patch (or disconnecting the associated nodes in the model). This interface between the adhesive and patch is a logical location to place the disbond. This is due to the post-mortem examination of the area of disbond. The separation occurred in the fabric carrier of the FM-73 film adhesive or at the surface interface of the pre-cured Boron/Epoxy patch and the FM-73 adhesive. In reality, for most repair situations, the patch surface preparation is not as extensive as that of the plate. This is true

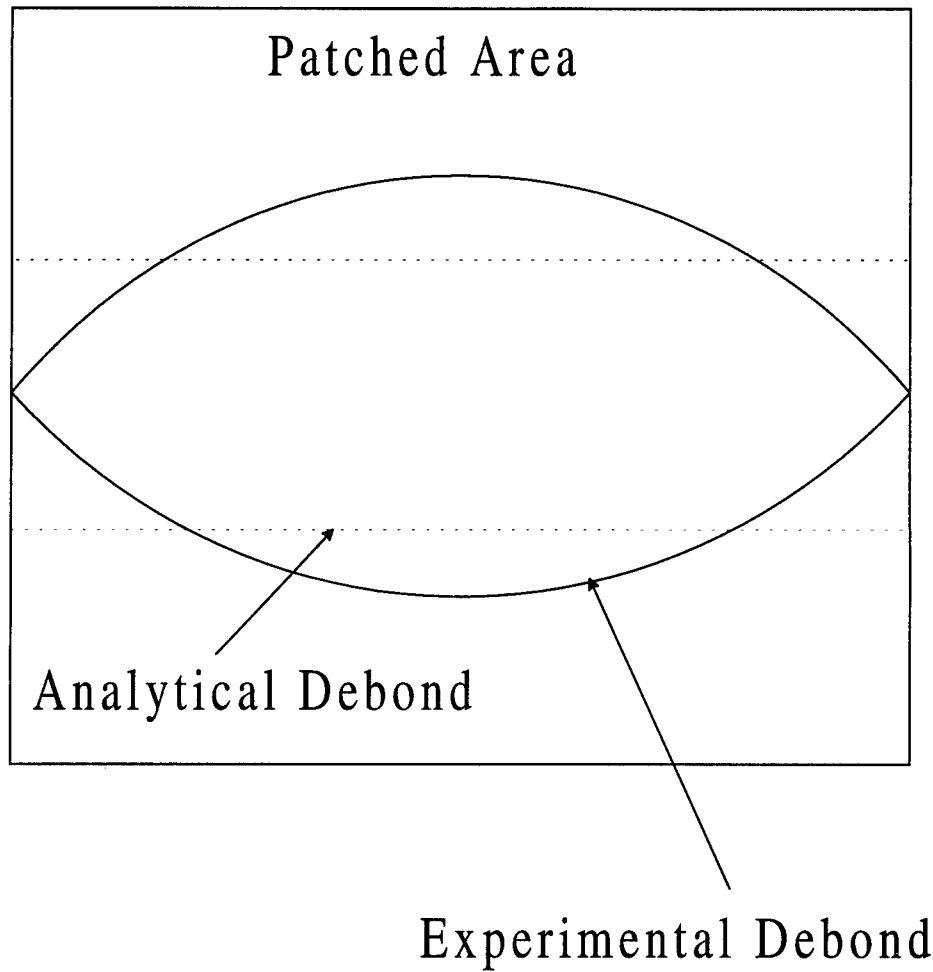


Figure 127. Experimental vs. Analytical Disbond Configuration

due to the fragile nature of the pre-cured patch before bonding; any amount of mishandling could cause flaws in the patch before it is bonded to the plate. Figures 128 , 129, and 130 show the results of the disbond modification for Specimens 7, 18 and 25. Again, these specimens were chosen for comparisons because they represent different cases involving thick plate, thin plate, and high stiffness ratio tests conducted in this study's test series. Note the increase in crack growth rates in the region between $2a=90$ mm and $2a=120$ mm. The increase in growth rate for the model predictions is due to the increased compliance of the model with disbond growth and the resulting increased stress intensity factor on the unpatched face due to increased bending. A dramatic change was seen for the calculated results of final growth rates in the long cracks. The incorporation of debond increases the crack growth rate by approximately 200% for the model of Specimen 7, and almost a magnitude (10 times) for Specimen 18, at crack length $2a=120$ mm. Although the model predictions moved further from the experimental data for crack growth rate, it was found that predictions by the model, with debond added, more closely approximated crack opening displacement, COD, as shown in Figure 120. Since COD is such a strong indicator of the magnitude of bending in these experiments, we should consider this change as a refinement of the model. It should also be noted that the disbond must be considered if the model is to be an accurate representation of the experiment. On a positive note, for the prediction of crack growth rate, the final growth rate changes (i.e. the shape of the crack growth rate curve near failure) are more accurately captured in the model with disbond added. Refer again to Figures 128, 129, and 130. Differences in the magnitude of crack growth rate between the model and experiment are likely due to other physical phenomenon not yet captured by the three layer model. These phenomena are described in the next section.

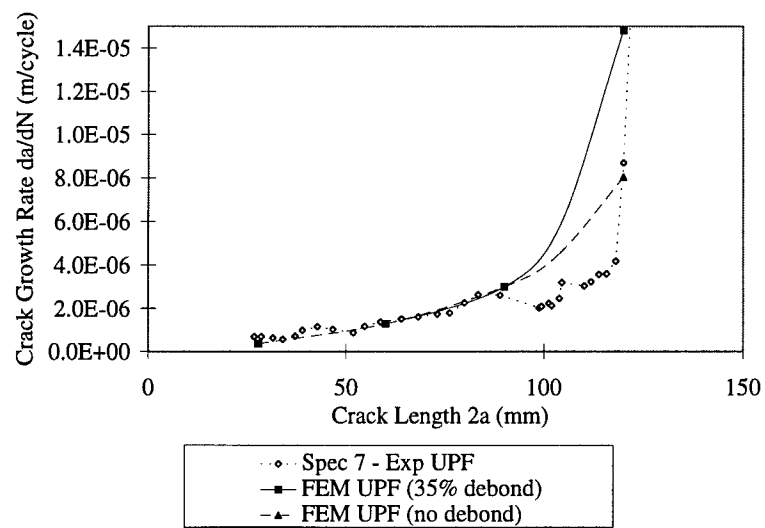


Figure 128. Experimental vs. Numerical Calculation of Crack Growth Rates - 35% disbond added at $2a = 120$ mm

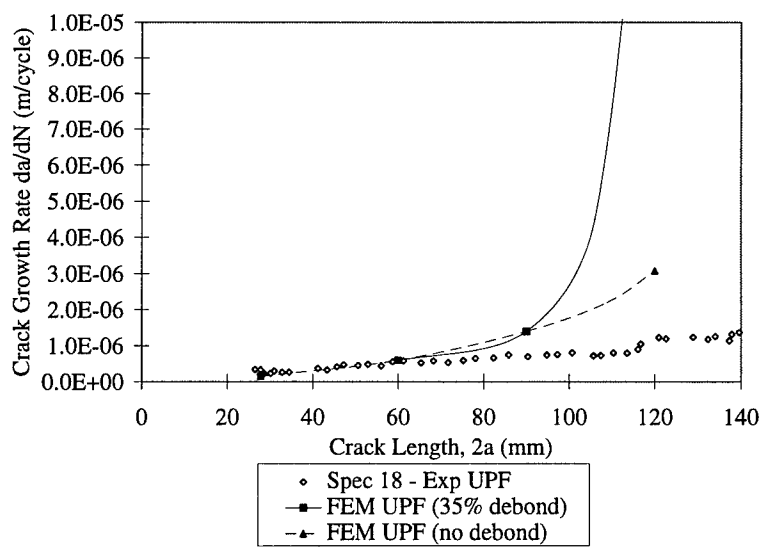


Figure 129. Experimental vs. Numerical Calculation of Crack Growth Rates - 35% disbond added at $2a = 120$ mm

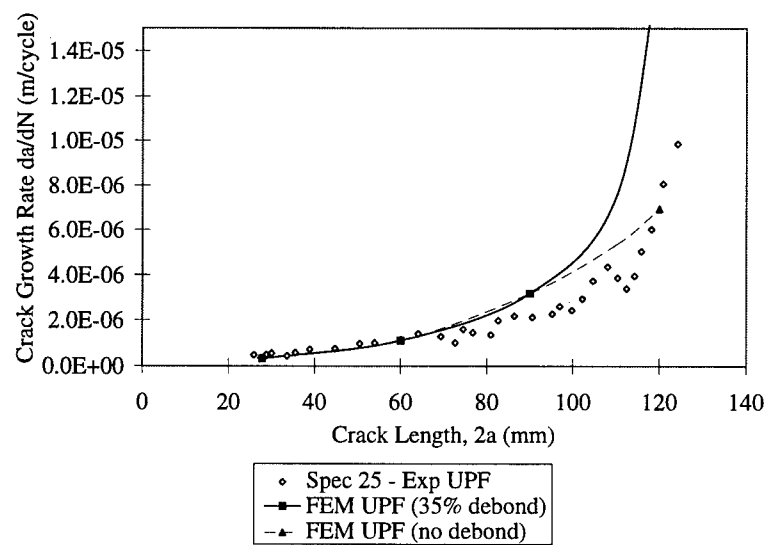


Figure 130. Experimental vs. Numerical Calculation of Crack Growth Rates - 35% disbond added at $2a = 120$ mm

5.7 Limitations of the 3-Layer Model

The 3-layer Mindlin plate model is a 2-dimensional linear-elastic model which is being used to develop predictions for a 3-dimensional physical problem. This approach obviously has this limitation, but, is useful because it is less costly computationally and is a simple, yet accurate approach to an extremely complicated problem. The model provided good predictions for thin (≤ 5 mm) plates with repairs on short cracks (less than $2a=50$ mm) in previous studies for 1 mm thickness panels [50, 51]. It also provided good predictions in this study (3.175 to 6.350 mm thicknesses), but the long crack is not fully characterized by the model results. The long crack solution must address increasingly larger amounts of crack tip plastic zone growth, which depends on the thickness of the specimen and the given crack length. Thick plates have more bending with load and therefore variations in the linearity and self-similar nature of the crack front exist (i.e. uneven crack growth). Thick plates also present some situations of mixed mode crack propagation due to the bending stresses, again dependent upon specimen thickness and the crack length. Although the three layer model was effective in bringing together most aspects of these variations for the experimental specimen configurations, it has not yet addressed the issue of plasticity at the crack tip. The model tends to overpredict the stress intensity factors and crack growth rates on the unpatched faces when cracks are long. Although these estimates are conservative in nature and provide an upper bound to the crack growth rates, improvements to the model are required, as described in the next sections. Yet another factor, which the model cannot yet evaluate, is the 'overload' phenomenon of crack growth retardation. This phenomenon is most likely caused by the rapid debonding of the patch caused by impending unstable crack growth on the unpatched face and is related to the plastic zone size and compressive stress area at the crack tips. (Figures 41 and 47 in Chapter 4 show the growth retardation phenomenon, with experimental data of Specimens 7,9,24, and 25. This phenomena occurred

when cracks reached 90 to 110 mm long. Figure 112 in Chapter 4 gives a graphical representation showing the physical correlation of the growth rate reduction and patch location.)

5.7.1 Effective Crack Length Modification

This section describes an attempt to improve the correlation of the FEM crack growth rate results to experimental measured data by incorporating an adjustment for lag between the unpatched and patched face crack lengths. When cracks are short in the repaired panel, there is little or no difference between mid-plane, patched, and unpatched face crack lengths. When the crack grew enough to produce a large crack lag, as discussed in Chapter 4, the differences in crack lengths between patched and unpatched faces were significant. An initial attempt to improve crack growth rate overpredictions from the FEM models was made by adjusting the models' crack lengths as compared to the experimental crack. In other words, due to the lag of the midplane and patched face crack lengths behind those of the unpatched face length, the model crack lengths were adjusted to account for these differences. The basis of this adjustment was to shift the predicted result of crack growth rates to the right on the crack growth rate versus crack length relationship, proportional to the amount of lag between the patched and unpatched faces. This decreases the resultant crack growth rates for a modeled crack length. This change provided the maximum change in the results when crack lengths were long and when panel thickness was large (i.e. when bending stresses were maximum). For crack lengths where patched to unpatched face crack length lag was small, adjustments to crack length was on the order of 1 mm. For longer length cracks in the thick panels, adjustments of up to 10 mm were used. Figures 131 and 132 display typical results of this crack length adjustment along with the previously incorporated disbond modification to the models. Note the shift right of curves with crack length adjustment. Significantly more improvement in the pre-

dictions for the thick plate are achieved with this modification. Minimal change occurs to the thin plate prediction because the correction is based on very small patched face crack length lag values.

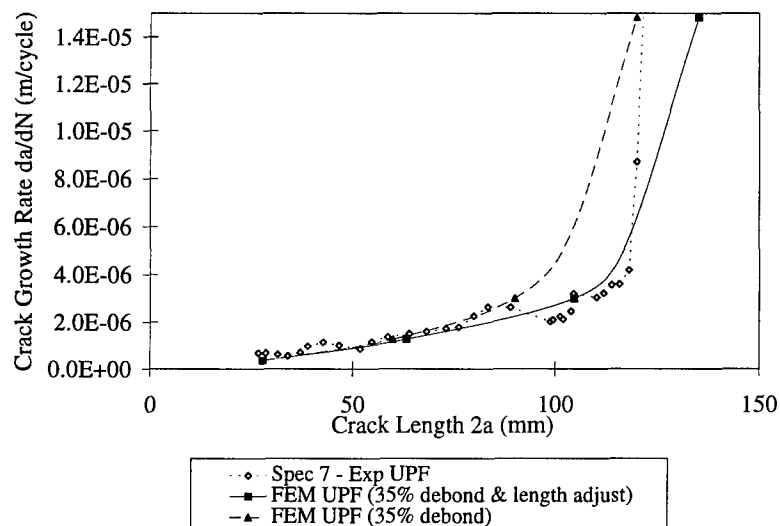


Figure 131. Experimental versus FEM Calculation of Crack Growth Rate - with Disbond and Crack Length Adjustment

The use of 2-dimensional elements and constraints which define through-the-thickness displacements as a linear function of mid-plane displacements, forces a finite element solution for an artificially long crack. For example, assuming a $2a=60$ mm long crack in the model may actually calculate the displacements and rotations for a $2a=70$ mm (dependent on load and bending) crack on the unpatched face. Therefore, it is prudent to assume the model result for $2a=60$ mm can be compared with an unpatched face, $2a=70$ mm crack's growth rate from the experiment. In order to determine the proper adjustment for the model's crack length, the experimental patched face crack lag must be known. (In this case data from eddy current measurements was used.) Figure 133 shows the difference between the assumed FEM crack length and the experimental crack front. It was assumed that the shape of the experimental crack front can also be approximated as linear for ease

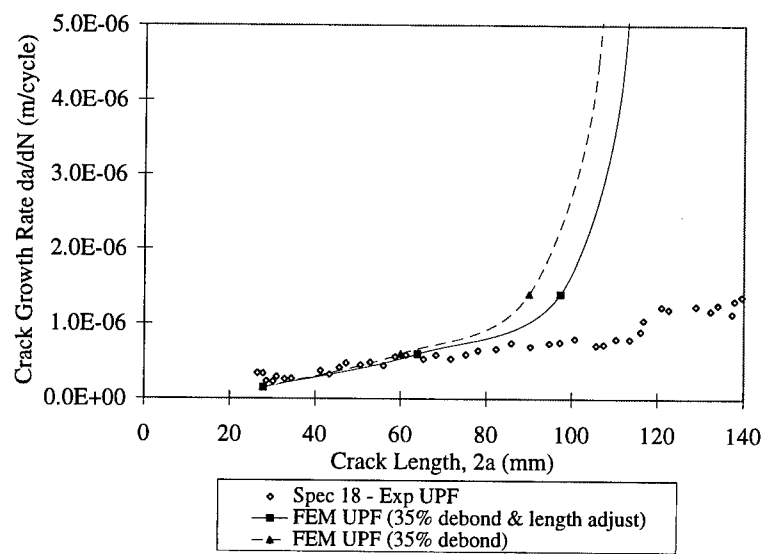


Figure 132. Experimental versus FEM Calculation of Crack Growth Rate - with Disbond and Crack Length Adjustment

of calculation. With this assumption, the resulting half center crack length, a , adjustment for the modelled unpatched face is the assumed model half crack length plus half of the difference in experimentally determined half crack lengths for the unpatched and patched faces, or half of the measured crack lag. As mentioned earlier, the adjustment, as defined, provided a significant improvement to the prediction of crack growth rates of long cracks for the 6.350 mm plates with repair. This extended the accurate region of the model (with the debond correction) from approximately $2a=80$ mm to crack lengths of up to $2a=110$ mm. In the case of the thin (3.175 mm) plate repair, there is only a small amount of crack lag; therefore, the adjustment provides only a small change in the model results. An additional note should be made here that this adjustment method results in large underpredictions of the crack growth rates for extremely long cracks (i.e. near failure).

Although this crack length adjustment method can dramatically improve the thick plate model's results for cracks from $2a=80$ to 110 mm, the benefit of this correction for the thin plate model at long crack lengths is minimal. This is due to the fact that there was a much smaller crack lag in the thin plates. Since the magnitude of the adjustment is directly dependent on the magnitude of the patched face crack lag, it does not provide much improvement to the thin panel results. This method, though it shows some promise in the thick plate cases, was determined to be insufficient for a generalized approach to modify the crack growth rate predictions. Therefore, an empirical weighting factor was developed in the next section (Section 5.7.2) to account for the differences between the numerical three-layer model results and the experimental data. This factor provides a more comprehensive correction to all of the models for a range of plate thicknesses, stiffness ratios, and crack lengths.

5.7.2 Empirical Weighting Factor

The empirical weighting factor described in this section was developed to improve the three-layer FEM model predictions of stress intensity factors. These factors are used with the Paris Law

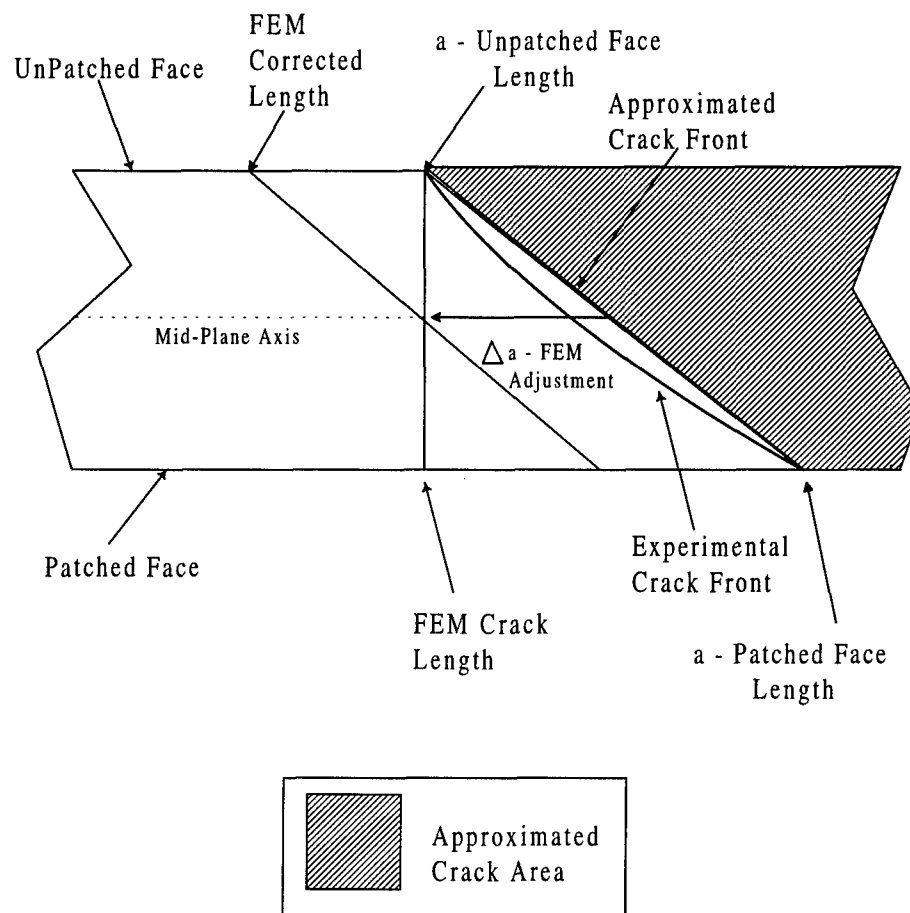


Figure 133. FEM Model Crack Length Adjustment for Effective Area

crack growth relation to calculate crack growth rates in repaired panels. The weighting factor was designed to take into account physical characteristics of the repair problem which were not captured in the original formulation of the linear-elastic 2-D finite element model. The factor used the experimental parameters of plate thickness, patch stiffness ratio, and crack length as empirical variables. These parameters were chosen as a result of their significant influence on crack growth behavior, as shown in Chapter 4. Equation 43 displays the form of modification to the Paris Law incorporating the weighting factor, $\Sigma(t, S, a)$, for determining the crack growth rates, da/dN , in repaired plates.

$$da/dN = C(\Sigma \cdot \Delta K)^m \quad (43)$$

The Paris Law parameters, C and m , are experimentally determined for a given plate thickness and loading conditions. The stress intensity factor range, ΔK , is determined using the 3-layer modeling method with debond modification, and Σ , the empirical weighting factor. The form of the factor, Σ , is as follows:

$$\Sigma = [A \times (1 + B \times (S - 1)) \times (1 + (D \times (t - 3.175)))]t \quad (44)$$

The variable t was the plate thickness, S was the patch to plate stiffness ratio, and the variables A , B , and D (functions of a) are defined as follows:

$$A = 0.4806 - 0.0146a + 0.0004a^2 - (4 \times 10^{-6})a^3 \quad (45)$$

$$B = -0.4523 + 0.0577a - 0.0020a^2 + (2.3333 \times 10^{-5})a^3$$

$$D = -0.2039 + 0.0061a - 0.0002a^2 + (2.5197 \times 10^{-6})a^3$$

where a equals the half-crack length. The above relations were developed and validated in this study for the following ranges of patches:

$$13.9 \leq a(mm) \leq 60 \quad (46)$$

$$3.175 \leq t(mm) \leq 6.350$$

$$1.0 \leq S \leq 1.3$$

Figures 134, 135, and 136 show the calculated unpatched face crack growth rates from Equation 41 compared with the uncorrected model with disbond, as well as experimental unpatched face crack growth rate data for the representative specimens. The results of crack growth rate predictions using this modification were encouraging because they allowed the model, with reasonable accuracy, to predict crack growth rates for all half crack lengths from $a=13.9$ to $a=60$ mm ($2a=27.8$ to 120 mm). The single exception to this conclusion is the 'overload' or growth rate retardation phenomenon. For the large irregularities caused by the retardation, additional work is still necessary to characterize the unpatched face plastic zone size and incorporate an elastic-plastic analysis of the resulting crack growth. This analysis might improve the model slightly but the improvements would be insignificant when compared to the scatter associated with fatigue data.

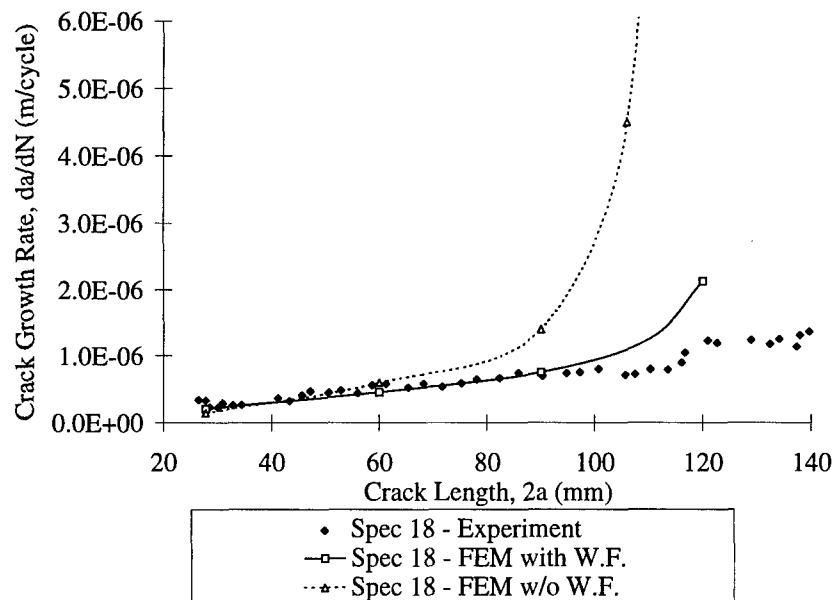


Figure 134. Weighting Factor Results Comparison to Experiment - 3.175 mm Plate, $S=1.0$, Full Width Repair

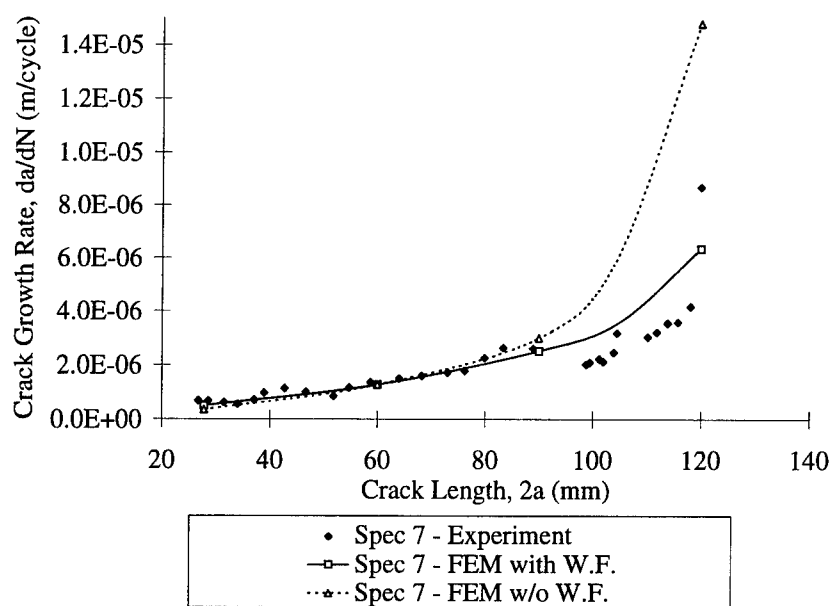


Figure 135. Weighting Factor Results Comparison to Experiment - 6.350 mm Plate, S=1.0, Full Width Repair

The summary of the predicted crack growth relative to the number of fatigue cycles for representative specimens are given in Table 23. These results were obtained by integrating the results of Equation 42 over crack length. Overall, predicted fatigue lives are in good agreement with experimental values. It should be noted here that scatter of data in fatigue lives is generally seen on the same order as the difference between prediction and experiment, i.e. it is not uncommon to scatter within two lifetimes. Predictions were calculated for specimens with finite width repairs, though only for growth within the uniform thickness patched area. Numbers contained in the table show the total predicted cycles to the given crack length starting at its measured starting crack length. Table 24 shows the predictive ability of the model with the weighting factor to determine the life-spans of repeat tests whose experimental data was not used in development of the correction factor Σ , in Equation 44. Tests 7a, 18a, and 25a were executed after the development of Equation

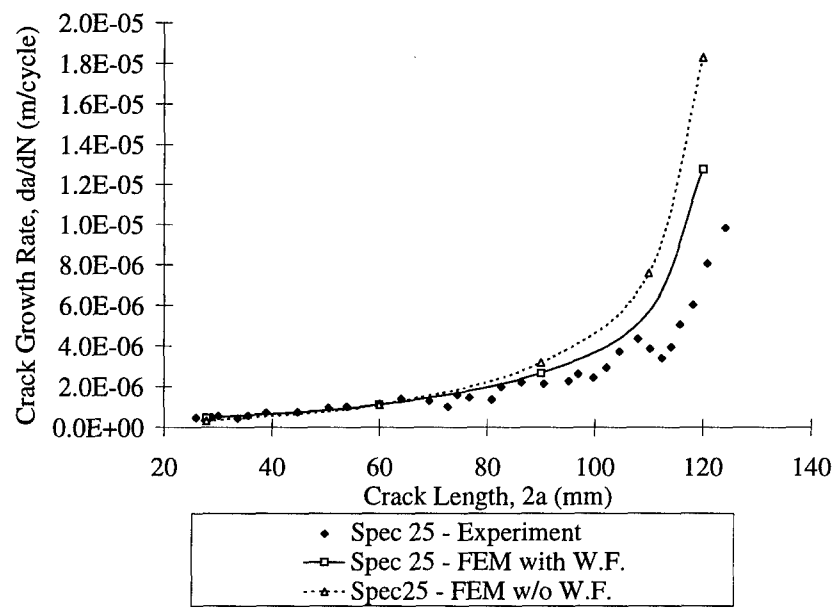


Figure 136. Weighting Factor Results Comparison to Experiment - 6.350 mm Plate, S=1.3, Full Width Repair

44 and these predicted results are in good agreement with experimental values when the scatter in fatigue literature is kept in mind. Thus, the approach and technique shown in this chapter and the weighted modification to the 3-Layer Mindlin plate model, can be used as a simple, economical 2-D (or pseudo-3-D) numerical approach to predict the crack growth rates in cracked structures of aging aircraft and similar vehicles, repaired with composite patches.

Table 23. Life Prediction Results for Weighted 3-Layer Mindlin Model

Specimen No.	Length, 2a	Prediction	Experiment	Ratio (Predicted
Full Width	(mm)	(Cycles)	(Cycles)	to Exp Life)
7 (t=6.350mm, S=1.0)	26.748	Start	0	-
	27.8	1041	862	1.20
	60	21342	20486	1.05
	90	29986	29213	1.03
	120	33901	35592	0.95
18 (t=3.175mm, S=1.0)	26.5	Start	0	-
	27.8	3245	1500	2.16
	60	73953	48511	1.52
	90	99067	73787	1.34
	120	111066	92268	1.20
25 (t=6.350mm, S=1.3)	25.903	Start	0	-
	27.8	2405	1809	1.33
	60	25370	26937	0.94
	90	33129	37910	0.87
	120	37023	42920	0.86
Finite Width				
22 (t=6.350mm, S=1.0)	25.315	Start	0	-
	27.8	2507	1886	1.33
	50	18903	23028	0.82
23 (t=6.350mm, S=1.3)	26.002	Start	0	-
	27.8	2276	1572	1.45
	50	21424	21305	1.01
26 (t=3.175mm, S=1.0)	25.164	Start	0	-
	27.8	6687	4394	1.52
	50	49224	37257	1.32

Table 24. Life Prediction Results for Weighted 3-Layer Mindlin Model-Repeat Tests

Specimen No.	Length, 2a	Prediction	Experiment	Ratio (Prediction
Full Width	(mm)	(Cycles)	(Cycles)	to Exp Life)
7a (t=6.350mm, S=1.0)	26.023	Start	0	-
	27.8	1776	1183	1.50
	60	22946	25857	0.89
	90	31589	34323	0.92
	120	35505	39038	0.91
18a (t=3.175mm, S=1.0)	25.992	Start	0	-
	27.8	4542	2228	2.04
	60	60086	52978	1.13
	90	84925	81330	1.04
	120	97198	105407	0.92
25a (t=6.350mm, S=1.3)	25.976	Start	0	-
	27.8	2310	1163	1.99
	60	26363	27495	0.96
	90	34121	37477	0.91
	120	36927	41086	0.90

6. Summary, Conclusions, and Recommendations

6.1 Summary

Budgetary constraints, both military and civilian commercial, are causing a demand to extend the usable lives and reduce the long-term costs of the current aircraft fleet. Bonded composite repair applied to cracked aluminum structural components is one alternative to direct replacement of these aging aircraft components. Repairs have been successfully tested on thin fuselage skins (1-3 mm) and similar thickness components but have not yet been fully characterized for use on 'thick' components: in particular for parts greater than 5 mm thick (such as lower wingskins and other load-bearing members).

Experiments are needed to examine the post-repair characteristics of these composite repairs. Also, an inexpensive modeling technique is required for prediction of the crack growth rates and for determination of inspection intervals after application of the composite patch. Hence, the research conducted in this study and the development/validation of an applicable modeling tool were focused in this direction.

A hybrid experimental-numerical study was accomplished to validate a pseudo-3D numerical modeling method for predicting crack growth rates in cracked panels repaired with composite patches. Tests were performed on center cracked aluminum panels for thicknesses ranging from 3.175 mm to 6.350 mm. Plate material properties and Paris Law constants for fatigue crack propagation were experimentally determined. Plates were repaired with unidirectional boron/epoxy composite patches. These repairs involved different lengths, patch to panel stiffness ratios, and widths. Thermally induced curvatures (measured as out-of-plane displacements) were quantified. Experimental fatigue test data for 120 MPa, $R=0.1$, and a sinusoidal 10 Hz frequency were collected from the repaired specimens. Data included measurements for the patched and unpatched face crack

growth, center crack opening displacement, surface strains, and disbonds. Eddy current measurements and post-mortem analysis of specimens showed significant crack lag between the patched and unpatched faces due to induced bending, the non-uniform crack front profile, and the mode of failure for the asymmetric repairs.

A three-layer Mindlin plate finite element modelling technique was used to provide accurate numerical calculations of the crack tip loads and displacements in the repaired panel. These quantities were then used to calculate strain energy release rates and, subsequently, stress intensity factors using the modified crack closure method. Fatigue crack growth rates were determined using material properties and the Paris Law crack growth relation.

6.2 Conclusions

Results from the experimental phase of this study provided the following conclusions:

(1) Changes in panel thickness directly influence crack growth rates in both unrepaired and repaired panels. At a given stress level, increased panel thickness causes increased crack growth rate and decreased life-span. The application of repairs increased life-spans over those of the unrepaired panels. The differences between crack growth rates of different unrepaired panel thicknesses were exaggerated when a repair was applied.

(2) The non-isotropic character of the repaired panels with a composite patch having a unidirectional lay-up causes coupled longitudinal and transverse bending in panels of finite width. Simple strength of material prediction methods, by themselves, are insufficient to characterize these coupled bending effects caused by thermal CTE mismatch in these laminates.

(3) Thermally-induced transverse bending was inversely proportional to longitudinal bending in thin panels. This coupled effect, which increases transverse curvature, causes increased bending (longitudinal) stiffness in thin plates, thus decreasing longitudinal bending due to the CTE mismatch.

Therefore, longer patches on thin plates reduce initial thermal curvature which increases the fatigue life.

(4) On the other hand, less benefit (crack growth rate reduction) is achieved by increasing the length of thick panel repairs. Longer patches on thick panels increase curvatures and thus increase bending stresses when the panel is loaded. Increased bending causes increased crack growth rates, and thus reduction a reduction in fatigue life.

(5) Increasing patch stiffness ratio increases repaired panel life-span. Results from tests of more stiff repairs show fewer crack growth anomalies (scatter or retardation) and crack growth rates are therefore more predictable.

(6) Patch width has only a small effect on crack growth rate. Similar crack growth rates were observed within patches' uniform thickness areas, regardless of width. Designs for patch width, excluding the tapered edges, should be therefore governed by the maximum allowable crack size.

(7) Disbond growth rate and size significantly affects crack growth rate. Disbond growth was minimal for short cracks and no taper disbonds were observed. Disbond growth is dependent on crack size rather than on patch configuration. Disbond growth initiates or accelerates when the crack growth reaches tapered areas in the patch or when the stress intensity factor for the crack exceeds its critical value. This disbond growth may also be due to crack growth rate retardation due to rapid specimen compliance changes.

(8) Asymmetric repairs cause significant plate bending which results in non-uniform crack front progression in thick specimens. The slower crack growth at the patched face crack is dependent upon the plate and patch thicknesses (or stiffnesses). This lag is existent in all plate thicknesses and for all patch sizes, though it is more prevalent with increasing plate thickness.

The following conclusions were drawn from the analysis performed with the numerical model:

(1) The three-layer Mindlin plate model consistently provides an accurate prediction of unpatched face crack growth rates for crack length less than $2a=50$ mm. For longer cracks, modification is necessary to accurately predict crack growth rates. With this modification (based on patch stiffness ratio, crack length, and panel thickness), the model is accurate predicting crack growth to within a factor of two up to $2a=120$ mm for the range of specimens tested in this study.

(2) This study shows the analysis method, using the three-layer Mindlin plate model, is a simple yet accurate tool for predicting the crack growth rates in cracked aluminum panels repaired with a bonded composite patch.

6.3 Recommendations for Future Research

Recommendations for further research in this topic area include:

(1) The effects of thermal residual stresses and deformations due to laboratory fatigue loading need to be quantified to extend the findings of this study to the repair conditions of restrained structure (with stringers etc.) on aircraft. This would allow the current model to predict the fatigue crack growth in restrained structures with only minor corrections.

(2) A parametric study into the effect of anisotropic laminate bending on repaired plate stiffness would provide the necessary insight for minimizing thermal bending effects. Quantifying the changes in stiffness due to the laminated plate properties would improve predictions of thermal bending.

(3) The effect of plasticity and when it must be incorporated needs to be studied for long cracks ($2a > 50$ mm). With more information, the 'overload' phenomena and crack growth retardation would become more predictable with the current modelling techniques.

(4) A method to incorporate simultaneous disbond growth and crack growth in the numerical model would provide more accurate predictions of fatigue crack growth rates after the initiation of disbond.

APPENDIX A Additional Crack Growth Rate Data

The figures contained in this appendix show, in more detail, the experimental crack growth rate data for selected specimens. Scales on the Figures have been changed from data in the body of this document to show only crack lengths up to $2a = 60$ mm. Curve fits shown on the charts are exponential fits to the data shown in the charts.

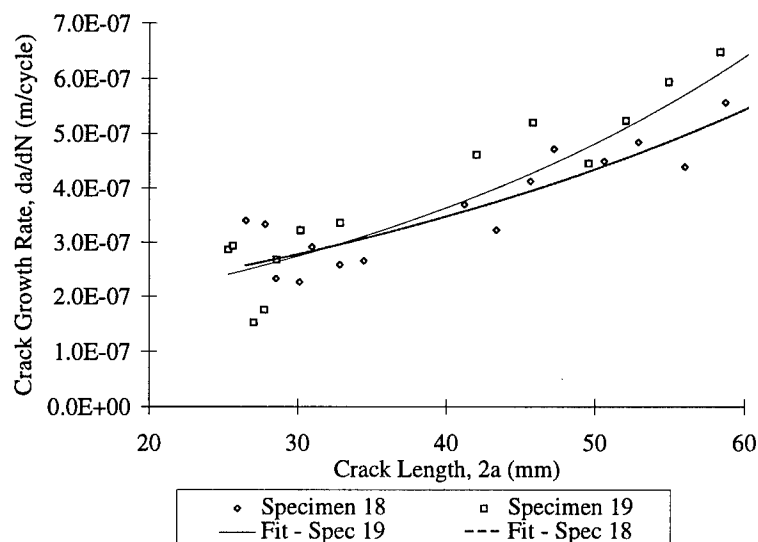


Figure 137. Short Crack Growth Rates, da/dN , 3.175 mm Thick Plates, $S=1.0$, Full Width Repairs

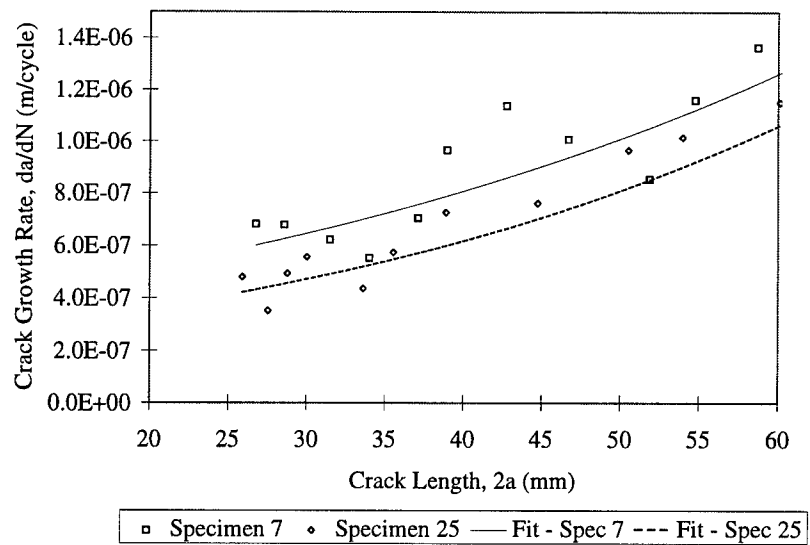


Figure 138. Short Crack Growth Rates, da/dN , 6.350 mm Thick Plates, 102 mm Long, Full Width Repairs

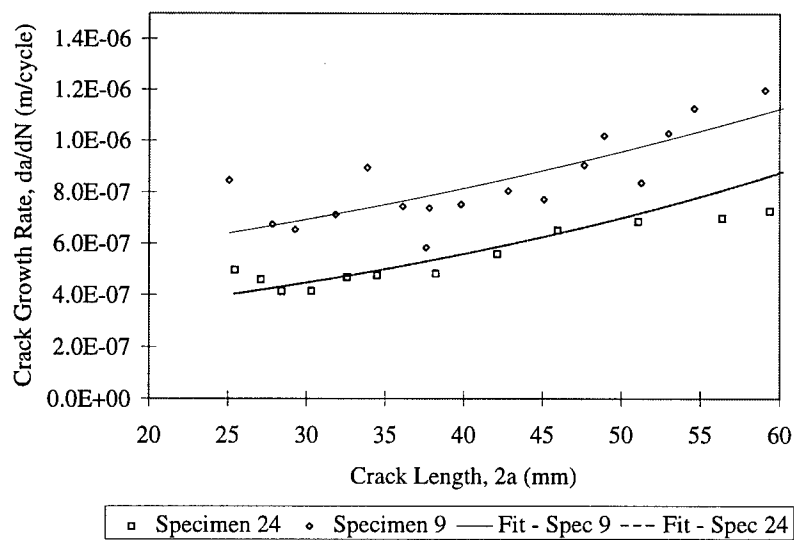


Figure 139. Short Crack Growth Rates, da/dN , 6.350 mm Thick Plates, 51 mm Long, Full Width Repairs

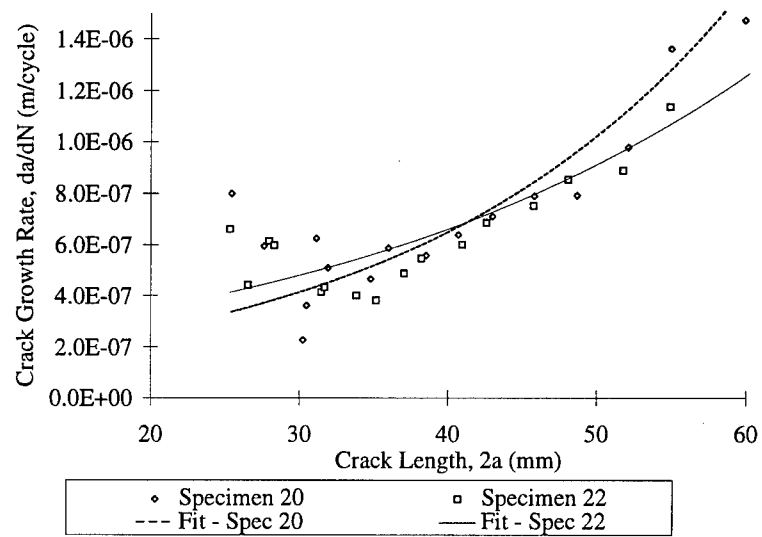


Figure 140. Short Crack Growth Rates, da/dN , 6.350 mm Thick Plates, $S=1.0$, 50 mm Wide Repairs

APPENDIX B Post-Failure Images

This appendix contains select pre and post-failure images of specimens detailing disbond and patch breakage characteristics. Note the longitudinal disbond size in each case is similar, as discussed in Chapter 4. No edge or corner debonds were noted and some patch failure was noted in the thin areas of tapers.

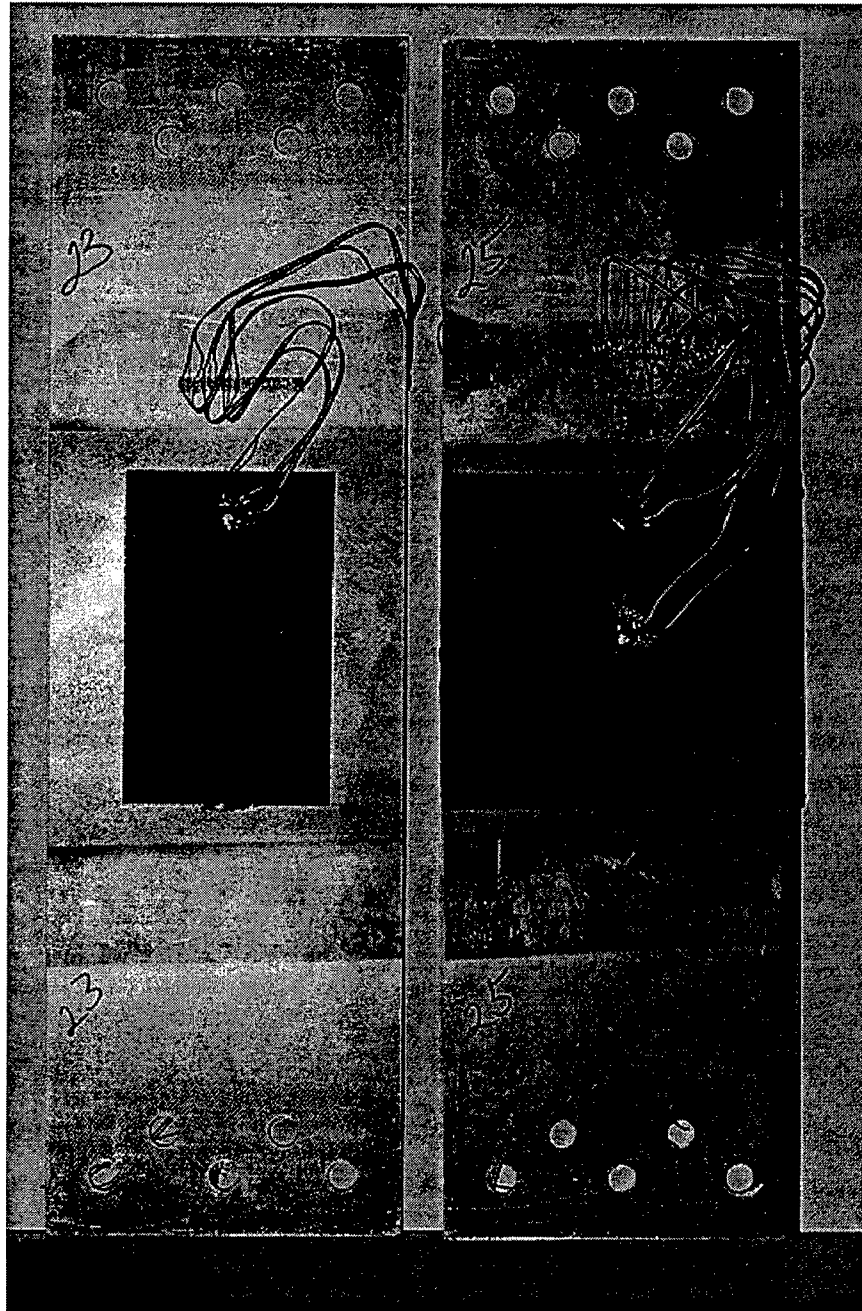


Figure 141. Pre-Failure Specimens - Full Width and Finite Width (50 mm Nom)

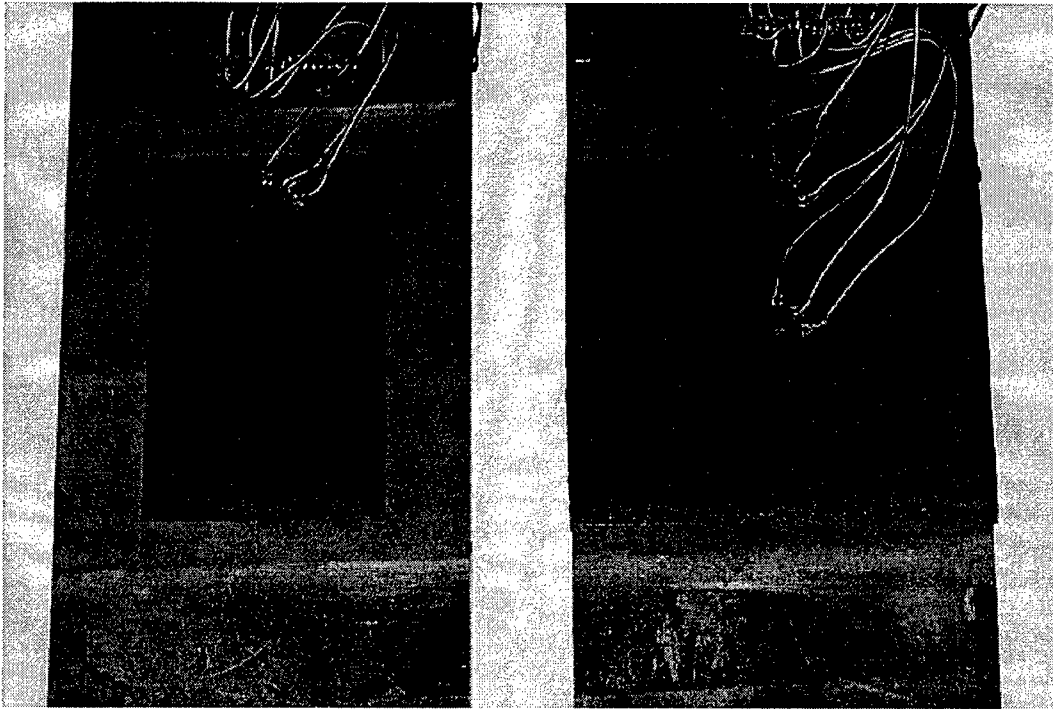


Figure 142. Pre-Failure Specimens - Close-up of Full Width and Finite Width Patches

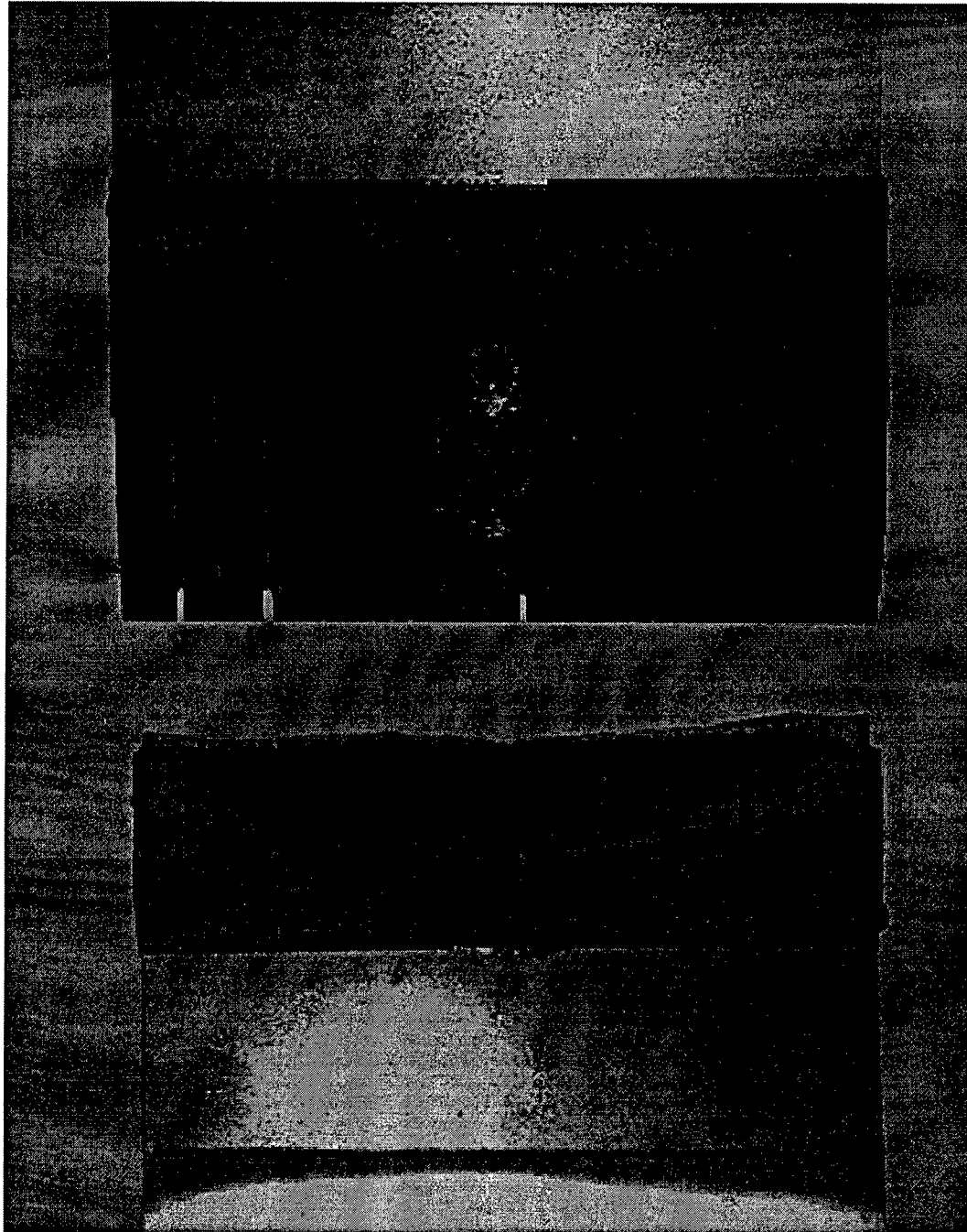


Figure 143. Post-Failure Full Width Repair - Adhesive Surface and Patch

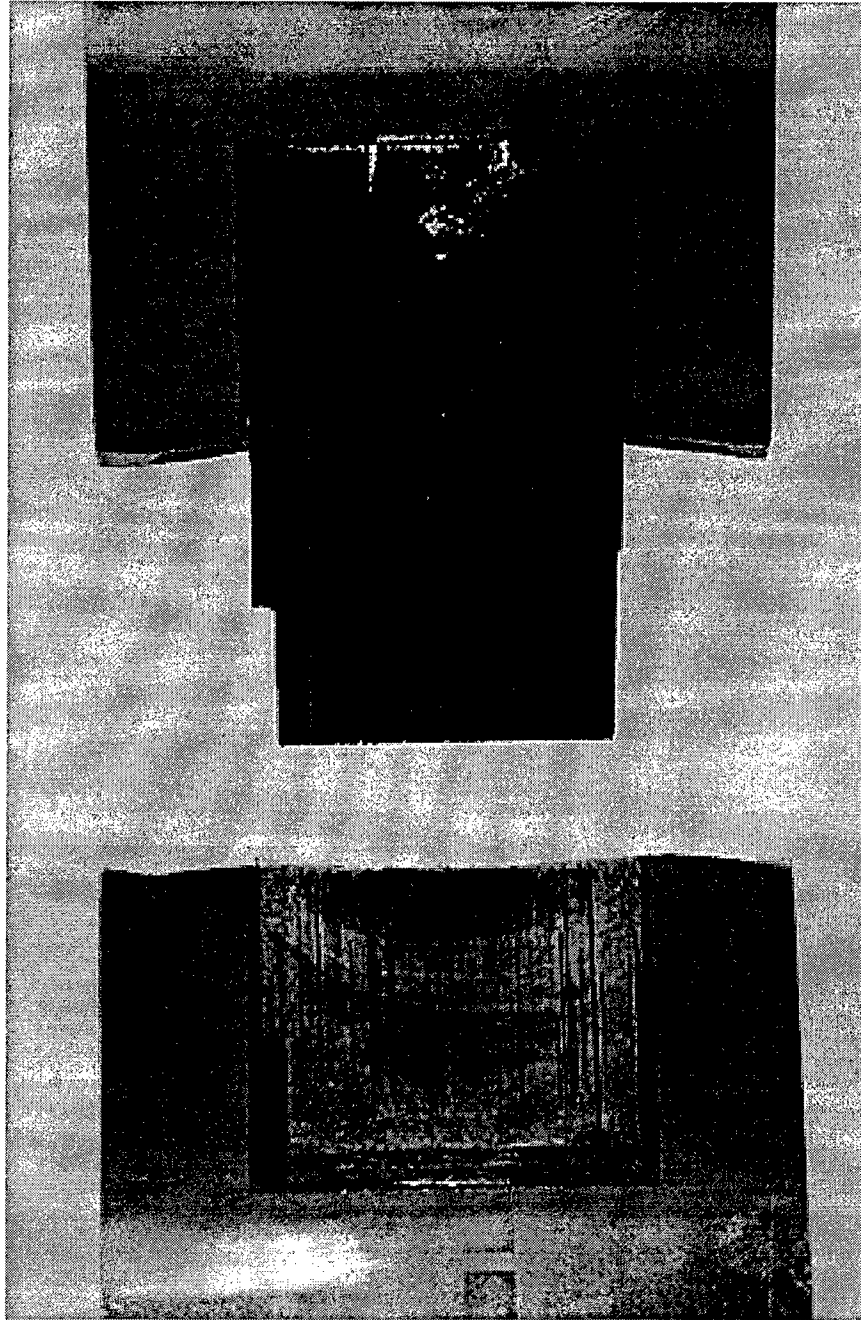


Figure 144. Post-Failure Finite Width Repair - 102 mm Long Adhesive Surface and Patch

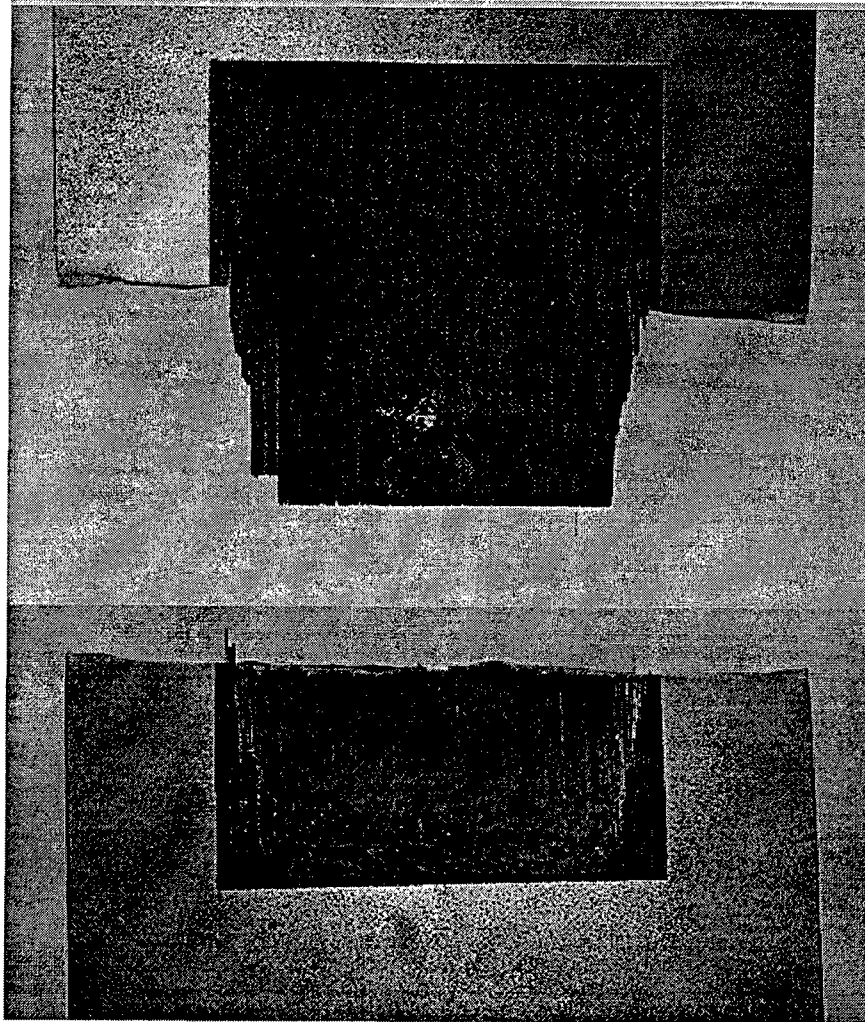


Figure 145. Post-Failure Finite Width Patch - 51 mm Long Adhesive Surface and Patch

APPENDIX C Repeat Tests

This appendix contains crack growth curves for patched specimen repeat tests.

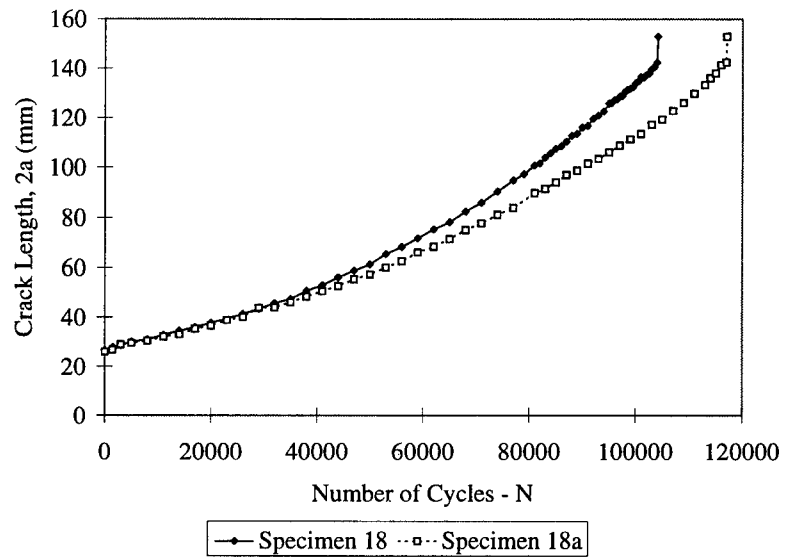


Figure 146. Repeat Test Comparison - 3.175 mm Thick Panel, 102 mm Long, Full Width, $S=1.0$ Repair

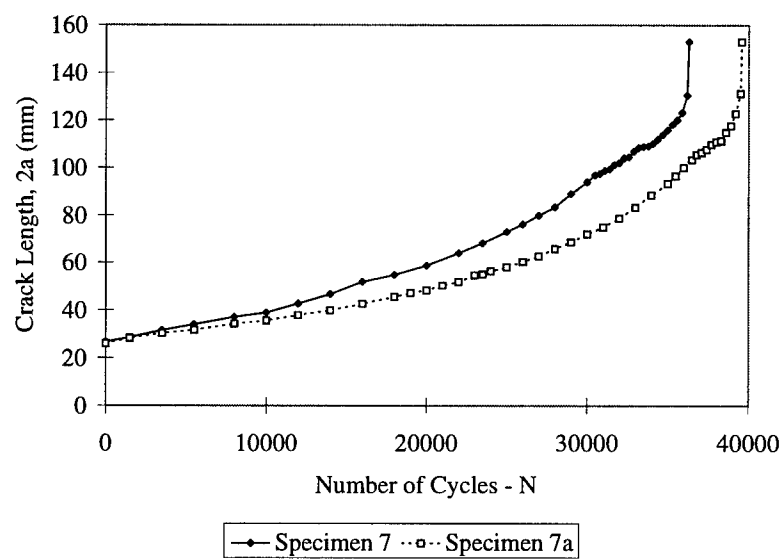


Figure 147. Repeat Test Comparison - 6.350 mm Thick Panel, 102 mm Long, Full Width, S=1.0 Repair

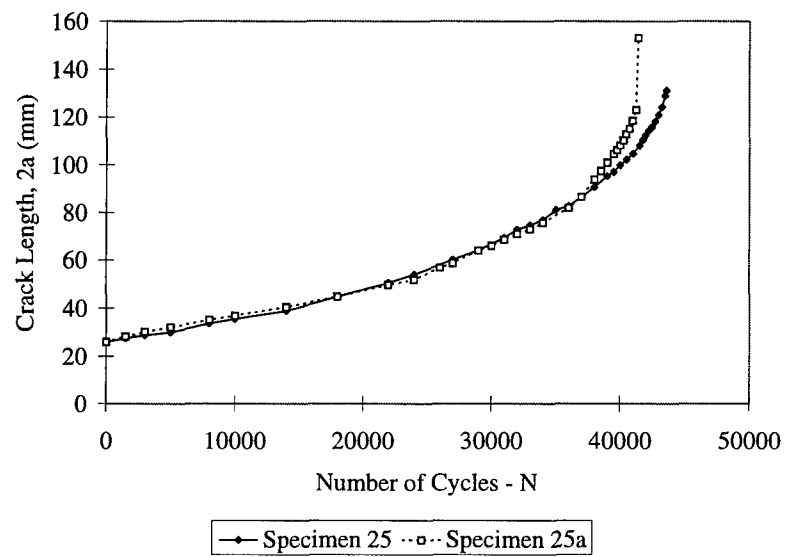


Figure 148. Repeat Test Comparison - 6.350 mm Thick Panel, 102 mm Long, Full Width, S=1.3 Repair

BIBLIOGRAPHY

- [1] "Certification of Shipped Specifications." Copper and Brass Sales Shipping Notice, 1995. 15 Sep, Dayton, OH.
- [2] Arendt, C. and C. T. Sun. "Bending Effects of Unsymmetric Adhesively Bonded Composite Repairs on Cracked Aluminum Panels." *Annual Report for Air Force Office of Scientific Research, Grant No. F49620-93-1-0377, prepared by A. F. Grant, Jr.* A9-1-A9-7. Purdue University, School of Aeronautics and Astronautics, 1994.
- [3] ASTM, "ASTM Standard E 647."
- [4] Baker, A. A. "Bonded Composite Repair of Metallic Aircraft Components – Overview of Australian Activities." (2) 1.1–1.14.
- [5] Baker, A. A., "F-111 Lower Wing Skin Repair Brief at AFIT - 1995."
- [6] Baker, A. A. *Bonded Repair of Aircraft Structures*. Martinus Nijhoff, 1988.
- [7] Baker, A. A. "Repair Efficiency in Fatigue-Cracked Aluminum Components Reinforced with Boron/Epoxy Patches," *Fatigue Fract. Engng Mater. Struct.*, 16:7 753–765 1993.
- [8] Baker, A. A., *et al.* "Repair of Mirage III Aircraft Using the BRFP Crack-Patching Technique," *Theor and Appl. Fracture Mechanics*, 2 1–15 1984.
- [9] Belason, E. B. "Bonded Doublers for Aircraft Structure Repair," *Aerospace Engineering*, July 13–18 1995.
- [10] Belason, E. B. "Fatigue and Static Ultimate Stress of Boron/Epoxy Doublers Bonded to 7075-T6 Aluminum with Simulated Crack." *18th Symposium of the International Conference on Aeronautical Fatigue, Melbourne, Australia*. 4 May 1995.
- [11] Broek, D. and J. Schijve. "The Influence of the Mean Stress on the Propagation of Fatigue Cracks in Aluminum Alloy Sheets," *National Aerospace Institute, Amsterdam, TR-M-2111* 1963.
- [12] Broek, D. and J. Schijve. "The Influence of Sheet Thickness on Crack Propagation," *Aircraft Engineering*, 38 11, 31–33 Nov, 1966.
- [13] Broek, David. *Elementary Engineering Fracture Mechanics*. Dordrecht: Martinus Nijhoff, 1987.
- [14] Caisheng, Z., M. Heller and YC. Lam. "Analytical Formulae for calculating stresses in unidirectional/cross-ply unbalanced laminates," *Composite Structures*, 24 333–343 1993.
- [15] Chue, Ching-Hwei, Li-Chung Chang and Jang-Shing Tsai. "Bonded Repair of a Plate with Inclined Central Crack Under Biaxial Loading," *Journal of Composite Structures*, 28 39–45 1994.
- [16] Denney, Jason Capt. *Fatigue Response of Cracked Aluminum Panel with Partially Bonded Composite Patch*. MS thesis, U.S. Air Force Institute of Technology, 1995.
- [17] Erdogan, F. "Crack Propagation Theories," *Aerospace Engineering, NASA-CR-901* 1967.
- [18] Forman, R.G., V.E. Kearney-R.M. Engle. "Numerical Analysis of Crack Propagation in Cyclic-Loaded Structures," *Journal of Basic Engineering*, 89D 459–464 1967.

- [19] Fredell, R., Dr. I. J. Schijve and A. Lizza. "Damage-Tolerant Repairs to Pressurized Fuselages: 'Soft-Patching' with GLARE Fiber Metal Laminates." *Presented to 18th ICAF Symposium, May, Melbourne, Australia*. 1995.
- [20] Fredell, R. PhD dissertation, Department of Mechanical Engineering, University of Delaware, 1992.
- [21] Fredell, R., R. Muller and L. Butkus. "Bonded Repair of Multiple Site Damage with GLARE Fiber Metal Laminate Patches." *Proceedings of the 1994 Aircraft Structural Integrity Program Conference, December, San Antonio, TX*. 1994.
- [22] Fredell, R., W. van Barneveld and Dr. A. Vlot. "Analysis of Composite Patching of Fuselage Structures: High Patch Elastic Modulus Isn't the Whole Story." *Proceedings of the 39th International SAMPE Symposium, April 11-14, Anaheim, CA*. 1994.
- [23] Fredell, R., W. van Barneveld and L. B. Vogelesang. "Design and Testing of Bonded GLARE Patches in the Repair of Fuselage Fatigue Cracks in Large Transport Aircraft." *Proceedings of the 39th International SAMPE Symposium, April 11-14, Anaheim, CA*. 1994.
- [24] Gallagher, J. *Damage Tolerant Design Handbook: A Compilation of Fracture and Crack Growth Data for High-Strength Alloys*. Technical Report MCIC-HB-01R, Volume 3, Metals and Ceramics Information Center - BATTELLE, Columbus Laboratories, December 1983.
- [25] Hagemaiier, Donald J. *Fundamentals of Eddy Current Testing*. Columbus, OH: The American Society for Nondestructive Testing, Inc., 1990.
- [26] Hart, Karl, "Structural Integrity of Aging Aircraft." Wright Laboratories Structures Division Briefing, 1994.
- [27] Heller, M. "Stress Intensity Factors for Patched Structures with No Out of Plane Bending Restraint." Aeronautical Research Laboratory - Minute Paper 8/4/93.
- [28] Heller, M. and R. Jones. "Numerical Analysis of Bonded Repairs For Fastener Holes with Three-Dimensional Cracks," *Engineering Fracture Mechanics*, 33 81-90 1989.
- [29] Heller, M., T. G. Hill J. F. Williams and R. Jones. "Increasing the Fatigue Life of Cracked Fastener Holes Using Bonded Repairs," *Theor. and Appl. Fracture Mechanics*, 11 1-8 1989.
- [30] Irwin, G.R. "Fracture," *Handbook Physik*, 6 551 1958.
- [31] Jin-long, Jiang and Zhao Ming-ban. "An Analysis of Bonded Repairs for Cracked Sheets with Composite Patch," *Chinese Journal of Aeronautics*, 5(3) 190-195 1992.
- [32] Jones, R., L. Molent A. A Baker and M. J. Davis. "Bonded Repair of Metallic Components: Thick Sections," *Theor. and Appl. Fracture Mechanics*, 9 61-70 1988.
- [33] Jones, R., M. Davis R. J. Callinan and G.D. Mallinson. "Crack Patching: Analysis and Design," *J. Structural Mechanics*, 10(2) 177-190 1982.
- [34] Jones, R. "Bonded Repair of Damage," *Journal of Aero. Soc. of India*, 36:3 193-201 1984.
- [35] Jones, R. and R. J. Callinan. "Finite Element Analysis of Patched Cracks," *J. Structural Mechanics*, 7(2) 107-130 1979.
- [36] Jones, R. and R. J. Callinan. "Thermal Considerations in the Patching of Metal Sheets with Composite Overlays," *J. Structural Mechanics*, 8(2) 143-149 1980.

- [37] Jones, R. and R. J. Callinan. "Bonded Repair To Surface Flaws," *Theor. and Appl. Fracture Mechanics*, 2 17-25 1984.
- [38] Jones, R., R. J. Callinan and K. C. Aggarwal. "Stress Analysis of Adhesively Bonded Repairs to Fibre Composite Structures." *ARL-STRUC-REPORT-386*. Department of Defence, Defence Science and Technology Organisation, Aeronautical Research Laboratories, Melbourne, Victoria, Commonwealth of Australia, 1981.
- [39] Jones, R., R. J. Callinan and K. C. Aggarwal. "Analysis of Bonded Repairs to Damaged Fibre Composite Structures," *Engineering Fracture Mechanics*, 17 37-46 1983.
- [40] Kan, H. P., M. M. Ratwani. "Composite Patch Repair of Thick Aluminum Structures - Final Report, Airtask No. WF41-400, PE 62241." *Report No. NADC-82139-60*. United States Navy - Naval Air Development Center, Warminster, PA 18974, 1983.
- [41] Kreyszig, E. W. *Advanced Engineering Mathematics*. New York: John Wiley and Sons, 1988.
- [42] Labor, J. D., M. M. Ratwani. "Development of Bonded Composite Patch Repairs for Cracked Metal Structure - Final Report." *Report No. NADC-79066-60 Vol I*. United States Navy - Naval Air Development Center, Warminster, PA 18974, 1980.
- [43] Lam, Y. C., Zhu Caisheng and M. Heller. "Stress Analysis of Plates with Bonded Unbalanced Laminates." Unpublished - To be Published in *Journal of Composite Structures*, 1995.
- [44] Lena, M. and C. T. Sun. "Repair of Cracked Aluminum Plates With Adhesively Bonded Composite Patches." *Annual Report for Air Force Office of Scientific Research, Grant No. F49620-93-1-0377, prepared by A. F. Grant, Jr.* A10-1-A10-5. Purdue University, School of Aeronautics and Astronautics, 1994.
- [45] Mallick, P. K. *Fiber-Reinforced Composites* (2nd revised Edition). New York: Marcel Decker, 1993.
- [46] Meyers, M.A. and K.K. Chawla. *Mechanical Metallurgy*. Prentice-Hall, Inc., 1984.
- [47] Muki, Rokuro and Eli Sternberg. "On the Stress Analysis of Overlapping Bonded Elastic Sheets," *Int. Journal of Solids and Structures*, 75-94 1968.
- [48] Naboulsi, S., S. Mall. "Characterization of Fatigue Crack Growth in Adhesively Bonded Repairs of Cracked Aluminum Panels."
- [49] Naboulsi, S., S. Mall. "Modeling of Cracked Metallic Structure with Bonded Composite Patch Using Three Layer Technique." To appear in "Composite Structures".
- [50] Naboulsi, S., S. Mall. "Thermal Effects on Adhesively Bonded Composite Patch Repair of Cracked Aluminum Panels." To appear in "Theoretical and Applied Fracture Mechanics Journal".
- [51] Naboulsi, S., S. Mall and J. Denney. "Analysis of Fatigue Crack Growth in Imperfectly Bonded Composite Patch Repairs of Cracked Aluminum Panels."
- [52] Ott, James. "NSTB Raps Aloha, Aviation System for Fuselage Failure," *Aviation Week and Space Technology*, 24-27 May 29, 1989.
- [53] Paul, J., R. A. Bartholomeusz and R. Jones. "Bonded Composite Repair of Cracked

Load-Bearing Holes," *Engineering Fracture Mechanics*, 48 455-461 1994.

- [54] Ratwani, M. M. "Analysis of Cracked, Adhesively Bonded Laminated Structures." *Paper No. 78483R, AIAA/ASME 19th Structures, Structural Dynamics and Materials Conference, Bethesda, MD.* 988-994. American Institute of Aeronautics and Astronautics Special Publications, 1290 Avenue of the Americas, New York, NY 10019., 1978.
- [55] Roach, D. "Performance Analysis of Bonded Composite Doublers on Aircraft Structures." *Composite Repair of Aircraft Structures - Vancouver Conference*. 1995.
- [56] Rose, L.R.F. "An Application of the Inclusion Analogy for Bonded Reinforcements," *Int. Journal of Solids and Structures*, 17 827-838 1981.
- [57] Rose, L.R.F. "An Cracked Plate Repaired by Bonded Reinforcements," *International Journal of Fracture*, 18 135-144 1982.
- [58] Rybicki, E.F. and M.F. Kanninen. "A Finite Element Calculation of Stress Intensity Factors by a Modified Crack Closure Integral," *Engineering Fracture Mechanics*, Vol. 9 931-938 1977.
- [59] Saff, C. R. and K. B. Sanger. "Part-Through Flaw Stress Intensity Factors Developed by a Slice Synthesis Technique." *National Symposium on Fracture Mechanics (15th:1982:College Park, MD) ASTM STP 833*. 24-43. American Society for Testing and Materials, 1982.
- [60] Schehl, N. D. and D. A. Stubbs. "In Situ Eddy Current Characterization of Fatigue Cracks." Unpublished - UDRI Final Report, Contract No. F33615-89-5643.
- [61] Sun, C. T., J. Klug and C. Arendt. "Analysis of Cracked Aluminum Plates Repaired with Bonded Composite Patches." Draft Received 28 Feb 1995, Doc No. 22237.
- [62] Tarn, Jiann-Quo and Kam-Lun Shek. "Analysis of Cracked Plates With a Bonded Patch," *Engineering Fracture Mechanics*, 40 1055-1065 1991.
- [63] Timoshenko, S.P. and J.M. Gere. *Mechanics of Materials*. Monterey, CA: Brooks/Cole Engineering Division, 1972.
- [64] Van Stone, Gooden and Krueger. "Advanced Cumulative Damage Modeling," *AFWAL-TR-88-4146* 1988.
- [65] Walker, E. K. "Effects of Environments and Complex Load History on Fatigue Life," *ASTM STP 462*, 1-14 1970.
- [66] Young, A., D. P. Rooke and D. J. Cartwright. "Analysis of Patched and Stiffened Cracked Panels Using the Boundary Element Method," *Int. Journal of Solids and Structures*, 17 2201-2216 1992.
- [67] Young, M. J. and C. T. Sun. "On the Strain Energy Release Rate for a cracked Plate Subjected to Out-of-Plane Bending Moment," *International Journal of Fracture*, 60 227-247 1993.

Vita

Capt. Joel J. Schubbe [REDACTED] he graduated from R. Nelson Snider High School in Fort Wayne, Indiana and received an appointment to the United States Air Force Academy in Colorado Springs, Colorado. He earned the degree of Bachelor of Science in Engineering Sciences and his commission in the USAF in May 1986. Captain Schubbe served as an Armament Systems Analyst at the Air Force Foreign Technology Division, Wright-Patterson AFB, Ohio until entering the School of Engineering, Air Force Institute of Technology, in May 1989. He earned the degree of Master of Science in Aeronautical Engineering in December 1990. Captain Schubbe then served as Aerospace Test Facilities Manager and Program Test Manager for Aerospace Systems at Arnold AFB, Tennessee until returning to the Air Force Institute of Technology, in July 1994. He and his wife, Sherry, have three children: Jonathan [REDACTED], Jeff [REDACTED], and Jacob [REDACTED].

[REDACTED]

Form Approved
OMB No. 0704-0188

1. ANDERSON, H. (1997) (leave blank)	2. REPORT DATE Jun 97	3. REPORT TYPE AND DATES COVERED Dissertation
--------------------------------------	--------------------------	--

Joel J. Schubbe, Capt, USAF

9. SPONSORING / MONITORING AGENCY NAME(S) AND ADDRESS(ES) Mr. Jim Rudd WL/FIB Wright-Patterson AFB, OH	10. SPONSORING / MONITORING AGENCY REPORT NUMBER
---	--

12a. DISTRIBUTION AVAILABILITY STATEMENT	12b. DISTRIBUTION CODE
	A

Aging Aircraft, Composite Patch Repair, Fatigue Crack Growth	15. NUMBER OF PAGES 251
--	----------------------------

		16. PRICE CODE
--	--	----------------

17. SECURITY CLASSIFICATION OF REPORT	18. SECURITY CLASSIFICATION OF THIS PAGE	19. SECURITY CLASSIFICATION OF ABSTRACT	20. LIMITATION OF ABSTRACT
UNCLASSIFIED	UNCLASSIFIED	UNCLASSIFIED	UNLIMITED